Communauté
UNIVERSITÉ Grenoble Alpes

THÈSE

Pour obtenir le grade de

DOCTEUR DE LA COMMUNAUTÉ UNIVERSITÉ GRENOBLE ALPES

Spécialité : **Sciences de la Terre, de l'Univers, et de l'Environnement**

Arrêté ministériel : 25 mai 2016

Présentée par

Yacine Benjelloun

Thèse dirigée par **Julia de Sigoyer**
et coencadrée par **Hélène Dessales**

préparée au sein du **Laboratoire ISTerre**
dans l'école doctorale **Terre, Univers, Environnement**

La branche médiane de la faille Nord Anatolienne dans la région d'Iznik : apports de la géomorphologie et de l'archéosismologie

The middle strand of the North Anatolian fault in Iznik region: insights from geomorphology and archeoseismology

Thèse soutenue publiquement le **27 novembre 2017**,
devant le jury composé de :

Yann Klinger
Directeur de recherche CNRS, Institut de Physique du Globe, Paris, Rapporteur

Klaus Reicherter
Professeur, RWTH Aachen University, Rapporteur

Attila Çiner
Professeur, Eurasia Institute of Earth Sciences, Istanbul Technical University, Président

Jean-Philippe Goiran
Chargé de recherche CNRS, Laboratoire Archéorient, Lyon, Examinateur

Julia de Sigoyer
Professeur, Université Grenoble Alpes, Directrice de thèse

Hélène Dessales
Maître de Conférence, École Normale Supérieure, Paris, Co-Encadrante de thèse

Remerciements

Je voudrais tout d'abord remercier les membres du jury qui ont accepté d'évaluer mon travail de thèse, Attila Ciner, Jean-Philippe Goiran, Yann Klinger et Klaus Reicherter. Je leur suis reconnaissant aussi bien pour les appréciations positives que pour les critiques acérées qu'ils m'ont adressées et qui permettront d'améliorer sensiblement la qualité des publications issues de cette thèse.

Mes encadrantes, Julia de Sigoyer et Hélène Dessales, ont bien évidemment joué un rôle crucial dans la réalisation de cette thèse qui, en raison d'un contexte géopolitique tendu, aurait bien pu ne pas démarrer ou peut-être sous une forme bien différente. Malgré toutes les difficultés qui ont accompagné cette thèse, Julia et Hélène ne m'ont jamais lâché, sont restées très impliquées et motivées tout du long et notamment durant les dernières semaines, fort intenses !. Pour tout cela, et pour avoir été à mes côtés depuis sept ans, je leur adresse un immense merci !

Jongler avec plusieurs disciplines et techniques a été aussi bien une difficulté qu'une chance. Cette thèse n'aurait pas pu se faire sans la participation de plusieurs collègues, notamment Julien Carcaillet, Stéphane Garambois, Philippe Guéguen, Laurent Baillet, Riccardo Vassallo, Laurence Audin, Olivier Bellier, Pascal Lacroix, Daniel Melnick, Julius Jara Muñoz, Pierre Sabatier, et ma stagiaire de master Catherine Py-Circan. Je dois également mentionner les autres membres appartenant de près ou de loin à l'équipe Cycle, qui m'ont toujours bien accueilli malgré mes préoccupations de recherche un peu exotiques. Je remercie également les collaborateurs turcs qui nous ont apporté une aide inestimable, Mustafa Sahin, Can Ciner, Serkan Gündüz, Mustafa Aktar, Cengiz Celik, Cengiz Yildirim, ainsi que les étudiants qui ont subi (dans la bonne humeur) mon encadrement tyrannique sur le terrain, Gamze, Süha, Bugra, Can, Pinar, Deniz et Figen. Le tableau ne serait pas complet sans l'équipe technique et administrative d'ISTerre qui a assuré les côtés financiers, logistiques et matériels du projet.

C'est maintenant le moment de remercier les collaborateurs moins "professionnels" mais tout aussi importants dans la conduite d'une thèse, mes co-bureaux Baptiste, Simon, Jorge, Laura, et Judith. Pour ce qui est des autres gens super croisés au labo et parfois en soirée mondaine, j'envoie mes salutations en vrac à Camille, Okba, Hugo, Caroline, Claudia, Olivier, Johann, Hugo, Gosia, Ana, Swann, Johanes, Gokhan, Léa, Mary-Grace, Lei, Jesus,

et tout ceux que j'aurai sûrement oublié... Et tant qu'on est dans les copains, j'en profite pour saluer les "anciens" que j'ai parfois pu recroiser pendant ces quatre ans, Thomas, Vincent, Mathieu, Léa, Sylvain, Jérémy, Thomas, Vivien, David, Aurélien, Anaïs, Amandine, Agnès, Thomas, Andréa, Jean, Mathieu, et Zoé.

J'en viens maintenant aux meilleurs, mes proches, en commençant par une des dernières arrivées dans la famille, ma très chère Maureen. Une des découvertes inattendues de cette thèse, mais sans conteste l'une des plus belles. On a fait un bout de chemin ensemble, riche en émotions de toutes sortes mais couronné de succès pour nous deux ! Pourvu que ça dure ! Ma plus grande gratitude va naturellement à mes parents, qui ont donné de leur personne pour que cette thèse puisse aboutir, au propre comme au figuré, et qui m'ont toujours soutenu dans mes choix depuis tout petit. J'ai aussi une pensée pour le reste de la smala, notamment ma sœur, mes tantes, mes oncles, mes cousins et cousines. Enfin, je dédie ce travail à mes grands-parents, ceux que je n'ai pas eu la chance de connaître, et ceux avec qui j'ai eu le plaisir de passer une bonne partie de mes jeunes années (et ça continue). C'est en grimpant sur les épaules de nos aïeux que nous parvenons à voir plus loin à chaque génération.

Résumé

La faille nord anatolienne (NAF), une zone de faille dextre longue de 1000 km est caractérisée par un fort aléa sismique. Elle accommode le mouvement vers l'ouest de l'Anatolie par rapport à l'Eurasie. Dans sa partie ouest, la NAF se divise en trois branches, dont une borde le sud de la mer de Marmara et du lac d'Iznik. Ce segment médian de la NAF (MNAF) présente aujourd'hui une très faible sismicité. Pourtant, plus de six séismes décrits par les auteurs anciens causèrent des destructions dans la ville d'Iznik (ancienne Nicée), un centre politique antique important. Notre étude vise à contraindre l'activité sismique récente de la MNAF dans la région d'Iznik à plusieurs échelles de temps, par une approche combinant géosciences et archéologie.

Le premier objectif de cette thèse est de développer l'étude des bâtiments anciens comme archives de la sismicité en observant leurs endommagements et réparations successifs. Je me suis concentré sur des infrastructures critiques comme la muraille défensive et l'aqueduc de Nicée. En appliquant plusieurs techniques de datation sur les bâtiments, j'ai pu identifier au moins trois séismes sources d'endommagement depuis le 6e siècle. La quantité de dommages permet d'estimer des intensités locales de VIII sur l'échelle macrosismique européenne. Grâce à des simulations numériques, je montre que les déformations visibles sur un obélisque romain au nord d'Iznik sont compatibles avec des magnitudes proches de Mw 7 pour des distances épicentrales inférieures à 15 km.

Cinq carottes de sédiments lacustres ont été prélevées autour d'une basilique submergée par le lac d'Iznik, découverte en 2014 à 20 m de la côte, à quelques kilomètres de la NAF. Afin de déterminer l'événement à l'origine de la destruction et submersion de la basilique, des restes organiques ont été datés au ^{14}C dans l'une des carottes. Un événement sismique entre le 15e et le 17e siècle a ainsi pu être identifié.

Le deuxième objectif de cette thèse est de contraindre la vitesse de glissement quaternaire sur la MNAF et de mieux comprendre la formation du lac d'Iznik à l'ouest de la ville. Les principales failles autour du lac ont été cartées avec un MNT de haute résolution dérivé d'images Pléiades. Les marqueurs géomorphologiques décalés par la MNAF ont fait l'objet de mesures systématiques. L'analyse statistique de ces décalages a mis en évidence six ruptures majeures préservées dans le paysage, avec des déplacements cosismiques entre 2 et 6 m. Un nouveau segment de faille normale actif, oblique à la MNAF et ayant décalé

l'aqueduc d'environ 2 m, a été identifié. Ceci prouve l'activité sismique de ce segment depuis le 3e siècle ap. J.-C.

Les variations de niveau du lac d'Iznik ont été explorées à différentes échelles de temps, depuis 23 ka, pour évaluer leur composante tectonique. Les âges de trois niveaux de terrasses lacustres au nord du lac ont été quantifiés par radiocarbone et ^{10}Be produit in situ. J'ai pu déterminer un taux de glissement horizontal minimum de 5.4±2.4 mm/yr. Le basculement vers le sud des paléorivages est compatible avec un taux de glissement vertical élevé sur la MNAF entre 2 et 6.5 mm/yr.

En travaillant sur la morphologie et les lithologies de la région d'Iznik, nous avons découvert des preuves d'épisodes glaciaires LGM. La morphologie en U de plusieurs vallées à l'est du lac d'Iznik, séparées par des sauts topographiques correspond à l'empreinte d'anciens glaciers. Cette hypothèse est confirmée par la présence de moraines en bord de vallée, de blocs erratiques portant des stries glaciaires, et de sédiments glacio-lacustres. La distribution spatiale de ces marqueurs nous a permis de reconstruire l'emplacement et le retrait vers l'est de ce glacier. Les âges absolus des dépôts postérieurs à la glaciation sont compatibles avec des proxies paléoenvironnementaux du lac d'Iznik et les études réalisées sur d'autres glaciers turcs LGM. Il s'agit de la première découverte de glaciers à si basse altitude en Turquie.

Mots-clés: archéosismicité, aqueduc, archéologie, géomorphologie, faille active

Abstract

The North Anatolian fault (NAF), a 1000 km-long dextral fault zone is known for its strong seismic hazard. It accommodates the westward motion of Anatolia, relative to Eurasia. In its western part, the NAF splits into three strands, one of which passing south of the Marmara sea and the Iznik lake. This NAF middle strand (MNAF) shows nowadays a very low seismic activity. However, several ancient authors mention the occurrence of more than six destructive earthquakes that impacted Iznik (old Nicaea), an important Hellenistic and Roman political centre. Our study aims to constrain the recent seismic activity on the MNAF in the Iznik area at different time scales through a multidisciplinary approach coupling earth science and archeology.

The first goal of this thesis is to develop the study of ancient buildings as archives of the seismicity by observing their successive damages and repairs. I focus my study on Nicaea's critical infrastructures such as the 3 km-long protecting walls and the aqueduct. Applying different dating techniques to the various materials of these buildings, I was able to identify three damaging earthquakes since the 6th century AD. The amount of damage allows to estimate local intensities at VIII on the European macroseismic scale. Thanks to numerical simulations, I show that the current deformation visible on a Roman obelisk north of Iznik is compatible with magnitudes close to Mw 7 for epicentral distances smaller than 15 km.

Five lacustrine sediment cores were taken from a basilica submerged in Iznik Lake, discovered in 2014 and located 20 m from the shore, a few kilometres away from the NAF. One of the objectives was to determine the event that caused the destruction of the basilica and its submersion. The ^{14}C ages obtained on the organic remains of one core makes it possible to identify a seismic event between the 15th and 17th centuries.

The second goal of this thesis is to constrain the Quaternary slip rate on the MNAF segments around Iznik Lake, a 313 km^2-large lake located just west of the city. The main faults around the lake were mapped using a high-resolution DEM derived from Pleiades images and geomorphic markers offset by the MNAF were systematically measured. The statistical analysis of the offsets revealed six major ruptures preserved in the landscape, with coseismic displacements between 2 and 6 m. A new active normal fault segment has been identified oblique to the main MNAF. It has vertically displaced the Roman aqueduct

of about 2 m, proving the seismic activity of this segment since the 3rd century AD.

Variations of Iznik Lake level have been explored at several time scales, from now to 23 ka ago, to assess their tectonic component. The ages of three levels of lacustrine terraces north of the lake were quantified by radiocarbon and in-situ produced ^{10}Be. Based on the age of the youngest deformed terrace (Tl3), a minimal horizontal slip rate of 5.4±3.4 mm/yr was estimated. The southward tilting of the lake paeloshorelines is compatible with a high vertical slip rate on the MNAF between 2 and 6.5 mm/yr.

While working on the morphology and lithologies of the Iznik area, we have discovered significant evidence for LGM glacial events. The U-shaped morphology of several successive valleys east of Iznik separated by topographic highs is interpreted as the print of past glaciers. This is confirmed by the presence of moraine deposits on the sides of the valleys, erratic blocks bearing glacial striations and glacio-lacustrine sediments. The geographical distribution of these markers enabled us to reconstruct the former location and eastward retreat of this glacier. The absolute ages obtained from deposits postponing the glaciation are compatible with paleoenvironmental proxies in Iznik Lake and previous studies of other Turkish LGM glaciers. This constitutes the first evidence of glaciation at low elevations in Turkey.

Keywords: archeoseismicity, aqueduct, archeology, geomorphology, active fault

Contents

Introduction **15**

A Context of the study **17**
A.1 Seismogenic faults and earthquake mechanisms . . . 17
A.2 The North Anatolian Fault: geological and geodynamical context . . . 22
A.2.1 The middle strand of the NAF . . . 30
A.3 Iznik Lake basin . . . 35
A.3.1 Morphology . . . 35
A.3.2 Hypotheses of formation . . . 35
A.3.3 Modern climate . . . 39
A.4 Objectives of the thesis . . . 39
A.5 Transverse methods . . . 40
A.5.1 High-resolution imagery . . . 40
A.5.2 Dating techniques . . . 43
A.5.2.1 Interactions of the cosmic flux with the atmosphere . . . 43
A.5.2.2 Carbon-14 (^{14}C) . . . 43
A.5.2.3 Beryllium-10 (^{10}Be) . . . 45

B First evidence of low-elevation LGM glaciers in Turkey **49**
B.1 Introduction . . . 49
B.2 Study area . . . 50
B.2.1 Geographical and geological setting . . . 50
B.2.2 Modern climate . . . 52
B.3 Material and methods . . . 53
B.3.1 Processing of a Pleiades-derived DEM and geomorphological mapping 53
B.3.2 Sediment sampling and dating . . . 53

B.4 Results . . . 53
B.4.1 Topographic and river profiles between Mekece and Gemlik . . . 53
B.4.2 Field evidence of past glaciations . . . 56
B.4.2.1 Morphological evidence . . . 56
B.4.2.2 Lithological evidence . . . 62
B.4.3 Post-glacial alluvial deposits . . . 64
B.4.4 Dating . . . 68
B.4.4.1 Radiocarbon dating . . . 68
B.4.4.2 Exposure ages from in-situ produced ^{10}Be . . . 68
B.5 Discussion . . . 73
B.5.1 Glacier reconstruction . . . 73
B.5.2 Timing of the glaciation and regional correlations . . . 76
B.6 Conclusion and perspectives . . . 78
B.7 Résumé . . . 78

C Segmentation and Quaternary behavior of the middle strand of the North Anatolian fault (MNAF) around Iznik Lake (NW Turkey) 81
C.1 Introduction . . . 81
C.2 Geological and geomorphological context . . . 83
C.3 Previous paleoseismological and slip-rate studies on the MNAF . . . 87
C.4 Fault geometry and segmentation analysis . . . 89
C.4.1 Pleiades images processing . . . 89
C.4.2 Fault segmentation . . . 89
C.5 Cumulated coseismic offsets . . . 93
C.5.1 Method of measurement and uncertainties . . . 93
C.5.2 Statistical analysis . . . 95
C.5.2.1 Segment analysis . . . 95
C.5.2.2 Total population analysis . . . 98
C.6 Horizontal slip rate estimation . . . 101
C.7 Vertical offsets along the MNAF . . . 103
C.7.1 Surface offsets . . . 103
C.7.2 Subsurface offsets . . . 106
C.8 Discussion . . . 109
C.8.1 Last earthquake slip and variability . . . 109

C.8.2 Past coseismic displacements . . . 112
C.8.3 Implications for the recurrence rate and future ruptures . . . 112
C.9 Conclusion . . . 113
C.10 Résumé . . . 114

D Archeoseismological study in Iznik **115**
D.1 From ancient Nicaea to Iznik . . . 115
D.1.1 History . . . 115
D.1.2 Construction materials and techniques up to now . . . 120
D.2 Archeological study of the aqueduct of Nicaea (Iznik, NW Turkey) . . . 124
D.2.1 Introduction . . . 124
D.2.2 Methods . . . 129
D.2.3 Description of the techniques of construction observed . . . 129
D.2.3.1 Techniques MR-0028 and AR-0004 . . . 130
D.2.3.2 Techniques MR-0034 and AR-0002 . . . 132
D.2.3.3 Techniques CF-0006 and MR-0033 . . . 134
D.2.3.4 Techniques MR-0041 and AR-0003 . . . 136
D.2.3.5 Techniques MR-0036, AR-0005 and MR-0143 . . . 136
D.2.3.6 Techniques MR-0035 . . . 141
D.2.3.7 Techniques MR-0142 . . . 142
D.2.3.8 Techniques MR-0038 . . . 142
D.2.3.9 Techniques MR-0144 . . . 143
D.2.4 Chronological bounds . . . 144
D.2.5 Relative chronology of the building phases . . . 144
D.2.5.1 Phase 1 . . . 144
D.2.5.2 Phase 2 . . . 146
D.2.5.3 Phase 3 . . . 147
D.2.5.4 Phase 4 . . . 147
D.2.5.5 Phase 5 . . . 147
D.2.5.6 Phase 6 . . . 148
D.2.5.7 Phase 7 . . . 149
D.2.5.8 Phase 8 . . . 149
D.2.5.9 Phase 9 . . . 149
D.2.6 On-fault displacement of the aqueduct east of Iznik . . . 149

D.2.7 Conclusions . . . 155
D.2.8 Résumé . . . 156
D.3 3 historical earthquakes revealed on the middle strand of the NAFZ by an archeoseismological study in Iznik . . . 157
D.3.1 Introduction . . . 157
D.3.2 Description of the buildings studied . . . 161
D.3.2.1 The Roman obelisk at Elbeyli . . . 161
D.3.2.2 The aqueduct of Iznik . . . 162
D.3.2.3 The walls of Iznik . . . 163
D.3.2.4 Other buildings . . . 166
D.3.3 Inventory of the archeoseismological observations . . . 166
D.3.3.1 The archeoseismological approach . . . 166
D.3.3.2 Results . . . 172
D.3.3.2.1 Location of the damage . . . 172
D.3.3.2.2 Azimuth of the damaged walls . . . 172
D.3.3.2.3 Oriented deformations . . . 175
D.3.3.2.4 Age of the damaged walls . . . 175
D.3.3.2.5 Repairs and time constraints on deformation episodes 177
D.3.3.2.6 Vulnerability analysis . . . 181
D.3.4 Modeling of the deformation of the obelisk . . . 182
D.3.5 Discussion . . . 186
D.3.5.1 Identification of deformation episodes . . . 186
D.3.5.2 Estimation of local intensity . . . 191
D.3.5.3 Comparison with paleoseismological and historical seismicity data . . . 194
D.3.6 Conclusions . . . 196
D.3.7 Résumé . . . 198

E Evolution of coastal environments since the Quaternary: impacts of climate and tectonics 199
E.1 Basilica study . . . 199
E.1.1 Historical and archaeological context . . . 199
E.1.2 Study of sediment logs . . . 200
E.1.3 Implications for past earthquakes . . . 204

E.2 Historical variations of lake and ground levels in Iznik 205
E.2.1 Lake level variations 205
E.2.2 Markers of ground level change 206
E.3 Quaternary shorelines 209
E.3.1 General morphology of the terraces and measurement of the deformation 209
E.3.2 Tectonic and climatic components of the lake level variations observed 215
E.4 Résumé 218

Conclusions and perspectives **219**

References **225**

Appendix A Historical seismicity of the MNAF region **247**

Appendix B Protocole d'analyse du ^{10}Be in-situ **257**

Appendix C Décalages latéraux mesurés le long de la MNAF **259**

Appendix D Données GPR supplémentaires **263**

Appendix E Fiches descriptives des techniques identifiées sur l'aqueduc **269**

Appendix F Sediment cores sampled on the basilica site **301**

Introduction

This thesis project originates from a collaboration developed between archeologists and geologists from the Ecole Normale Supérieure and the Institut de Physique du Globe in Paris. This collaboration focused on the multidisciplinary study of Roman hydraulic structures like aqueducts and water distribution networks in cities, from a joint archeological, geological and environmental perspective. Previous works in Italy and southern France had shown that aqueducts could be studied as archives of paleoclimate and past seismicity. The analysis of such natural phenomena for the historical period benefits a lot from the additional data provided by human sciences. This multidisciplinary perspective often makes it possible to work on intermediate time scales that are less accessible by conventional approaches. In the case of earthquake science, geophysical observation networks can monitor intensively the largest and most active fault zones, which are generally easily mapped in the landscape and produce big ruptures quite frequently. Large ruptures also happen on less active, secondary fault segments but with longer recurrence times, and with slow deformations harder to detect. In some cases the seismic potential of such structures is underestimated or even ignored. In the Mediterranean area, apparent paradoxes rise from the comparison between the observed absence of modern seismicity in zones where several big earthquakes are described in the past. The Eastern Anatolian fault zone and the northern segments of the Levant fault are good examples. Another illustration of this kind of paradox exists at the western termination of the North Anatolian fault zone (NAFZ). South of the main active fault that crosses the Marmara Sea run two parallel secondary strands, known as the middle and southern strand of the NAFZ. Although almost no seismicity has been monitored recently on the middle strand, the neighbouring cities were affected by several destructive earthquakes in the past 2000 years.

Located 3 km north of the middle strand of the North Anatolian fault (MNAF), the city of Iznik was chosen as a very promising study site to experiment the potential of a joint archeological, geomorphological and seismotectonic approach.

The city had been a significant political centre during the Roman period, and presents very rich archeological remains, completed by the impressive discovery in 2014 of an ancient basilica submerged in the lake. These well preserved remains can be used as markers of the historical tectonic activity. The historical earthquake catalog seems quite complete, but

the lack of good paleoseismological data increases the value of such an archeoseismological study.

The presence of Iznik Lake is linked to a variety of morphological markers, potentially deformed by the active faults, and enlarges the possible research scopes. This site, and the combining of approaches, thus raise important questions about the characteristics of the middle strand as part of the western termination of the North Anatolian fault.

The current information on the middle strand of the NAFZ is rather puzzling. Few geophysical studies have addressed its seismic potential in the last 30 years, and it was even suspected to be an inactive fault (Le Pichon et al., 2014). Although the calendar of the past seismicity in the last 2000 years is quite well known for Iznik region, the precise locations of the past ruptures are not well constrained. A better seismic hazard assessment of the MNAF region requires to know: (1) the fault segmentation, (2) the typical magnitudes that can be expected on this fault, as well as (3) the range of recurrence times between big earthquakes. The presence of several well preserved ancient buildings of different periods makes Iznik a good working field to test the possibilities of an archeoseismological approach in this regard. On the longer term, it is also important to quantify the horizontal slip rate of the MNAF at different space and time scales, in order to know the speed of stress accumulation. The morphology around Iznik Lake basin can also be used to retrieve the vertical slip on the central segments of the MNAF.

In the first chapter of this thesis, the seismotectonic and geographic context of the study are presented. The main techniques used throughout the different sections of this work are also introduced. The three next chapters follow a chronological logic.

Chapter B is dedicated to the chronological frame of the late Pleistocene and Holocene sedimentary formations that mainly compose the environment of the MNAF and Iznik Lake basin. Field evidence of glacial imprint in the valleys crossed by the MNAF are also presented. Chapter C is focused on the long term segmentation and Holocene seismic behaviour of the MNAF in the surroundings of Iznik Lake basin. The study focuses on a set of laterally displaced geomorphic markers to retrieve the last major earthquakes that ruptured the fault.

The archeological approach, based on the study of buildings, is developed in chapter D. First, the history of Iznik and the evolution of the local construction techniques through time are introduced. Then the techniques and phases of construction of Iznik aqueduct are analyzed for the first time. Finally, an archeoseismological approach is applied on Iznik buildings to find several episodes of earthquake damage.

The final chapter of the thesis is focused on the environment of Iznik Lake. This chapter makes the link between the long term vertical deformation occuring on the MNAF south of the lake and the historical variations of the coast line. It also introduces the possible future of this project through preliminary results on a basilica discovered in the western part of Iznik, today submerged by the lake waters.

Chapter A

Context of the study

A.1 Seismogenic faults and earthquake mechanisms

The idea that great earthquakes might be especially associated to peculiar mechanical discontinuities appeared in the last quarter of the 19th century, when it was observed that most earthquakes were located on the mountain lines (Hoernes, 1878; Louderback, 1942). Those discontinuities, designated as faults, are major zones where finite lithospheric deformation takes place. Many tectonic faults active today are located on older preexisting geological structures, inherited from previous deformation stages, and exist as broad fractured zones several hundred of meters wide. Due to plate tectonics motion, fault zones see stress accumulate in the rigid upper crust, until a certain threshold is reached. At this point, the volume of rock across the fault breacks suddenly and generates an earthquake: the accumulated energy is liberated as radiating elastic waves propagating and reaching the surface. Faulting can only occur on a limited depth in the upper crust because below a certain depth, the pressure and temperature conditions imply that rock deformation occurs plastically. However, some deep-focus earthquakes were also discovered several hundred kilometers below the surface in subduction zones (Wadati, 1935). It has been proposed that these deep earthquakes could be linked to mineral transition phases of mantle peridotites (Wang et al., 2017). The particular depth that defines the elastic thickness of the crust was estimated in the late 1890's as ∼10 km and extended to 20-50 km by experimental works (Van Hise, 1904; Adams, 1912; Bridgman, 1936, 1945).

In the period of time separating two successive earthquakes, the interseismic phase, the deformation observed by geodesy far from a given fault zone corresponds to the tectonic plate's motion. When this relative motion decreases to virtually zero toward the fault line, the fault is "locked" and stress is accumulated (Fig. A.1). The stress accumulated during the interseismic period is released during the earthquake (coseismic phase). Contrary to the interseismic period, during an earthquake the larger displacements are measured near

the fault line and decrease away from the fault (Fig. A.1). In the last decades, progress in geodesy and seismology has led to introduce a postseismic phase following an earthquake during a few days to several months, which includes replicas, aseismic slip and viscous crustal deformation (Savage and Prescott, 1978).

The interseismic, coseismic, and postseismic phases are the main stages of the earthquake cycle (Fig. A.2). As we will see below, knowing the frequency of this cycle is an important matter in earthquake risk mitigation. However, observations suggest that the time separating two cycles and the coseismic slip in each cycle are for many fault zones not constant nor regular (Migowski et al., 2004; Schlagenhauf et al., 2011). Not all fault zones move by producing surface-rupturing earthquakes. In some cases, slow relative motion takes place in an aseismic manner. This slow "creep" phenomena is observed on certain sections of the San Andreas Fault (Steinbrugge et al., 1960) and along the Ismetpasa segment of the North Anatolian Fault Zone (Ozener et al., 2013a; Bilham et al., 2016).

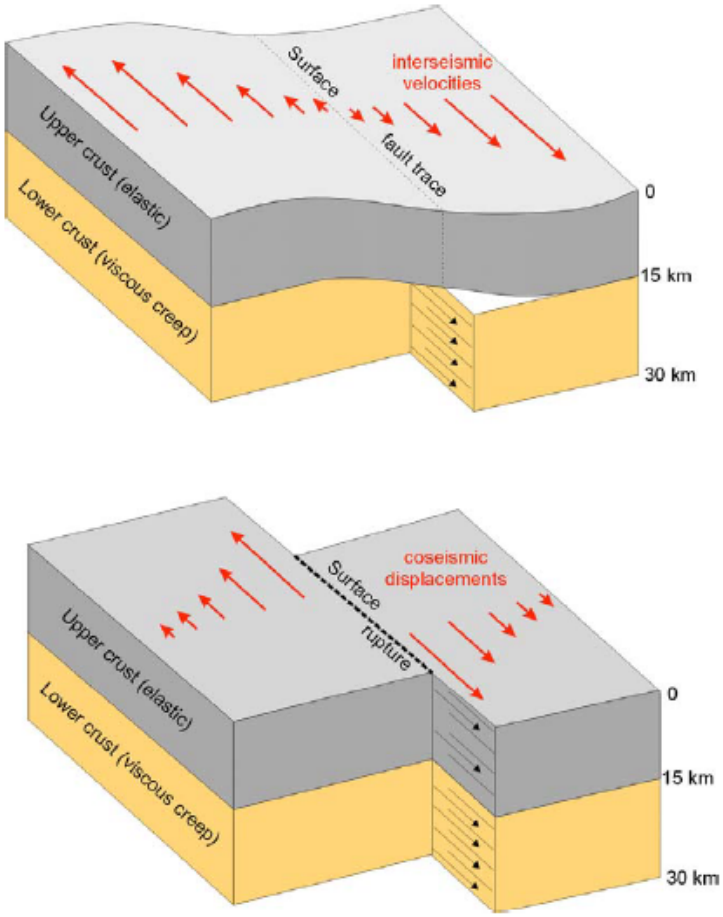

Figure A.1: Tectonic behavior of the crust during the interseismic (top) and coseismic (bottom) periods for a locked strike-skip fault, following Reid (1910)'s theory of elastic rebound.

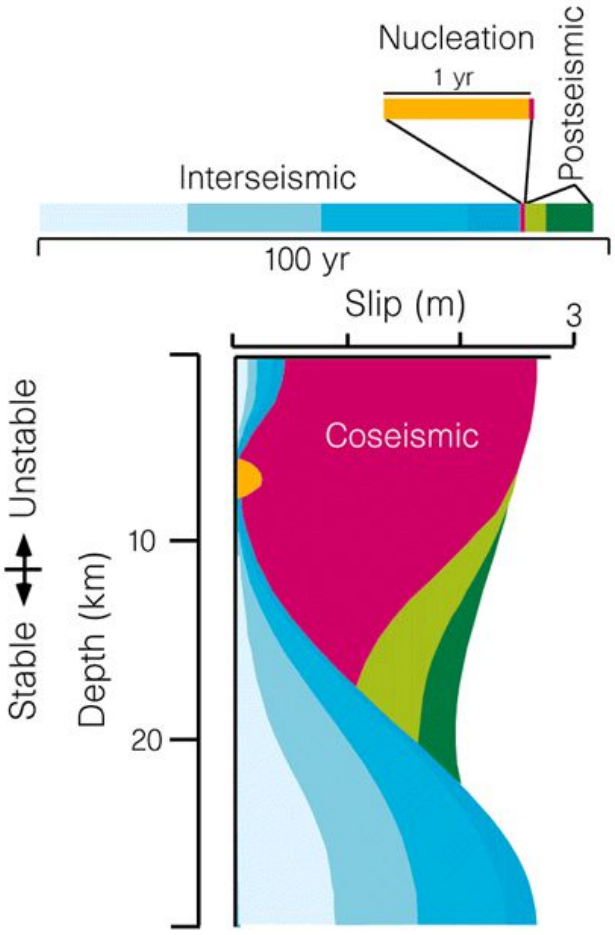

Figure A.2: Evolution of slip with depth during the different phases of the seismic cycle for a strike-slip fault (Scholz, 1998 after Tse and Rice, 1986).

Big earthquakes can produce significant surface shaking which, in populated areas, generally causes great damage to civil infrastructures. The conjunction of the effects of the earthquake proper with all its derived natural and societal effects (i.e. fires, landslides, tsunamis, floods, interruption of vital services to the population, destruction of buildings...) often results in high casualties. This justifies the need to assess the seismic risk. Seismic risk is defined as the combination of the vulnerability and seismic hazard of a given site. The vulnerability depends on the individual responses of the buildings and on social aspects, including the application of seismic codes in the organization of the city. Seismic hazard includes three components: the seismic source, the wave propagation, and the site effect. To assess seismic hazard in a given area, fundamental parameters of earthquake occurrence need to be investigated, such as the time scale of **damaging earthquake repetition**,

the **magnitude range** to expect, the **size of the affected area** and the **intensity of shaking**.

Knowing the frequency of big earthquakes is in many cases difficult because the instrumental record of seismicity has only been working for around one century, which represents a very small fraction of a fault's history. The historical accounts of past earthquakes can extend our knowledge up to ∼2000 BC even if they often provide fragmentary data without precise locations and magnitudes. By contrast, it is possible to observe earthquake recurrence times as high as several millenia. That is why many, slow-deforming or recently inhabited areas do not have any report of past earthquakes, and repetition times can only be constrained by finding geological evidence of faulting.

Gutenberg and Richter (1954) have observed that earthquake occurrence follows a peculiar magnitude-frequency relationship, known as the "Gutenberg-Richter (GR) law" (Fig. A.3) :

$$Log(N) = a - bM$$

where N is the cumulative number of earthquakes with magnitudes equal to or greater than M occurring during a given period of time, and a and b are constant. a indicates the total seismicity rate of the region while b describes the ratio between big and small earthquakes and is generally close to 1 for tectonic earthquakes.

On some faults, very big earthquakes have also been found to occur more frequently than the GR law would suggest (Scholz, 2002). These big events are called "characteristic earthquakes" and there are still debates on whether certain fault zones present such a behavior (Page and Felzer, 2015). It appears that different fault zones can follow different behaviors on a multi-millennial time scale, which led to the development of several recurrence models (Fig. A.4) having different consequences regarding seismic hazard analyses (Sieh, 1981; Schwartz and Coppersmith, 1984; Youngs and Coppersmith, 1985). It is important to note that the geographical scale of observation (i.e. whole fault system or segment) is likely to influence the perceived fault behavior (Wesnousky, 1994). This is the reason why seismotectonic studies must encompass variable spatial and temporal scales. Documenting the fault behaviour at these different scales involves acquiring data on the calendar of seismicity on each fault segment, on the characteristics of the earthquakes, and constraining long and short term slip rates.

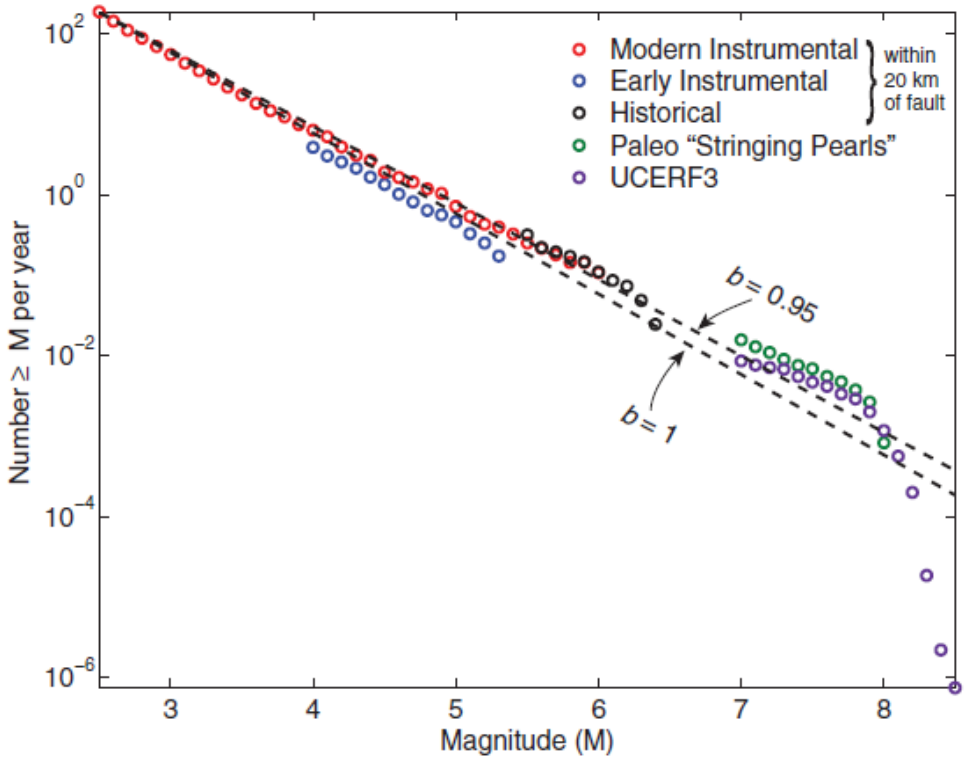

Figure A.3: Distribution of the Southern San Andreas Fault zone seismicity with magnitude for different catalogs and models. Each catalog is consistent with a GR law, represented as broken lines (taken from Page and Felzer, 2015).

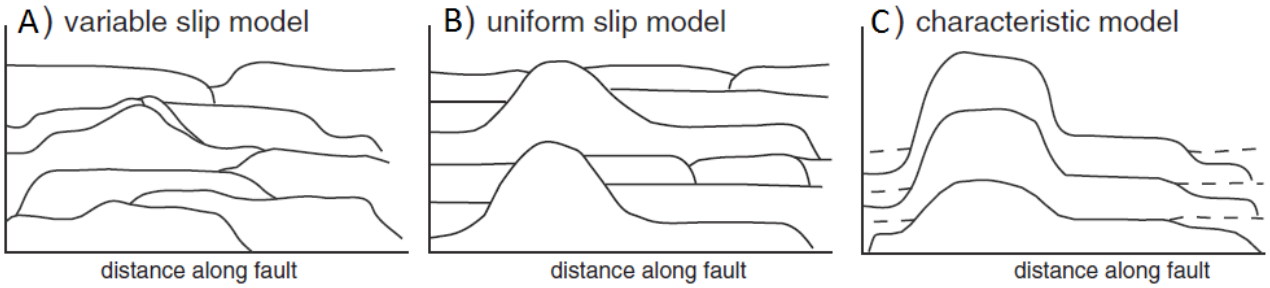

Figure A.4: Schematic models of slip accumulation with earthquake recurrence along strike. (A) In the variable slip model, earthquakes of variable size happen randomly in time and space so that the long-term slip rate remains uniform. (B) In the uniform slip model (Sieh, 1981), localized big earthquakes happen with the same slip distribution, while the surrounding sections of the fault are ruptured by smaller, more frequent events so that the long-term slip rate remains uniform. (C) In the characteristic earthquake model, the fault is also ruptured by large event that keep the same slip distribution but presents a deficit of moderate earthquakes so that the long-term slip rate varies along-strike (taken from Zielke et al., 2015).

A.2 The North Anatolian Fault: geological and geodynamical context

The North Anatolian Fault Zone (NAFZ) is a ∼1500 km long right-lateral strike-slip structure and one of the most active continental faults in the world. The tectonic significance of this fault zone was only recognized in the late 20th century, with the series of major earthquakes that ruptured the fault over 800 km from east to west between 1939 and 1999 (Ketin, 1968; Barka, 1999). Since its development, the NAFZ has been accommodating the relative motion of the Eurasian and Anatolian plates with a velocity of about 20 mm/yr (McClusky et al., 2000; Fig. A.5).

The main active tectonic structures in Anatolia are linked to the northward motion of the Arabian plate relative to Eurasia, causing the lateral escape of the Anatolian block, along the NAFZ in the north and a "conjugate" structure in the southeast, the East Anatolian Fault Zone (EAFZ). At the continental scale, the NAFZ is an arcuate structure that operates the link between the Eurasia-Arabia collisional contact in the east, and the Aegean extensive area (McKenzie, 1972).

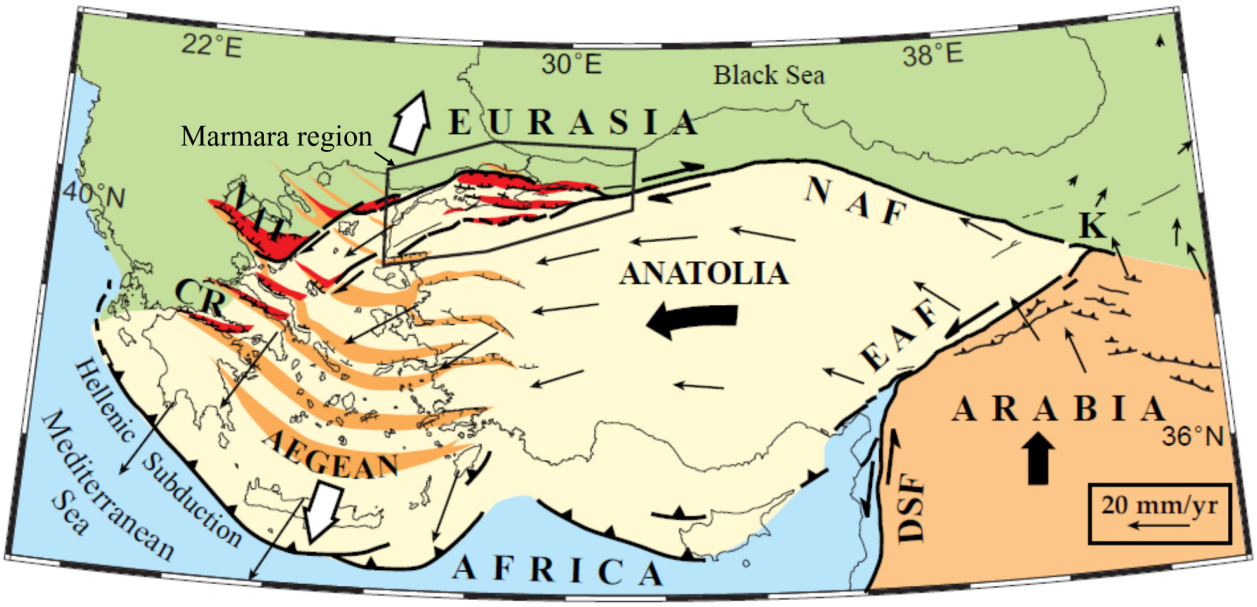

Figure A.5: General geodynamic setting of Anatolia. The velocity field is from Reilinger et al. (1997). K=Karliova triple junction, EAF=East Anatolian Fault, DSF=Dead Sea fault, NAT=North Anatolian Trough, CR=Corinth Rift(from Armijo et al., 1999).

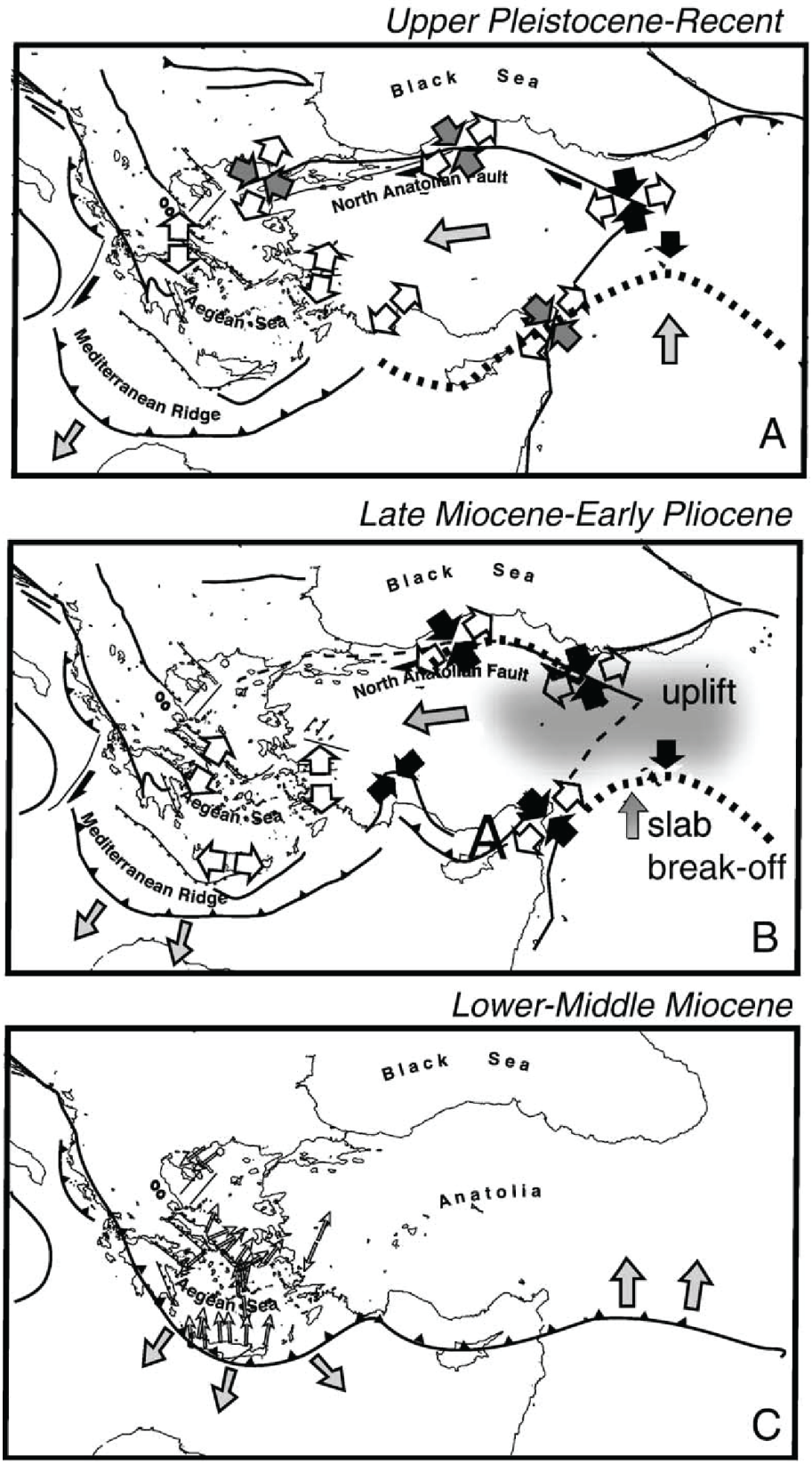

Figure A.6: Formation mechanism and propagation of the NAFZ in northern Anatolia, superimposed on the current coastline. Black and grey arrows indicate shortening direction while white arrows indicate extension (from Faccenna et al., 2006).

The collision between Eurasian and Arabian continents along the Bitlis-Pontides belt occurred in the late Oligocene, leading to the closure of the regional branch of the Tethys ocean and the stacking up of continental fragments, volcanic arcs and oceanic terrains along a suture zone (Şengör et al., 1985). In the meantime, extension began in the Aeagean. The initiation of the NAFZ has been generally assumed to be triggered by this combination of collision in eastern Anatolia and extension in the Aegean region (Fig. A.6).

The underlying mechanics of Anatolia westward motion have been debated and related to various models driven either by the eastern collision or by the retreat of the Hellenic trench (Faccenna et al., 2006). The NAF formation initiated within a wider keirogen called the North Anatolian Shear Zone (Şengör et al., 2014), and associated with compression. From a large area cut by various faults activated and deactivated through time, the deformation was progressively concentrated on a narrow zone composed of only few strands after the Messinian, so that most deformation in Anatolia is today accommodated by the northern strand of the NAF (NNAF) (Fig. A.7). According to Armijo et al. (2002), the fault zone grew, possibly from eastern Anatolia, by westward propagation through the lithosphere over ∼10 Ma, and reached The Corinth Rift at 1 Ma (Armijo et al., 1996). This propagation to the west is associated to a modification of the regional tectonic regime from transpression to transtension at the beginning of the Quaternary (Bellier et al., 1997). The western termination of the NAF lies in the Marmara region. There, the NAF bifurcates into several strands (two or three depending on the authors), and probably exploits preexisting rifts from the Aegean extension, which themselves follow inherited structures from the paleotectonic stages (Şengör and Yilmaz, 1981; Şengör et al., 1985; Şengör et al., 2005). Since the late Miocene-Pliocene around 3-4 Ma, the tectonics of Marmara region are dominated by the strike-slip mechanism along the NAF strands (Barka, 1992).

The fault visible today presents itself as a zone of crushed rocks a few kilometers wide. In the east of Anatolia, close to Karliova, the fault zone intersects the EAFZ that strikes NE-SW and joins the Dead Sea Fault Zone near Antakya and northern Syria (Allen, 1969). This region is known as the Karliova triple junction between Eurasia, Anatolia and Arabia (Fig. A.5). In most of central Anatolia, the NAFZ appears as a unique fault strand, except in the region of Niksar where the eastern segments bifurcate to the southwest on more than 200 km and form a large restraining bend. A limited duplication is visible west of Bolu, with two small segments passing just south of Düzce (Barka and Kadinsky-Cade, 1988; Fig. A.7). The western termination of the NAFZ is more complex and extends to the north of the Aegean Sea. In northwestern Anatolia, the relative continuity of the fault zone decreases and gives way to more, overlapping fault segments dominated in the south by an extensive tectonic regime (Koçyigit and Özacar, 2003).

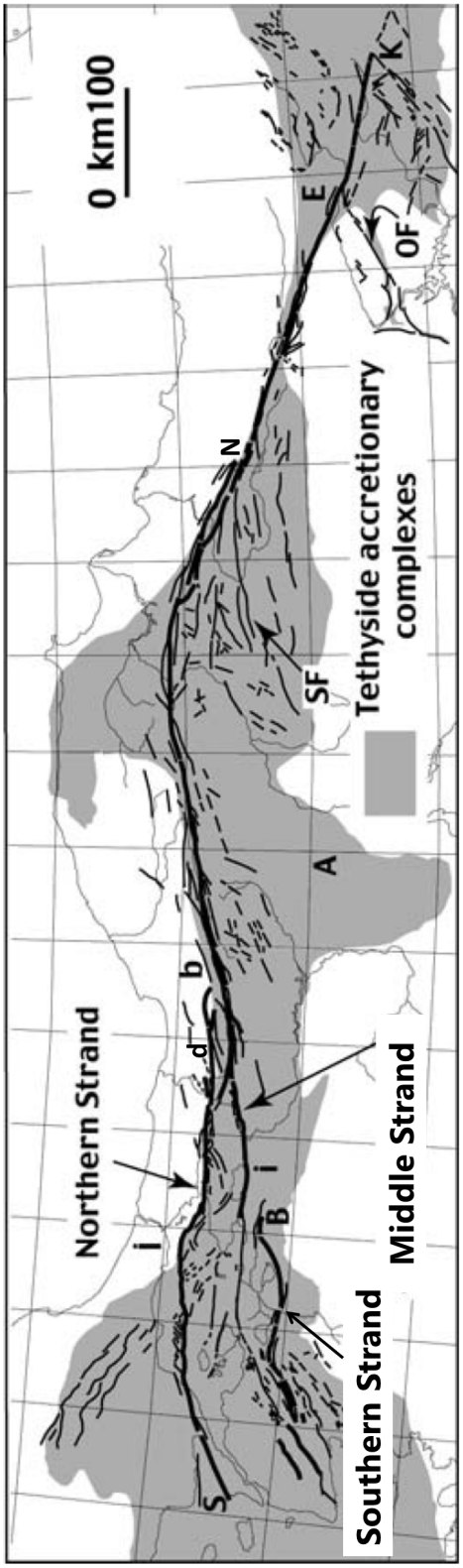

Figure A.7: Large scale fault geometry and segmentation of the NAFZ and associated structure inside the keirogen (modified from Şengör et al., 2005). b=Bolu, d=Düzce, i=Iznik Lake, A=Ankara, B=Bursa, I=Istanbul, E=Erzincan, OF=Ovacik fault, SF=Sungurlu fault.

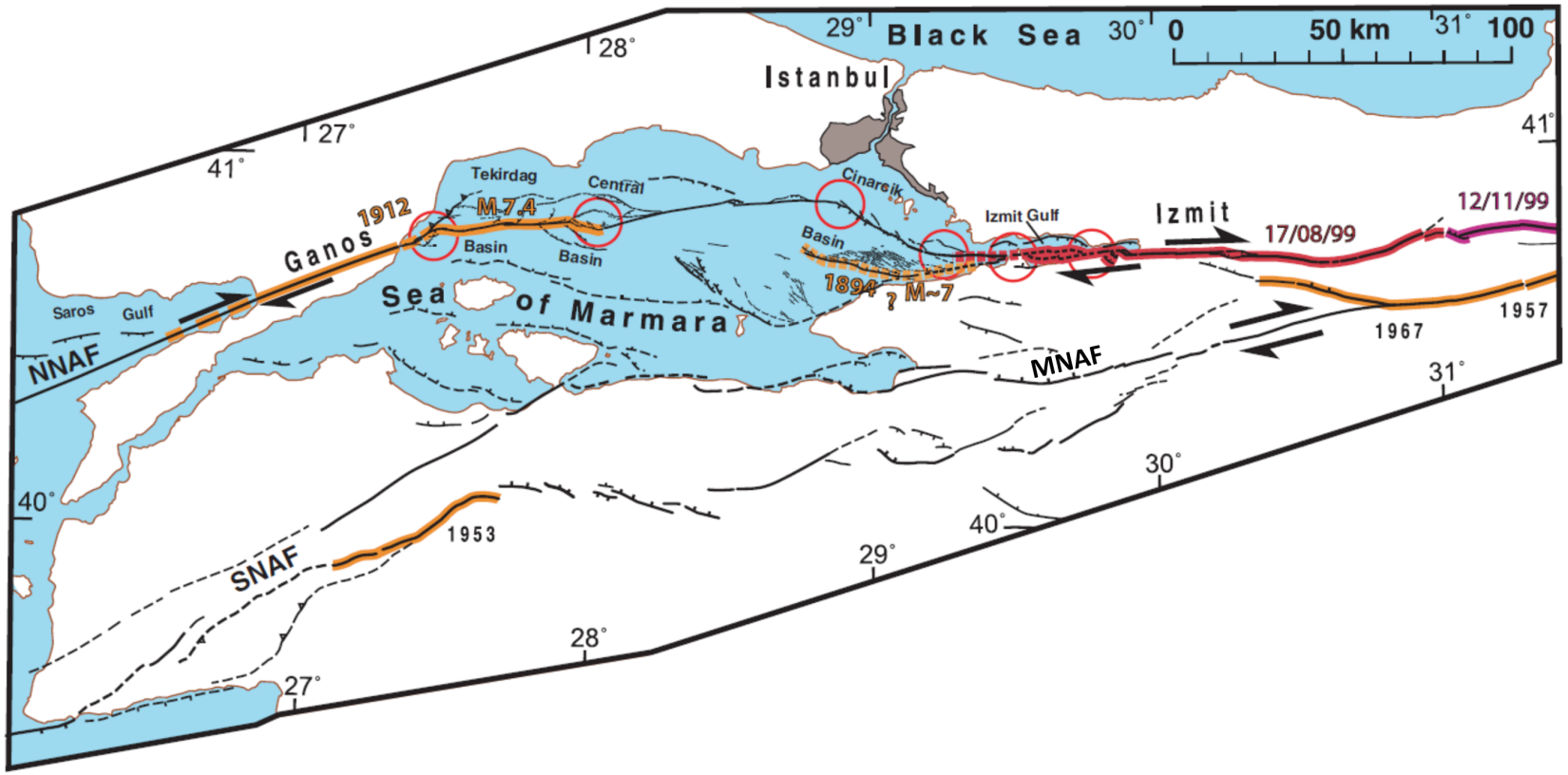

Figure A.8: Segmentation of the NAFZ in the Marmara region. The fault segments that broke during recent ruptures are highlighted in colour. Significant geometric complexities in the Marmara Sea are shown with red circles (from Pondard et al., 2007).

In its western part, The NAF is divided into three strands. The northern strand (NNAF), which continues the main fault zone in the Marmara Sea from Izmit Gulf to Gelibolu Peninsula, locates most of the total slip of the NAFZ, about 80%, and is likely to produce a major earthquake in the next decades (Hubert-Ferrari et al., 2000; Parsons et al., 2000). The southern strand (SNAF) which crosses the land south of the Marmara Sea is the other major NAFZ strand with about 20% of the total slip (Armijo et al., 2002; Flerit et al., 2003). This southern strand subdivides to form a third, middle strand (MNAF) composed of several successive segments separated by pull-apart type basins (Fig. A.8). In the Sea of Marmara, the NAF is interpreted by Armijo et al. (2002) as a segmented fault system including pull-apart structures suggesting a transtensional tectonic regime, whereas Le Pichon et al. (2001) describe a continuous, purely strike-slip fault. Both interpretations have serious earthquake hazard implications on whether a future rupture propagating on the central segment in Marmara Sea could be stopped by step-overs.

Geological reconstructions suggest a mean crustal motion on the NNAF between 14 and 20 mm/yr during the last 3-4 Ma, in agreement with the GPS measurements (Schindler, 1997; Le Pichon et al., 2001). Armijo et al. (1999) have measured a total lateral displacement of $\sim$85$\pm$10 km over the last 5 Ma in the Marmara region, which is consistent with a relative stability of the long-term regional kinematics until today. This measurement, as well as the time when the NAF reached the Marmara region, were however disputed (Yaltırak et al., 2000; Şengör et al., 2005). In eastern Anatolia, a similar total displacement was estimated (Şengör et al., 1985; Şengör et al., 2005). An age of 10 Ma for the NAF initiation in eastern Anatolia would thus imply that the average long-term slip rate was twice as fast in the Marmara region (Armijo et al., 1999).

The paleoseismic history of the NAF is quite well known for the last centuries, especially on the northern strand, since the area has been inhabited by important civilizations since Ancient Times and is the place of growing trenching studies. Numerous reliable data are available and cover almost two seismic cycles since $\sim$1500 AD. Historical seismicity suggests that the major earthquakes on the NAF occur in rapid successions, separated by a few centuries of relative quiescence (Ambraseys, 1970). As earthquakes tend to occur at the tip of previous rupture zones where the stress has increased, propagating earthquake sequences can develop along the NAF during some cycles, breaking the entire fault length east of Marmara (Pondard et al., 2007). Stein et al. (1997) have reviewed the historical data for the last millenia and identified three main sequences of earthquakes in the last millenia : 967-1050 AD in the central part eastward, 1254-1784 with a mainly eastward progression of ruptures starting from the Marmara Sea in 1509, and 1939-1992 (Fig. A.9). This last sequence benefited from modern seismological instruments and a better documentation. It started with Erzincan earthquake in 1939 and continued westward with seven other ruptures between 1942 and 1999, leaving the Marmara Sea segments as the only portion of the NAFZ to have not been ruptured in the last century. In contrast to the eastern NAF, the Marmara Basin stands as a geometrical and mechanical complexity that can stop or

delay earthquake ruptures (Fig. A.8). Paleoseimological studies suggest that this region is characterized by shorter recurrence times and isolated events, possibly switching between the different strands (Pondard et al., 2007; Fraser et al., 2010).

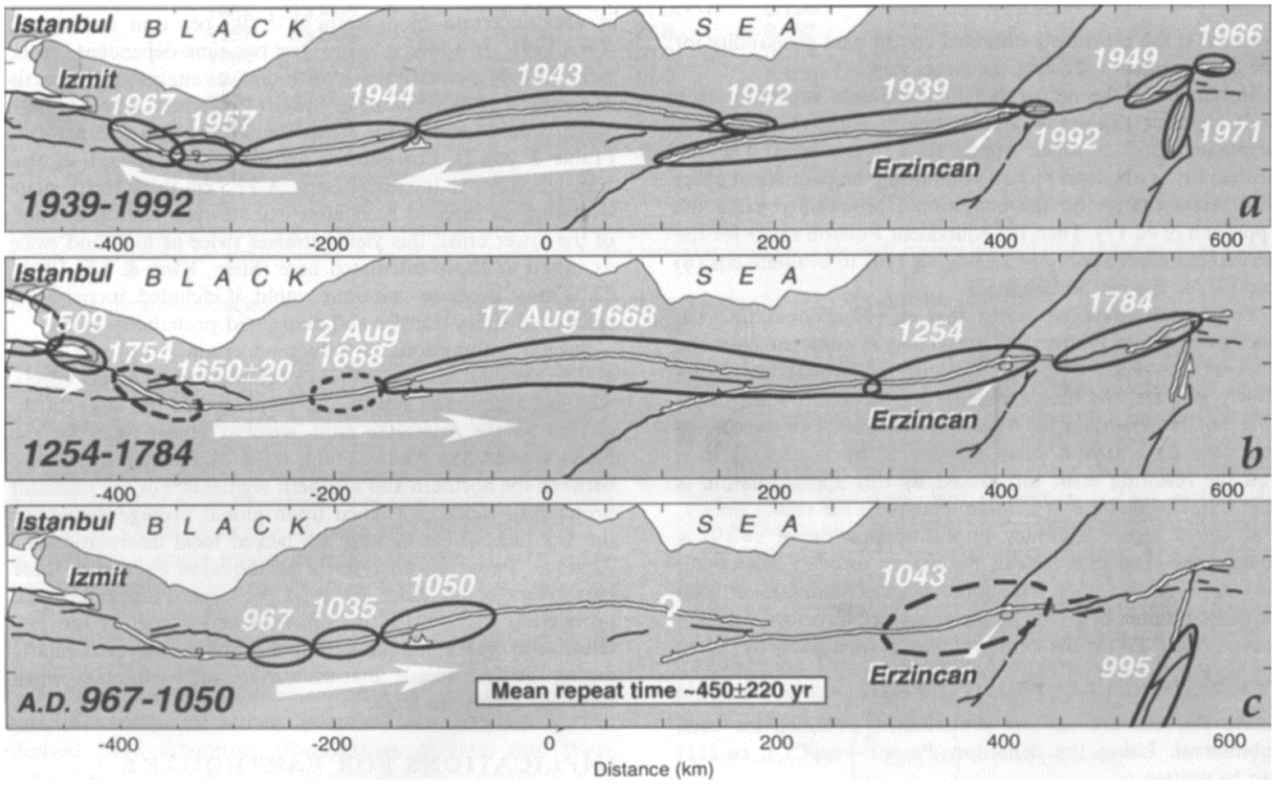

Figure A.9: Earthquake propagation sequences along the EAF and NAF east of Marmara identified from the historical catalog (from Stein et al., 1997).

The recent surface ruptures on the NAF presented a large-scale en-echelon pattern, in which the rupture propagates across relatively short segments not exceeding a few kilometres in length, and it is not frequent to find uninterrupted rupture along hundreds of kilometers. This is consistent with the segmented geometry of the fault zone that was observed during the first fine scale field works (Barka and Kadinsky-Cade, 1988). Aseismic creep has also been well documented for several decades in the central section of the NAF on the Ismetpasa segment, with velocities as high as ∼10 mm/yr (Cakir et al., 2005; Karabacak et al., 2011; Kaneko et al., 2013; Bilham et al., 2016; Rousset et al., 2016).

Modern microseismicity is concentrated along the main tectonic active structures which are the three strands of the NAFZ (Fig. A.10). It consists mainly of extension earthquakes, of magnitudes lower than 5. The last medium size earthquake in the area happened in Gemlik Bay on 2006 November 24th (Mw=5.1) with a dextral mechanism, raising debate on the current activity of this fault segment (Le Pichon et al., 2014). Three microseismicity

gaps are visible (1) in the middle of the Marmara Sea, (2) between Izmit and Yalova, and (3) between Mekece and the Karsak pass along the MNAF (Fig. A.10). These segments are blocked to a significant depth (15-20 km). The first one is known to be a critical area for a potential big rupture (Hubert-Ferrari et al., 2000; Parsons et al., 2000) whereas the second one located the 1999 August 17th rupture. The seismic history of the third one is less known, but no earthquake with a magnitude over 6 has been observed in the last 200 years (Stein et al., 1997). It has been proposed to be in a quiescence state, but could be a candidate for a future rupture. It has been observed that earthquakes typically nucleated in the microseismicity clusters and then propagated along the segments showing fewer activity such as seismicity gaps. This is the reason why our study will focus on the fault segments between Mekece and Gemlik.

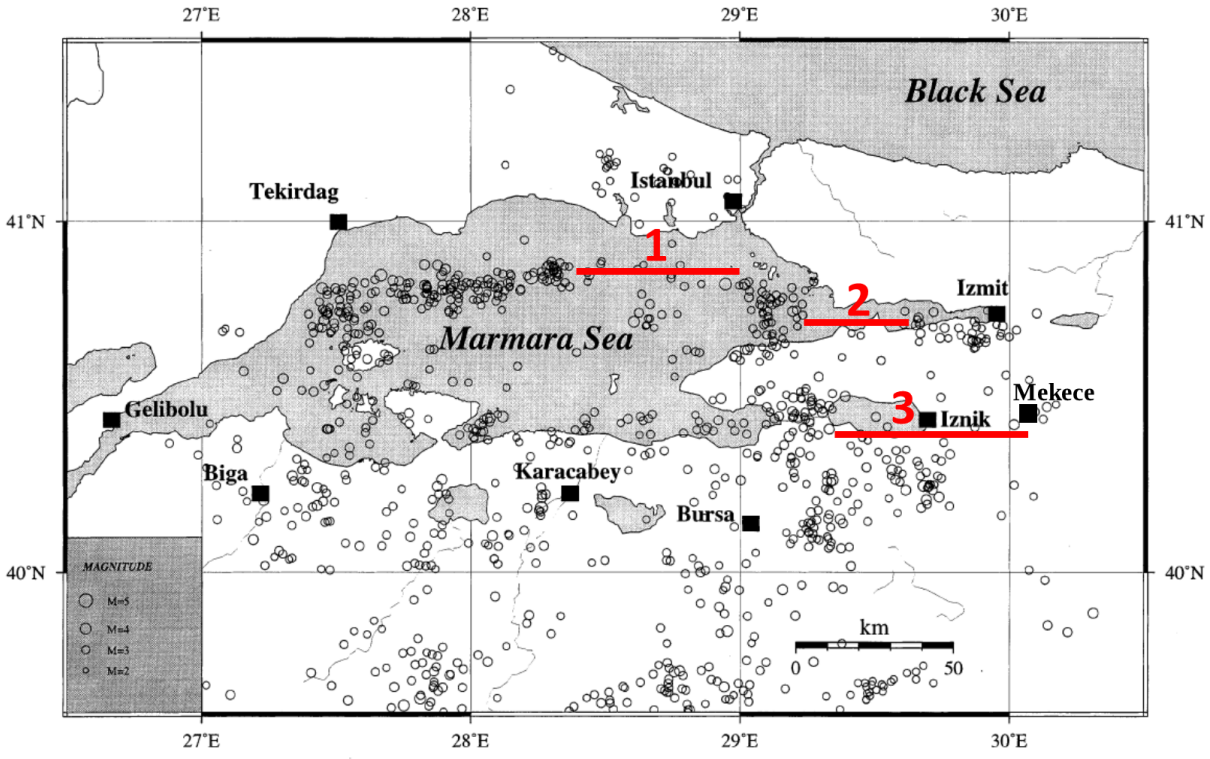

Figure A.10: Instrumental seismicity of the Marmara region between 1986 and 1996. In red are located the microseismicity gaps mentioned in the text (modified from Gürbüz et al., 2000).

A.2.1 The middle strand of the NAF

The middle strand of the NAF (MNAF) was quite intensively studied in the eighties and early nineties as part of a Turkish-Japanese collaboration (Isikara and Honkura, 1986; Honkura and Isikara, 1988, 1989, 1990; Honkura and Işikara, 1991; Ikeda et al., 1991). Toksöz et al. (1979) had reported this fault east of Gemlik Gulf to be a seismic gap, like the parallel segment on the NNAF west of Izmit, which could locate a future major rupture. This work included geological observations of Quaternary faulting, paleoseismological trenching, subsurface geophysical surveys, and seismicity monitoring. It was especially observed that the local seismicity was very low even for small magnitudes, contrary to the northern strand where earthquake swarms were noticed. After the 1999 earthquakes, and relying on the slip rate recorded on the NNAF (Fig. A.11), scientists considered that the main risk was focused on the central Marmara fault segment, and the research activity on the MNAF decreased. Nevertheless, the past earthquake scenarios for the MNAF remain very uncertain. It is therefore crucial to acquire new data for seismic hazard assessment.

Given that the relative motion across the MNAF and SNAF is small (<10 mm/yr) and much lower than the one on the NNAF (∼25 mm/yr), the latter tends to dominate the geodetic signal (Fig. A.11) and most studies amalgamate the two southern strands into a unique tectonic discontinuity (Armijo et al., 2002; Flerit et al., 2003). That often makes it difficult to extract a specific individual slip rate for the MNAF. Straub et al. (1997) have computed a 2-3 mm/yr slip rate across the MNAF in the Gemlik Gulf, which is significantly lower than the 20-25 mm/yr of the NNAF in the Marmara Sea. Relying on this GPS slip rate and using a 7-8 km offset of the coast line in the Gemlik Gulf and of supposedly older oblique faults east of Iznik Lake, Öztürk et al. (2009) have deduced a 3.7-2.6 Ma age for the initiation of the MNAF east of the Marmara Sea. Using GPS observations and block modelling, Reilinger et al. (2006) and Meade et al. (2002) have observed that the slip rate increases from east to west along the MNAF. More recently, Ergintav et al. (2014) have estimated a 5±2 mm/yr horizontal slip-rate across the Gulf of Gemlik.

Several bathymetric and seismic surveys were done in Iznik Lake and Gemlik Gulf, which allowed to refine the fault geometry (Yaltırak and Alpar, 2002; Alpar et al., 2003; Kurtuluş and Canbay, 2007; Kuşçu et al., 2009; Öztürk et al., 2009; Vardar et al., 2014). The most important work realized recently that focused on this fault strand was Dogan (2010)'s PhD thesis, which was partly published (Doğan et al., 2015) and includes sedimentary stratigraphy observations, morphotectonic analyses, tectonic stress reconstructions and paleoseismological trenching between Geyve and Gemlik. GPS surveys were also carried out near Iznik and did not detect any relative motion between the stations located 1.5 km across the fault line, thus ruling out creep occurence on this fault segment (Akay and Ozener, 2009; Ozener et al., 2013b). This GPS array was concentrated in the first kilometers around the fault and could not be used to properly quantify a slip rate. The fault passing south of Iznik could be a "locked" segment accumulating tectonic stress.

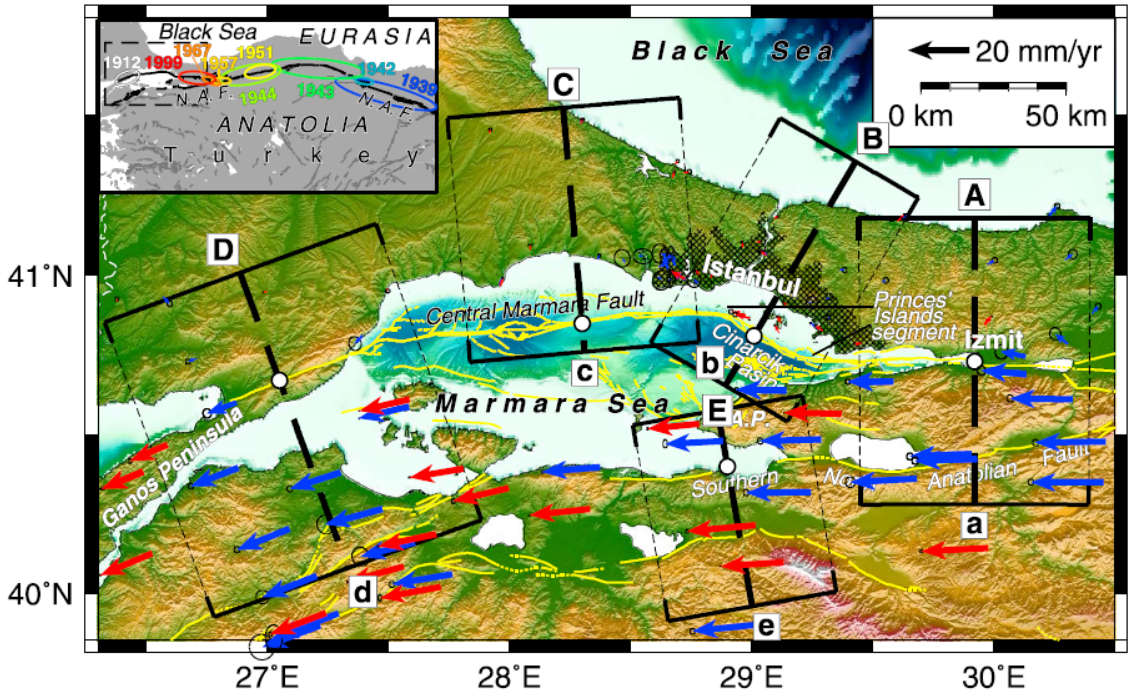

Figure A.11: GPS velocities measured in the Sea of Marmara, with respect to Eurasia (continuous stations in red and survey sites in blue). Active faults are drawn in yellow. The insets displays the twentieth century sequence of major earthquakes on the NAF (from Ergintav et al., 2014).

The MNAF east of the Marmara Sea is commonly divided into three main segments : the Geyve, Iznik and Gemlik segments , separated by releasing stepovers (Barka and Kadinsky-Cade, 1988; Özalp et al., 2013; Cambazoğlu et al., 2016; Murru et al., 2016). These stepovers correspond to three topographic depressions: the Pamukova plain, Iznik Lake, and Gemlik Gulf (Fig. A.12). Further west, the Zeytinbagi and Bandirma segments, separated by a pull-apart basin, can also be included in the MNAF system (Fig. A.12). The fault segments east of Gemlik follow very well inherited lineaments of the suture zone, belonging to the Pontides geological ensemble (Fig. A.13). They result from the collision between Laurasia and Gondwana which closed the Paleo-Thetys in the end of the Mesozoic. Fragments of Laurasia constitute the area north of the NNAF (Istanbul-Zonguldak zone, IZZ) and also the western edge of the Armutlu peninsula (Rhodope-Pontide fragment). The rest of the peninsula located between the NNAF and the MNAF belongs to the Sakarya block, a part of the northern margin of Gondwana which, after colliding with the IIZ, was burried in depth and underwent metamorphism. It includes an ophiolite and metamorphised sediments. Another part of the Sakarya block, south of the MNAF, was not dragged in depth and do not show traces of metamorphism (Şengör and Yilmaz, 1981; Yılmaz et al., 1995, 1997).

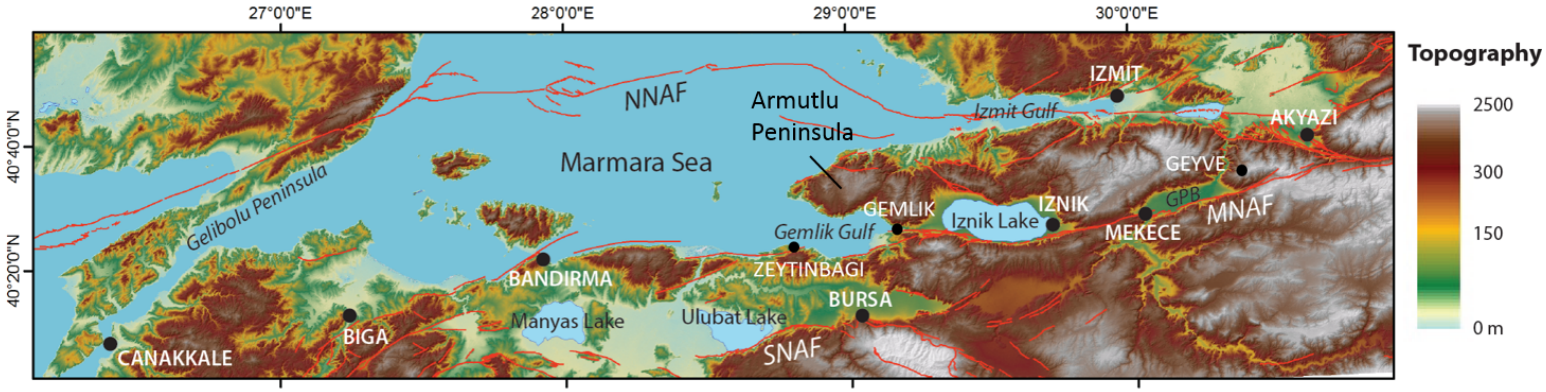

Figure A.12: Segment geometry of the NAFZ in the Marmara region. The active fault segments, drawn in red, were taken from Emre et al. (2011). NNAF, MNAF and SNAF: northern, middle and southern branches of the NAF. GPB : Geyve-Pamukova Basin.

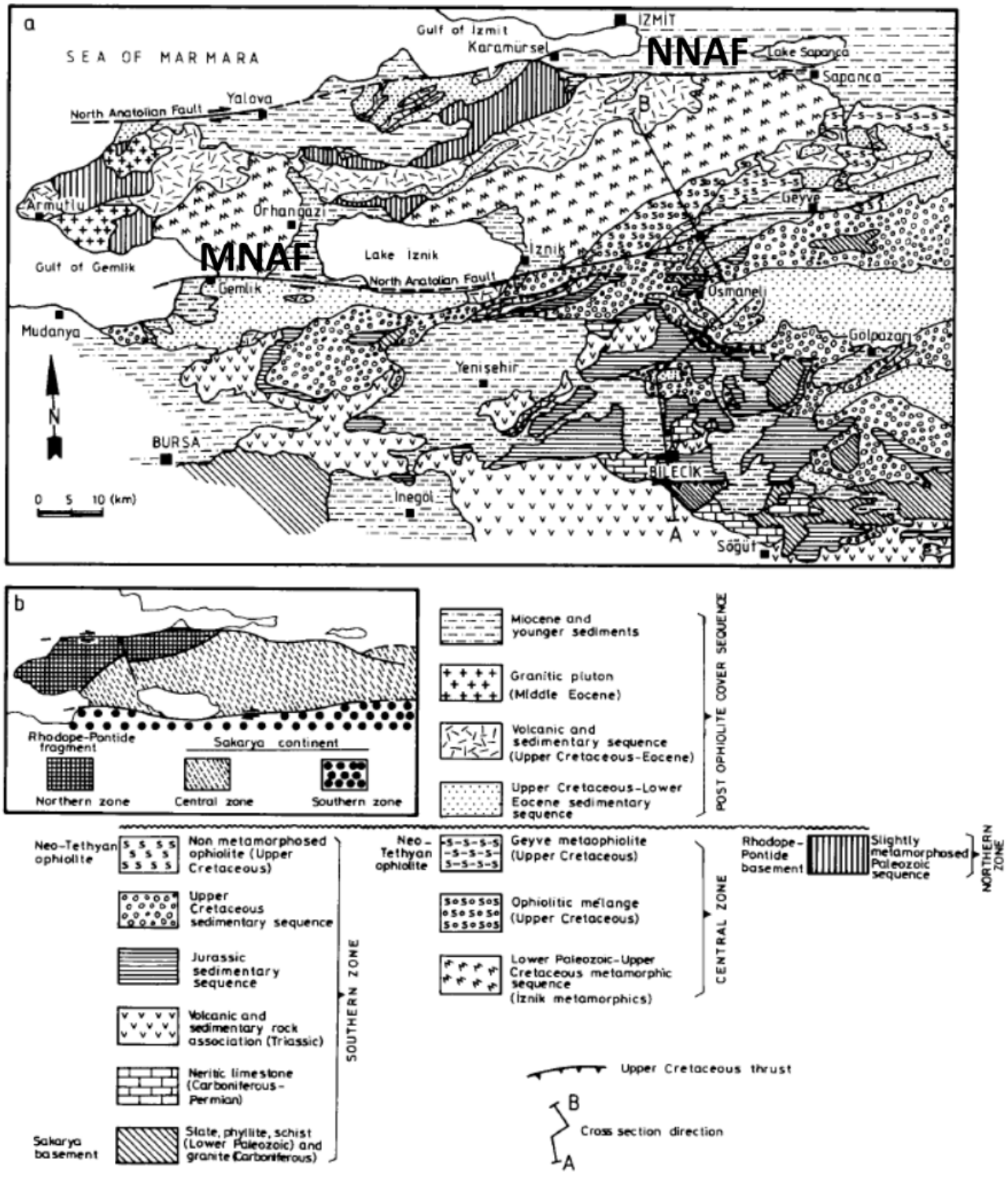

Figure A.13: Geological map of the Armutlu peninsula (from Yılmaz et al., 1995).

In terms of paleoseismicity, a 2500 years recurrence of big earthquakes (magnitude over 7) on the MNAF was proposed by Öztürk et al. (2009) with coseismic displacements up to 5 m, relying on a trenching study west of the lake which only found one 2000 years old event (Uçarkus, 2002; Uçarkus et al., 2003). Other paleoseismological works found more frequent and recent events (Honkura and Işikara, 1991; Barka, 1993; Özalp et al., 2003; Dogan, 2010). In the best cases, these studies did not find more than two well dated events, so it is difficult to derive a relevant recurrence on such short, statistically unsignificant records of past ruptures. The low tectonic activity currently observed on the MNAF significantly constrasts with the historical seismicity registered for this area, which is quite well known thanks to numerous texts (Fig. A.14). According to the historical record, no less than eleven earthquakes caused destruction in Iznik during the last two millenia. And among these eleven earthquakes, seven probably ruptured on the MNAF, according to historical seismicity studies (Ambraseys, 2009). This historical record for the MNAF is partly confirmed by the paleoseismological studies carried out on this fault strand. The compilation of the results of the trenches dug across the MNAF suggests the occurrence of at least four earthquakes during the last two millenia (Ikeda et al., 1989, 1991; Yoshioka and Kusçu, 1994; Uçarkus, 2002; Özalp et al., 2013).

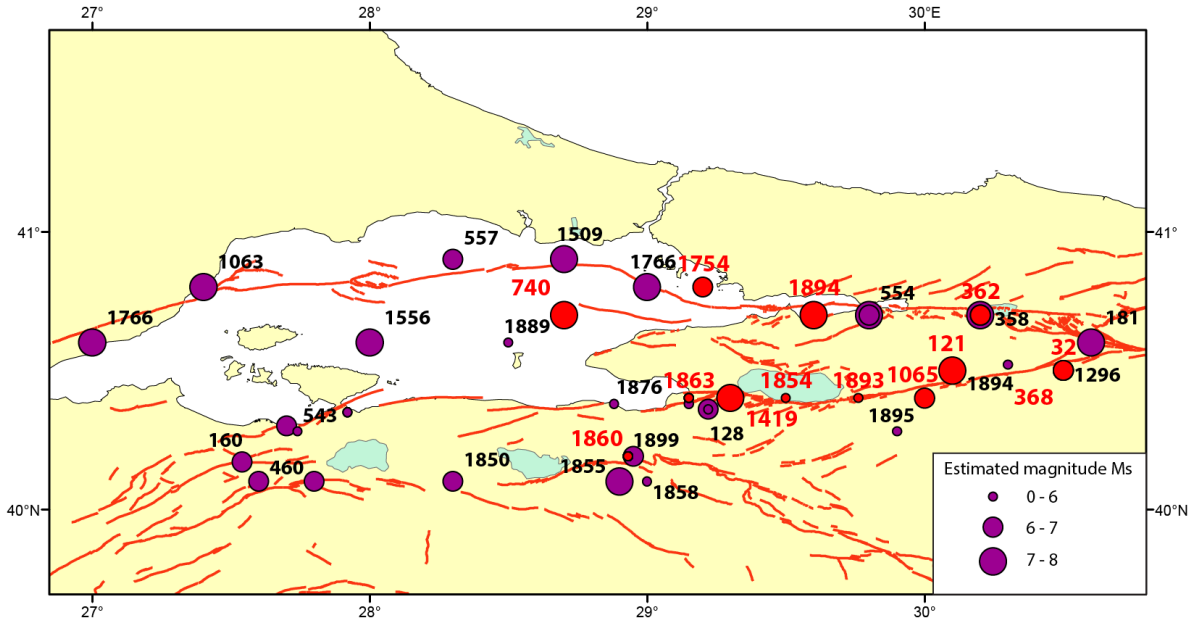

Figure A.14: Historical earthquakes known for the Marmara region before 1900. The active faults are drawn in red. The red earthquakes are reported to have produced damage in Iznik. The size of each circle refers to the estimated magnitude of the earthquake.

A.3 Iznik Lake basin

A.3.1 Morphology

Among the different basins located along the MNAF trace, Iznik Lake stands as the largest lake in the Marmara region and one of the largest freshwater lakes of Turkey with a surface of 313 km^2. Its surface stands 83 m above the sea level and it presents a maximum depth of about 80 m. Iznik Lake is bordered by two mountain ranges, the Samanli in the north and the Katirli in the south (Fig. A.15). Larger alluvial plains are developed east and west of the lake around Iznik and Orhangazi towns respectively (Fig. A.15). These plains, as well as the whole southern shore, include well developed alluvial fans, some of which are still active (Ikeda et al., 1991).

The watershed of the lake covers a 1246 km^2 wide area. The main rivers feeding the lake are the Sölöz (southwest), Nadir (northwest), Kurudere (northeast), Karadere and Kirandere (east). The deltas of the Karadere and Sölöz streams are particularly developed. In the west, the lake waters flow to the Marmara Sea by its only outlet, the Gölyatagi stream. After crossing the alluvial plain south of Orhangazi, it incises a very narrow valley, the Karsak pass, before reaching the Gulf of Gemlik.

The lake, 30 km long and only 10 km large, shows a E-W elongated shape with and bathymetry reveals three sub-basins (Fig. A.15). The western sub-basin (∼20% of the lake surface) is shallow and flat. The rest of the lake is composed in the east of two E-W sub-basins separated by a ridge. The southern sub-basin is the deepest one and looks clearly controled by the fault segments located along the southern shore (Nazik et al., 2011). On the northern shore, two other oblique faults separate the basement rocks and the alluvia. In the northwest, the Orhangazi fault (OF on Fig. A.15) displays markers of both normal and dextral activity with large triangular and right-laterally offset channels. In the northeast, the Boyalica fault (BF), previously mapped as a normal fault (Öztürk et al., 2009), also presents some right-laterally displaced channels but significant normal slip markers are not visible along strike.

A.3.2 Hypotheses of formation

The case of the formation of Iznik Basin is part of a wider discussion on the neotectonic evolution of the Marmara region. Some basins crossed today by the NAF strands have been considered as pull-apart structures directly linked to the fault activity (Armijo et al., 2002), while other authors consider many basins and ridges to predate the strike-slip fault system (Le Pichon et al., 1999, 2001; Alpar and Yaltırak, 2002; Yaltırak and Alpar, 2002). In this second framework, the NAF influenced the shape of several basins aligned on its trace.

Most studies on Iznik Lake Basin traditionnally attribute its existence to the neotectonic activity on the MNAF by a pull-apart or transtensional mechanism (Bargu, 1982), sometimes invoking in addition the oblique normal faults north of the lake (Yaltırak, 2002). Öztürk et al. (2009) do not support this hypothesis as they consider the Iznik basin too large to have been formed by the MNAF only. They argue that a lake already existed before the development of the MNAF. Following this, the elongated ellipsoidal sub-basin in the south of the lake was developed afterwards under the influence of the Sölöz releasing stepover. More recently, Doğan et al. (2015) compared the shapes of the Iznik and Geyve-Pamukova basins with results from analogical models (Wu et al., 2009) and concluded that they can be formed with transtensional and pure strike-slip pull-apart mechanisms respectively (Fig. A.16).

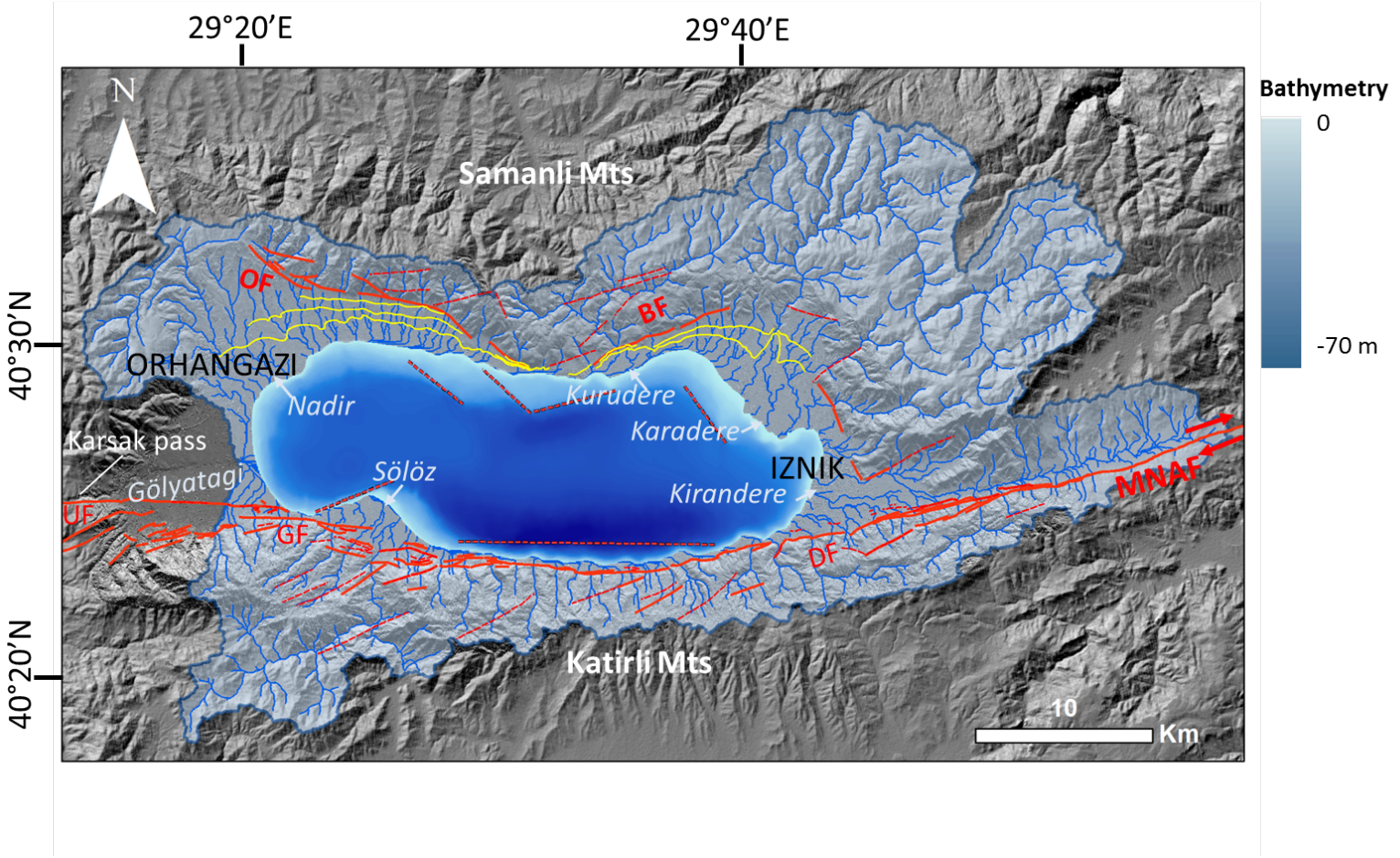

Figure A.15: General geomorphology of Iznik Lake basin. The lake watershed is superimposed in light blue with its main rivers on a shaded SRTM digital terrain model. Active faults are drawn in red, and Quaternary lacustrine terraces in yellow. The bathymetry is courtesy of Iznik DSI (State hydraulic works). OF=Orhangazi fault, BF=Boyalica fault, DF=Dirazali fault, GF=Gürle fault, UF=Umurbey fault.

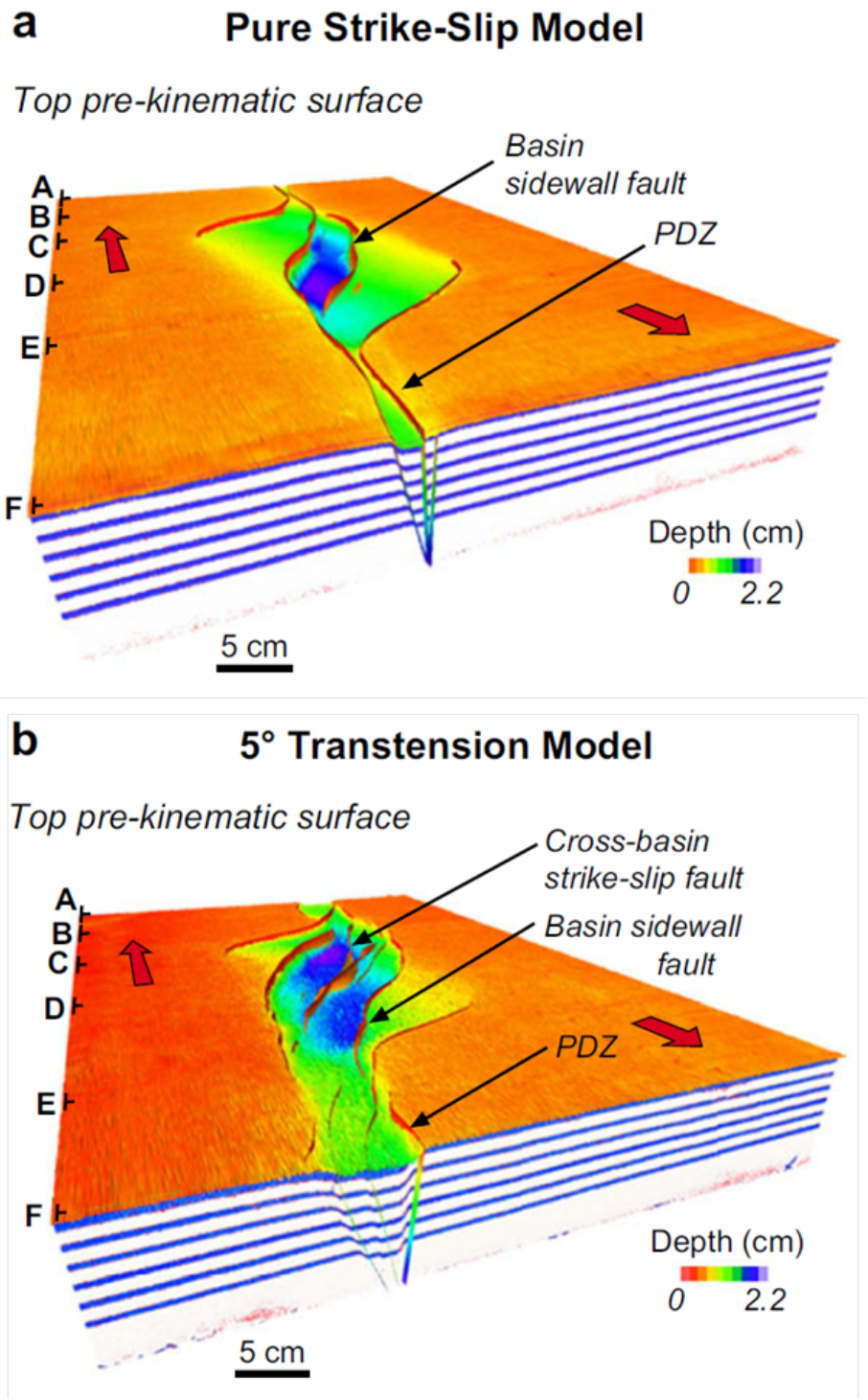

Figure A.16: Analogical models of pure strike-slip (a) and transtensional (b) pull-apart basins, invoked by Doğan et al. (2015) for the formation of Geyve-Pamukova and Iznik Lake basins respectively. PDF = principal deformation zone (from Wu et al. (2009)).

A.3.3 Modern climate

The lake is located in the Mediterranean climate zone, with warm, dry summers and mild, wet winters. The regional climate is under the influence of the Marmara Sea and is characterized by mean annual precipitations of 500-600 mm/yr, with most rains falling during the winter and in spring. Average temperatures range between 24 °C in July and 6 °C in January (Franz et al., 2006), with a mean annual temperature of 14 °C (DSI, 1974). The lake level shows small variations of about 50 cm linked to seasonal changes of the precipitation-evaporation balance. Nowadays, the system is strongly anthropized and higher levels are regulated by pumping systems. There is also an intense agricultural activity and some industries around the lake which require water pumped from the lake (Akkoyunlu, 2003).

A.4 Objectives of the thesis

Following the previous description, the seismic risk in the MNAF area is clearly underestimated. This thesis aims to complete our knowledge of the Quaternary behaviour of this fault strand. The study is more specifically focused around the Iznik Lake from Mekece to Sölöz (Fig. A.12 and A.15), which was identified as a seismicity gap and may present a significant earthquake potential. The first objective of this work is therefore to improve the seismic hazard assessment of this fault zone by: (1) precising the segmentation of the fault, (2) measuring the offsets of multiple geomorphic markers that result from coseismic displacements cumulated through time, (3) quantifying the long term slip rate of the fault. The analysis of the traces of past earthquake damage on the buildings in Iznik will also allow to (4) complete the calendar of the seismicity, (5) locally constrain the typical intensity associated with historical ruptures and discuss their possible magnitudes.

The second objective of this thesis is to develop a novel approach integrating data from different sources like geomorphology, sedimentology, geophysical prospecting, building archeology, and history. Each discipline has its strong points for a certain space and time scale, but also its proper limitations. For example, tectonic gemorphology can especially document long term processes and major fault ruptures occurring on tens to hundreds of kilometers, but can hardly resolve precisely their absolute chronology. By contrast, archeological data can constrain the occurrence of damage with a precision of a few years or decades but only provide local information and are much more delicate to convert into quantitative earthquake parameters. The data gathered from different sources can occasionaly lead to apparent contradictions. These contradictions must be used to discuss the limits of each method, but also to build new scenarios and new hypotheses. This way, this thesis aims to explore the complementarity between methods, and propose some guidelines for future pluridisciplinary studies in active fault zones.

A.5 Transverse methods

The scope of our study spans different scales in space and time. During this work, we used several specific analysis techniques and methods that will be described in the corresponding chapters, but also transversal tools that are relevant for various applications throughout the whole study. In the following sections, we present the high-resolution satellite image dataset that was mainly used to map and measure geological and geomorphological features. It was also used to locate and interprete the archeological observations in a larger context. Then, we introduce the dating methods that were applied to sediments and archeological material.

A.5.1 High-resolution imagery

For this study we needed to have quality images of Iznik area to map the morphological and tectonic features and prepare more specific field works. We benefited from satellite images acquired with the Pleiades satellites. These two twin satellites, Pleiades 1A and Pleiades 1B were launched in 2011 and 2012 on a quasi polar heliosynchronous orbite 694 km far from the earth surface (Fig. A.17). They are equipped with a push-broom sensor able to image 20 km wide swathes. Images are acquired in four spectral bands with a 2.8 m resolution and as a panchromatic (black and white) image with a 0.7 m resolution (Berthier et al., 2014). As the two satellites can capture a same feature from different locations, the two resulting stereo images can be processed into a very precise digital elevation model (DEM).

The DEM was processed using the AMES Stereo Pipeline software developed by the NASA (Broxton and Edwards, 2008; Moratto et al., 2010; Shean et al., 2016). A couple of stereo images is characterized by an epipolar geometry, which corresponds to all the geometric relationships (or tie points) between two images of the same scene shot from different angles (Fig. A.18). The processing is composed of three main steps. First, the two images are prepared with corrections of their alignment and radiometry. Then, the program correlates both images by looking for tie points which present a spatial shift. In the final step, the triangulation, the program builds the epipolar lines for each couple of tie points. For this, the software needs to have a model which relates the coordinates in the image to the geodetic coordinates of the field. In the case of Pleiades images, we use the Rational Polynomial Coefficients (RPC) which represent a universal camera model (Fraser et al., 2006).

The DEM is a useful tool for geomorphology purposes but also enables to orthorectify the raw Pleiades image with the topography and capture angle to obtain a planimetric picture. It is then possible to do precise and accurate measurements on the image. The minimal resolution achievable for the DEM corresponds to three times the resolution of the



Figure A.17: Artistic view of the twin Pleiades satellites. Courtesy of the CNES.

optical image and is about 2 m. The vertical relative uncertainty depends on the slope values in the captures scene and the B/H parameter (Lacroix et al., 2015). This last parameter is defined as the ratio of the baseline between the two acquisitions of the pair (B) and the mean distance between the satellite and the center of the images (H). In high relief environments, a too high B/H ratio will prevent the satellites from capturing steep-sided areas, which will result in data gaps (Fig. A.19). In general, the uncertainty will increase for steeper slopes and for higher B/H ratios. In our case (B/H ratio of 0.2), this uncertainty is lower than 50 cm.

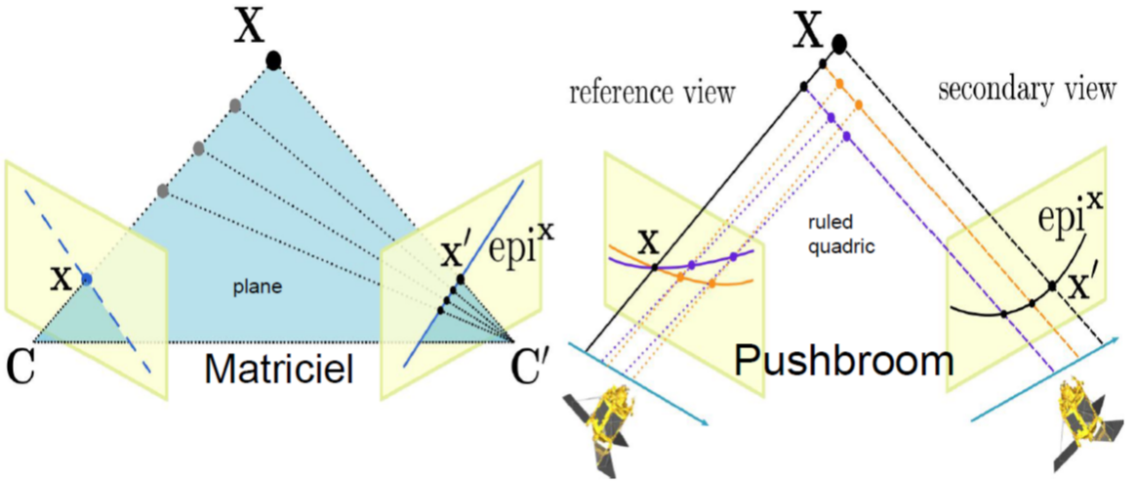

Figure A.18: Principle of the epipolar geometry and application for a classical focal-plane camera (left) and a pushbroom camera (right). Depending on the satellites' positions, a unique point on the reference image can correspond to several points on the other image, aligned on an epipolar line. For the pushbroom camera, the tie points are not located on a line but on a curve. In practice, a linear approximation is done on small windows (source of the image: Pascal Lacroix).

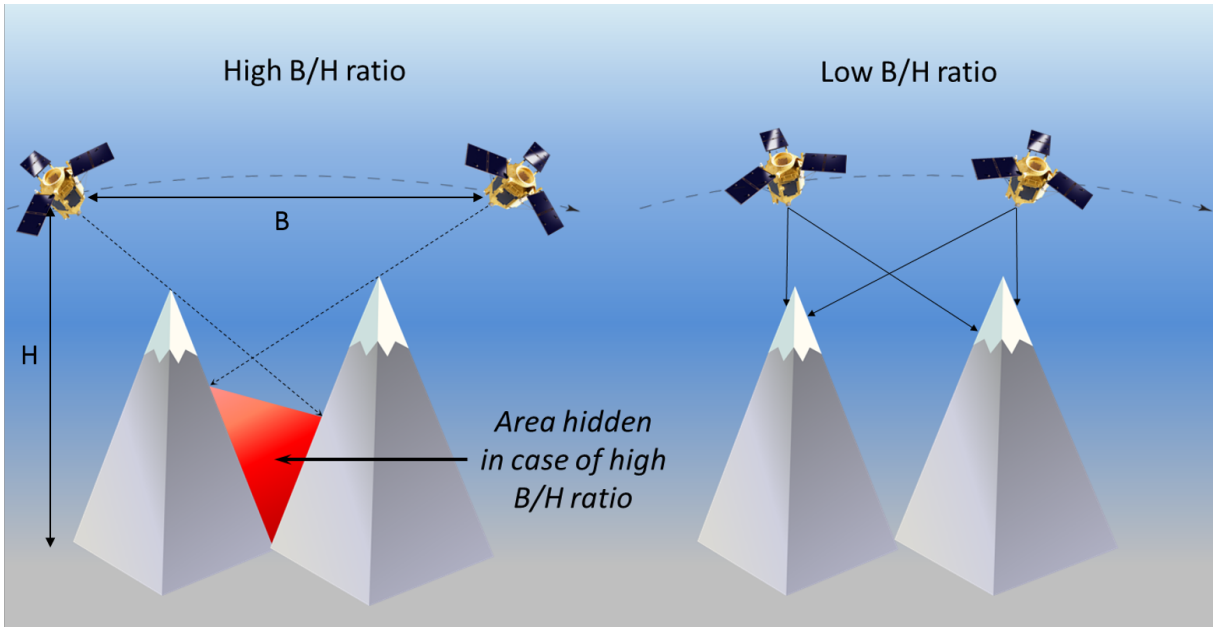

Figure A.19: Consequences of different B/H ratios on the data acquisition. Courtesy of Airbus Defence and Space.

A.5.2 Dating techniques

In many cases, the natural and anthropic features observed on satellite images or on the field need to be dated to extract relevant information. These chronological data will for example give the age of occurrence of a specific phenomena (e. g. formation of a given sedimentary unit, construction of a building) and, combined with spatial measurements, will enable to estimate the speed of certain processes (e. g. fault slip). Depending on the selected dating method, the obtained chronology will be absolute if ages are related to a reference date, or relative, in which case only the order of occurrence of successive events are known. In the following sections, we will present the dating methods used in this study. These methods rely on the quantification of radioactive isotopes, such as carbon-14 (^{14}C) and beryllium-10 (^{10}Be), in the material sampled. The presence of these isotopes, called "cosmogenic", in the atmosphere or in superficial rocks, is originally produced by the galactic cosmic radiation impacting the Earth (Gosse and Phillips, 2001).

A.5.2.1 Interactions of the cosmic flux with the atmosphere

In the upper atmosphere, cosmic high-energy particles arrive with sufficient energy to cause nuclear reactions. The interaction of this primary radiation with the atmospheric particles is responsible for a cascade of particles and reactions. These newly formed particles in the atmosphere constitute what is commonly referred to as "secondary radiation". As long as the secondary particles have sufficient energy, the cascade of reactions continue down through the atmosphere and the first meters of the lithosphere. At this level, the particle flux is dominated by neutrons and muons, which break apart the atoms encountered through spallation interactions, generating the cosmogenic nuclides. Due to these successive interactions, the neutrons lose energy and are no longer able to cause spallation. These low-energy nucleons called "thermal neutrons" are ultimately absorbed by atomic nuclei and are another source of cosmogenic nuclide production.

A.5.2.2 Carbon-14 (^{14}C)

^{14}C results from the absorption of thermal neutrons into ^{14}N in the atmosphere. ^{14}C is a radioactive isotope of carbon and is assimilated by living organisms during their lives, with a ^{14}C/^{12}C ratio similar to the atmospheric ratio. When the organism dies, carbon exchanges with the atmosphere stop and the amount of ^{14}C will decrease by radioactive disintegration through time, with a half-life of 5730±40 years. Comparing the measured 14/12 ratio in a sample with the modern atmospheric ratio, if assumed constant through time, will provide the age of the organism's death (Taylor, 1997). Some additional corrections are generally needed. In the 1960's, it was observed that the ages provided by radiocarbon and by other independent methods presented systematic differences. Due to variations of the

cosmic radiation and the geomagnetic field shielding, the production rate of radiocarbon in the atmosphere did not remain constant through time (Mazaud et al., 1991). The nuclear tests occurred between 1955 and 1980 also increased the amount of atmospheric ^{14}C. Using other dating methods like dendrochronology and U/Th dating, calibration curves were established that enable to convert radiocarbon ages (^{14}C-ka) into accurate calendar ages (Cal-ka, Reimer et al., 2013; Fig. D.3). Other effects have often to be considered depending on the sampling context. Isotopic fractionation may occur during the carbon's assimilation and will shift the organism's ratio from the atmospheric ratio. For marine or lacustrine samples, the assimilation of atmospheric carbon through the water column is not immediate and these organisms tend to exchange carbon with waters older than the atmosphere in average (Stuiver and Braziunas, 1993). This "reservoir effect" requires to reduce the age obtained. The uncalibrated ages are commonly given "before present" (BP), which actually means before 1950. This dating method is valid for ages between a few years and about 50 ka.

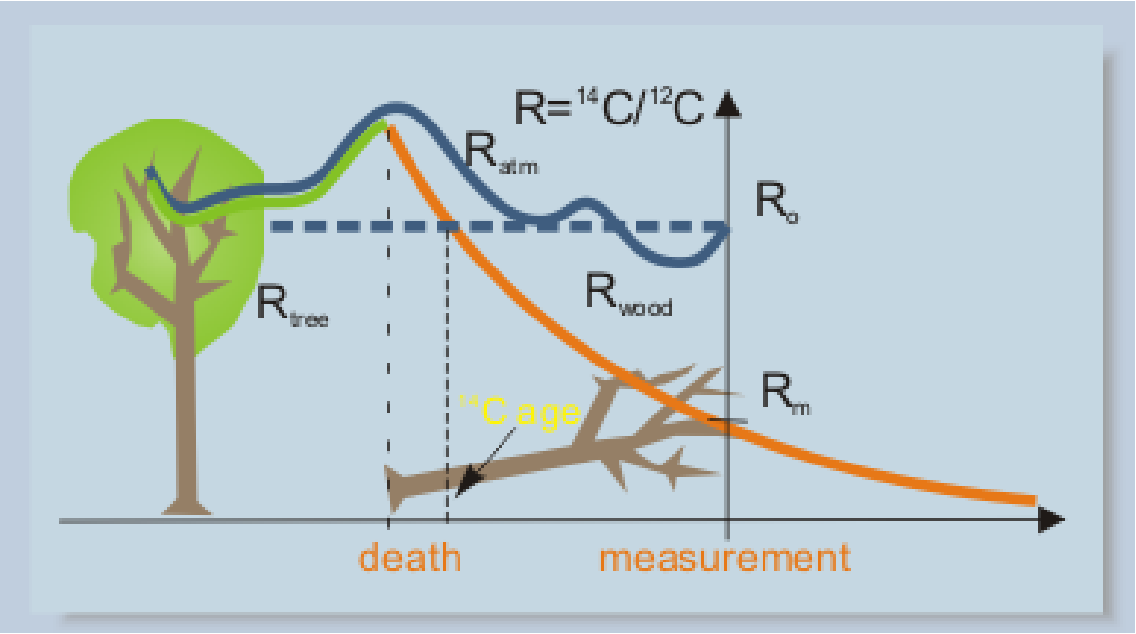

Figure A.20: Principle of radiocarbon evolution. After the death of the organism, the exchange of carbon with the atmosphere stops and the concentration of radiocarbon decreases exponentially according to its half-life. Using this exponential law, the measured concentration of radiocarbon can be converted into an age. To account for the variations of the atmospheric ratio, the radiocarbon age needs to be calibrated (source of the image: Poznan Radiocarbon Laboratory.

A.5.2.3 Beryllium-10 (^{10}Be)

Rocks and sediments durably exposed to cosmic radiations can be dated by quantifying in-situ produced cosmogenic isotopes like ^{10}Be (Terrestrial Cosmogenic Nuclide, TCN). This method is based on the measurement of the time during which the sampled surface or landform have been exposed to cosmic rays. ^{10}Be is sampled in rocks containing quartz, where it is produced through spallation and negative-muon capture on oxygen and silica atoms (Fig. A.21).

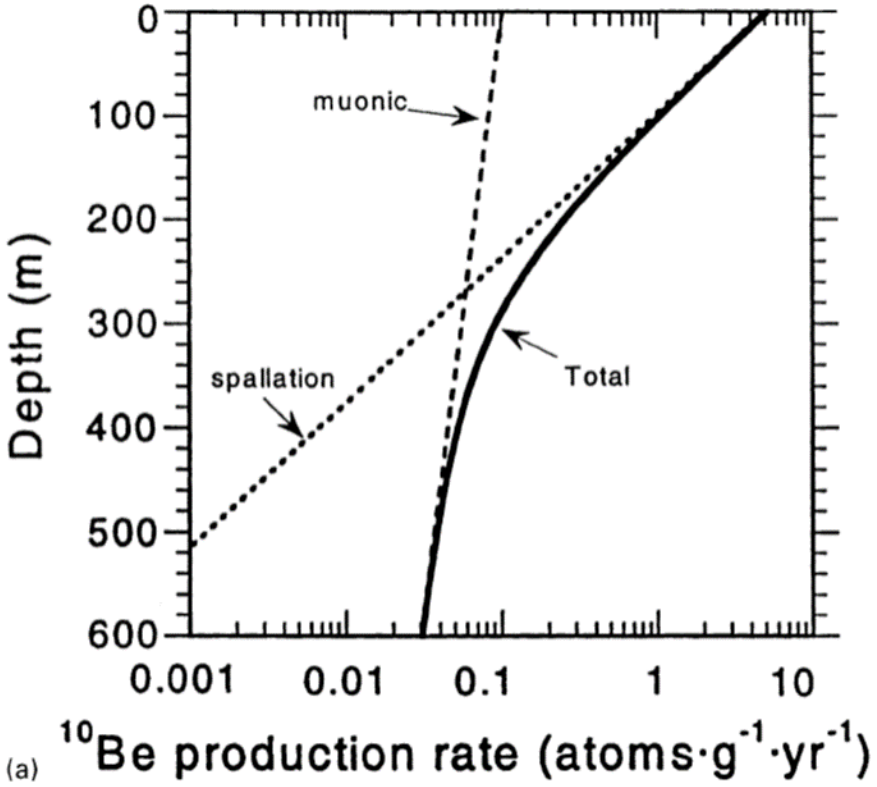

Figure A.21: Evolution with depth of the production of 10Be in quartz arenite (a). Contributions of the different particles are detailed (from Gosse and Phillips, 2001).

The production varies in space, and needs be determined for each sampling site. For that, we use a reference production rate at sea level and high latitude (SLHL). This reference rate is calculated from the nuclide concentration measured on a sample precisely dated by another independant method. It is then normalized for the sea level and high latitudes by adjusting for scaling factors. These scaling factors are physical models that describe the variability of cosmic ray with latitude and altitude. When the cosmic particles arrive to the Earth, they are deflected by the geomagnetic field depending on their energy. This deflection is stronger for higher latitudes. As a consequence, the production rates at the

poles are about twice as high as at the equator (Fig. A.22a, Robinson et al., 1995). The altitude needs also to be corrected for because the cosmic flux is attenuated as it crosses the atmosphere and progressively loses energy. As a result, for high latitudes, the production rate at sea level is six times lower than at 2000 m asl (Fig. A.22a, Stone, 2000). The scaling factors are used to correct the reference production rate for the altitude and latitude of the sampling site.

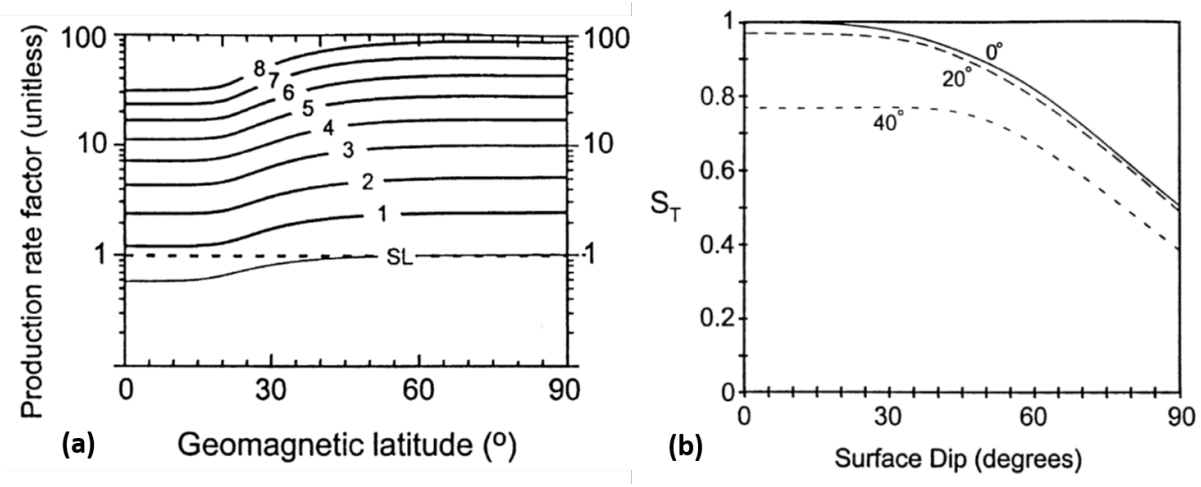

Figure A.22: Factors modulating the surface production rate. (a) Scaling factor for different latitudes and elevations (indicated as contours in km), after Lal (1991). SL=sea level. (b) Topographic scaling ST as a function of the dip angle of the sampled surface and the shielding by surrounding topography, represented as curves (from Gosse and Phillips, 2001).

Local factors have also to be considered. The production rate is affected by the topography around the sampling site and the local slope. A part of the cosmic particle flux will be blocked if high reliefs are present close to the site, which will decrease the in-situ production (Dunne et al., 1999). That is why a correction for this "shielding" effect is applied (Fig. A.22b). In certain contexts, the sampled surface is persistently covered by ice, water, or superficial materials that attenuate the cosmic ray. Depending on the nature and thickness of this cover, the production rate can decrease significantly, in which case an additional correction is required (Grischott et al., 2017).

In the subsurface rocks, the cosmic ray energy is quickly dissipated and the nuclide production decreases with depth following an exponential law. For example, in the case of beryllium-10, the total production decreases by one order of magnitude in the first 1.5 m. This dissipation is more or less fast depending on the nature of the particle (neutrons, muons) so the relative contribution of these particles in the nuclide production varies with depth (Fig. A.21). This evolution with depth is especially used when the exposure age is estimated from several samples taken at different depth in the sedimentary unit.

The evolution of cosmogenic nuclides concentration C (in atoms/g of quartz - ^{10}Be -

or atoms/g of rock - ^{36}Cl) with time t and depth z is described by the following equation (Lal, 1991):

$$C(z,t) = C(z,0)e^{-\lambda t} + \frac{P(z)}{\lambda + \mu\epsilon}(1 - e^{-(\lambda+\mu\epsilon)t})$$

where

- P(z) is the nuclide production rate (at./g/yr) at a depth z
- λ is its decay constant
- μ is the absorption coefficient, i.e. the ratio between the sample density and the mean attenuation length (g.cm^{-2}) which describes the absorption of the different particles from the secondary flux in the matter
- ϵ is the erosion rate (g.cm^{-2}.an^{-1}).

C(z,0) corresponds to the amount of nuclides inherited from previous exposures and, if not taken into account, will shift the surface concentrations to higher value and lead to the computation of an age older than the age of the sampled surface. The nuclide concentration equation presents two other unknowns: the age and the erosion rate. Therefore, with a single surface sample, one needs to assume negligible erosion from field evidence to compute the exposure time. Assuming $\epsilon = 0$, the previous equation can be written for a surface sample:

$$C(0,t) = C_0 e^{-\lambda t} + \frac{P_0}{\lambda}(1 - e^{-\lambda t})$$

which allows to compute the exposure age if the inheritance is known or neglected. Note that the age obtained is considered a minimal age, under this hypothesis of no erosion. For higher erosion rates, the same measured concentration corresponds to longer exposure times. With time, the nuclide concentration increases until an equilibrium is reached between the gain from production and the losses due to erosion and radioactive decay (Fig. A.23). This equilibrium is reached faster for higher erosion rates. In this case the measured concentration cannot give a reliable age but will constrain the erosion.

Another way to solve the equation is to use several samples taken along a depth profile. This method is commonly used for sedimentary formations like alluvial terraces. It requires to take a number of samples higher than the number of searched parameters (i.e. at least four samples to resolve the age, erosion and inheritance). In this case, the shape of the depth-profile curve will be characteristic of a given set of exposure time, erosion rate, and inherited concentration (Dunai, 2010; Hidy et al., 2010). By a Monte Carlo approach, a large number of synthetic curves are generated for various sets of paramaters. The synthetic curves are compared to the measured curve and the best fitting parameters are stored. When enough good models have been found, the distribution of the stored values for each parameter provides a most probable estimation and its uncertainty. The space of solutions explored for the parameters can be reduced with a priori constrains, which reduces the computing time. The sampling method especially allows to easily check for inherited concentration. As

nuclide production becomes negligible at depth, a non zero concentration measured in the deeper samples indicates the approximate amount of inheritance.

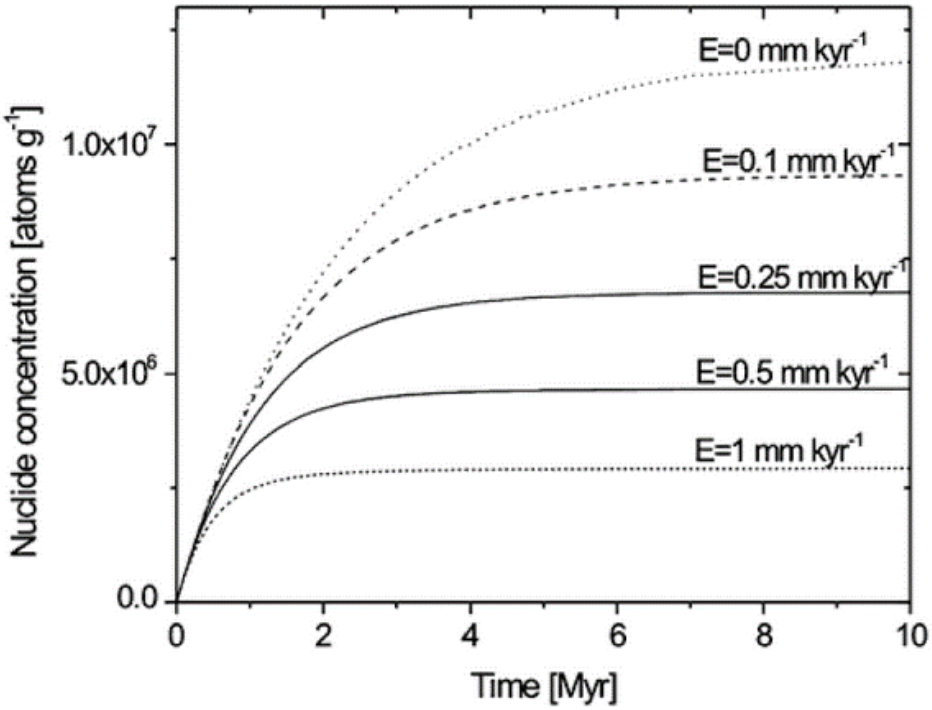

Figure A.23: Evolution of 10Be concentration with time of exposure and for different erosion rates, represented as curves. The higher the erosion rate, the sooner a secular equilibrium is reached when the production is compensated by the radioactive decay and the erosion. Under the assumption of secular equilibrium, a measured concentration will give an estimate of the erosion rate (from Ivy-Ochs and Schaller, 2009).

Chapter B

First evidence of low-elevation LGM glaciers in Turkey

The content of this chapter will be submitted to the journal *Geomorphology* as an article by Yacine Benjelloun, Julia de Sigoyer, and Julien Carcaillet.

B.1 Introduction

The study of former climate variations during the Quaternary is an important issue to understand the formation and evolution of past landscapes, as well as their impact on prehistorical and historical societies. Documenting the timing, speed and amplitude of these past oscillations also enables to consider the current climate change in a wider temporal frame (deMenocal et al., 2000). Among the various proxies used to reconstruct past climates, glaciers present the advantage of a high sensitivity to temperature and precipitation changes (Nesje, 2005). They can provide a very good signal of the current climatic evolution, and even when they no longer exist, their remains in terms of deposits and morphological printing can also be used to recover information on past climates (Hoelzle et al., 2007). Such past glacial traces are well known across Europe, but are also more and more documented in less investigated countries such as Turkey. Though less famous, several glaciers still exist in Turkey (Sarikaya et al., 2011), and geological evidence suggests that the glacial extent was much larger in the past (Ciner, 2003). In recent years, the knowledge of the climatic conditions prevailing during the last glacial maximum (LGM) in Turkey has indeed significantly progressed thanks to the description of past glacial markers in various areas (Sarikaya et al., 2014; Sarikaya and Ciner, 2015; Zreda et al., 2011). Although most of these past glaciers have been especially found in the higher mountain ranges of southern and eastern Anatolia, a few pieces of evidence have also been identified closer to the Marmara Sea in the Uludag Mountains (Fig. B.1) between 2500 and 1900 m above sea level (asl) (Akçar

et al., 2014; Birman, 1968; Zahno et al., 2010). Our study shows that it is even possible to uncover glacial traces further north and at lower elevations. We present the results of our field studies in the southeastern Marmara region, around Iznik Lake, where several glacial markers were identified, and completed by the interpretation of a high-resolution DEM.

B.2 Study area

B.2.1 Geographical and geological setting

The study area is located in the Northwestern part of Turkey, west of the Marmara Sea and south of Izmit Gulf, between Gemlik Gulf and Mekece (Fig. B.1). The area east of Gemlik Gulf is made of several successive basins crossed by the middle strand of the North Anatolian fault (MNAF, Fig. B.1b). In the east, the Geyve-Pamukova basin (GPB) is a large 24 km long flat depression essentially covered by the alluvia of the Sakarya River. This basin is followed in the west by a smaller 10 km long basin that ends in the west by a much narrower corridor centered on Kaynarca village along the Kirandere valley. This corridor makes then way for the alluvial plain of Iznik Lake, located at 83 m asl. Iznik Lake is the largest freshwater lake in the Marmara region and the fifth larger natural lake in Turkey. The lake itself has been studied for paleoenvironmental purposes (Franz et al., 2006; Miebach et al., 2016; Nazik et al., 2011; Roeser et al., 2012; Ülgen et al., 2012; Yaltırak et al., 2012), but its age and mechanism of formation have only been addressed by few studies (Doğan et al., 2015; Öztürk et al., 2009). The lake is today linked to the Marmara Sea by the Gölyatagi stream in the west through the Karsak pass, but it may not have always been the case in the past (Geyer et al., 2001). The area is bordered in the north by the Samanli Mountains culminating at around 900 m in the west and until 1080 m in the east, while the Katirli Mountains in the south show significantly higher elevations of 1275 m in the west, decreasing eastward.

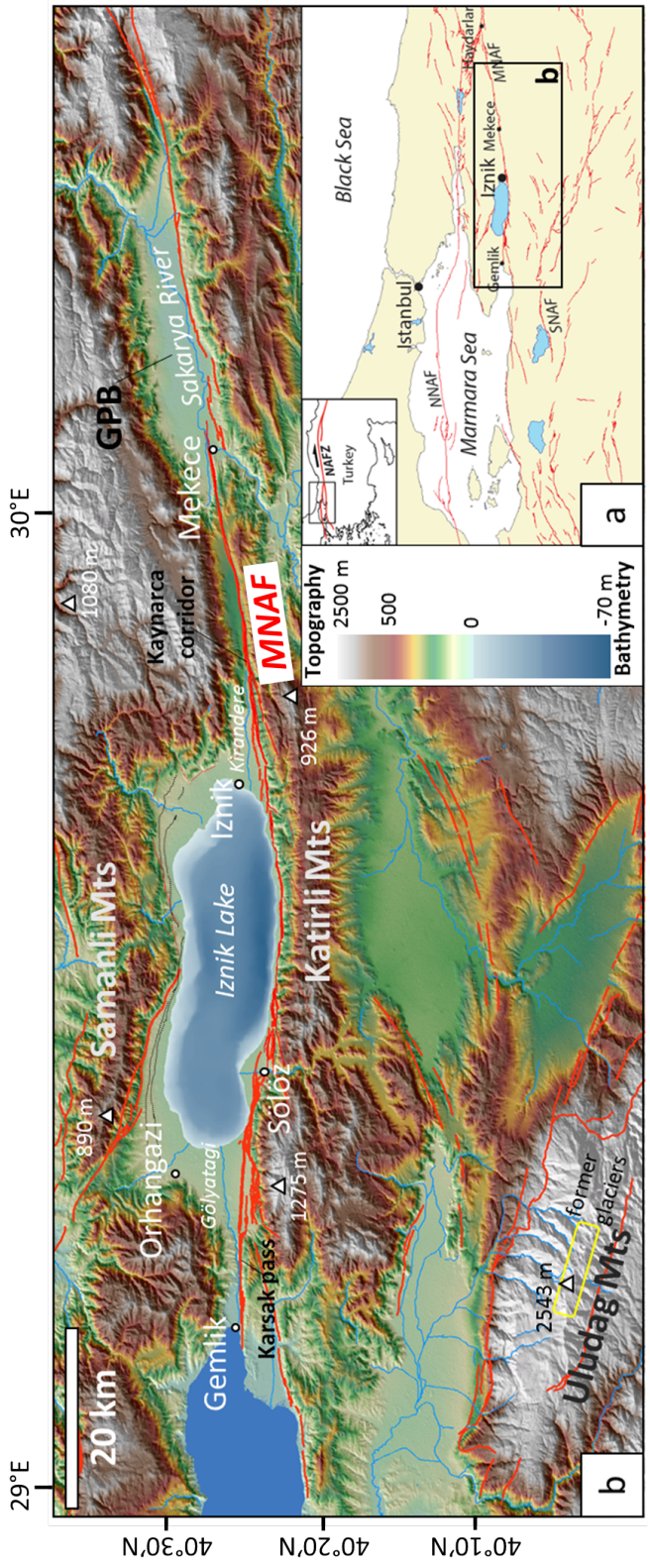

Figure B.1: (a) General location map. (b) SRTM shaded DEM along the MNAF with the major active faults (red) and rivers (blue). In yellow are located past glacial landforms studies by Zahno et al. (2010) on the Uludag mountain ridge. GPB=Geyve-Pamukova Basin. The bathymetry of Iznik Lake is courtesy of DSI (Devlet Su Isleri, State Hydraulic Works). The three lacustrine terraces north of Iznik Lake are delimited with black dotted lines. The main active faults were taken from Emre et al. (2011) and some additional ones were mapped during this study. The main summits around Iznik Lake are indicated with triangles. The study is focused on the Gemlik-Mekece valley.

The Gemlik-Mekece zone is a contact zone between three different geological units roughly separated by the MNAF. The Rhodope-Pontide fragment, NW of the lake, is composed of a weakly metamorphosed Paleozoic sequence containing amphibolite, hornblende schists, metabasite and intrusive leuco-granite (Yılmaz et al., 1995). The other terrains surrounding the MNAF belong to the Sakarya unit. In the hanging wall of the MNAF (north of the fault) lie some Upper Cretaceous metamorphosed ophiolitic assemblages, and Upper Cretaceous to Oligocene sediments. In contrast, the south of the MNAF is made of unmetamorphosed clastic sediments of the Sakarya units. All these units were covered by volcanic and sedimentary deposits between the end of the Cretaceous and the Eocene. The whole area was uplifted and covered by lacustrine and fluvial deposits around Iznik Lake and in the other basins formed during the Neogene (Emre et al., 1998). By the end of Pliocene, a compressive stage led to the development of a network of NE-SW and NW-SE faults, before the NAF appeared as a straight E-W fault zone. The MNAF is likely to have (re)activated since ∼5 Ma an older vertical tectonic contact which separated the northern and southern unit of the Sakarya continent (Bargu, 1982; Barka, 1992; Özcan et al., 2012; Yılmaz et al., 1995). Three levels of lacustrine terraces are developed north of the lake, presumably following the last Pleistocene glaciations (Ikeda et al., 1991; Fig. B.1b). İslamoğlu (2009) estimated a middle Pleistocene age for the uppermost terrace from bivalve assemblages. Alluvial fans are still active today in Iznik and Orhangazi plains and along the south coast of the lake. A karst developed in the carbonate massif close to Iznik in the northeast, which is often associated to glacial landscapes (Cilgin et al., 2014).

B.2.2 Modern climate

The study area is located in a climatic transition zone between the Mediterranean and Pontic climates. While warm dry summers and mild wet winters are characteristic of the Mediterranean climate, the Pontic climate is defined by an absence of summer drought with higher precipitation through the year and lower mean temperatures. Average temperatures range between 24 °C in July and 6 °C in January, with a mean annual temperature of about 14.4 °C near the lake, and 8-10 °C in higher parts of the catchment. The mean annual precipitation is about 630 mm, with most precipitation falling in winter and spring (Akbulak, 2009; Franz et al., 2006; Miebach et al., 2016).

B.3 Material and methods

B.3.1 Processing of a Pleiades-derived DEM and geomorphological mapping

Pleiades images (70 cm resolution) covering the area between Gemlik Gulf Iznik Lake and Karatekin were processed into a 2 m resolution DEM with the NASA Ames Stereo Pipeline software (Broxton and Edwards, 2008; Moratto et al., 2010; Shean et al., 2016). Several topographic and river profiles were extracted between Gemlik and Mekece with the RiverTools^{TM} 4.0 and ArcGIS softwares. The Quaternary surfaces were first mapped in a preliminary way using the Pleiades derived DEM. The units identified on the DEM were investigated, confirmed and described in the field in terms of lithology and relationship with the other surrounding units.

B.3.2 Sediment sampling and dating

When possible, datable material such as charcoal or organic matter was sampled in the different sediments encountered on the field: lacustrine terraces Tl1 (15TUR3) and Tl2 (15TUR4), and fluvio-glacial deposits in the south of Kaynarca corridor (15TUR7). These samples were dated by the Poznan Radiocarbon Laboratory (http://www.radiocarbon.pl/) and on ARTEMIS mass spectrometer at the LMC 14 in France with the ^{14}C method. The radiocarbon ages were converted into calendar ages with the IntCal13 calibration (Reimer et al., 2013) using Oxcal 4.2 program (Bronk Ramsey, 2009).

Each lacustrine terrace was sampled along a vertical profile to be dated using the in-situ produced terrestrial cosmogenic nuclide (TCN) method. Each profile consists of series of samples, commonly collected on the surface of the terrace (2), in the first 1.5 m below the surface (3-4) and deeper to constrain the inherited nuclide content (1-2). We sampled pebbles made of silicate material in order to have ∼100 g of quartz per sample. The beryllium was extracted in ISTerre (Grenoble) following the protocole detailed in appendix B and quantified at the ASTER Accelerator Mass Spectrometer in Aix-en-Provence.

B.4 Results

B.4.1 Topographic and river profiles between Mekece and Gemlik

The topographic profiles drawn between Gemlik and Mekece present at several points some bulges (arrows in Fig. B.2). Most of these bulges correspond to topographic features also identified on the field and interpreted as successive frontal moraines or glacier retreat

points. The E-W river profiles extracted in the same areas also show several anomalies (Fig. B.3). At the eastern end of Kaynarca corridor and between Iznik Lake and Karsak pass, the river profile is rather concave and thus far from an equilibrium stage. In the other convex river sections, several knickpoints are visible (arrows and orange dots in Fig. B.3) and are generally correlated with the topographic bulges (possible frontal moraines) identified on the topographic profiles and on the field.

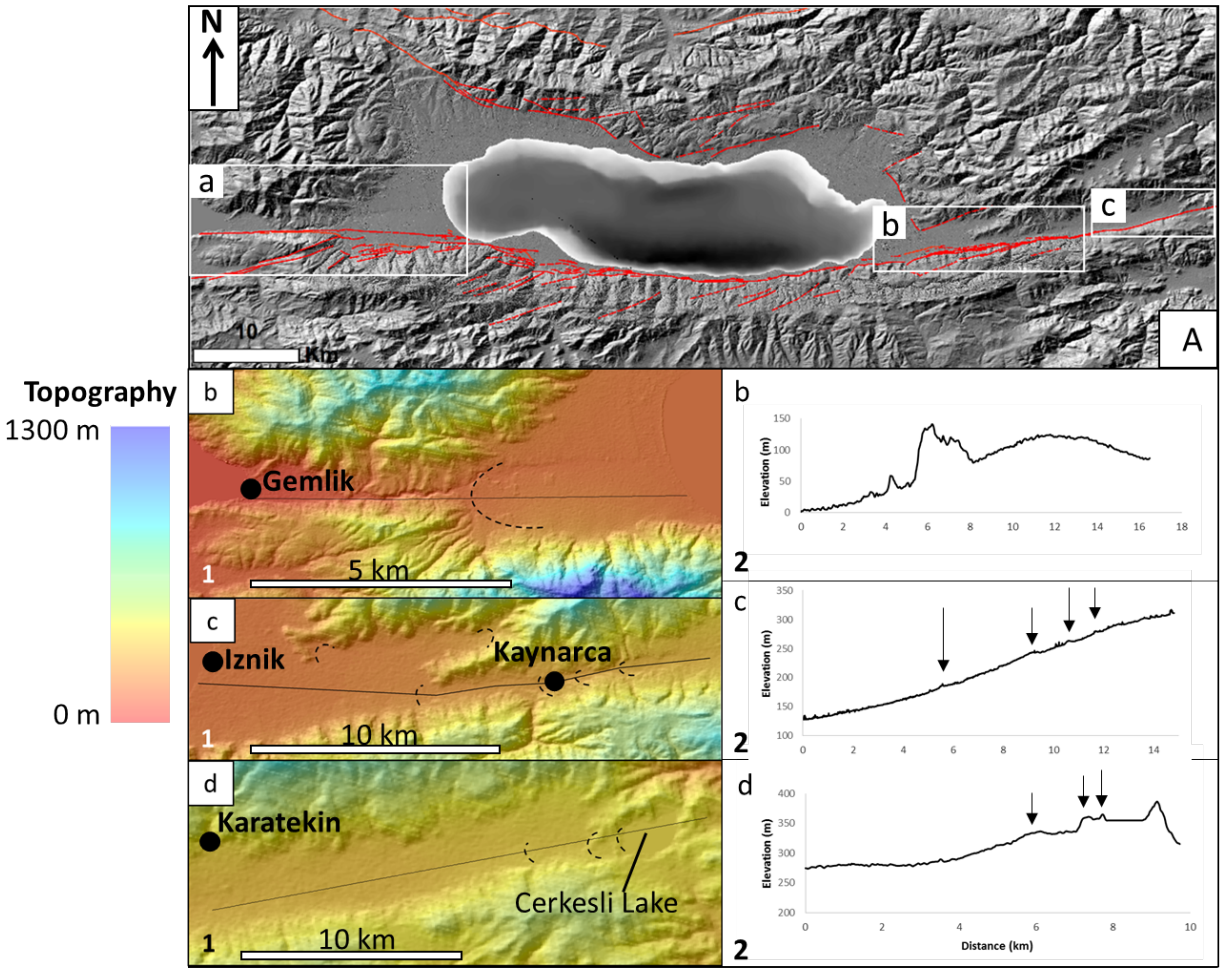

Figure B.2: (A) Shaded DEM of the study area. The three white boxes (b, c, d) are zoomed in below on the left column. b1, c1 and d1 show zoomed DEMS of selected zones. The black straight lines correspond to the topographic profiles shown respectively on the right column (b2, c2, d2). The traces of past glacier retreats identified with the topography, river profiles (Fig. B.3) and field observations are drawn with broken lines on the DEMs (1, left) and pointed with arrows on the profiles (2, right).

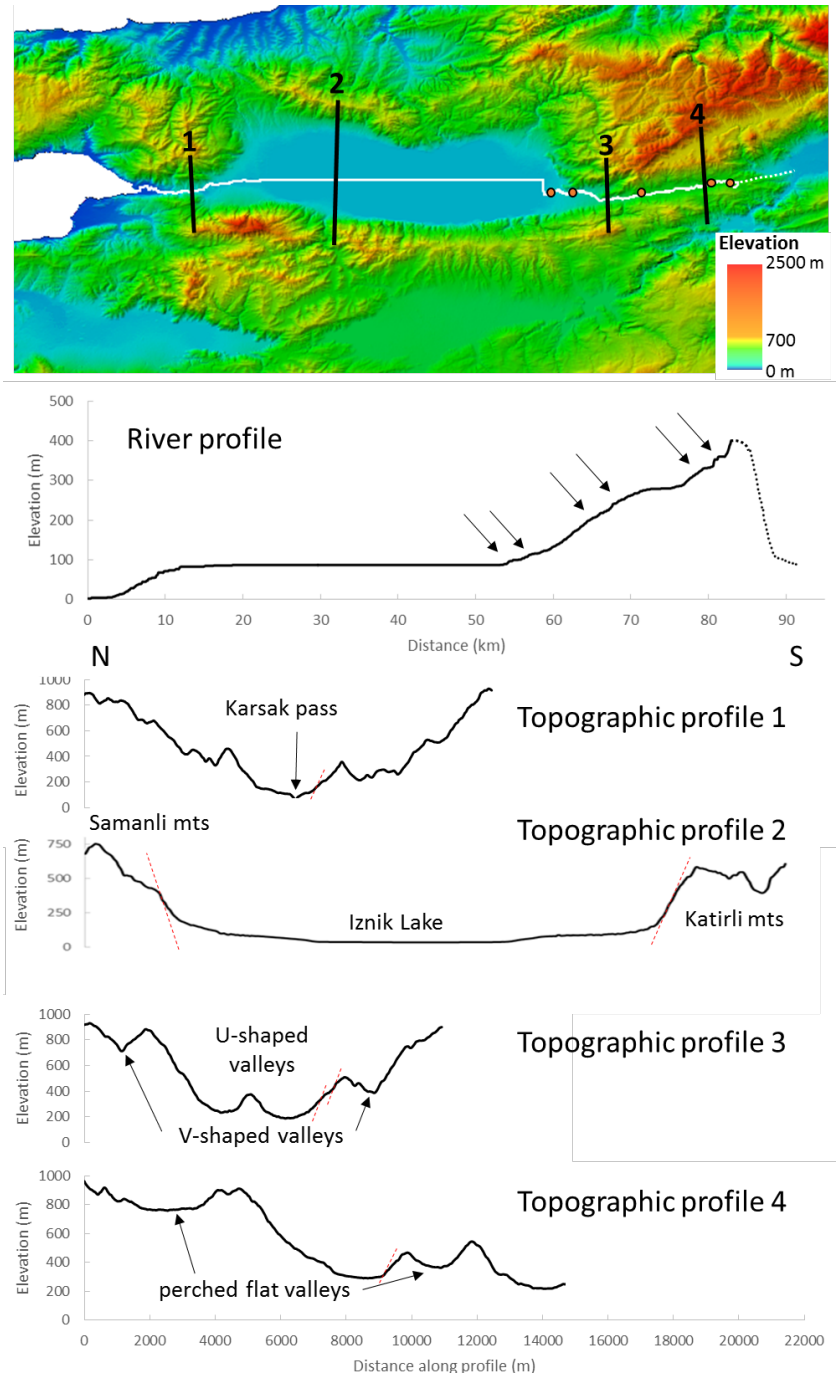

Figure B.3: (a) Shaded DEM of the study area. The white line represents the path of the river profile shown in (b). The orange dots indicate the location of major knickpoints. (b) EW river profile (Kirandere valley-Iznik Lake) between Mekece and Gemlik. A more detailed view of the profile along the Karsak pass is added. The arrows indicate the location of major knickpoints. In the east, the river profile is continued by a topographic profile with a broken line in order to show the major drainage divide with the GPB. (c) N-S topographic profiles perpendicular to the main valleys. On the topographic profiles are located the main geographical, morphological features, and active faults (red broken lines).

B.4.2 Field evidence of past glaciations

The different pieces of evidence for past glaciations encountered on the field are summarized on Fig. B.4 to B.8.

B.4.2.1 Morphological evidence

The Kirandere valley (see the map Fig. B.1), in the east of the lake, has a wide flat bottom and a U-shaped profile that is very suggestive of glacial morphology (Fig. B.3 profiles 3 and 4, B.5 and B.6a). The valley becomes much narrower at one point (located as B.5a,b in Fig. B.4), which is likely to be a past glacier retreat point, surrounded by remains of frontal moraines. This narrow zone is immediately bordered on the west and east by an over-dug zone. This bulge is also visible on the topographic profile (Fig. B.2c) and river profile (Fig. B.3). Some of the southern tributaries of the Kirandere river display a significant left-hand inflexion as they cross the frontal moraines in the valley, seen west and east of Kaynarca village as well as 1.5 km further east, before a much larger valley (Fig. B.7a). In the absence of moraines, the southern tributaries joining the Kirandere valley rather show a right-hand inflexion linked to the dextral slip on the MNAF segments.

At the eastern end of this large valley, Cerkesli Lake stands at a significantly higher elevation compared with the valley (Fig. B.2d) and could be a lake of glacial origin, limited on its western side by a former glacier retreat ridge. Further west of the lake, there is another very visible croissant-shaped bulge limiting a small flat surface next to the lake, which is interpreted as the frontal moraine left by the glacier retreat (Fig. B.8f).

Glacial morphologies are also observed in smaller adjacent valleys. The cabonate massifs located west of Karatekin show a U-shaped abrasion that seems to have been overprinted later by the fluvial incision (located as 9d,e on Fig. B.4). South of Besevler village (Fig. B.8d), a wind gap valley shows a U-shaped profile, which indicates glacial erosion. This adjacent valley could have been a furcation of the main glacier occupying the Kirandere valley. Numerous polygenic striated erratic blocks (Fig. B.8c) lie on the ground of this valley, and there aslo seems to be a central moraine in the middle. This latter moraine was later incised by a river as its summit exhibits fluvial traits. The south of this valley is significantly narrower and shows a V-shaped profile. A relief covered by trees could be interpreted as en end moraine. North of Karatekin lies a very wide and flat "plateau" perched 500 m above the main valley (Fig. B.8e) that may represent a perched glacial valley.

Other glacial morphologies are observed NE of Iznik on a N-S trending carbonate massif. Here again perched flat valleys are developed inside the massif and erratic blocks are observed within this valley. We note that in general, there is no particular correlation between the flat valleys and soft geological terranes that could explain otherwise these morphologies.

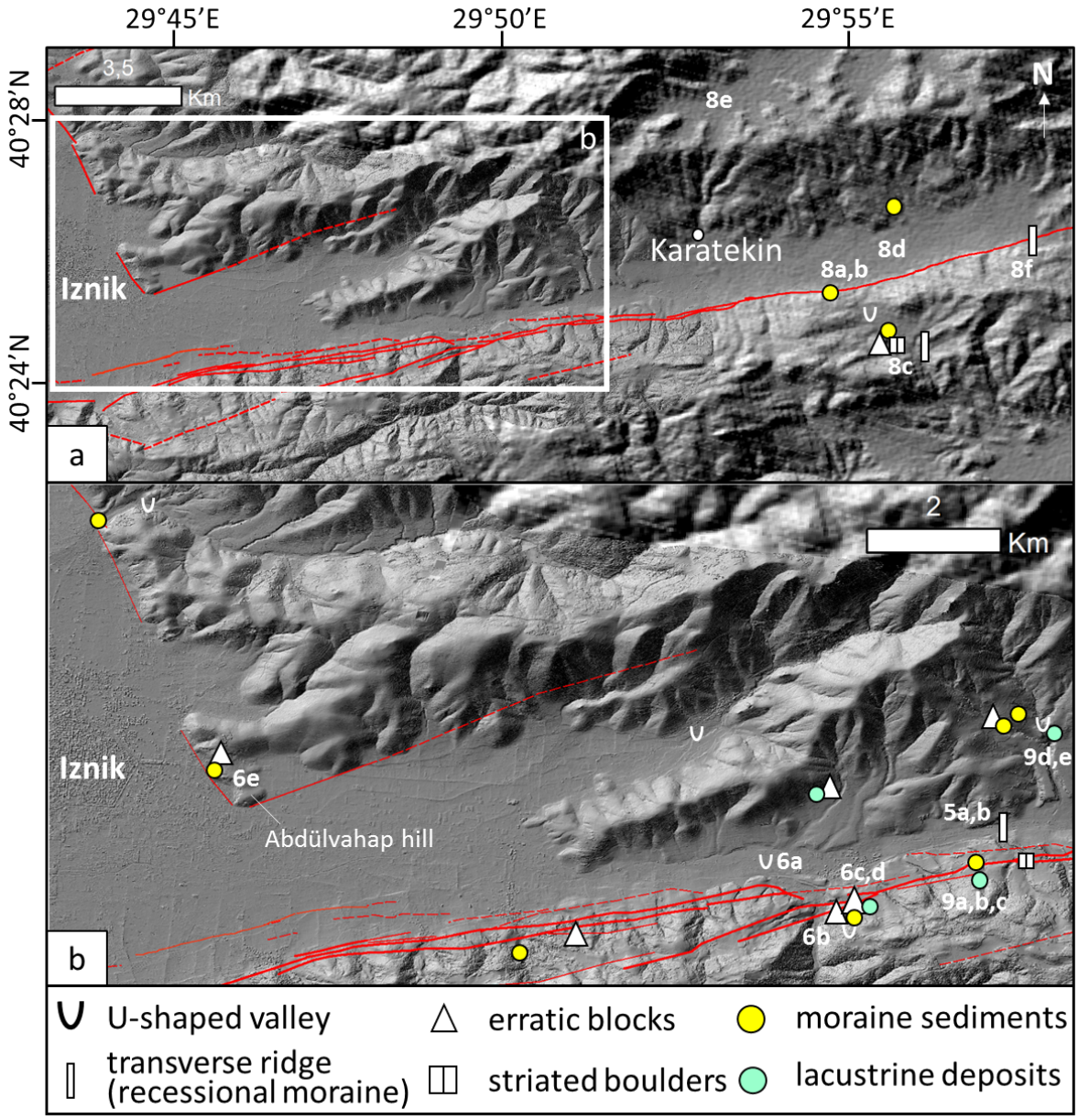

Figure B.4: Map (DEM) between Iznik and Karatekin along the Kirandere valley gathering the field evidence of past glaciations. (a) represents a general view when (b) represents a zoomed view on the Kirandere valley. Certain features observed are photographed in Fig. B.5 the numbers refer to these photographs.

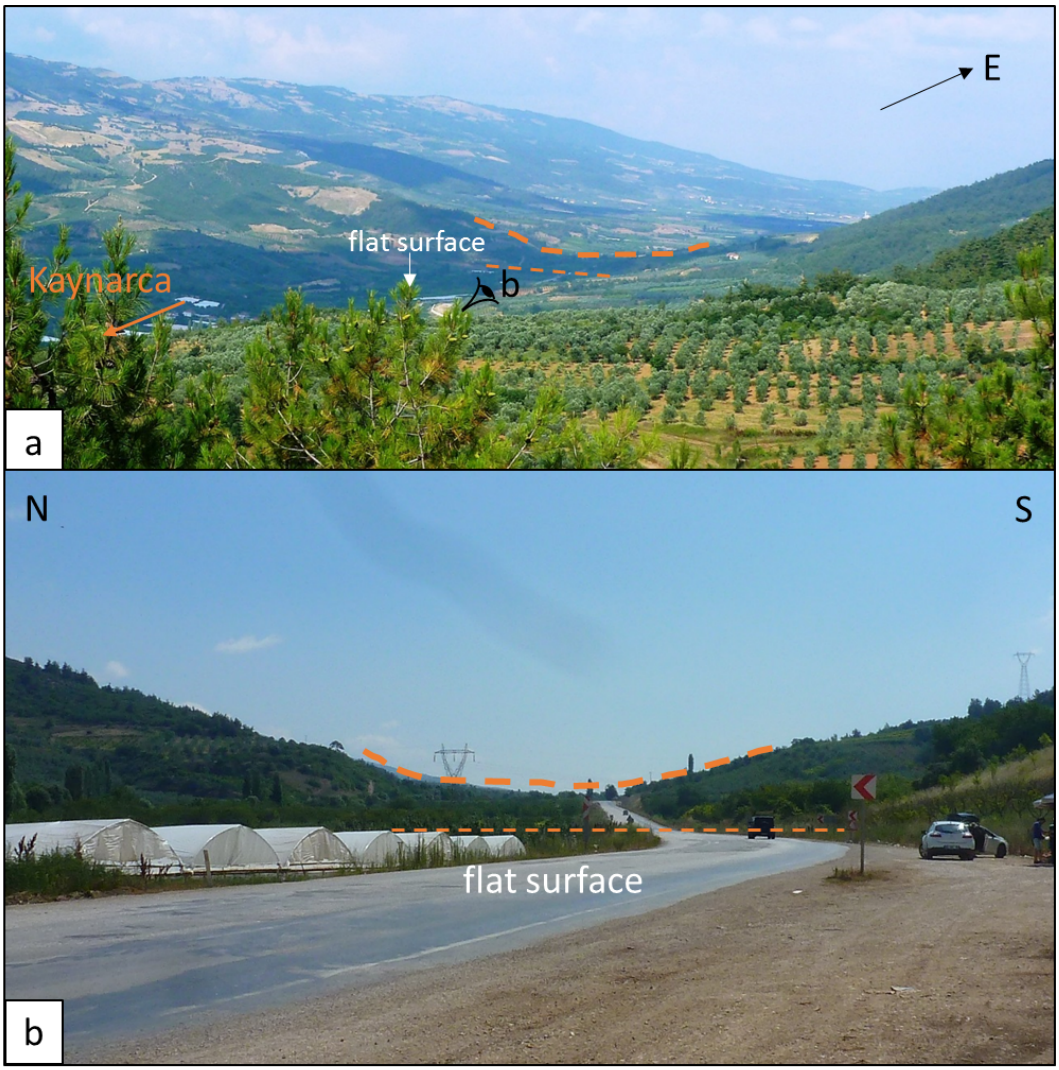

Figure B.5: Morphology of the valleys east of Kaynarca (see Fig. B.4 for location). (a) End moraine (transverse ridge) surrounded by two deeper areas; (b) closer view at the foot of the moraine where the topographic bulge is well visible. The U shape is shown with a thick broken line while the flat surface is shown with a thin broken line.



Figure B.6: Evidence of glaciations encountered on the field west and south of Kaynarca (see Fig. B.4 for the location of each shot). (a) U-shaped valley around Kaynarca seen from the southwest, underlined by a broken line. (b) Erratic blocks of limestone on moraine deposits. The local basement is made of conglomerates, sandstones and clays. (c) Erratic block of conglomerate lying on a cheminée de fée above moraine deposits. (d) Detail of the block lying on the top of the cheminée de fée, a conglomerate of mostly quartz gravel in a white matrix. (e) Erratic blocks on the smooth relief of Abdülvahap hill.

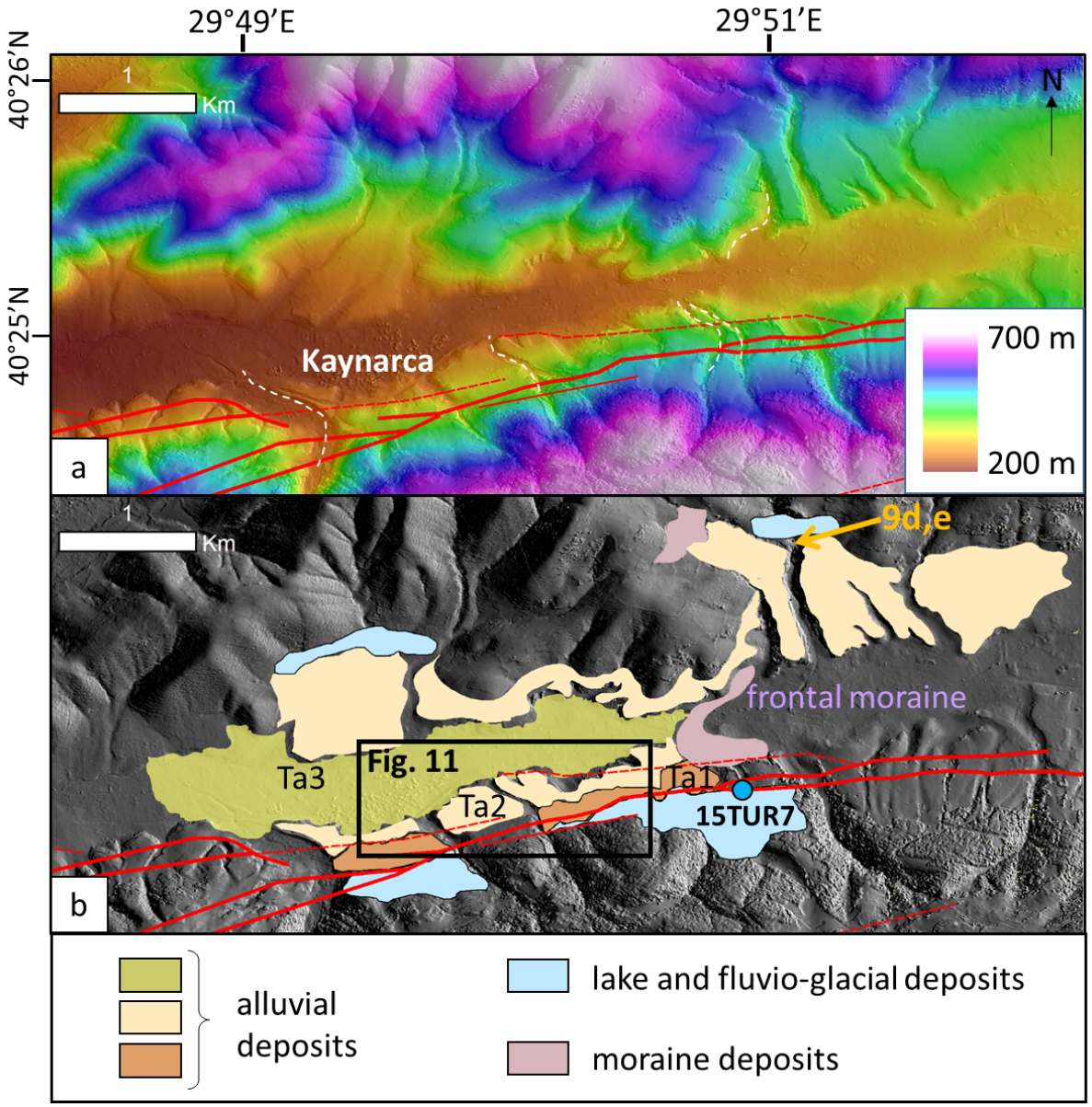

Figure B.7: (a) Shaded DEM of Kaynarca corridor colored according to the elevation. The left-hand inflexions of some rives next to glacier retreat points are drawn in white. (b) Geomorphological map of the sedimentary deposits associated to the glaciations and the post-glacial alluvia (fans and alluvial terraces Ta), with location of sampling site 15TUR7 in fluvio-glacial deposits.

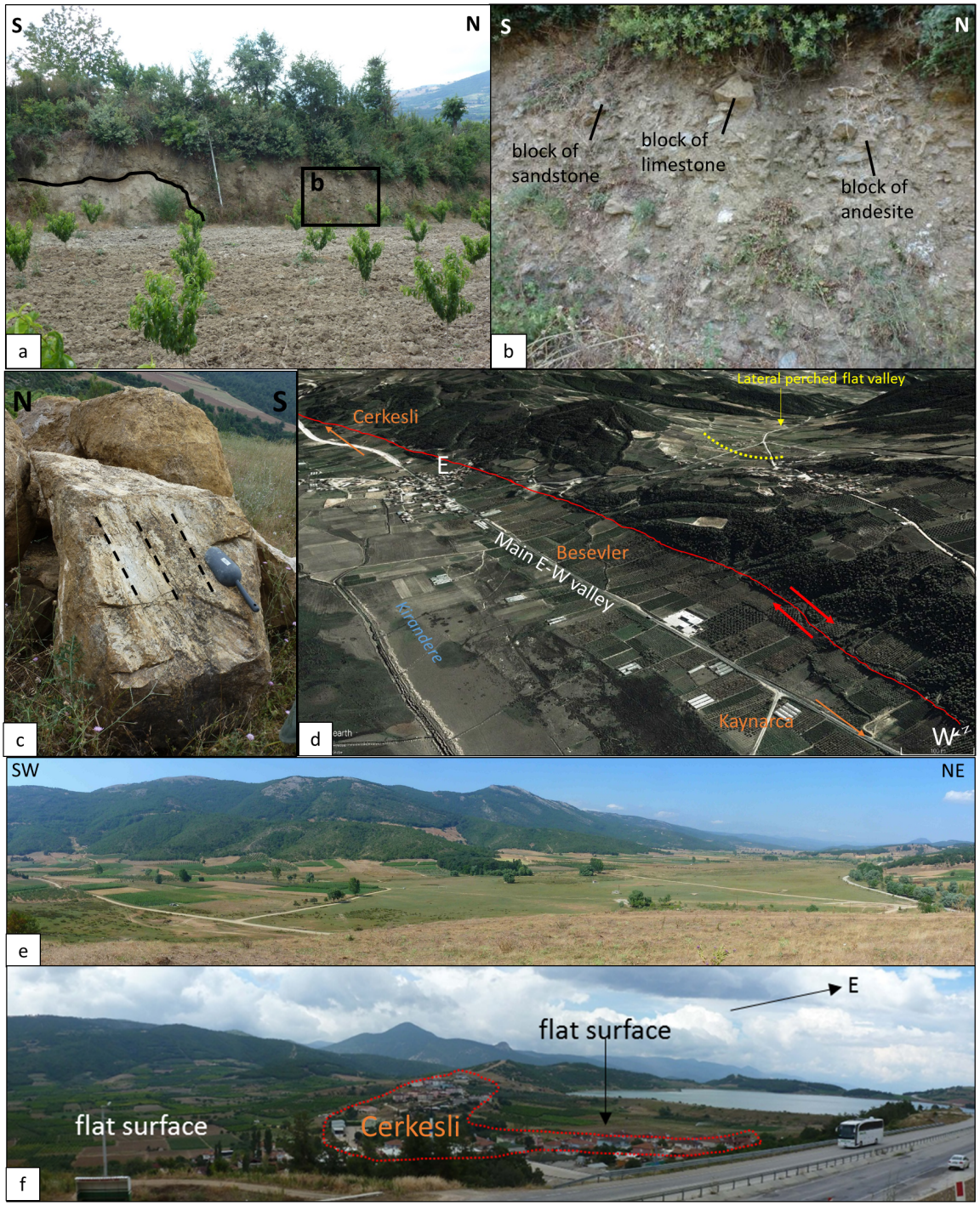

Figure B.8: Evidence of past glaciations encountered on the field near Cerkesli (see Fig. B.4 for the location of each photo). (a) Moraine deposits lying on folded sandstones with an erosive contact (black line). (b) Detailed view of the moraine deposits including various and sometimes allochtonous blocks of different lithologies. (c) Block of limestone showing glacial striations. (d) Google Earth view of a lateral perched valley south of the main Kirandere valley. the active MNAF is drawn in red. (e) Perched flat "plateau" northeast of Karatekin. (f) Possible frontal moraine (in red) west of Cerkesli Lake.

B.4.2.2 Lithological evidence

Lateral moraines are locally observed along the sides of the Kirandere valley in a high position (Fig. B.7 and B.8a,b). Moraines are present as unorganized deposits containing sharp blocks and unrounded pebbles of various lithologies (rhyolite, limestone, sandstone, conglomerate...) into a very fine matrix of glacial flour (Fig. B.8b). On the surface, erratic blocks of various lithologies (mainly limestone, sandstone and conglomerate) are visible at several places (Fig. B.4, B.6b,c,d and B.8c). At some locations on the top of the moraines at 380 m asl, lacustrine silt-marl deposits, sometimes containing dropstones and soft pebbles were encountered, probably related to the debacle at the end of the glaciation (Fig. B.9a,b,c). At a lower elevation, rather flat deposits of alluvial terraces (containing round pebbles) lie structurally on the moraine, the lacustrine sediments or the bedrock.

Moraine deposits and erratic blocks were also found in the adjacent valleys (Fig. B.4). The smoothly curved morphologies surrounding Abdülvahap hill east of Iznik, at the southern tip of the massif, are covered by erratic blocks (Fig. B.6e). Down the hill facing Iznik lake, U-shaped channels have been dug into the basement rocks and filled with more or less organized sediments of fluvio-glacial type.

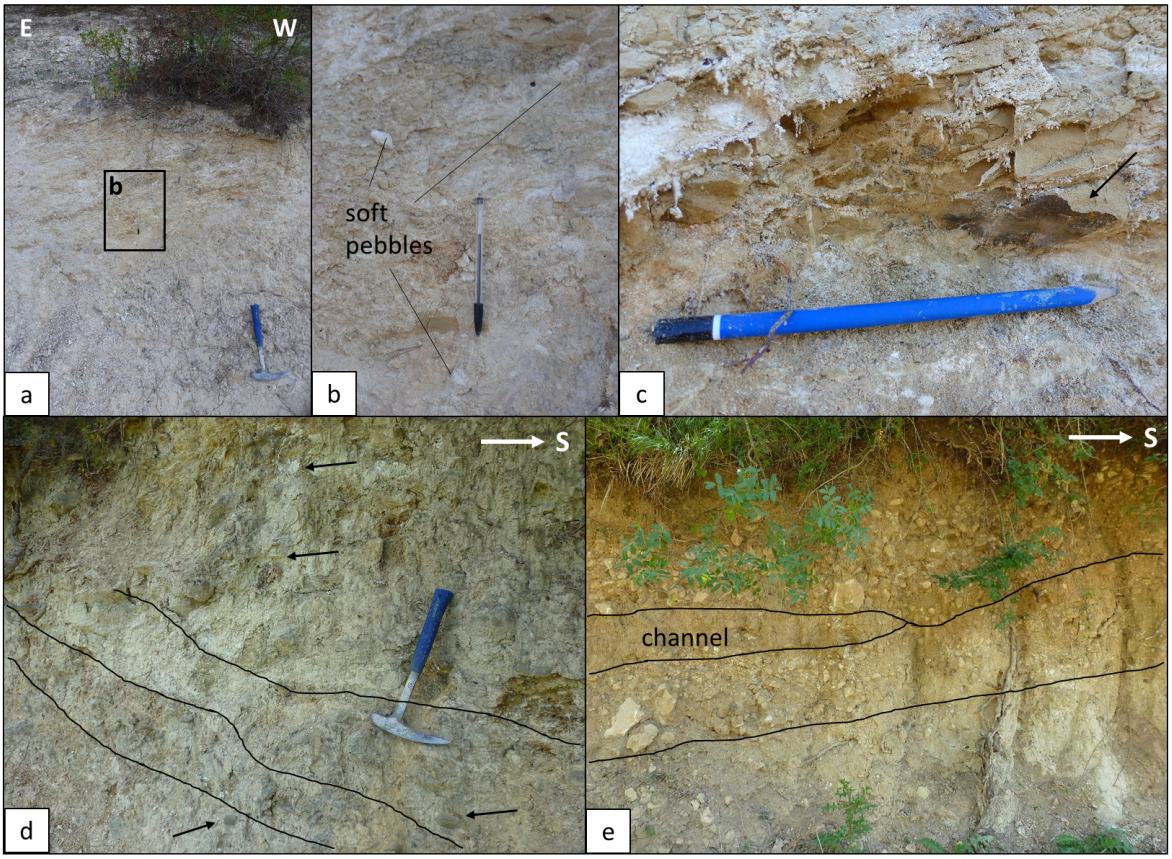

Figure B.9: (a) Outcrop of fine marly deposits interpreted as glacial lacustrine sediments south of terrace Ta1 (see Fig. B.4 and B.7b for location). (b) Detailed view showing the occurrence of dropstones or soft pebbles in the lacustrine deposits. (c) Detailed view in the same outcrop showing ripple marks (arrow). (d) Dark and white finely stratified carbonate lake deposits located west of Karatekin, containing round pebbles (arrows) and with a bedding slightly titlted toward the Kirandere valley. (e) Fluviatile sediments interpreted as part of a topset deltaic sequence. See Fig. B.4b and B.7a for locations.

B.4.3 Post-glacial alluvial deposits

At the same elevation (392 m asl) on both sides of the Kirandere valley close to Karatekin village,on top of the lateral moraines, fine white deposits of glacio-lacustrine marl are observed with a slight tilted stratification trending towards the valley (Fig. B.9, suggesting the existence of a paleo lake in this valley. At the same elevation (located as 9d,e in Fig. B.4b) within a small valley tributary of the Kirandere river, a sequential stratigraphy characteristic of a deltaic top set is observed (Fig. B.9e,f). This deltaic sequence lies on the massive limestone of the bedrock. North and above this zone, erratick blocks are found again (Fig. B.9g). These formations suggest here also the existence of a former lake linked to the glaciation that emptied before the deposition of the alluvial terrace over the glacial sediments.

Other important post-glacial alluvial formations are visible on the northern shore of Iznik Lake (see Fig. B.1 and B.10a for location), where a series of three fluvio-lacustrine terraces (Tl1, Tl2 and Tl3) were deposited (Fig. B.10). While most of the outcrops display quite typical alternations of fine sand and coarse gravels, Tl2 also displays coastal beachrocks containing shells of bivalves. These beachrocks were covered after their emersion by continental tufa deposits linked to the local tectonic activity as they are aligned with an active fault (Fig. B.10f,g).

Alluvial sediments posterior to the glaciation were mapped and described on both sides of Kaynarca corridor (Fig. B.7 and B.11). Three levels of alluvial terraces (Ta1,Ta2,Ta3) are preserved in the south. In general, these deposits overlay the moraine deposits with an erosional contact. Therefore, most preserved moraines at the surface are located at a higher elevation. The base of Ta1 (Fig. B.11e) is made of fine clay levels containing organic residues overlain by much coarser sediments with big round or angular blocks 1 m above the clay levels. This could be interpreted as a transition between a lake environment contemporary of the late glaciation and a fluvial sedimentation after the glacial outburst. The two younger terraces, Ta2 and Ta3, show quite homogeneous sedimentations at depth with alternations of fine and coarser pebbles. North of Kaynarca, a flat fan surface at 270-280 m asl could be contemporary of Ta2 (see Fig. B.4 for location and Fig. B.7b). The surface is covered by erratic blocks. In the northern side of the valley, just east of Kaynarca corridor, very flat alluvial surfaces of silty sediments containing a few pebbles were deposited at 307 m asl above a limestone and schist basement.

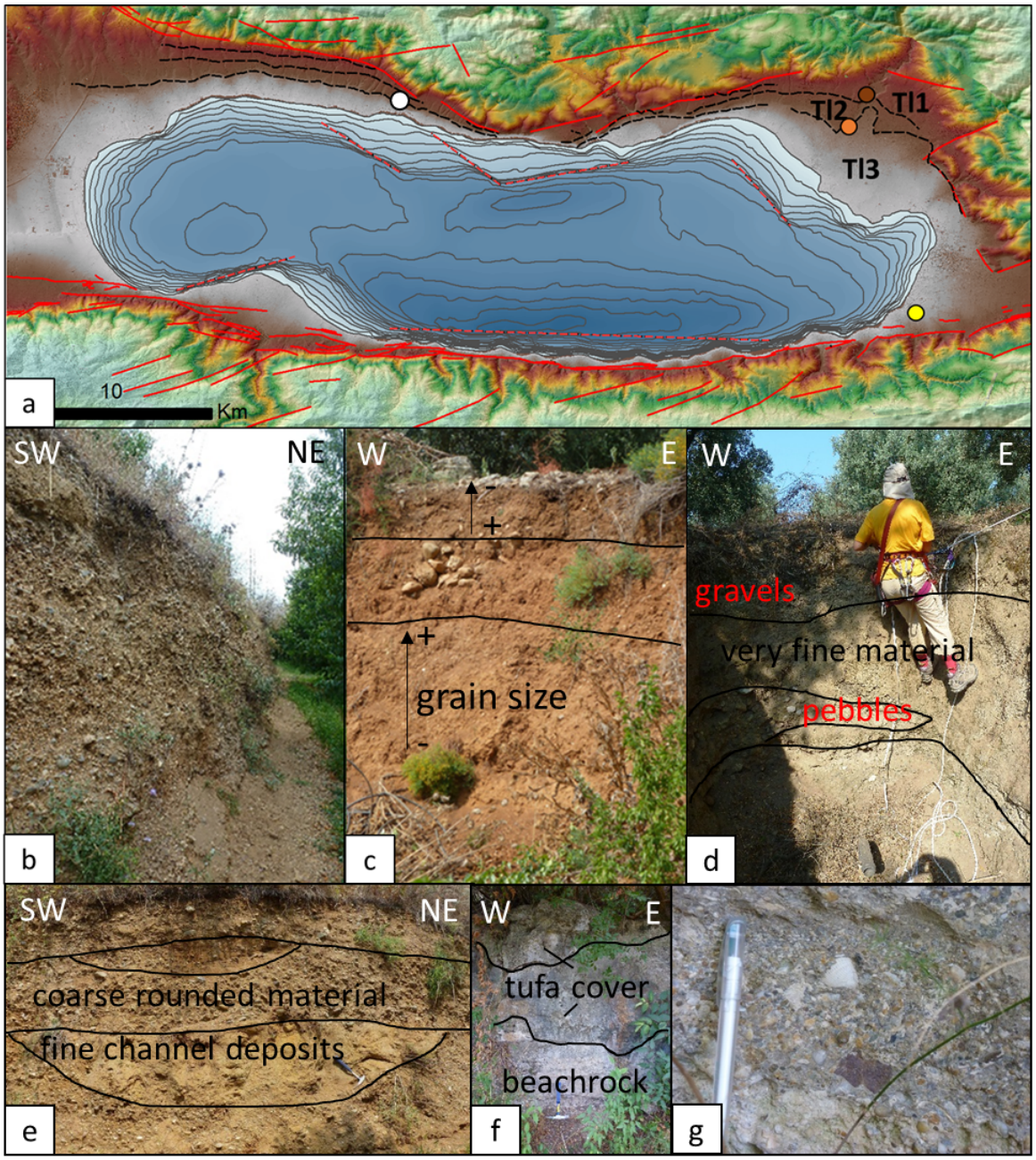

Figure B.10: (a) DEM showing the location of the sampling sites in the fluvio-lacustrine terraces Tl around Iznik Lake. The white circle indicates the location of emerged beachrock sediments in Tl2, later covered by continental tufa. The isobaths spacing is 5 m. (b,c,d) Field photos of Tl1, Tl2 and Tl3 respectively, showing graded bedding and vertical coarse-fine material alternations. (e) Detailed view of Tl1. (f) Outcrop of beachrocks in Tl2 covered by tufa. (g) Detailed view of the beachrock.

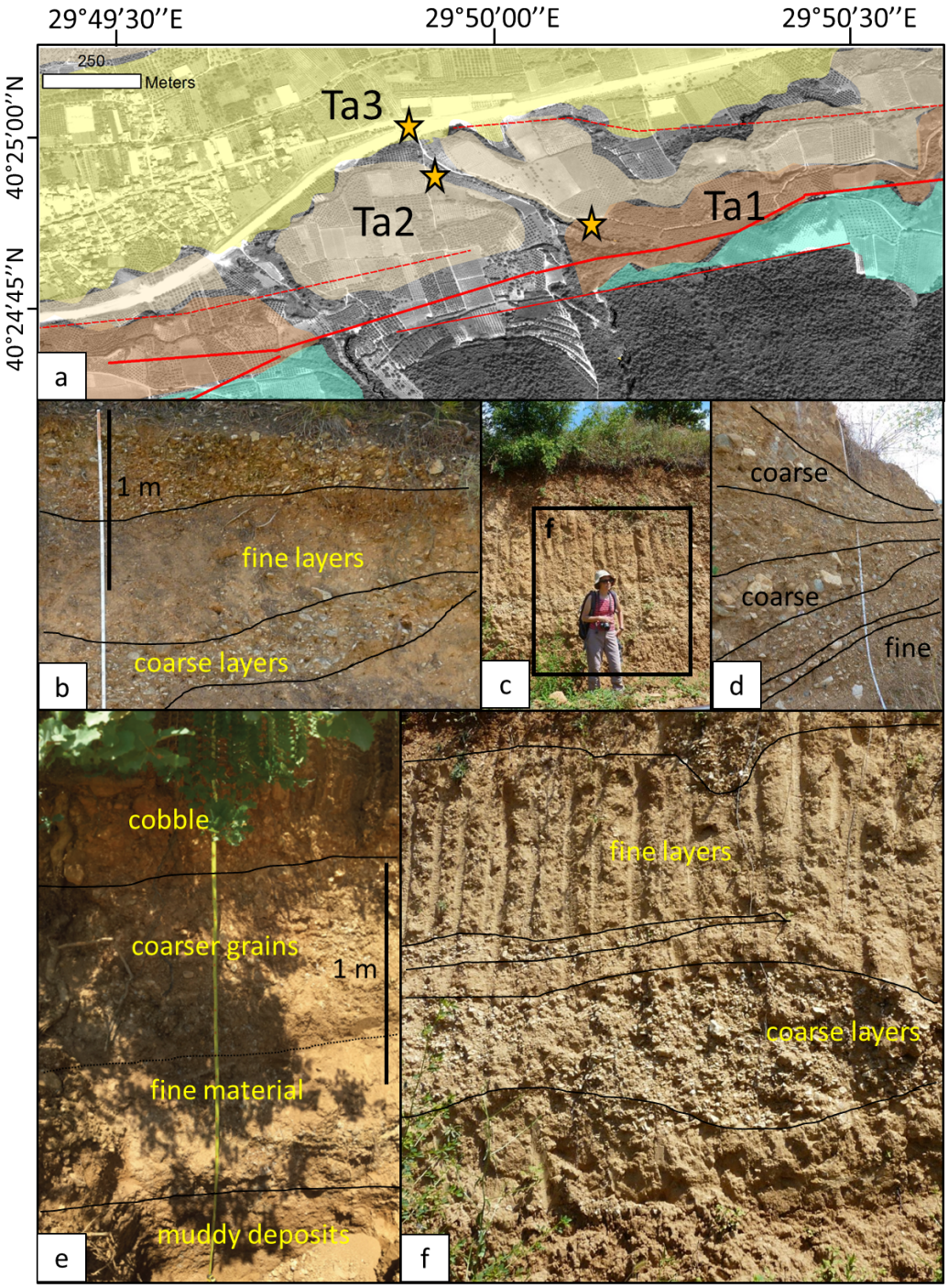

Figure B.11: (a) Pleiades map showing the location of the alluvial terraces near Kaynarca and the sampling sites. (b,c,d) Field photographs of sampling sites in Ta1, Ta2 and Ta3 respectively. (e) Detailed view of the base of Ta1, with a transition from dark clay sediments to bigger pebbles and cobbles. (f) Detailed view of the stratification in Ta2. All the outcrops exhibit vertical alternations between fine and coarse material typical of alluvial sediments.

Sample	Location (lat,lon)	Description	Age BP	Calibrated age AD
15TUR3CH3	40.49633,29.68133	Tl2, 1-1.10 m from the top	3570±70	-1917±217
15TUR3CH4	40.49633, 29.68133	Tl2, 1.10-1.30 m from the top	9440±90	-8814.5±330.5
15TUR4CH6	40.50308, 29.68600	Tl1, 3 m from the top	2220±60	-258±143
15TUR4CH2	40.50308, 29.68600	Tl1, 3.60 m from the top	8160±100	-7187±752
15TUR4CH1	40.50308, 29.68600	Tl1, 3.80 m from the top	19050±310	-21100±692
15TUR7CH5	40.41593, 29.84870	gouge in fluvio-glacial (?) deposits	24500±160	-26561.5±370.5
15TUR7CH6	40.41593, 29.84870	gouge in fluvio-glacial deposits	42500±1500	-44607±2875

Table B.1: Radiocarbon ages of the sediments sampled on the field. The ages BP were calibrated with the OxCal 4.2 software (Bronk Ramsey, 2009) using the IntCal calibration (Reimer et al., 2013).

B.4.4 Dating

B.4.4.1 Radiocarbon dating

The results of the ^{14}C dating are shown in Table B.4.4.1. The dates obtained in Tl1 and Tl2 are younger than expected as most ages obtained are mostly Holocene, and some ages obtained in both terraces surprisingly overlap. The maximum ages obtained in Tl1 are older than in Tl2 (around 20 and 10 ka respectively).

The ages obtained in fluvio-glacial deposits (site 15TUR7, see Fig. B.7 for location) deformed by a strand of the MNAF range between 25 and 45 ka (Table B.4.4.1), which corresponds to the end of the pre-LGM period (Yokoyama et al., 2000).

B.4.4.2 Exposure ages from in-situ produced ^{10}Be

The results are presented in Table B.2 and Fig. B.12.

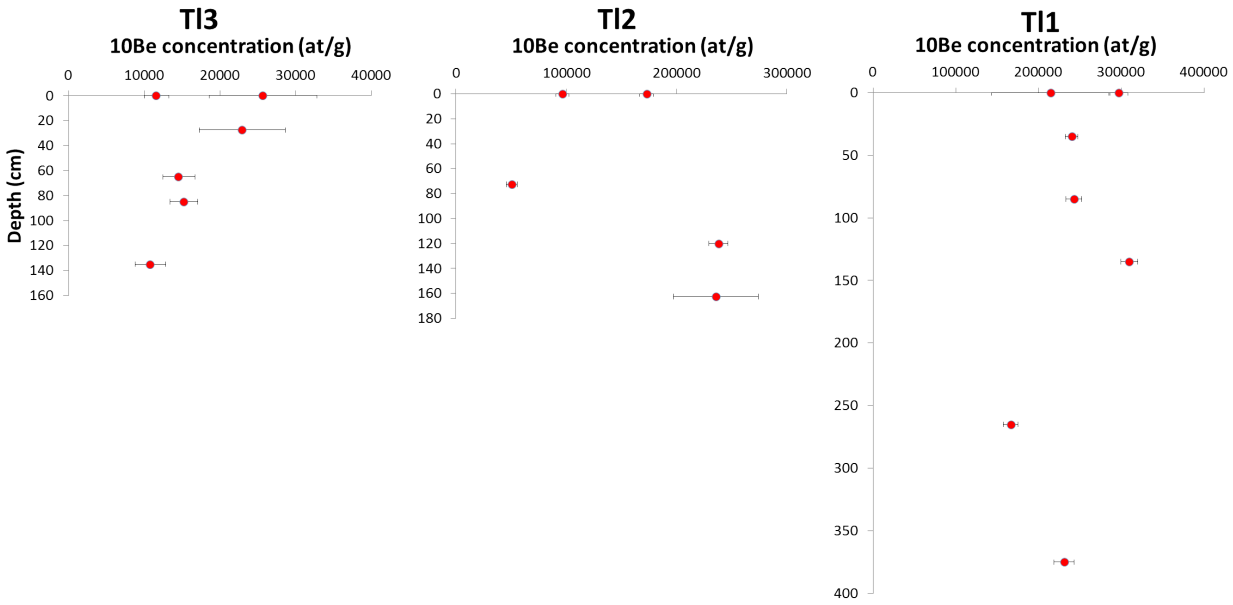

Figure B.12: ^{10}Be concentration (at/g) versus depth profiles measured for the three lacustrine terraces.

Terrace	Sample code	Depth (cm)	Dissolved mass quartz (g)	Mass spike (g)	$^{10}Be/^{9}Be$ ratio (blank corrected)	1σ AMS error (%)	10Be (at/g)	Total measurement error (%)	Sampling site location
Tl3	I5TUR5-0a	0	17,18	2,9880E-04	9,9129E-15	12,19	11 643	14,18	40,39744°N - 29,69657° E
Tl3	I5TUR5-0b	0	18,48	2,9900E-04	2,3170E-14	27,31	25 718	27,60	94±4 m asl
Tl3	I5TUR5-20	20-35	2,86	3,0100E-04	3,4277E-15	21,70	22 981	24,86	
Tl3	I5TUR5-60	60-70	10,74	2,9950E-04	8,0123E-15	11,93	14 577	14,48	
Tl3	I5TUR5-80	80-90	16,35	2,9800E-04	1,2254E-14	10,07	15 251	11,89	
Tl3	I5TUR5-130	130-140	6,79	2,9760E-04	3,8083E-15	14,61	10 819	18,69	
Tl2	15TUR3-0a	0	20,55	3,0430E-04	1,7851E-13	3,46	172 845	3,52	40,49633°N - 29,68133°E
Tl2	15TUR3-0b	0	18,51	3,0780E-04	8,9092E-14	5,96	96 443	6,08	127±3 m asl
Tl2	15TUR3-60	60-85	20,82	2,9890E-04	5,3093E-14	9,33	50 497	9,54	
Tl2	15TUR3-110	110-130	19,94	2,9050E-04	2,4513E-13	3,61	237 919	3,64	
Tl2	15TUR3-150	150-175	17,04	2,9930E-04	2,0041E-13	16,27	235 779	16,28	
Tl1	I5TUR4-0a	0	20,84	2,9790E-04	2,2687E-13	33,36	215 052	33,36	40,50308°N - 29,68600°E
Tl1	I5TUR4-0b	0	20,51	2,9730E-04	3,1365E-13	3,78	296 712	3,80	164±3 m asl
Tl1	I5TUR4-30	30-40	20,55	2,9580E-04	2,5537E-13	3,11	240 367	3,15	
Tl1	I5TUR4-80	80-90	23,55	2,9810E-04	2,9258E-13	3,92	242 836	3,94	
Tl1	I5TUR4-130	130-140	20,51	2,9840E-04	3,2630E-13	3,31	309 820	3,32	
Tl1	I5TUR4-260	260-270	22,20	2,9660E-04	1,8477E-13	5,29	166 452	5,33	
Tl1	I5TUR4-370	370-380	20,77	2,9800E-04	2,4349E-13	5,22	230 881	5,24	

Table B.2: Characteristics of the terrace samples and results of the nuclide measurements. The $^{10}Be/^{9}Be$ ratio of the blank is 6.19994E-15 with an analytical uncertainty of 19%.

The concentration-depth-profiles obtained were modelled with a Monte Carlo approach using the code *^{10}Be profile simulator version 1.2* developed by Hidy et al. (2010). This approach enables to find the combination of parameters that best fit the measured profile, including the exposure age, the erosion rate and the inherited TCN concentration. In a first stage we assumed that the terrace surface was not covered during the exposure. The half-life of ^{10}Be (1.387±0.012 Ma) was taken from Chmeleff et al. (2010). We used a reference production rate of 4.13 atoms.g^{-1}.a^{-1} for the neutron induced spallogenic production at sea level and high latitude (Stroeven et al., 2015). This rate is scaled to the sampling site's altitude and latitude using the scheme of Lal (1991) modified by Stone (2000). The muonic production is calculated using the theoretical equations of Heisinger et al. (2002b,a) and determined at the sampling site's elevation and for a given depth following the approach of Balco et al. (2008). The cumulative bulk density of the material above each sample was assumed constant over depth, with an average value of 2.2 g/cm^3, previously measured in similar gravel-based terraces (Hidy et al., 2010). For the first simulations, the initial parameters for age, inheritance and erosion rate were allowed to vary largely.

For terrace Tl3, the simulator was not able to produce solutions when all the data were included, especially because one surface sample (15TUR5-0a) showed a very low concentration comparable to the deepest sample (Fig. B.12). We assumed this sample to be an outlier, likely to originate from recent excavation and deposition during agricultural work. After excluding this outlier, we ran the simulation until 250,000 solutions were found within the 2σ confidence window, giving a most probable age of $4.9^{+2.3}_{-3.6}$ ka. This involves an inheritance of ∼7900 at/g (Fig. B.13).

Terrace Tl2 profile presented more complexity, especially because the two deepest samples (15TUR3-110 and 15TUR3-150) have the highest nuclide concentrations of all the dataset. They are likely to belong to a previous deposition sequence which was eroded before the onset of a new sedimentation sequence above. An erosion limit can actually be seen on the profile sampled in the field at a depth of 1 m (Fig. XX). Therefore, we recomputed excluding the two deep samples. The algorithm could not converge towards a solution for the three remaining data points, even when we allowed worse models to be accepted by increasing the χ^2 parameter. We also tested excluding one surface sample with the biggest concentration (15TUR3-0a), which allowed the algorithm to converge. The other surface sample 15TUR3-0b seems more reliable as it shows a nuclide concentration intermediate between the surface samples of the younger and older terraces. Keeping instead the sample 15TUR3-0a would lead to a similar age as Tl1. With two samples, it is logically impossible to determine at the same time statistically robust solutions for age, erosion rate and inheritance. To narrow down the solution space, we constrained the initial inheritance close to the concentration of sample 15TUR3-60, and the initial age below the age obtained for Tl1. We finally obtained 250,000 solutions within the 2σ confidence window, giving a most probable age of $14.9^{+4.5}_{-4.3}$ ka (Fig. B.14). This age is in average larger than the oldest radiocarbon age of 10.8 ka found in the terrace, but with the uncertainties the difference is

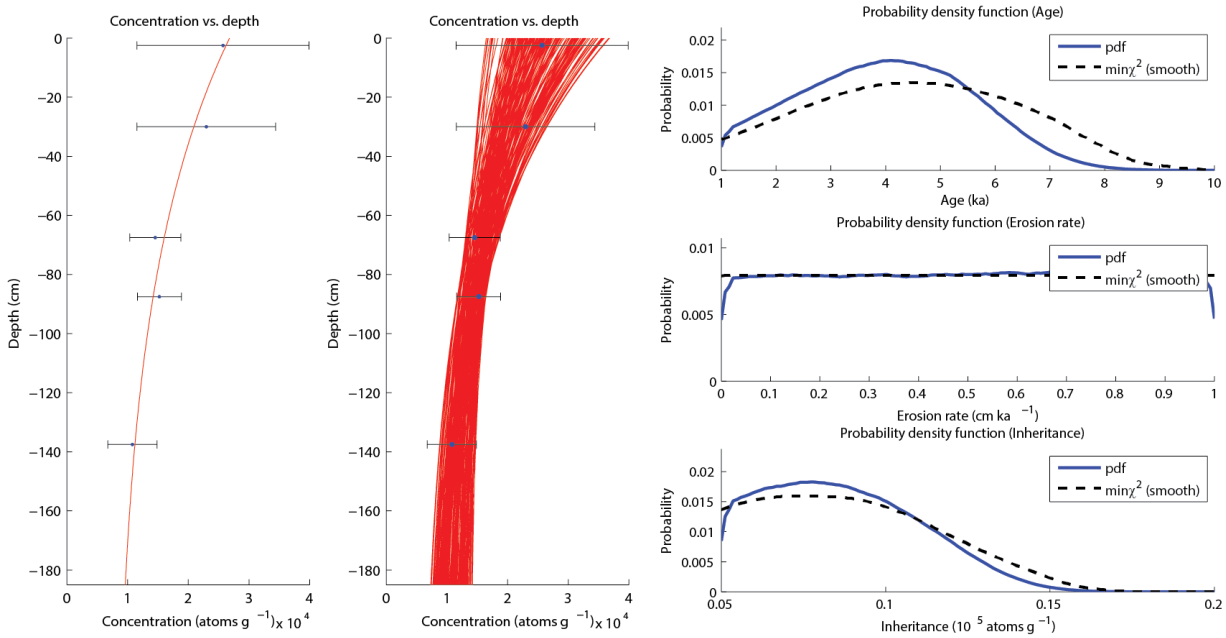

Figure B.13: Result of the Monte Carlo simulations for terrace Tl3. The left profile shows the best fit obtained while the centre profile shows all the solutions found for the parameter solution spaces defined as inputs. The graphics on the right show the probability density functions (solid lines) and the minimum χ^2 distributions (dashed lines) for the exposure age, erosion rate and inheritance concentration.

less significant (Table B.4.4.1).

Terrace Tl1 profile presents one point (15TUR4-130) with a high concentration, larger than the surface samples, which is incompatible with the theoretical depth profile. We can note that the deepest sample also shows a relatively high concentration, comparable with the shallower samples. It has been observed in previous studies than because of potentially complex transport histories, pebble samples may not have a constant inheritance with depth. We ran the simulation only excluding sample 15TUR4-130. The algorithm was not able to find solutions in the 2σ confidence window, and we had to increase the χ^2 cut-off value to 10. The 250,000 solutions obtained provide a most probable, modal age of $22.8^{7.1}_{5.4}$ ka (Fig. B.15). This age is in the same range as the oldest radiocarbon age of 23050 ka found in the terrace (Table B.4.4.1).

In a second stage, we conside that the terraces may have been temporarily covered under a certain depth of lake water before their total emersion. When the water depth gets lower than a few meters, the shielding of the water on cosmic rays incoming is only partial. For example, under 1 and 4 m of water, this shielding is around 50 and 10% respectively. In this hypothesis, some nuclide production occurred before the complete emersion of the terrace that we want to date. This could therefore lead to an overestimation of the age.

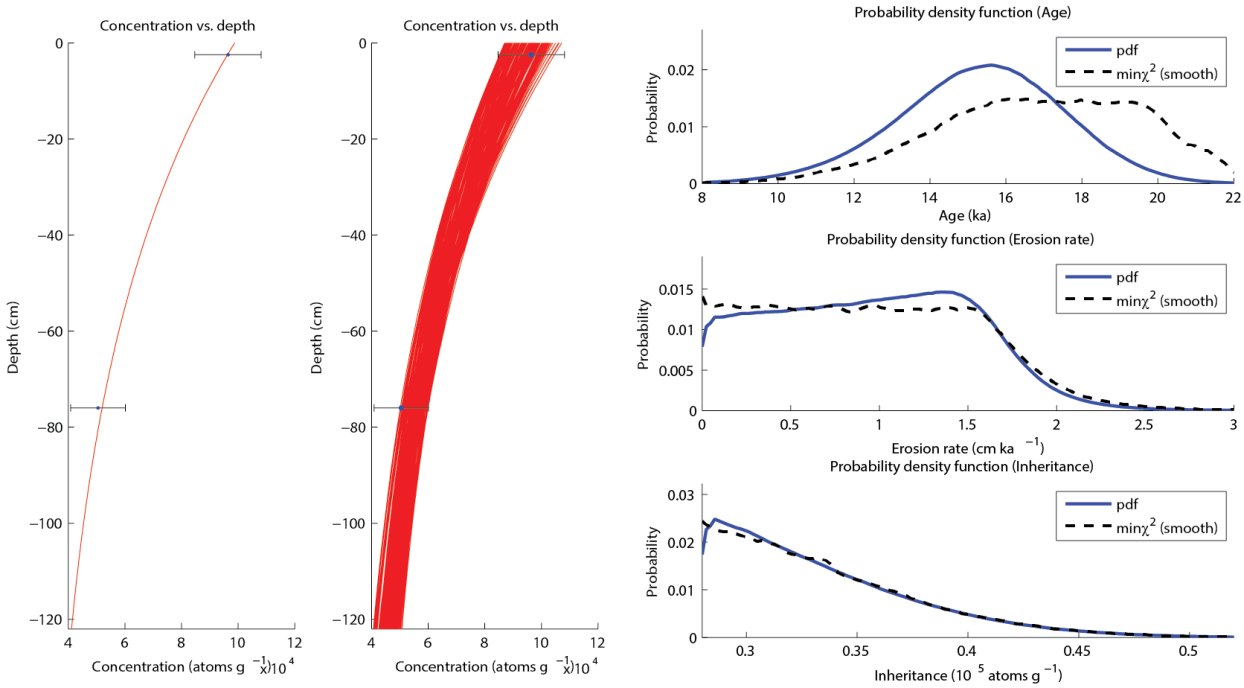

Figure B.14: Result of the Monte Carlo simulations for terrace Tl2. The left profile shows the best fit obtained while the centre profile shows all the solutions found for the parameter solution spaces defined as inputs. The graphics on the right show the probability density functions (solid lines) and the minimum χ^2 distributions (dashed lines) for the exposure age, erosion rate and inheritance concentration.

But differences in ages between terraces would be conserved in case of a similar emersion scenario for all. In order to estimate the order of magnitude of this effect, we ran the simulations a second time with the nuclide concentrations decreased by 10%. We logically obtain slightly smaller exposure ages for Tl1, Tl2 and Tl3 of $20.9^{+6.0}_{-3.5}$ ka, $13.1^{+3.5}_{3.8}$ ka and $4.1^{+2.4}_{-2.9}$ ka respectively. We can conclude that the water cover hypothesis does not change the ages obtained significantly. We note that the new age obtained for Tl2 is in average closer to the radiocarbon age.

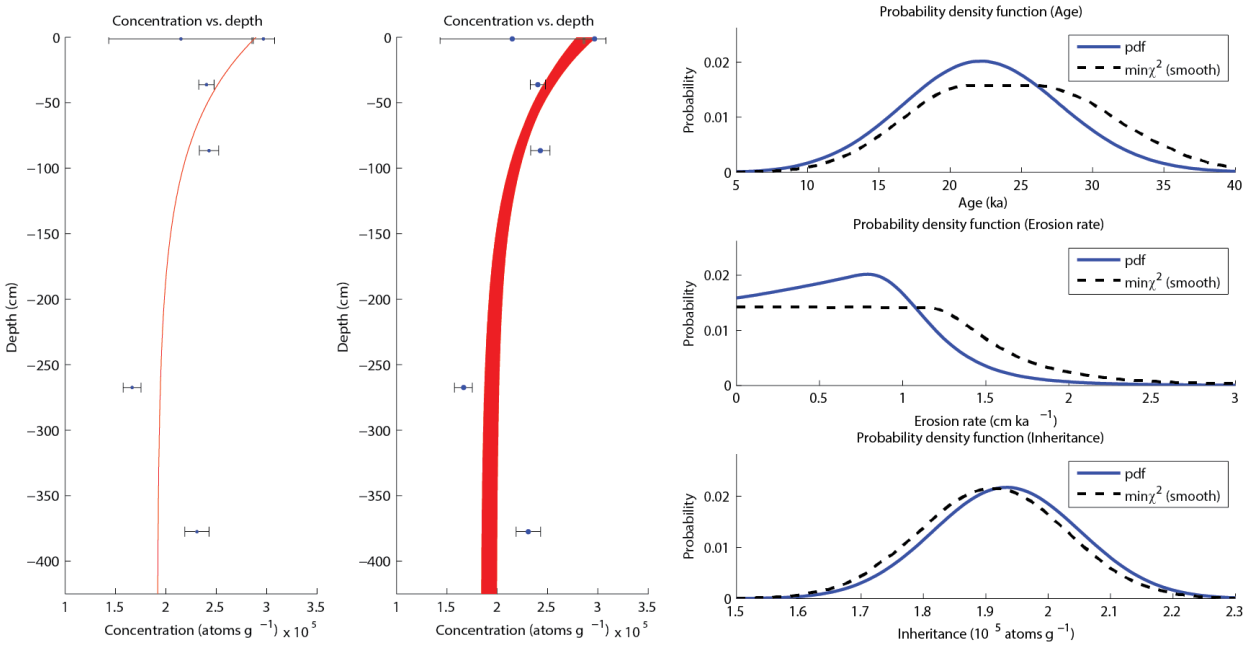

Figure B.15: Result of the Monte Carlo simulations for terrace Tl1. The left profile shows the best fit obtained while the centre profile shows all the solutions found for the parameter solution spaces defined as inputs. The graphics on the right show the probability density functions (solid lines) and the minimum χ^2 distributions (dashed lines) for the exposure age, erosion rate and inheritance concentration.

B.5 Discussion

B.5.1 Glacier reconstruction

Using the field evidence, the larger scale morphologies visible on the DEM and the different profiles extracted, we are able to reconstruct the original extent of the glaciers and follow their progressive regression (Fig. B.16 and B.17). The area west of the lake was not investigated on the field in as much details as the eastern valleys, and the possible glacier extent to Karsak pass is very uncertain (Fig. B.2b). The river profile of the lake outlet (Gölyatagi stream) also shows a recent disturbance on its topography (Fig. B.1 and B.3b) as the river is far from its hydrological equilibrium. All these features combined would suggest that the glacier reached the Karsak pass at its maximal extent.

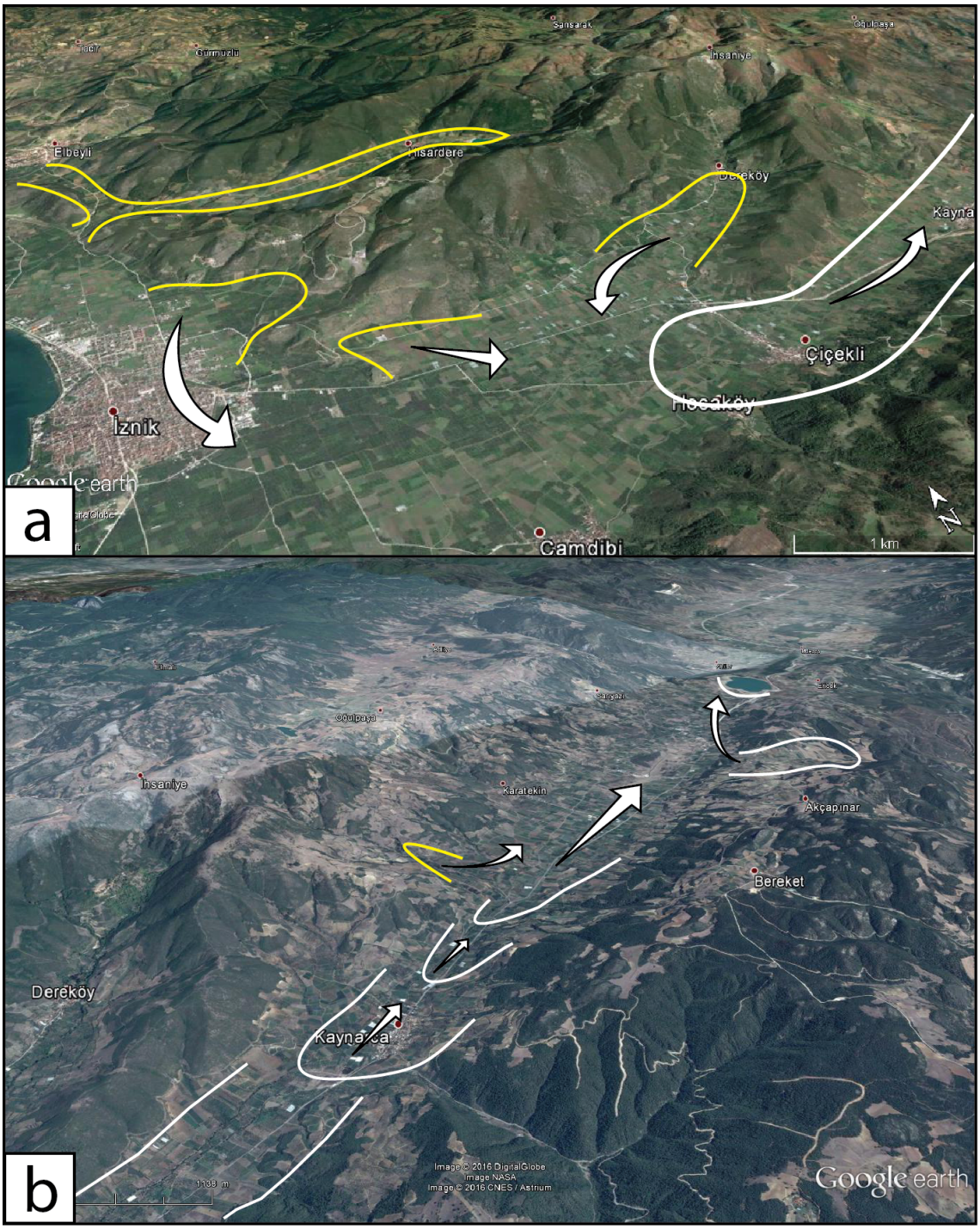

Figure B.16: Google Earth views showing the reconstruction of the past glacier extent and retreats west of Kaynarca (a) and east of Kaynarca (b). The successive extensions of the glacier during retreats are drawn in white, while lateral cirque morphologies are drawn in yellow.

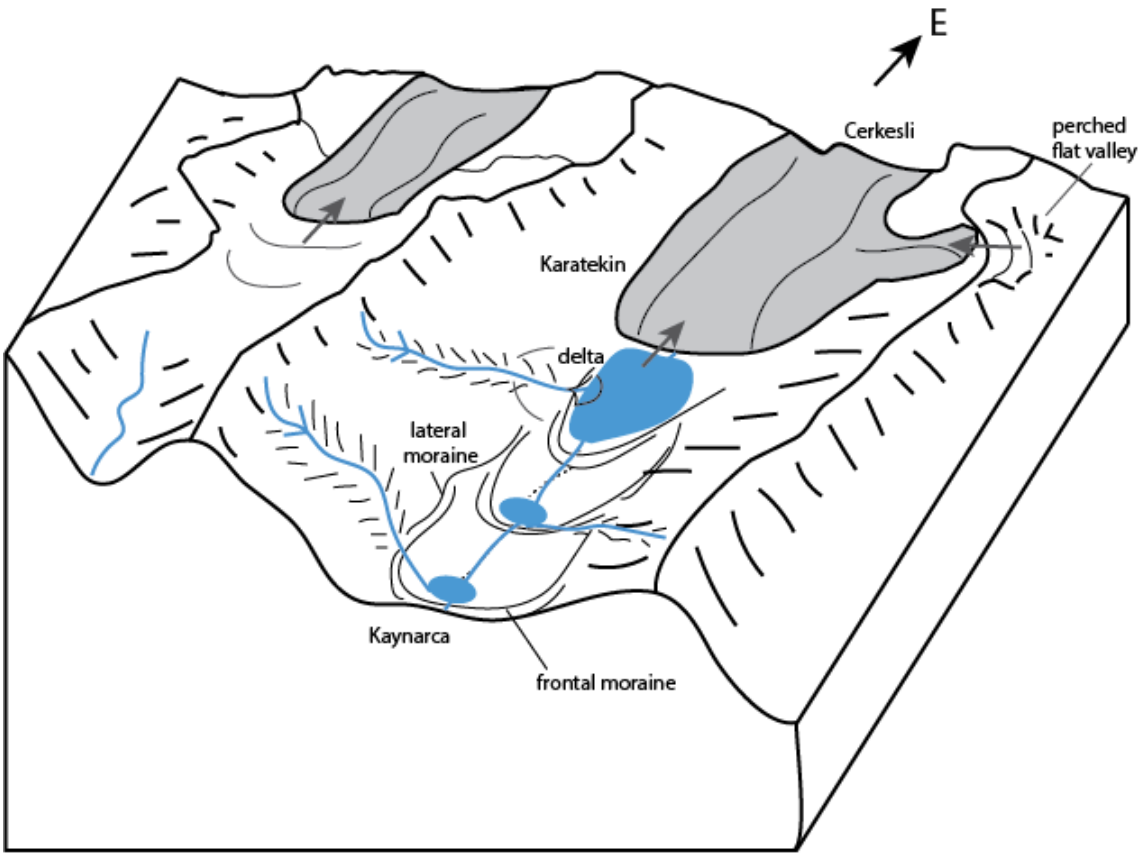

Figure B.17: Schematic sketch of the landscape east of Kaynarca during the glaciers retreat eastward (grey arrows). Moraines are deposited on the sides and at the front of the retreating glacier. Behind the successive transversal ridges and at the front of the glacier (in grey), small lakes can develop. This explains the deposition of elevated fluvio-lacustrine sediments and deltaic sequences as shown on Fig. B.9).

The successive traces of the glacier retreat are more visible in the areas east of Iznik Lake along the Kirandere valley. The carbonate massifs NE of Iznik were significantly eroded by the glacier leading to the formation of perched valleys where many erratic blocks of limestones were transported. The glacier regression patern follows then the main E-W axis of the valleys between Cerkesli Lake and Kaynarca along the MNAF, with several retreat stages concentrated around Kaynarca. On the sides of the Kirandere valley, the glacier enabled the formation of perched lakes fed by tributary rivers as proved by the small delta observed above Karatekin village. The glacial abrasion preceding the last retreat visible in the east is associated with Cerkesli Lake, which is crosscut by segments of the MNAF, in a similar way to Iznik Lake, showing the dextral activity of the fault since the last glaciation.

B.5.2 Timing of the glaciation and regional correlations

The chronology of these glaciation markers can be constrained from the dating realized on the sediments sampled on the field and from the results of other independent studies such as lake cores analyses (Roeser et al., 2012). The ^{14}C ages obtained in fluvio-glacial sediments (moraines) in the south of Kaynarca corridor of ∼25 and 43 ka are contemporary of the glaciation. The three fluvio-lacustrine terraces, on the northern shore of Iznik Lake, formed at the very end of Pleistocene and in the Holocene, postpone the glacier regression. The glaciation in Iznik area can thus be estimated older than the higher age found in the oldest terrace Tl1, which is around 20 ka.

Previous studies on sediment cores from Iznik Lake have documented the chronology of the major climatic variations since 36 ka, including the LGM (Miebach et al., 2016; Roeser et al., 2012). According to these studies, between 30 and 28 ka, the steppe-type vegetation pollen found in low to moderate concentrations around Iznik Lake suggest a dry and cold climate with a rather sparse vegetation cover in spite of rapid warmer episodes. Between 28 and 18 ka, the pollen productivity is even lower and compatible with a cool and dry steppe and low precipitation rates. The pollen data seem to agree with mineralogical and limnological parameters, such as a low endogen carbonate production and a low lacustrine bioproductivity recorded between 31 and 17 ka, indicating lower summer temperatures. Interestingly, Roeser (2014) reports the occurence of dropstones within the clay matrix in this same unit of the lake sediments, suggesting the occurence of at least a partial ice cover of the lake. However, the undisturbed preservation of the Y2 tephra layer at 22 ka precludes any important ice-cover in the end of the LGM period (Roeser et al., 2012). After 18 ka, increasing pollen concentrations and lake productivity mark the termination of the LGM and the transition towards denser vegetation and a warmer climate. The major climatic stages deduced from the lake sediments seem therefore compatible with the time constraints given by our dating, with a significant glacier extent and moraine formation before 20 ka BP, followed by increasingly warmer conditions and alluvia deposition in the end of Upper Pleistocene. Another interesting point is that the oldest sediments yet sampled in Iznik

Lake date back from 36 ka (Roeser et al., 2012). While it may be possible to core deeper in the sediments with technical improvements, this provisional minimum age for the onset of Iznik Lake sedimentation suggests that Iznik Lake existed when the last great glaciers developed.

At a regional scale, several studies have recently demonstrated the existence of well-developed glaciers mainly during the LGM in Turkish mountains (Sarikaya and Ciner, 2015). The majority of the paleo-glacial formations began to develop much before the LGM around 29-35 ka and probably reached their maximum size by 21 ka. The modeling of those glaciers suggests that their environment was 8-11 ˚ C colder than today (Sarikaya et al., 2014). Close to the Marmara Sea, the only evidence of glaciers was so far located in the Uludag Mountains, 40 km south of our study area (Birman, 1968). Zahno et al. (2010), followed by Akçar et al. (2014) showed that the glaciers reached their maximal advance between 25 and 20 ka, before the deglaciation started around 18 ka, which is in very good agreement with our proposed scenario in Iznik area. The 22 ka lower bond for an ice-cover on Iznik Lake indicates that the deglaciation started earlier in our study zone, which is reasonable given the much lower elevation. Akçar et al. (2014) possibly found the first evidence of an Anatolian pre-LGM glaciation in the eastern Uludag (Karagöl valley) at around 38 ka. We could possibly relate the oldest sediments in Iznik Lake as well as the oldest age found in 15TUR7 moraines to this pre-LGM glacial event.

However, the glaciers previously identified in Turkey were all found at elevations higher than our evidence. The glacial morphologies of the Uludag mountains were not seen below 1800 m for the LGM (Akçar et al., 2014). Lower moraines were found by Zreda et al. (2011) at 1100 m and dated around 10 ka BP in the Taurus mountains, in south-central Turkey. This low figure, found for a lower altitude than our study area, is still higher than the elevation of our markers, which stand below 1000 and m. Some of them were encountered below 400 m, closer to the current sea level. These findings are therefore rather unexpected. Other scenarios might be invoked to explain some of these markers (fluvial erosion, flash-flood or colluvial deposits, tectonics), but we could not propose a suitable scenario that encompassed the whole set of markers, and we conclude that the glacial hypothesis is worth considering. The estimated equilibrium line altitude (ELA) for the most extensive Pleistocene glaciers is estimated around 2200 m for northwestern Turkey (Hugues and Woodward, 2017), and at the scale of the Mediterranean region, the determined ELAs do not fall below 1000 m. In this frame, it is difficult to understand the formation of glaciers in our study area, because the glaciers are logically not expected to exist below the equilibrium line. For the time being, and while an alternative comprehensive scenario has not been proposed, our findings should encourage to reconsider the local ELA estimates and search for other markers in such overlooked, low elevation regions.

It is also important to note that the level of the Sea of Marmara was significantly lower during the last glacial period compared with today. Several studies using both high-resolution seismic profiling and biostratigraphical and petrological analyses of the sediments

have shown that the Sea of Marmara level fell to about 100 m below the present level during the LGM and the early phase of the deglaciation, between 25 and 13 ka (Aksu et al., 1999; Ergin et al., 1997; Smith et al., 1995). Given the depth of the Dardannelles Straight sill at about -65 m, the Sea of Marmara became isolated from the Aegean Sea and existed as a freshwater lake which level was controlled by the spill-over height across the straight (Çağatay et al., 2000, 2003; Eriş et al., 2011). Therefore, the areas where we found traces of past glaciers were higher than today relatively to sea level.

B.6 Conclusion and perspectives

Our observations suggest the possible existence of low-elevation glaciers between Gemlik and Mekece during LGM. This glacier was probably the main agent shaping the large-scale landscapes of this areas made of successive valleys of different sizes. The few ages collected in sediments contemporary and posterior to the glaciation suggest that these glaciers were developed between 25 and 20 ka, with a probable retreat beginning no later than 22 ka. A pre-LGM glacial event is nonetheless not excluded. The underway dating of erratic boulders, paleo-lake deposits and the fluvial terraces in the south of Kaynarca which formation closely follows the deglaciation will enable to confirm these first clues and further constrain the glacier regression in time and space.

B.7 Résumé

Ce chapitre présente les premières traces d'empreinte glaciaire du LGM (Last Glacial Maximum) à basse altitude en Turquie. Des traces de glaciers de cette période ont déjà été étudiées dans les montagnes du sud et de l'est de l'Anatolie, mais aussi entre 2500 et 1900 m d'altitude dans le massif de l'Uludag situé 40 km au sud de notre zone d'étude. Ce sont des marqueurs précieux pour reconstituer les climats passés.

L'étude du MNT haute-résolution dérivé d'images satellites Pléiades a permis de mettre en évidence plusieurs bourrelets topographiques en forme de croissant, associés à des anomalies du profil des rivières suivant les vallées allongées entre Mekece et Iznik. Ces anomalies sont interprétées comme les marqueurs de retrait d'anciens glaciers. Des indices morphologiques et lithologiques de la présence de glaciers observés sur le terrain sont aussi présentés : vallées en U, moraines frontales et latérales, lacs et vallées perchés, blocs erratiques portant parfois des stries glaciaires. Des dépôts de type lacustre et fluviatiles, associés à une séquence deltaïque ont aussi été identifiés, surélevés par rapport à la vallée principale. Ceci suggère la présence d'anciens lacs en front de glacier.

Les dépôts glaciaires sont couverts par des alluvions postérieures, notamment une série de trois terrasses lacustres (Tl1 à Tl3) au nord du lac d'Iznik. Une autre série de terrasses

alluviales (Ta1 à Ta3) est présente sur les bords de la vallée étroite de Kaynarca. La base de la terrasse la plus ancienne Ta1 présente une succession de faciès interprétée comme la transition d'un environnement lacustre à une sédimentation fluviatile suite à la débacle glaciaire. Deux âges radiocarbone de 25 et 45 ka ont été obtenus dans des dépôts fluvio-glaciaires. Les terrasses lacustres ont été datées par carbone 14 et beryllium 10 produit in situ, avec des âges de 20.9, 13.1 et 4.1 ka pour Tl1, Tl2 et Tl3 respectivement.

A partir de tous ces marqueurs, une reconstruction de l'étendue passée du glacier et de son retrait progressif est finalement proposée. Les datations réalisées contraignent la fin de cet épisode glaciaire vers 20-25 ka. Ceci est en accord avec les variations climatiques documentées jusqu'à 36 ka dans des carottes sédimentaires du lac d'Iznik, mais aussi avec les âges des autres glaciers turcs. L'âge plus ancien de 45 ka pourrait correspondre à un épisode pré-LGM identifié dans l'est du massif de l'Uludag. La datation en cours de blocs erratiques et des terrasses alluviales devrait permettre de préciser ces premiers éléments.

Chapter C

Segmentation and Quaternary behavior of the middle strand of the North Anatolian fault (MNAF) around Iznik Lake (NW Turkey)

The contents of this chapter will be submitted to the journal *Tectonics* as an article by Yacine Benjelloun, Julia de Sigoyer, and Stéphane Garambois.

C.1 Introduction

Seismic hazard in the highly inhabited areas of northwestern Turkey is mainly linked to the activity of the North Anatolian fault zone (NAFZ), a 1000-km long, dextral strike-slip structure that accommodates the relative motion between the Eurasian and Anatolian blocks with a total geodetic slip estimated around 3 cm/yr (Fig. C.1; McClusky et al., 2000; Meade et al., 2002). During the 20th century, the NAFZ was almost entirely ruptured by a series of major earthquakes from Erzincan in 1939 to Düzce and Izmit in 1999 (Stein et al., 1997; Hubert-Ferrari et al., 2000). A seismic gap now remains for the fault segment in the Sea of Marmara close to Istanbul and a major earthquake is expected in the next decades (Parsons et al., 2000). The areas east and south of the Sea of Marmara are also at risk due to the presence of two secondary strands of the NAFZ known as the middle and southern strands (MNAF and SNAF, Fig. C.1). The hazard on these strands is much less constrained but they could together locate as much as 25% of the total slip of the NAFZ (Armijo et al., 2002; Flerit et al., 2003) with slip rates lower than 1 cm/yr (5±2 mm/yr estimated on the MNAF near the Marmara Sea by Ergintav et al. (2014)). While the SNAF produced a 7.5 magnitude earthquake in 1953 (Kürçer et al., 2008), no major earthquake

ruptured on the MNAF during the instrumental period, and very few seismicity has been recorded (Tsukuda et al., 1988; Gürbüz et al., 2000; Bariş et al., 2002). These observations have led to discuss the possible deactivation of this branch (Le Pichon et al., 2014). This current quiescence strongly contrasts with a significant historical activity documented by several chronicles mentioning the destruction of Iznik and other surrounding cities located close to the MNAF during repeated, major earthquakes for the last 2000 years (Ambraseys and Finkel, 1991; Ambraseys, 2002, 2009). A realistic seismic hazard assessment in this area is however precluded because key parameters like the precise locations and rupture lengths of those historical events as well as long-term slip-rates along different segments of the MNAF have not been constrained yet.

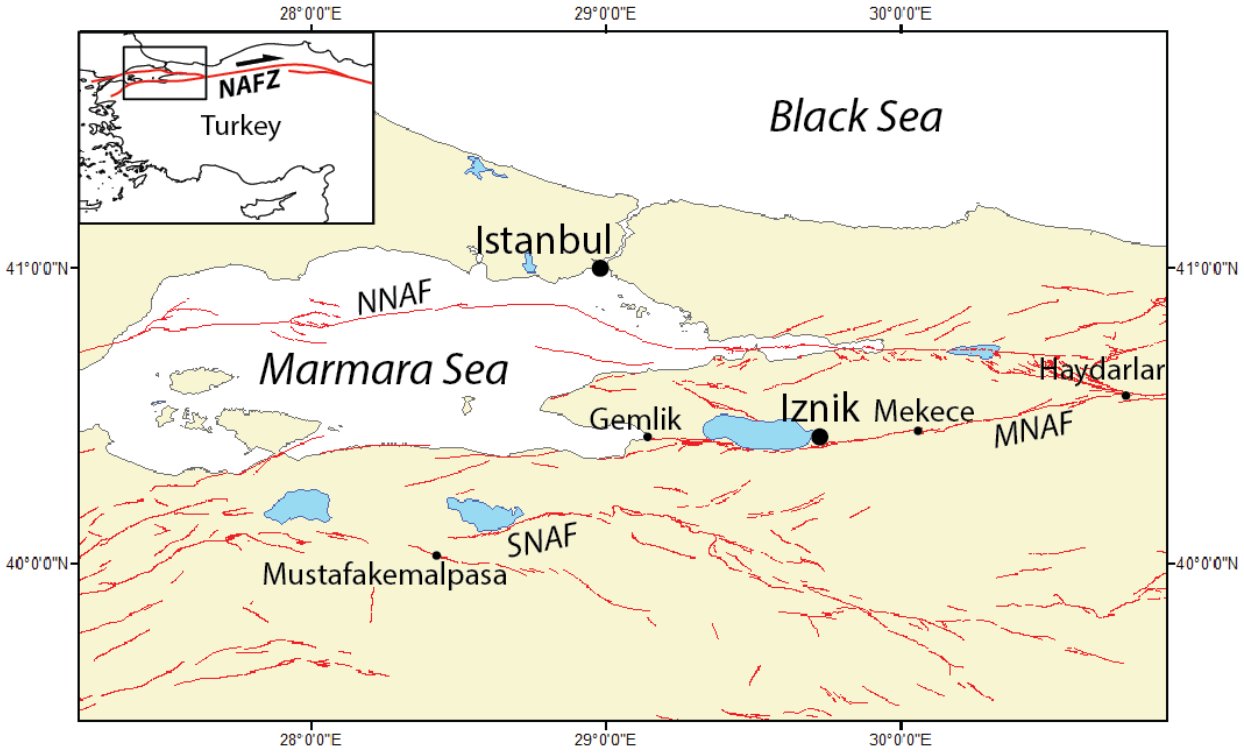

Figure C.1: General location map. The active faults are drawn in red and were taken from Emre et al. (2011).

In the last decades, the development of high-resolution satellite imagery has made it possible to finely measure the deformation and characterize the geomorphology of tectonically active regions on a large scale (Siame et al., 1996; Fu et al., 2004; Klinger et al., 2011). These new datasets enable not only to precisely map active faults on several tens of kilometres, describe their segmentation and therefore provide useful information on the possible extension of a given rupture, but also to document the long-term slip distribution along the fault through inventories of offset geomorphological markers. This approach has been

successfully employed since the 1960s on various faults to extract coseismic slip values from cumulative offset measurements and also discuss the impact of segmentation in modulating the cumulated displacement along-strike (Sieh and Jahns, 1984; Wallace, 1968; Barka, 1996; McGill and Rubin, 1999; Manighetti et al., 2015; Zielke et al., 2015; Ansberque et al., 2016).

In this study, we use a set of high-resolution Pleiades images to map the MNAF on its western part centred around Iznik Lake, and measure a series of lateral and vertical displacements recorded by geomorphological markers. A statistical analysis of this dataset enables to extract and discuss the coseismic displacement of several past earthquakes and the slip distribution along the fault. Additional field measurements, sampling and dating allow us to control certain offset values obtained from the satellite images, and derive a Quaternary slip-rate. We also show evidence of both long term and short term vertical slip on the fault from the measurement of large faceted scarps south of the lake and smaller surface and subsurface offsets along the fault.

C.2 Geological and geomorphological context

The formation of the NAF initiated some 11-13 Ma ago within a wider pre-existing shear zone which became progressively narrower through time (Şengör et al., 2014). From the Messinian and during the Pliocene, the NAF functions as a narrow zone, cutting and deforming several basins inherited from the previous compressive stages (Barka, 1992; Yılmaz et al., 1995). While the deformation is concentrated on a narrow zone in the eastern and central part of the NAFZ, it is structured on a wider area west of Haydarlar (Armijo et al., 1999; Fig. C.1). The middle and southern strands show oblique kinematics, with local complex partitioning of the deformation between dextral strike-slip and extensional regimes (Koçyigit and Özacar, 2003).

Extrapolating a geodetic slip-rate of 5±2 mm/yr to the longer term, the 7-8 km of total lateral offset measured in the Gulf of Gemlik suggest that the activity of the MNAF in the western Marmara region began around 2 Myr ago (Yaltırak and Alpar, 2002). From its separation from the main NAFZ in the east to the Marmara Sea, the MNAF runs along the south border of several successive basins: the Geyve-Pamukova basin, a smaller valley between Mekece and Iznik, the Iznik Lake and the Gulf of Gemlik (Fig. C.2a and C.3). Most of these basins have been interpreted as pull-aparts controlled by the MNAF activity (Doğan et al., 2015), but several studies argue for a more complex mechanism due to oblique strike-slip or propose that the basins predate the initiation of the MNAF (Yaltırak, 2002; Öztürk et al., 2009). The mountain range lying directly south of the fault is composed of Upper Cretaceous sedimentary rocks and volcaniclastic rocks of Eo-Oligocene age (Bargu, 1982; Yılmaz et al., 1995; Özcan et al., 2012). Around and within Iznik Lake, the MNAF is associated to other active faults linked to strike-slip tectonics (Riedels, extensional faults,...) which, depending on their orientations, seem to also accommodate a part of the regional

tectonic strain (Fig. C.4). Depending on the location, the fault segments cut into this basement or into the younger Quaternary fans and alluvia covering the bottom of the basins and the plains surrounding Iznik Lake.

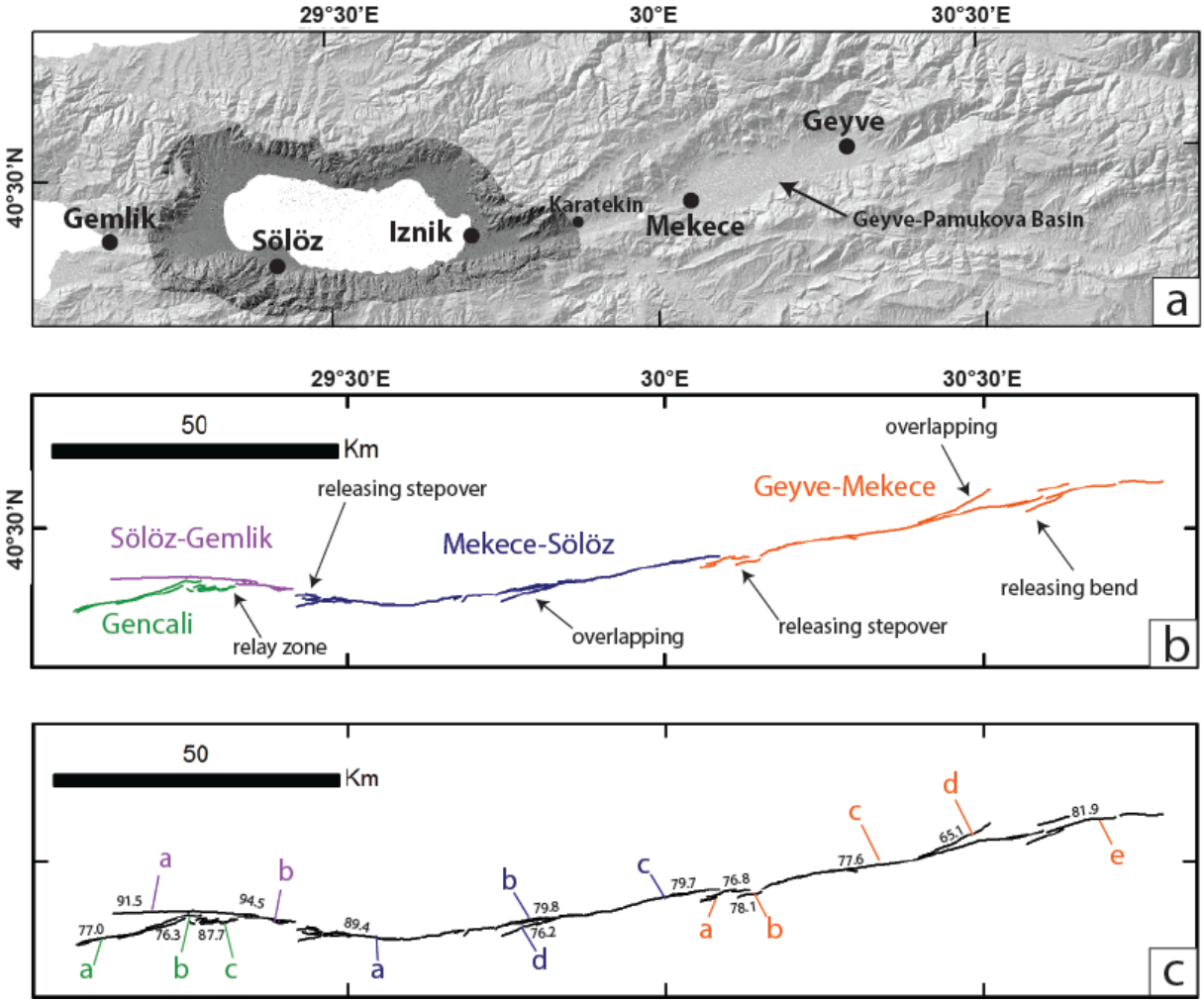

Figure C.2: (a) Shaded DEM derived from the orthorectified Pleiades images (dark grey) superimposed on the SRTM model (light grey). (b) Major segments map. (c) Secondary segments map. Numbers indicate the fault orientations.

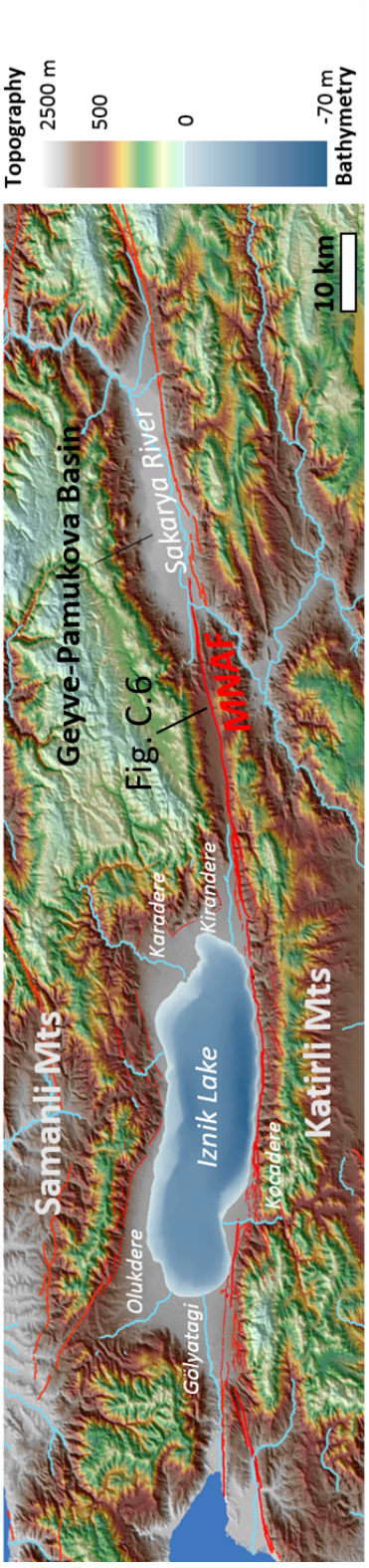

Figure C.3: General morphology of the MNAF region. The topography is superimposed on a shaded SRTM DEM. The active faults are drawn in red and the main rivers in blue.

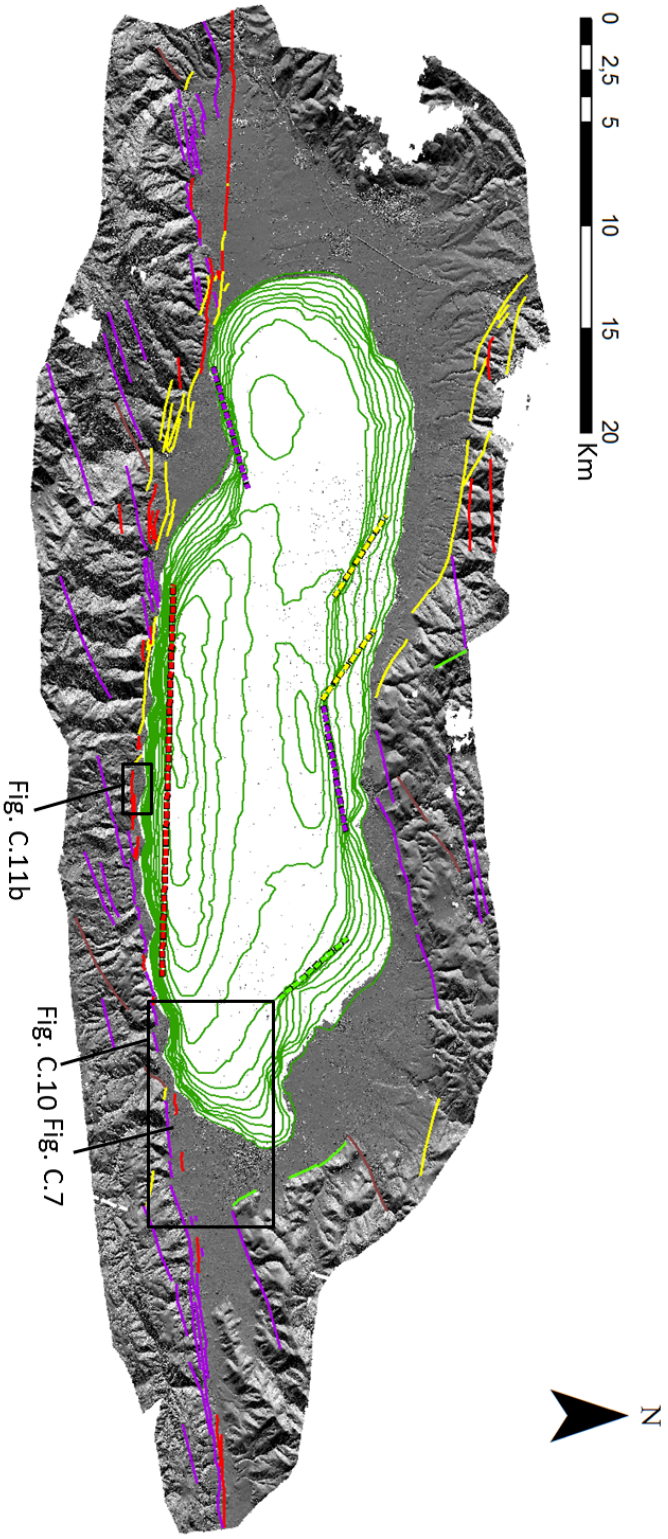

Figure C.4: Shaded Pleiades DEM of Iznik region with the main faults mapped and colored according to their direction (top). Red: Y-shear, purple: P shear, yellow: Riedel shear, brown: X-shear, green: extensional faults. The contours on the lake bottom are at a 5-meter interval.

Currently, the study area is characterized by a mild Mediterranean climate, with most precipitation falling in winter and spring. The mean annual precipitation is about 630 mm (Akbulak, 2009; Miebach et al., 2016). West of Mekece, a 1257 km^2 large drainage area is centred on Iznik Lake with four main rivers: the Olukdere and Karadere in the North, the Kocadere in the southwest and the Kirandere in the east which flows parallel to the MNAF. Another stream, the Gölyatagi dere connects the lake to the Sea of Marmara (Fig. C.3). The eastern segment of the MNAF is linked to another system, associated to the Sakarya River, the third longest river of Turkey, collecting waters from the Anatolian plateau to the Black Sea. The river crosses the MNAF in the Geyve-Pamukova basin with a ∼20 km apparent right-lateral offset that Koçyigit (1988) linked to the fault activity (Fig. C.3).

C.3 Previous paleoseismological and slip-rate studies on the MNAF

A significant number of paleoseismological trenches have been realized all along the MNAF and led to the identification of at least four different ruptures during the last 4000 years (Fig. C.5). Yoshioka and Kusçu (1994) studied a site near Geyve and identified a 3rd century BC rupture and a later undated one. In the same area, an unpublished trenching work by Akyüz et al. (2014) led to the identification of three possible earthquakes. In the east of Iznik, the last rupture was dated between 1280 and 1750 AD (Ikeda, 1988; Honkura and Işikara, 1991) but Fraser et al. (2010) consider the results of this study short and imprecise. On the same segment, Barka (1993) opened nine trenches and found three ruptures since ∼2000 BC but none of them were dated precisely. West of Iznik lake, Ikeda et al. (1989, 1991) proposed a mid-19th century event from archaeological remains found in a natural fault exposure. In Gemlik, Özalp et al. (2013) found a contemporary event and a penultimate one dated between the 12th and 18th centuries. Interestingly, these late events were not found in the four trenches excavated on the same segment by Uçarkus (2002), who only found a 2000 years old event. So far, the largest trenching work has been done by Dogan (2010) who opened 11 trenches on various fault segments between all along the MNAF, but in many cases, very few or no age data could be retrieved, which makes it difficult to discuss whether the identified ruptures are independent from each other. In terms of earthquake recurrence, the compilation of these studies is quite inconclusive either because of their fragmentary results or their occasionally contradictory findings, when close trenches lead to different results.

The only proper estimation of the long-term horizontal slip rate on the MNAF was done by Gasperini et al. (2011) who used the right-laterally displaced edge of a 11,250 years old submerged delta in Gemlik Bay and deduced a 3.7±0.7 mm/yr minimal rate, comparable to the rates derived from GPS measurements (Straub et al., 1997; Ergintav et al., 2014). Another value can be derived from the 16±1 km long offset of the Sakarya

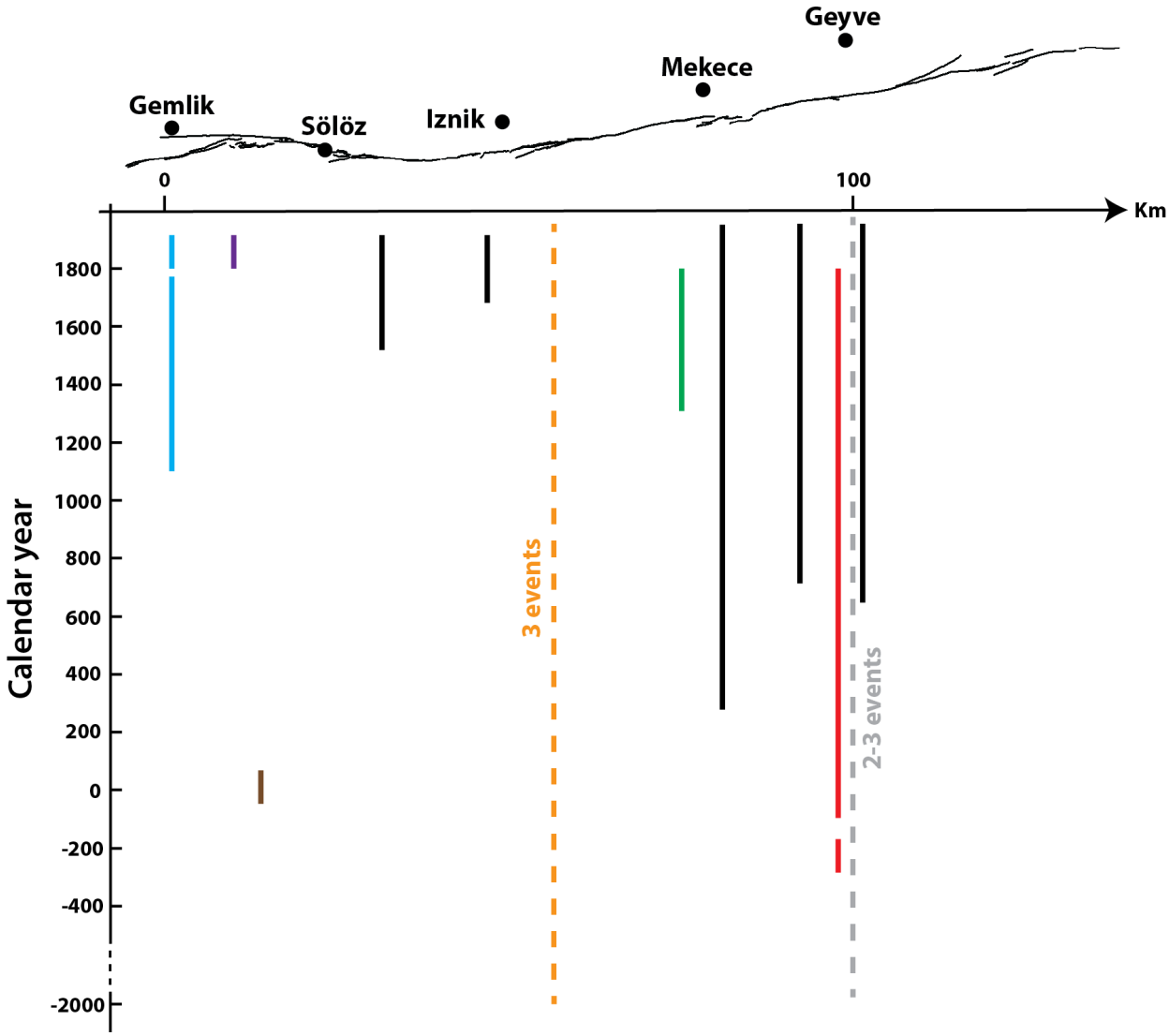

Figure C.5: Synthetic sketch of the previous paleoseismological studies along the MNAF. The trenching results are located in space horizontally. Each bar represents an individual rupture identified in the trench. The length of the bar indicates the uncertainty of its time constraints. The trenches were done by Özalp et al. (2013) in blue, Uçarkus (2002) in brown, Ikeda et al. (1989, 1991) in purple, Dogan (2010) in black, Honkura and Işikara (1991) and Ikeda (1988) in green, and Yoshioka and Kusçu (1994) in red. The orange broken line corresponds to the work of Barka (1993) who found three ruptures posterior to ∼2000 years BC. The grey broken line corresponds to the unpublished work of Akyüz et al. (2014) who found 2 or three undated ruptures.

river in the Pamukova plain (Özalp et al., 2013). Emre et al. (1998) found no river deposits before the Pleistocene, which results in a minimal 5 mm/yr slip rate, slightly higher than the rate computed in Gemlik Bay but in agreement with the GPS estimate of Ergintav et al. (2014). The vertical slip was constrained by (Ikeda et al., 1991) who estimated a 1.4 mm/yr minimal rate from tilted post-glacial beachridges on the western shore of Iznik Lake. Given the current uncertainty on the slip-rate and the general lack of proper age constraints for the last earthquake on most of the MNAF segments, it is actually very delicate to estimate the amount of slip accumulated since the last big rupture.

C.4 Fault geometry and segmentation analysis

C.4.1 Pleiades images processing

4 stereo-couples of Pleiades images (70-cm resolution) covering the area between Gemlik Gulf, Iznik Lake and Karatekin were processed into a high resolution DEM with the NASA Ames Stereo Pipeline (ASP) software (Broxton and Edwards, 2008; Moratto et al., 2010; Shean et al., 2016) without using ground control points (Fig. C.2a). The original Pleiades images have a resolution of about 50 cm, while the derived DEM has a horizontal resolution of 2 m and an absolute vertical precision lower than 10 m. The DEM was then used to orthorectify the original optical images still with the ASP software. The orthorectified Pleiades images and their DEM were used to map the main faults visible.

C.4.2 Fault segmentation

The determination of the fault zone segmentation is an important preliminary step to properly interpret the set of deformation markers seen along the fault. It can also provide first-order constraints on the maximum length and magnitude of earthquake that can be expected depending on where the nucleation occurs. The relative geometry of the successive segments (azimuth difference, width and length of the stepovers...) is also thought to control whether a given rupture is likely to propagate through several segments (Aki, 1984; Barka and Kadinsky-Cade, 1988). Fig. C.2b,c and Table C.1 shows the result of our detailed fault mapping on the Pleiades images and their associated DEM. For the area east of 29.88°E which was not covered by our Pleiades images, we used Google Earth images, an SRTM elevation model and the active fault map of Emre et al. (2011). The different segments identified are generally clearly separated by a stepover or a significant direction change. A few segments also appear overlapping each other (e. g. sub-segments b and d of Mekece-Sölöz segment).

The MNAF is composed of three major segments over a total length of 135 km. In the east, the Geyve-Mekece (GM) segment borders the south of the Geyve-Pamukova basin

with a constant azimuth of ∼80°. The western end of this big segment consists in a quite narrow releasing stepover around the town of Mekece, and makes way for the 65-km long Mekece-Sölöz (MS) segment. This segment can be decomposed into two main areas. In the east, between Mekece and Iznik, the fault runs in a narrow valley with a similar direction to the previous segment with a mainly horizontal motion (sub-segments b to d in Fig. C.2c, Fig. C.6) while in the west, it follows the southern coast of Iznik Lake with an E-W orientation and presents very clear evidence of significant vertical motion with a succession of triangular facets all along sub-segment a. These facets disappear in the west around Sölöz delta where a larger releasing stepover stands. West of the lake, between Sölöz and Gemlik, a much shorter segment runs along a narrow pass with a roughly E-W direction. To these three major segments we chose to add the Gencali fault in the west, which overlaps a great part of the Sölöz-Gemlik (SG) segment with a similar orientation before a major change to the southwest. On a large scale, we can note that the segments become much shorter westward with an azimuth change from NE-SW to E-W, more oblique to the mean strike of the MNAF.

Fourteen secondary segments could be individualized along the fault with lengths ranging from 3 to 30 km. As the segment length decreases westward, the number of sub-segments decreases as well (5 between Geyve and Mekece, 2 between Sölöz and Gemlik). Most of these secondary segments overlap on a same segment and between segments, such as GM sub-segments a and b locating the Mekece releasing stepover with sub-segment MSc.

Major segments	Length (km)	Mean azimuth	Sub-segments		
			Label	Length (km)	Mean azimuth
Gencali	30.0	81.3	A	15.4	77.0
			B	8.1	76.3
			C	6.5	87.7
Sölöz-Gemlik	27.2	92.8	A	19.6	91.5
			B	7.6	94.5
Mekece-Sölöz	65.0	83.2	A	26.9	89.4
			B	8.8	79.8
			C	16.8	79.7
			D	12.5	76.2
Geyve-Mekece	76.7	79.4	A	6.8	76.8
			B	3.4	78.1
			C	30.5	77.6
			D	11.3	65.1
			E	24.7	81.9

Table C.1: Segments of the MNAF with their large scale geometrical characteristics. For the location of sub-segments, see Fig. C.2c.

Figure C.6: Interpreted panorama of the MNAF at the eastern end of Mekece-Sölöz segment (see Fig. C.3 for location). In the field, the MNAF segments are generally marked in the topography by a slope break. Typical features of strike-slip faults are found along the MNAF. Several rivers present a right-lateral offset when they cross the fault trace. When the lateral displacement becomes too important, the river finds another course and the connexion with the original lower stream is cut. This abandonned stream is called "beheaded". The rivers can also be diverted by "shutter ridges" that move along the fault line and block the drainage.

C.5 Cumulated coseismic offsets

C.5.1 Method of measurement and uncertainties

Major ground rupturing earthquakes can generate meter-scale deformations that can be preserved in the morphology through several seismic cycles. In the case of strike-slip ruptures, it is generally possible to measure in the days following the earthquake a series of anthropic or natural laterally displaced markers such as roads, fences, walls, field or vegetation lines, terrace risers or gullies. This kind of measurements have evidenced that the coseismic slip located on the fault can vary significantly along-strike. However on longer time scales, erosive and sedimentary processes are likely to erase the small offsets after the rupture while the larger displacements will be preferentially preserved. Thus, Holocene morphological markers can show large values of offset representing the result of cumulated coseismic displacement. If new markers are formed between the earthquakes, the compilation of a large number of offset measurements will give several ranges of values as the younger markers preserve a smaller number of displacements.

Along a 50-km long portion of the MNAF, we systematically identified and measured more than 100 offsets using the ortho-rectified Pleiades images, shades DEMs, slope maps and contour maps. The displaced markers considered were river channels, gullies, terrace risers and more occasionally vegetation lines and ridges. For each marker, we define piercing points, i. e. points that were aligned before the displacement, and we project these points on the fault trace when necessary. The piercing points across the fault are then realigned by retrodeformation, which gives the offset value (Fig. C.7). When one marker is displaced by several parallel fault strands, the offset value to be considered is the sum of the measurements on each fault line (Zielke et al., 2015). A limited number of displaced markers were also measured on the field. The complete dataset can be found in appendix C.

The uncertainty of the offset measurement originates from two factors: (1) the resolution of the imagery data used (50 cm for the ortho-rectified Pleiades images, 2 m for the DEM), and (2) the accuracy of the measurement itself, which can be estimated by taking the minimum and maximum amounts of retrodeformation that keep the alignment of the marker (Manighetti et al., 2015; Ansberque et al., 2016). We also use a quality factor (good, average, bad) which reflects the intrinsic quality of each marker in providing a relevant measure. For example, a high angle relative to the fault azimuth, a high sinuosity or a doubt about the tectonic nature of the offset will lower the marker quality.

Figure C.7: Example of offset measurement (see Fig. C.4 for location). (a) Orthorectified Pleiades image with the MNAF drawn in red and a dextrally offset river crossed by the fault trace (blue arrows). (b) The retro-deformation realigns the deformed river across the fault and gives an offset measurement of 28±4 m.

C.5.2 Statistical analysis

The 106 measurements obtained range between 2 and 180 m, with a majority of values lower than 30 m (Fig. C.8b). For the following analysis of this dataset, we exclude the areas of structural complexity such as inter-segments zones and stepovers. These areas have a higher probability of displaying slip values significantly lower than the maximum coseismic displacement during a given rupture. Therefore, they could improve the risk to confuse the accumulation of two locally low displacements for one bigger rupture and thus distort our analysis (McGill and Rubin, 1999; McCalpin, 2009; Manighetti et al., 2015). For the same reason, before considering a common analysis of our complete dataset on a 60 km length, we need first to examine subsets on individual segments to check for potential slip variability between them.

In order to identify the most significant offset ranges along the fault that could represent cumulated past ruptures, we use the approach developed by McGill and Sieh (1991). Each offset measurements is represented by a Gaussian distribution, the preferred measured value being the center of the Gaussian probability density function (PDF) and the uncertainty being its 2σ width. The individual PDFs inside the subset analyzed are then summed into a cumulative offset probability distribution (COPD) curve, on which we extract the peak values indicating the most frequent and/or the most precise offsets measured.

C.5.2.1 Segment analysis

Table C.2 presents the best constrained offset values extracted from the COPD peaks computed for each sub-segment studied. We also analyzed the dataset separately by quality. It is important to note that the number of measurements on segment SG is three times smaller than the others (10 values against 30-36 values for MS sub-segments), mainly because of its smaller length. Two observations arise from this first step: (1) on most sub-segments and for several offset ranges, similar peaks are found between isolated quality groups; (2) several similar offset values are preserved on different sub-segments. It is possible to identify five cumulated displacement ranges well constrained on several sub-segments around 3, 5, 9, 11-12 and ~16.5 m. Among these five ranges, the 5 and 11-12 m especially correspond to numerous measurements. It is also interesting that despite a very small number of measurements on segment SG, it was possible to reveal three of these five ranges, some of which could not be retrieved on adjacent segment MSa. The smallest offset value found on all the sub-segments but one ranges between 2 and 3.5 m. We can note that this value is of the same order as the increments between the five best constrained offsets that ranges between 2 and 5 m.

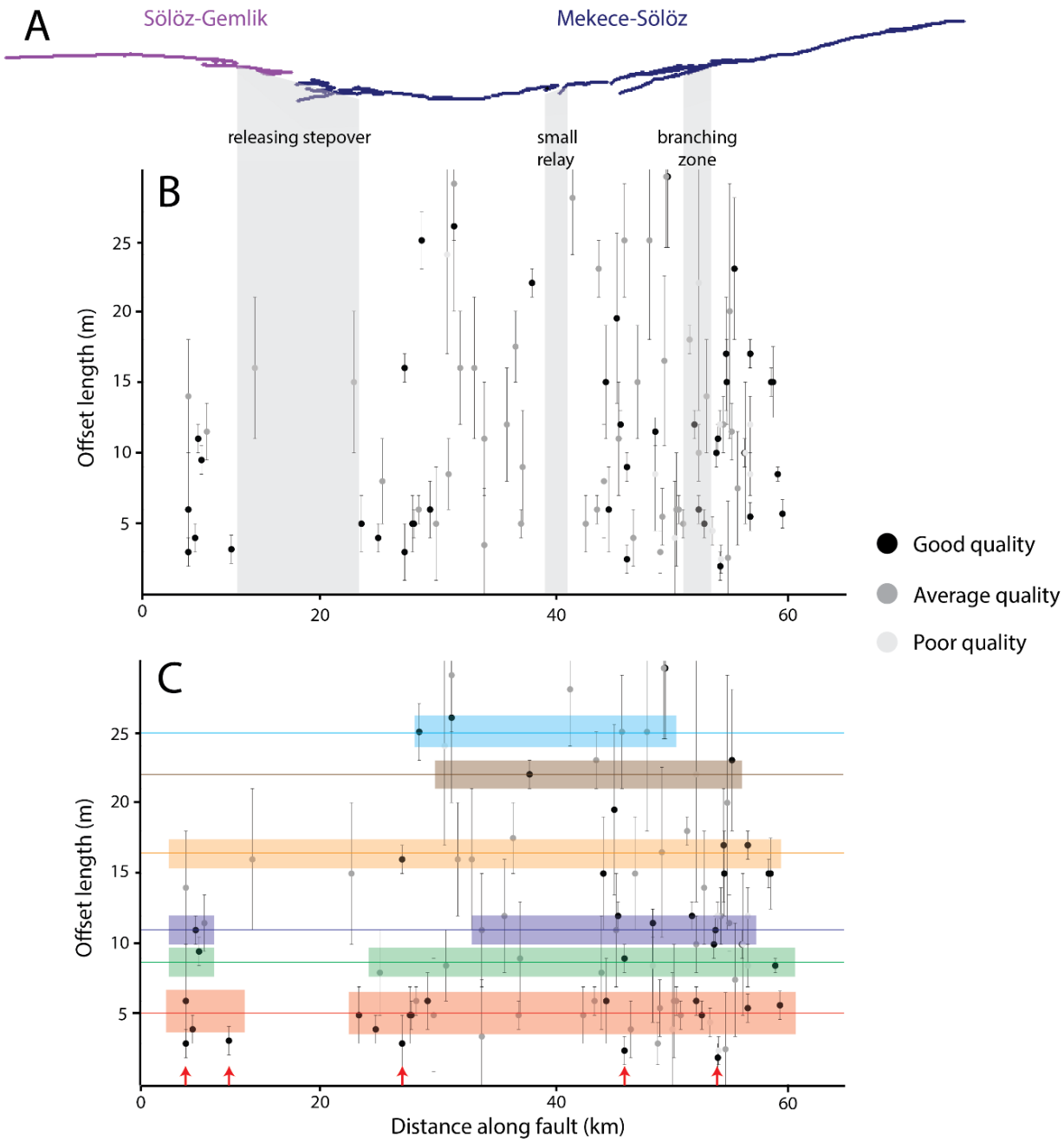

Figure C.8: Offset inventory along the MNAF. (a) Segmentation map. (b) Measured offsets in the range 0-30 m with their uncertainties. The main structurally complex areas excluded from the analysis are delimited in grey on the fault map and the offset diagram. The three data qualities are drawn with different grey tones. (c) The COPD values and their uncertainties determined from the good quality subset are represented as horizontal colour lines and bars and superimposed on the spatial offset distribution. The red arrows indicate the smaller offsets measured falling outside the first COPD peak (see C.5.2 for discussion).

SG		MSa			MSb			MSc			Mean offset values (m)
Q1	**Q2**	**Q1**	**Q2**	**Q3**	**Q1**	**Q2**	**Q3**	**Q1**	**Q2**	**Q3**	
3.4					2.6			2.1	3	3	2.8
		4.5	**5.6**			**5.6**	**6.3**	**5.6**		4	5.3
10.2			10		9.2			8.7		**9.1**	9.4
	11.9				**11.7**	13		**10.7**	**11.2**	**11.9**	11.7
		16	16.7		**16.8**			**16.8**			16.6
									18		
		22.1				23					
		25.4		24							
			28.4		28						
				34							
					40						
	43										
						47.6					

Table C.2: Best constrained cumulative offsets along each segment, discriminated by quality (Q1: good, Q2: average, and Q3: bad). Offsets are derived from the peaks of the COPD curves in the range 0-50 m. The values indicated in bold are constrained by several offset measurements. The values have been aligned among the different segments according to their similarity. The average values showed in the last column were computed for the offsets represented on at least three segments. For the name of the segments, see Fig. C.2b,c.

C.5.2.2 Total population analysis

We have seen that the two segments studied exhibit similar cumulated offset values. At the sub-segment scale, some discrepancies exist across the Sölöz stepover on sub-segments SGb and MSa (Fig. C.2c). The first COPD peak found for SG at 3.4 m is not observed on MSa who display a first peak around 5 m. The COPD peak at 11-12 m seen on the other sub-segments is not found either on MSa. To test the robustness of these peaks at the segment scale, we expand the analysis on the complete dataset (Fig. C.9, Table 3). For each quality subset, we extract the best COPD values from the peaks visible on the summed PDF curves. Following Manighetti et al. (2015), we also attribute to each value an uncertainty equal to the half-width of the Gaussian that best approximates the peak shape. Therefore, when the peak mainly results from a single measurement, the uncertainty of the COPD value is the same as that on the measurement. The COPD for good quality measurements show four major peaks at about 5, 11, 16 and 22 m. Two other peaks, both constrained by one measurements, are visible at 9 and 25 m. The last one corresponds to a quite uncertain measurement while the former is associated to a more precise field measurement that also corresponds to an offset range already seen on all the sub-segments in C.5.2.1. The subsets for average and bad qualities obviously contain more fragmentary information but overall display common peaks with the good quality subset. The 16 m offset cannot be retrieved from these lower qualities but instead the average quality subset displays a 17.5 which is of the same order given the uncertainties.

The comparison of this complete analysis with the previous segment analysis reveals that the well-constrained offset range at 3 m, that was visible on three sub-segments and included good quality measurements, disappears from the total population COPD curve for the good and average quality groups. Interestingly, the bad quality COPD shows this offset range but in the absence of a major peak at 5-6 m. It is clear on Fig. C.9a and b that the large COPD peak around 5-6 m corresponds to a series of numerous measurements ranging from 2 to 6 m. Given the common uncertainties associated, the PDF summation gives a wide, slightly asymmetrical peak. However, the fact that two separate peaks at 2-3 and 5-6 m were found independently within individual segments and among different segments leads us to discuss whether the big 5 m peak in the COPD curves may hide two separate displacements.

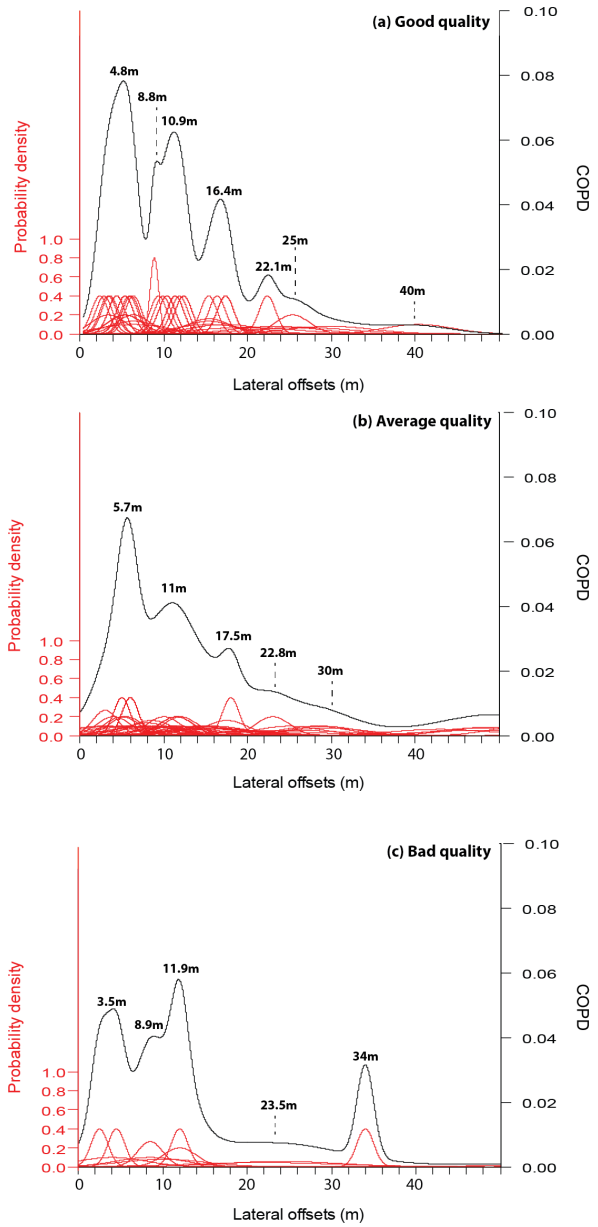

Figure C.9: Statistical analysis of the complete offset measurements in the range 0-50 m. The subset of each quality group is analyzed separately. The red curves are the individual PDFs of measured offsets. The black curves are the summed PDF curves or COPD curves. The best constrained peak values are precised (see Table 3).

Good quality		**Average quality**		**Bad quality**	
COPD (m)	*Error (m)*	*COPD (m)*	*Error (m)*	*COPD (m)*	*Error (m)*
4.8	1.9	5.7	1.3	3.5	1.6
8.8	*1*			8.9	1.5
10.9	1	11	1.5	11.9	1
16.4	1.4				
		17.5	*1*		
22.1	*1.1*	*22.8*	*2*	23.5	8
25	*2*				
		30	4		
40	*4*			*34*	*1*
Slip increments (m)	*Error (m)*	*Slip increments (m)*	*Error (m)*	*Slip increments (m)*	*Error (m)*
4.8	1.9	5.7	1.3	3.5	1.6
4	2.1	5.3	2.0	5.4	2.2
2.1	1.4	6.5	1.8	3	1.8
5.5	1.7	5.3	2.2	11.6	8.1
5.7	1.8	7.2	4.5	10.5	8.1
2.9	2.3				
15	4.5				

Table C.3: Best constrained cumulative offsets and slip increments determined for the entire dataset in the range 0-50 m. The quality groups are analyzed separately. The COPD values indicated in italics are constrained by only one measurement. The slip increments are the amounts of slip that separates successive COPD values. For the way of calculating the uncertainties, see text.

The spatial distribution of the offsets measured along the part of the MNAF studied is shown in Fig. C.8c. The superposition of the COPD values found for the best quality subset shows that almost all data points are within uncertainties close to these statistically constrained values. More significant discrepancies arise for the smallest measured offsets, including good quality points, especially in the east where several points seem much less likely to be linked to the 5-6 m peak.

The increments between successive COPD values for the different quality groups show quite contrasting features (Table C.3). For the good quality subset, most increments range around 5 m while two increments are closer to 2-3 m, which is similar to the smallest offsets measured. The increment values for the average quality subset are more homogeneous but are bigger in average and closer to 6 m. Finally, the bad quality subset displays similar ranges to the good quality. All the subsets also exhibit larger increments between 10-15 m, which always correspond to the last COPD peaks (Table C.3). These large values of cumulated slip cannot be reasonably interpreted as the result of only one earthquake and suggest that they are the sum of several displacements which were not preserved separately in the morphology.

C.6 Horizontal slip rate estimation

Traditionally, horizontal slip rates are constrained by dating sedimentary units like alluvial terraces or fans laterally displaced by the fault. This kind of estimation will be preferentially done with large offsets (several hundreds of meters) affecting old sediments (i.e. 10-100 ka BP) in order to reduce the relative uncertainties on the calculated ratio. It should be noted that one measurement will give a minimum slip rate because the formation of the offset can be younger than the deposition of the sediments. During our field missions around Iznik Lake, we were not able to identify very large displacements in sediments that can be conveniently dated. East of the lake, alluvial terraces cut by the MNAF are present but their risers are overall parallel to the fault and the offset gullies are probably quite recent and significantly younger than the terraces they incise. Southeast of the lake, the MNAF segments have displaced relatively young markers, mostly small streams, but the lacustrine terrace Tl3 that they incise has been dated with in-situ produced ^{10}Be to $4.1^{+2.4}_{-2.9}$ ka (Fig. C.10, see also section B.4.4). Among the markers identified in the alluvial plain south of Iznik Lake, the biggest quality 1 offset measured was 22±1 m on a river located ∼3.5 km west of Dirazali village (Fig. C.10). A minimal value for the slip rate in the 2σ confidence interval is given by the ratio between the offset measured and the maximum age of the marker. We obtain a minimal slip rate of 5.4±3.4 mm/yr. It is in the same range, though higher in average, as the rate estimated by Gasperini et al. (2011) on Gemlik segment and also in agreement with the recent GPS estimation at 5±2 mm/yr.

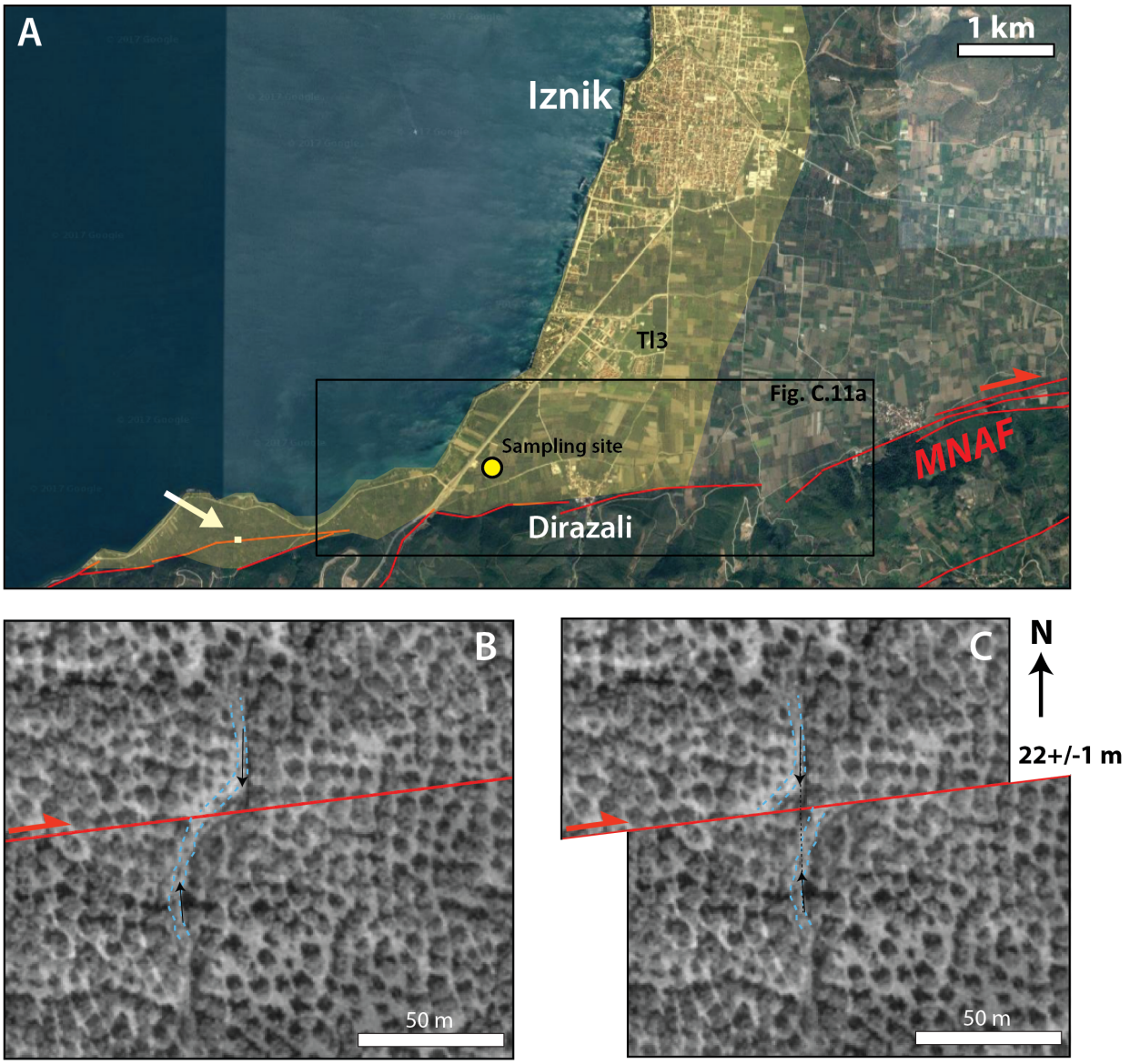

Figure C.10: (A) General location of the marker used to derive a minimum horizontal slip-rate on the MNAF (white arrow). This marker corresponds to the largest good quality offset present in the youngest sedimentary formation Tl3 (mapped in yellow). The yellow dot locates the sampling site for ^{10}Be dating. Pleiades images of the present-day and retro-deformed morphologies are shown in (B) and (C) respectively.

C.7 Vertical offsets along the MNAF

C.7.1 Surface offsets

While most traces of Quaternary surface deformation along the MNAF are related to strike-slip motion, it was possible to identify and measure a more limited number of vertical offsets, sometimes associated with horizontal displacements (Fig. C.11b and C.12a). The vertical offsets were estimated on topographic profiles extracted from the Pleiades DEM. The offset value is obtained by measuring the vertical gap between the projections of the far-field slopes on both sides of the fault, and correcting for possible rotations of both upthrown and downthrown blocks (Slemmons, 1957; McCalpin, 2009). The maximum values measured range between 10 and 15 m on the sides of the lake, with a maximum of almost 20 m around the centre. In the east of the studied area, it was possible to measure in two locations a significant range of different vertical offsets, both on alluvial plain surfaces and inside river channels. The former logically show higher values, over 6 m. Interestingly, all the channel offsets are associated to lateral displacements of 4-7 m, which implies that these vertical offsets may have been produced during the last big ruptures on the MNAF. On two points, the vertical displacement thus appears of the same order as the horizontal. It is difficult to know whether the variability in all these values is associated to different ages of markers or a variable amount of cumulated slip along-strike.

On a larger time scale, repeated normal faulting on the MNAF together with fluvial incision on the scarp have led to the development of several facets bordering the lake shore separated by narrow valleys (Fig. C.11). Whenever these facets presented a well-developed triangular shape with a clear summit, we measured their vertical height (difference between the scarp's foot and top elevations) and slope along-strike, as represented on Fig. C.12b. The slope values range between 23 and 32° with a wide "plateau" of values above 30°and a sharp decrease on the sides of the lake. The facet slope is generally considered a good proxy of the vertical slip-rate (Petit et al., 2009; Tsimi and Ganas, 2015). Using the empirical relationship of the latter authors, the largest slope values measured would correspond to a ∼0.7 mm/yr vertical slip rate. The convex distribution of the slopes suggests that normal faulting on the MNAF has been especially active along Iznik Lake shore and much reduced on its sides. The facet heights display smaller variations along-strike, mostly ranging around 120 m, excepted in the central part where two much higher facets exist.

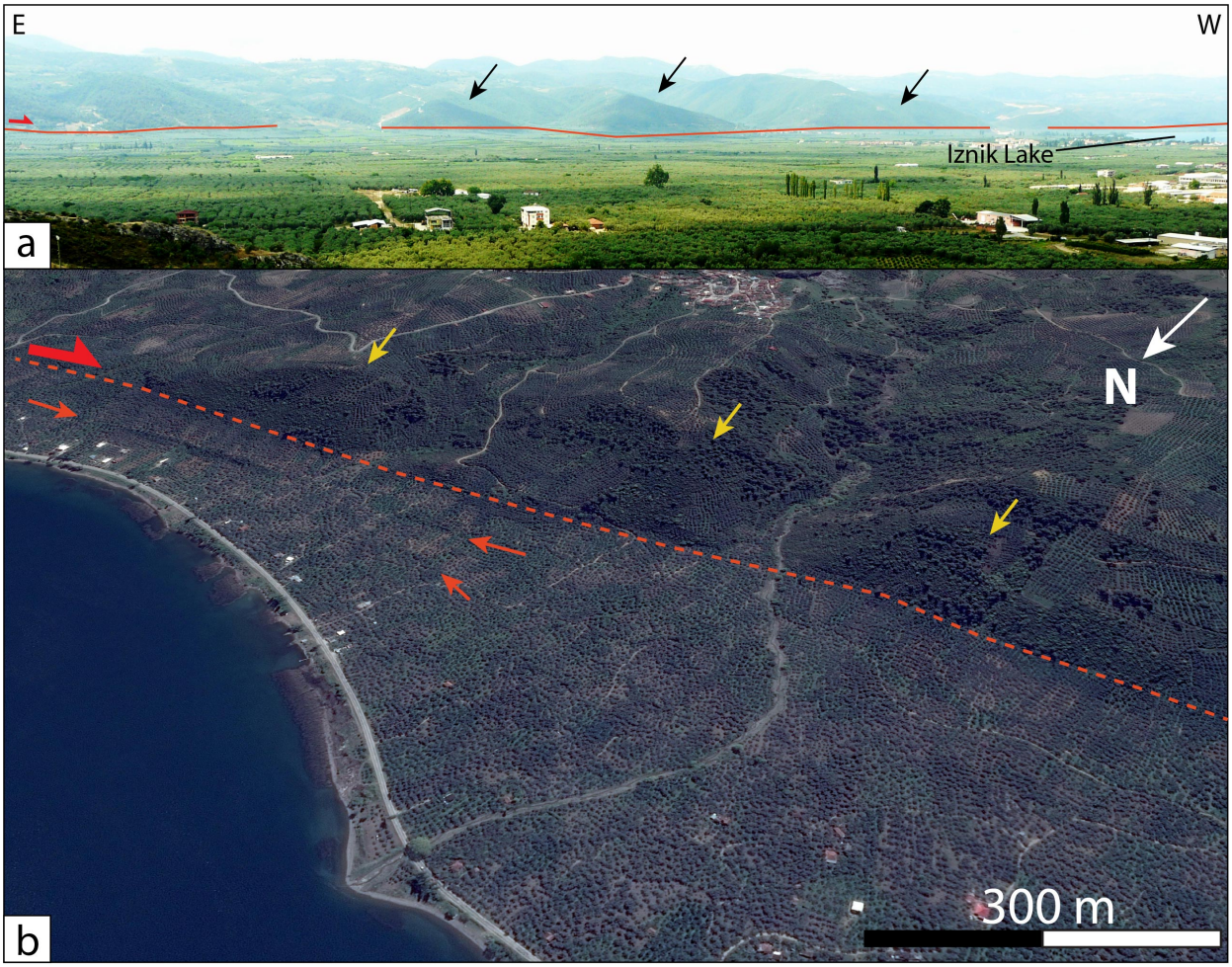

Figure C.11: Example of vertical slip markers along the MNAF south of Iznik Lake. The fault segments are drawn in red. (a) Triangular facets (black arrows) at the southeast corner of the lake (see Fig. C.10A for location). (b) Eroded triangular facets (yellow arrows) and smaller, more recent scarps in front (delimited by the red arrows, see Fig. C.4 for location).

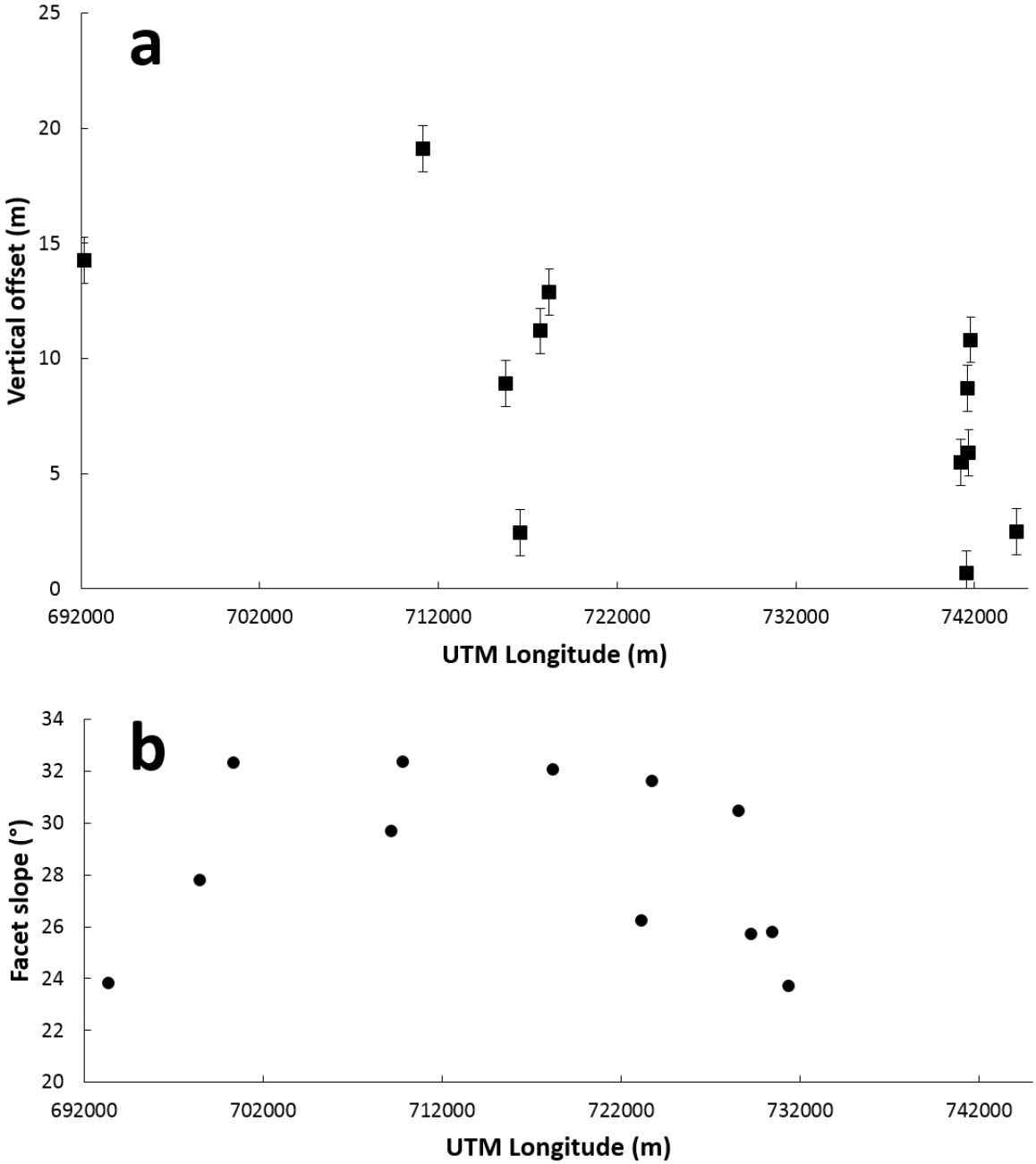

Figure C.12: Markers of vertical slip along the MNAF on sub-segment MSa. (a) Recent vertical offsets measured along the fault line. The highest values (>6 m) were measured on alluvial plain surfaces while the lower values were measured in river channels also laterally displaced during the last big earthquake. (b) Slope values of the triangular facets along the MNAF. The central section shows almost constant values around 30°while the sides are marked by a sharp decrease and the disappearance of well developed facets.

C.7.2 Subsurface offsets

On several sites along the MNAF showing clear evidence of recent strike-slip faulting, preliminary ground-penetrating radar (GPR) surveys were done to try to image the fault in the first meters under ground and detect potential vertical and horizontal buried offsets. Two transversal profiles are presented for sites located on the Mekece-Iznik segment about 3.5 km southeast of Karatekin village (Fig. C.13a,b). The profiles were acquired with a 250 MHz shielded antenna in the upslope direction. Several acquisitions were also performed parallel to the fault on both sides to detect horizontally displaced buried features but the results were not conclusive (see appendix D).

The first site (Fig. C.14a) is a small gully crossing the fault with a 8-9 m dextral displacement. The gully is surrounded by dense vegetation and borders an agricultural field. Vertically offset reflectors are seen on the GPR profile between 4 and 5 m, where the fault is expected to run at the surface (Fig. C.13c). The second site (Fig. C.14b,c) is also a flat field delimited on the sides by two higher terrace risers. It was possible to measure two successive lateral offsets of ∼3 m each. The two corresponding fault strands can be seen on the GPR profile (Fig. C.13d). The southern fault is the most clear with several reflectors close to the surface being relatively downthrown between 37 and 43 m along the profile. Another less certain anomaly can be spotted around 13 m on the profile and could be associated to the smaller surface offset. Given the soft and conductive nature of the subsoil, the presented GPR data only enable to detect the discontinuities related to faults. The measurement of the buried offsets would need a more complete set of acquisitions and a fine surface topographical survey. The more precise location of the faults gathered from these preliminary data could still be a useful information to prepare trenching work.

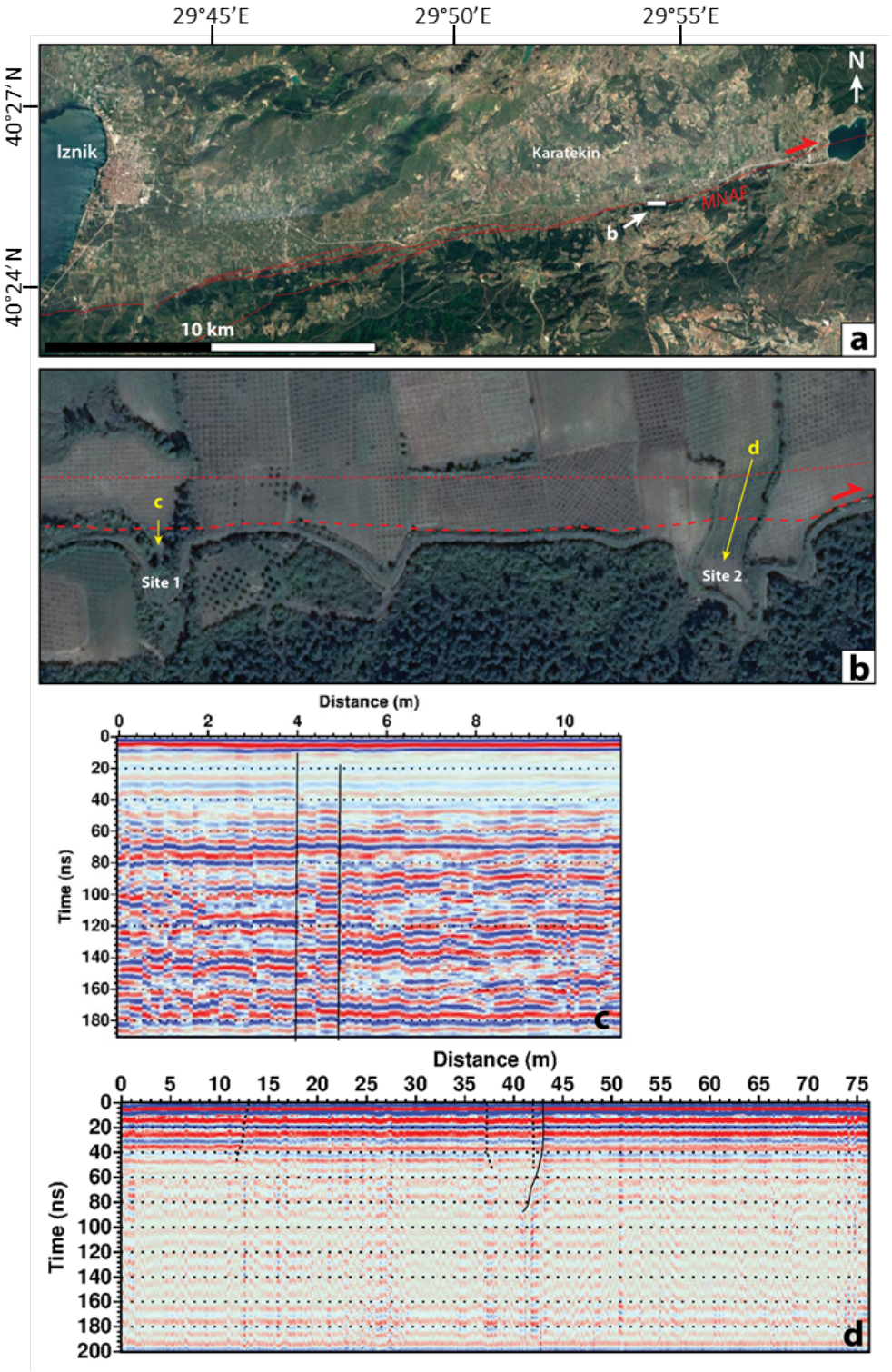

Figure C.13: GPR surveys across the MNAF. (a) General location map with the fault drawn in red. The survey sites are located inside the small white box. (b) Google Earth closer view on the two survey sites with the GPR profiles drawn in yellow. The arrow indicates the direction of the acquisition. The possibly crossed fault strands are drawn in red. (c,d) Results of the GPR acquisition on both profiles. The interpreted faults are drawn as black lines. Less certain faults are drawn as dotted lines.

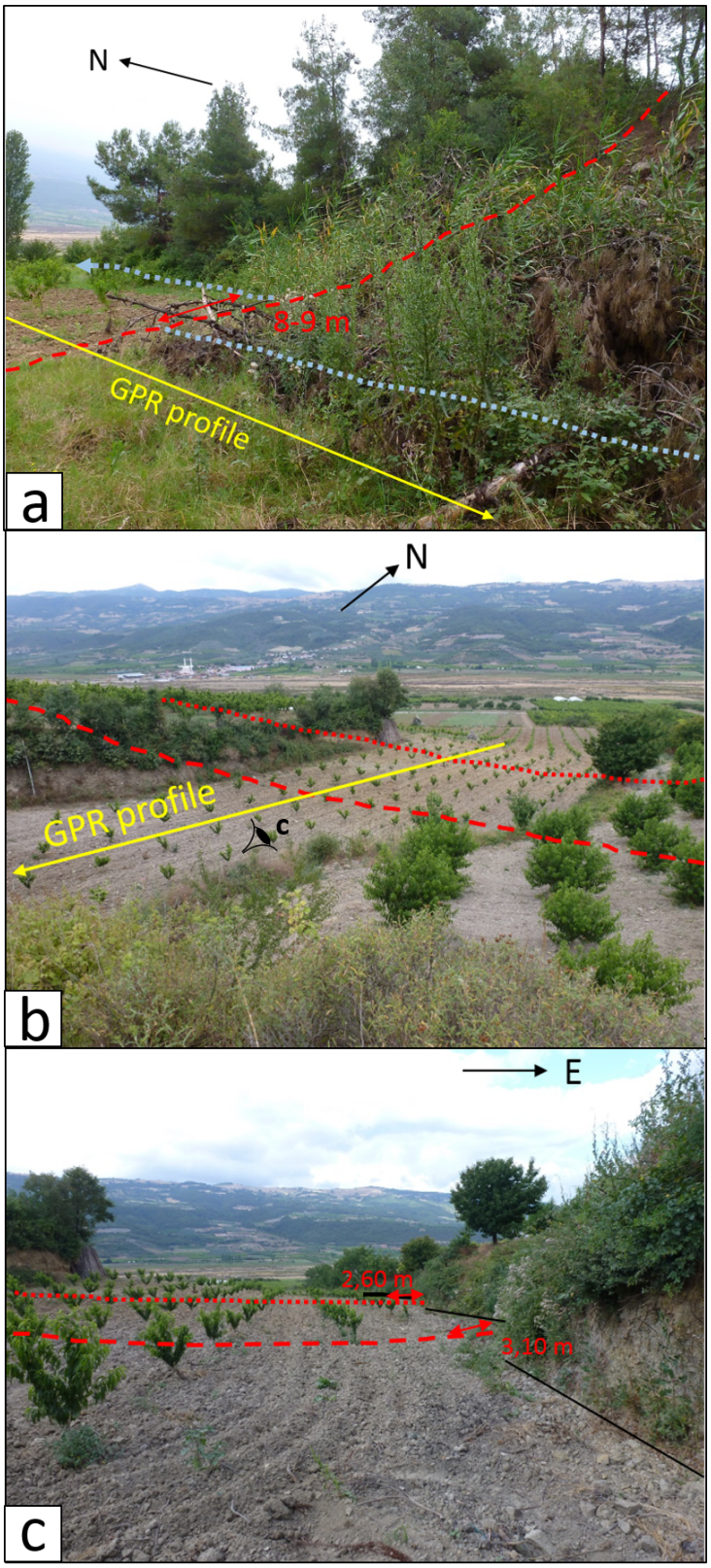

Figure C.14: Field photos of GPR survey sites 1 (a) and 2 (b,c).

C.8 Discussion

C.8.1 Last earthquake slip and variability

The comparison between our offset measurements and the COPD peaks obtained (Fig. C.8c) shows that almost all measurements with their uncertainties can be linked to a cumulated displacement affecting in general the entire fault length studied. However, as remarked in section C.5.2.2, several points among the smallest values measured fall off the range of the first COPD peak that could be interpreted as the last major earthquake. Such points are found on the sides of the Sölöz releasing stepover and in the east of our study area between 45 and 55 km along fault. This points could result from along-strike coseismic slip variability, which is commonly observed during historical ruptures (Langridge et al., 2002), or from a later earthquake. The latter option would imply that the first COPD peak corresponds to two cumulated displacements of ∼3 and 2 m instead of a single 5 m slip rupture. A similar issue has been reported by McGill and Sieh (1991) who interpreted a series of offsets ranging between 2 and 6 m as resulting from two successive earthquakes on the Garlock fault in California, because of their bimodal distribution. However, in their study of the Emerson fault (California), McGill and Rubin (1999) evidenced that offsets from a single earthquake could actually produce a bimodal histogram. Among several methods, these authors propose to compare the slip gradients associated to these smaller offsets with the maximum gradients observed during modern earthquakes, calculated on similar length scales. If we consider the five offsets in our good quality subsets smaller the 5 m COPD peak (red arrows on Fig. C.8c), we obtain slip differences lower than 500 cm (Table C.4, Fig. C.15). Moreover, when the uncertainties on the offset measurements are included, it appears that most offset differences are not significantly different from zero. McGill and Rubin (1999) had observed slip differences of 400-550 cm on a 15 km scale, which is not significantly different from our own results (Fig. C.15). Also, the markers associated with these smaller offsets are not morphologically different from the others displaced by ∼5 m, and do not seem particularly younger. Therefore, we cannot exclude the single rupture hypothesis and it is reasonable to assume that these smaller values result from coseismic slip variability along strike, maybe linked to fault branching, segmentation or azimuth changes.

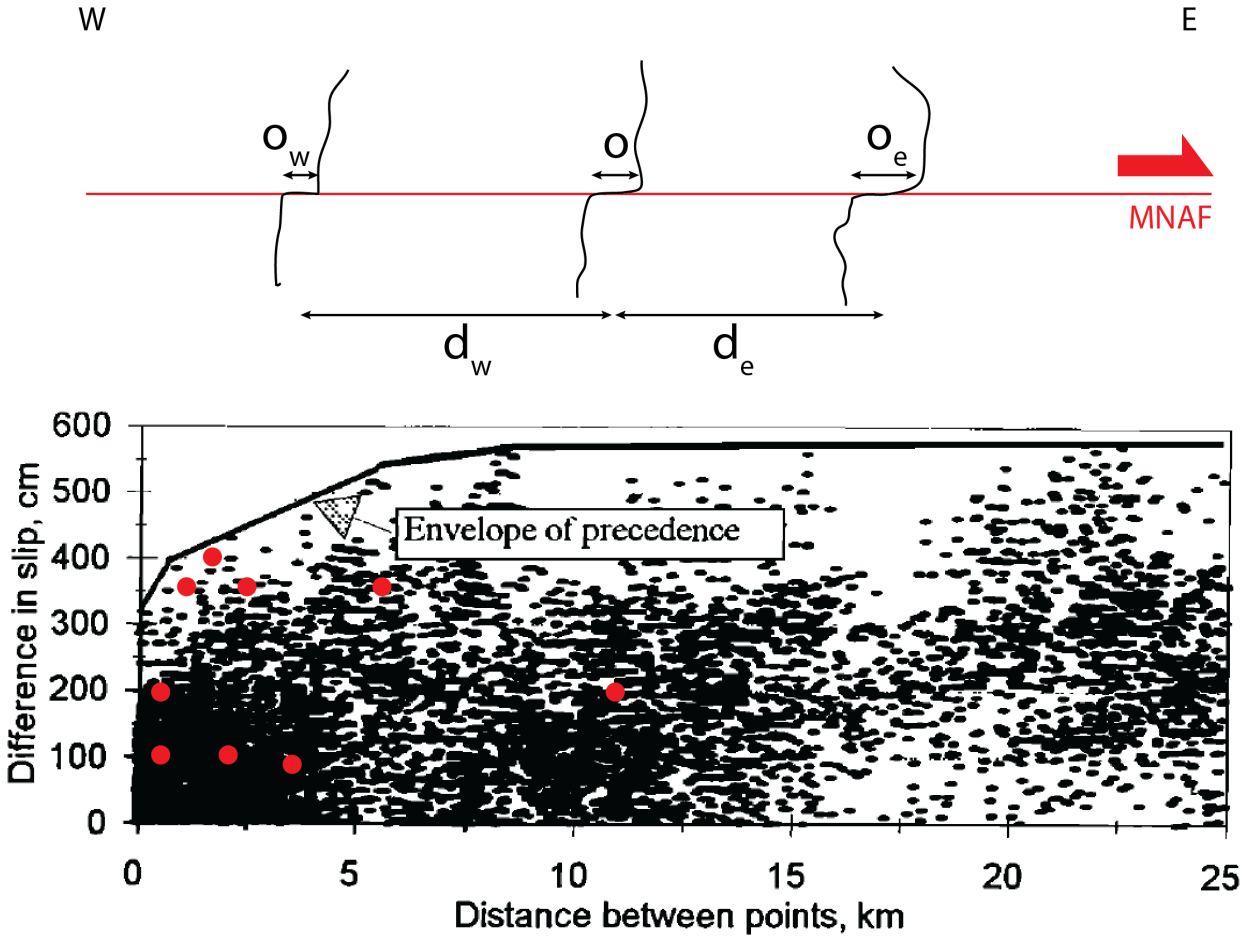

Figure C.15: Principle of the measurement of offset differences. To test if several observed lateral offsets of different amplitudes can be produced during the same rupture, we compute the differences between adjacent offsets ($|o\text{-}o_w|$ and $|o\text{-}o_e|$ in the sketch on top). These differences are then plotted against the distance between the markers (d_w and d_e) and compared with the values collected along the 1992 Landers rupture (black dots on the diagram at the bottom, taken from McGill and Rubin, 1999). The values computed for this study are reported in red.

Marker number	Distance along fault (km)	Offset measured (m)	Uncertainty (m)	Distance between points (km)	Offset difference (m)	Uncertainty (m)
159a	8.92	3	1	0.58	1.00	1.41
T55	12.59	3.2	1	3.09	0.80	1.41
				11.09	1.80	2.24
148a	27.36	3	2	2.25	1.00	2.24
				0.67	2.00	2.83
T37	46.32	2.5	1	1.55	3.50	3.16
				6.12	3.50	1.41
80	54.28	2	1	1.84	4.00	1.41
				2.55	3.50	1.41

Table C.4: Slip gradients associated to the smallest offsets measured (see Fig. C.8c for location). For each marker except 159a, the gradients reported were calculated with points located west, then east of the marker.

C.8.2 Past coseismic displacements

The COPD peaks found show the occurrence of at least six earthquakes preserved in the landscape. The increments between these peaks indicate coseismic displacements of 4.8, 4, 2.1, 5.5, 5.7, and 2.9 m. The uncertainties on these values range between 1.4 and 2.5 m. The fact that the different segments studied display very similar offset ranges suggests that they do not present significant long-term slip variability along-strike. It can thus be hypothesized that these COPD peaks correspond to major earthquakes having ruptured both segments. This scenario is especially credible for the four last ruptures identified. Such a rupture along the fault length studied of 60 km would produce a moment magnitude Mw 7.2 earthquake with a maximum coseismic displacement of ∼2.4 m (Wells and Coppersmith, 1994). This last value is of the same order as the smallest COPD peaks found at 2.1±1.4 and 2.9±2.3 m. The four other earthquakes identified show in average higher coseismic displacement between 4 and 6 m, which corresponds to slightly larger magnitudes around Mw 7.3 and rupture lengths up to almost 100 km. This suggests that the MNAF can generate big ruptures propagating accross the stepovers between its successive segments.

C.8.3 Implications for the recurrence rate and future ruptures

The coseismic slip variability of the past earthquakes may imply that the time elapsed between the successive ruptures also varied significantly. Using the long-term horizontal slip rate determined in section C.6, we can estimate typical durations necessary to accumulate enough strain to generate the coseismic displacements extracted from the COPD curve. With a 5 mm/yr rate, 2, 3, 4 and 5 m of horizontal deformation are accumulated in 400, 550, 750, 1000 years respectively. The combined results of paleoseismology and historical seismology on the MNAF seem to indicate that after one or several major ruptures around the 15th century on the segments between Gemlik and Mekece, a series of smaller earthquakes happened from west to east between Mustafakemalpasa and Iznik Lake in the second half of the 19th century (Ambraseys, 2000, 2009; Özalp et al., 2013). It is not really known whether those earthquakes produced surface ruptures and significant displacement, especially east of Sölöz, but the historical studies suggest that it was not the case as they describe very small earthquakes of surface wave magnitude Ms 5 or lower. We can thus assume that these 19th century events did not release a significant part of the stress accumulated since the 15th century. Under these assumptions and given the uncertainty associated to the slip rate, we cannot exclude that the MNAF has accumulated enough stress to produce an earthquake of magnitude 7 or more. Even less is known for the Geyve-Mekece segment for which the last historical rupture might be the September 1065 earthquake (Ambraseys, 2002), implying a bigger amount of accumulated stress.

C.9 Conclusion

Using a combination of field observations, subsurface geophysical aquisitions, and the analysis of high-resolution satellite images, we have demonstrated that the segments of the MNAF in the southeast of the Marmara region have been significantly active during the Holocene. The fault displays morphological features typical of strike-slip deformation, associated with a slightly lesser vertical component. We were able to uncover the traces of six major surface rupturing earthquakes preserved in the landscape, characterized by coseismic horizontal displacement ranging from 2 to 6 m, which indicates magnitudes over 7. Some of these ruptures apparently affected two major segments of the fault from Mekece in the east to the Marmara Sea near Gemlik. We have estimated a minimal long-term horizontal slip rate of 5.4±3.4 mm/yr on the Mekece-Sölöz segment south of Iznik, which confirms the results of previous studies. It is interesting to note that the last slip rate of 5±2 mm/yr estimated by GPS (Ergintav et al., 2014) seems slightly larger than the geological rates, which may suggest that the geological studies tend to underestimate the actual value or that the fault relative motion have accelerated in the last millenia. According to the historical catalogues of seismicity, the last big event described on this fault strand happened in the early 15th in the western part of the fault strand studied. Taking into account the current uncertainty on the slip rate, the MNAF may already have the potential to generate a destructive earthquake in the future decades. We also emphasize the fact that the date of the last big rupture in the eastern part of the MNAF is not well constrained and that the time elapsed since might be even bigger than in the west, with the possibility of a big earthquake in the next decades. This could be verified by extending the study to the Geyve-Mekece segment of the MNAF.

C.10 Résumé

Ce chapitre est consacré à la paléosismicité holocène de la branche médiane de la faille nord anatolienne (MNAF) dans la région du lac d'Iznik. L'activité tectonique de cette branche est actuellement débattue car la sismicité y est très faible et peu de contraintes existent sur sa vitesse de glissement à différentes échelles et les derniers séismes qui s'y sont produits. Bien qu'aucun séisme ne soit connu sur cette faille pour le dernier siècle, les textes historiques mentionnent de nombreux événements ayant sérieusement affecté la ville d'Iznik et ses alentours depuis 2000 ans. La compilation des études de tranchées réalisées sur la faille permet d'identifier au moins trois ruptures indépendantes sur les derniers 2000 ans.

Dans un premier temps, des images satellites Pléiades à haute résolution ont permis d'établir la segmentation fine de cette branche de faille. La faille s'étend sur 135 km entre Geyve et Mekece et peut être décomposée en trois segments majeurs, auxquels nous ajoutons un dernier segment, la faille de Gencali, qui suit une orientation NE-SW à partir du milieu du segment Sölöz-Gemlik. Ces segments principaux sont à plus petite échelle subdivisés en segments plus petits qui se chevauchent souvent. Dans un deuxième temps, nous avons fait des mesures systématiques le long de la faille sur des marqueurs sédimentaires et morphologiques décalés latéralement par la faille. L'analyse statistique de ce jeu de données nous a permis d'identifier six séismes préservés dans le paysage. Le dernier grand séisme sur la MNAF entre Gemlik et Mekece, est associé à un glissement cosismique de 4.8±1.9 m. Ceci est compatible avec un séisme de magnitude Mw 7.3 capable de rompre les deux segments occidentaux sur 95 km. Les glissements cosismiques des séismes identifiés varient entre 2 et 5 m, ce qui suggère que le temps écoulé entre chaque rupture n'est pas constant.

La MNAF présente également le long de son tracé des traces de glissement vertical à plusieurs échelles de temps. Certains des décalages latéraux mesurés sont associés à un déplacement vertical, qui peut atteindre jusqu'à 20 m. Cette composante verticale a pu être confirmée en profondeur par des acquisitions au géoradar à travers deux portions de faille. Une série de facettes triangulaires typiques des escarpements de faille normale existe également au sud du lac d'Iznik et leurs pentes suggère un glissement plus intense le long du lac et s'atténuant sur les côtés.

A partir d'un décalage de rivière mesuré au sud-ouest d'Iznik sur le segment Mekece-Sölöz, couplé à la datation de la terrasse incisée par cette rivière, nous estimons une vitesse de glissement horizontale minimale de 5.4±3.4 mm/an sur ce segment de faille. Cette valeur est similaire à celle d'une étude précédente dans le golfe de Gemlik et dans la marge d'erreur basse des mesures GPS. La sismologie historique suggère qu'aucun grand séisme ne s'est produit sur la MNAF depuis au moins le 15e siècle. En considérant les erreurs associées aux vitesses de glissement, on ne peut exclure que la faille ait déjà accumulé assez de contrainte tectonique pour produire un séisme important dans les prochaines décennies.

Chapter D

Archeoseismological study in Iznik

D.1 From ancient Nicaea to Iznik

D.1.1 History

The surroundings of Iznik Lake have been inhabited since the Neolithic (French, 1967; Roodenberg and Roodenberg, 2008; Gerritsen et al., 2013). The city itself was founded as Antigoneia by Antigonus I, one of Alexander the Great's successors, in 315 BC. Several years later, the city was captured by another successor of Alexander, Lysimachus, who renamed it Nicaea in tribute to his deceased wife. From the early 3rd century BC, the city's political importance grew in Bithynia and Nicaea became one of the most important urban centres of Asia Minor, prospering from its location at the crossroad of major trade and military routes, as well as from its large, fertile territory. At that time, it already presented its current configuration: four gates, and streets intersecting one another at right angles. The hellenistic kings also built the first fortifications (Abbasoglu and Delemen, 2003).

Nicaea and Bithynia came under Roman rule in 72 BC and during all the following period, the city attracted the interest of the emperors (Fig. D.1). The city was struck by an earthquake in 121 AD during Hadrian's reign (117-138), and rebuilt with imperial help. During the reign of Valerian (253-260), a Goth army attacked the region and burned the city. Following this event, a first, ∼5 km long, defensive belt of walls, which is still visible today, was built (Foss, 1996). The construction started under Gallian's rule (260-268) and ended under Claudius Gothicus (268-270). In the fourth century, the city suffered from several earthquakes (see appendix A), but also from the founding of Constantinople which attracted resources and population away from Nicaea. It gained nonetheless a prestigious religious role when it held the First Ecumenical Council in 325 (Sahin, 2003). Later on, the city started to decline, so much so that some of its public buildings had to be restored by Justinian (527-565) and disappeared from the sources until the early 8th century.

In 716 and 727, the city suffered attacks by the Umayyads. The walls were apparently damaged close to the Istanbul Gate in the north and around the northwestern gate. The war damage was aggravated by a destructive earthquake in 740. Significant rebuildings of the walls occurred during the reigns and Leo III (717-741) and Michael III (842-867). The latter is responsible for major works with the addition of new towers. In 787, Nicaea served again as the meeting-place of the Seventh Ecumenical Council. In the late 10th century, the Byzantine general Bardas Skleros attempted to seize the imperial throne and led a wide-scale rebellion in Asia Minor. In 978, the rebel besieged the city, which caused significant destructions on some parts of the walls. After leaving Nicaea for the East, he was eventually defeated the following year (Holmes, 2005). The city was probably even more damaged by a major earthquake in 1065, followed by quick rebuilding.

Another period of political trouble occurred in the late eleventh century, when several generals rebelled against the central power in Anatolia. At that time, both the rebels and the emperors tried to do alliances with the neighbouring Seljuq Turks (Cahen, 1948; Norwich, 1993). This allowed the Turks to penetrate further in Anatolia and progressively control a growing territory known as the Sultanate of Rum, with Nicaea as its first capital (Fig. D.1). The city went back to the Byzantine Empire during the First Crusade in 1097. The southern part of the walls were damaged and one tower in particular was entirely destroyed. Reconstructions were ordered by Alexios I Komnenos (1081-1118) and Manuel I Komnenos (1143-1180). These troubled times gave way to a flourishing period for the city under the Lascarid dynasty. During the Fourth Crusade in 1204, Constantinople was sacked and siezed by the Latins who took control of a great part of the Byzantine Empire's territory (Nicolle, 2011). In the meantime, Byzantine aristocrats managed to keep a few small independent states (Fig. D.1). Nicaea became this way capital of its own self-proclaimed Empire (Angold, 1991). Theodore I Laskaris and its successor John III Doukas Vatatzes did impressive rebuilding works on the walls and added a second belt of outer walls. In 1261, Michael VIII Palaiologos recaptured Constantinople and restored the Byzantine Empire.

While the Turks advanced and gained power in Anatolia at the beginning of the 14th century, it seems that Nicaea suffered continuous emigration. In 1329, the Ottomans besieged Nicaea and the inhabitants eventually surrendered in 1331. From the testimony of travellers, the city had already lost most of its population a few years after the conquest and presented an overall ruined aspect intra muros (Defremery and Sanguinetti, 1968). The Ottomans carried out significant construction work after the conquest, especially in the 15th century, and the city quickly regained a dynamism, though shortlived, with the construction of several mosques and religious foundations. The decline of the construction activity that followed might reflect a real decline of the city or the end of the patronage by the viziers of the Candarli family. In the middle of the 15th century, the local administration centre wass transferred to Izmit and the city lost any political importance. In 1402, Iznik was sacked by the armies of Timur, but that did not prevent it from prospering. We find the same kind of description by almost all travellers from the 16th to the 19th century (Raby, 1976),

who reported a rather poor condition and a small population (the 1520 census counts 2000 inhabitants, to be compared to the 25-30,000 people for the Byzantine period). Despite this political and economic weakness, Iznik was a famous centre of ceramic production in the 16th and 17th centuries. The description from Texier (1862) tells us that in the 19th, most of the area inside the walls was still used for agriculture and that only the very center was built up (Otto-Dorn, 1941; Rabbel et al., 2015). This was still the case at the beginning of the 20th century (Fig. D.2) until the 1920's (Lowry, 2003). Several destructions affected the city in 1921 during the war with Greece.



Figure D.1: Political evolution of Anatolia after the Roman conquest (top, from Pera Air, 2016), before Nicaea's siege in 1097 (center, from Wikipedia, 2017a) and after the Fourth Crusade (bottom, from Wikipedia, 2017b).



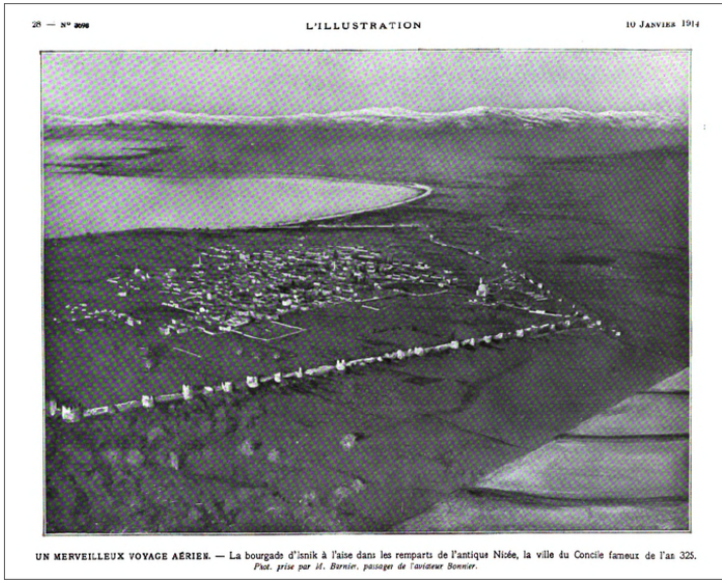

Figure D.2: Left: Map of Iznik drawn by Texier (1862), showing that most of the intra muros space is made of fields and idle land, and only the very center is built. Right: Aerial photograph of Iznik published in the French magazine "L'Illustration" in 1914.

D.1.2 Construction materials and techniques up to now

The first buildings still visible in Iznik use a variety of materials and techniques. A simple rubble masonry with bands of terracottas was used for the original 3rd century walls (Fig. D.3a), while the towers exclusively used a terracotta superstructure. Ashlars were reserved for the base of the fortifications (Fig. D.3b). According to Foss (1996), triumphal arches were build by Vespasian (69-79 AD) at the location of the gates currently visible. After an earthquake in 121 AD, emperor Hadrian ordered many reconstructions, including the triumphal arches. It is possible that the ashlar framework visible as inner gates dates back from these periods. Another early building using both ashlar and stone masonry is the city theatre (Fig. D.3c). This building is well known by archeologists studying Roman construction processes as it is specifically mentioned in several letters exchanged between emperor Trajan (98-117) and Pliny the Younger, governor of the Bithynia province. During its construction, the walls were already affected by stability problems, most probably because of the soft ground and described as "sinking, and cracked from top to bottom" (letter XLVIII). Despite being used as a stone quarry in later periods, some parts of the theatre are still preserved fairly enough, and the features described by Pliny on the walls are not observed on the current, finished building.

The successive reconstructions of the defensive walls from the 8th century reused a lot of ashlars spoiled from earlier buildings. Contrary to the 3rd walls, several defensive works of Leo III only employ marble ashlar. The base of the 9th towers and walls, which use a similar style as the original fortifications, is made of reused ashlars. However, the terracottas of this period are of a different, thicker fabric. In the construction history of Byzantine Nicaea, there is a tendency to reproduce the previous styles with the new materials and techniques available (Foss and Winfield, 1986). The mixed use of ashlar for low courses and brick masonry for superstructures is also well illustrated by Aya Sofia, a presumably Justinian construction (Brounoff, 1925). The new towers of Alexios I Komnenos are entirely made of ashlar spoils, including Turk gravestones, which are the only remains of their first occupation of Nicaea (Fig. D.3d).

A peculiar construction technique, the "recessed brick" appears in Nicaea in the late 11th century and has been associated to the repairs following the 1065 earthquake (Fig. D.3e). It consists in covering with mortar one of two brick courses, which gives the impression of large bands of mortar separating the brick courses (Schneider and Karnapp, 1938; Foss and Winfield, 1986). The technique is actually attested in Constantinople at a similar time. It seems to have originated in the late tenth century and remained in use after the eleventh (Ousterhout, 2008).

The walls were covered during the Lascarid period by a new white coating which can still be seen in some places (Kravari 2004; Fig. D.3f). This preoccupation for appearance is also present in several new towers built by Theodore I which have a very distinct style with the use of only spoils for the lower half and a superstructure in terracottas featuring various

decorations. After the Lascarids, they did not underwent major changes. The Palaiologan masonries are commonly made of alternated courses of rubble and terracottas. The late fortifications also show regularly placed square beam holes (Fig. D.3d).

The masonry techniques of the Ottomans are greatly inspired from the Byzantines, but the Ottomans use a finer mortar while the Byzantine mortar commonly includes fragments of terracotta (Grélois, 1998). Most buildings use mixed rubble and terracottas (Fig. D.4a), while more prestigious works like mosques use finely cut marble ashlars, sometimes in combination with rubble and terracottas (Fig. D.4b).

Contemporary buildings in Iznik sometimes imitate the ancient styles but most modern houses and public buildings use standard concrete blocks and mortar (Fig. D.4c). Very few older houses still display traditional techniques using especially "bricks" of mixed adobe and straw, assembled within wooden beam frames. However, in the smaller villages scattered around Iznik Lake, these traditional houses are very common, and sometimes combine parts in bricks (Fig. D.4d and e). Even though this kind of house is today associated to lower living standards, they are of great cultural value because they may give us the best picture of what common housing in Iznik was like during the Byzantine and early Ottoman times.



Figure D.3: Examples of Roman and Byzantine construction. (a) Walls of the 3rd century. (b) Triumphal arch in marble ashlars at the eastern gate, integrated in the 3rd century terra cotta framework. (c) View of the theatre from the south. The base of the walls is made of ashlars while the superstructures are built with a rubble stone framework. (d) Southwestern corner of the fortifications with from the front: the outer wall, a Komnenoi tower, and a Lascarid tower with beam holes. (e) Example of recessed brick tower. (f) Detail on the Lascarid white coating covering the inner facing of the inner walls.

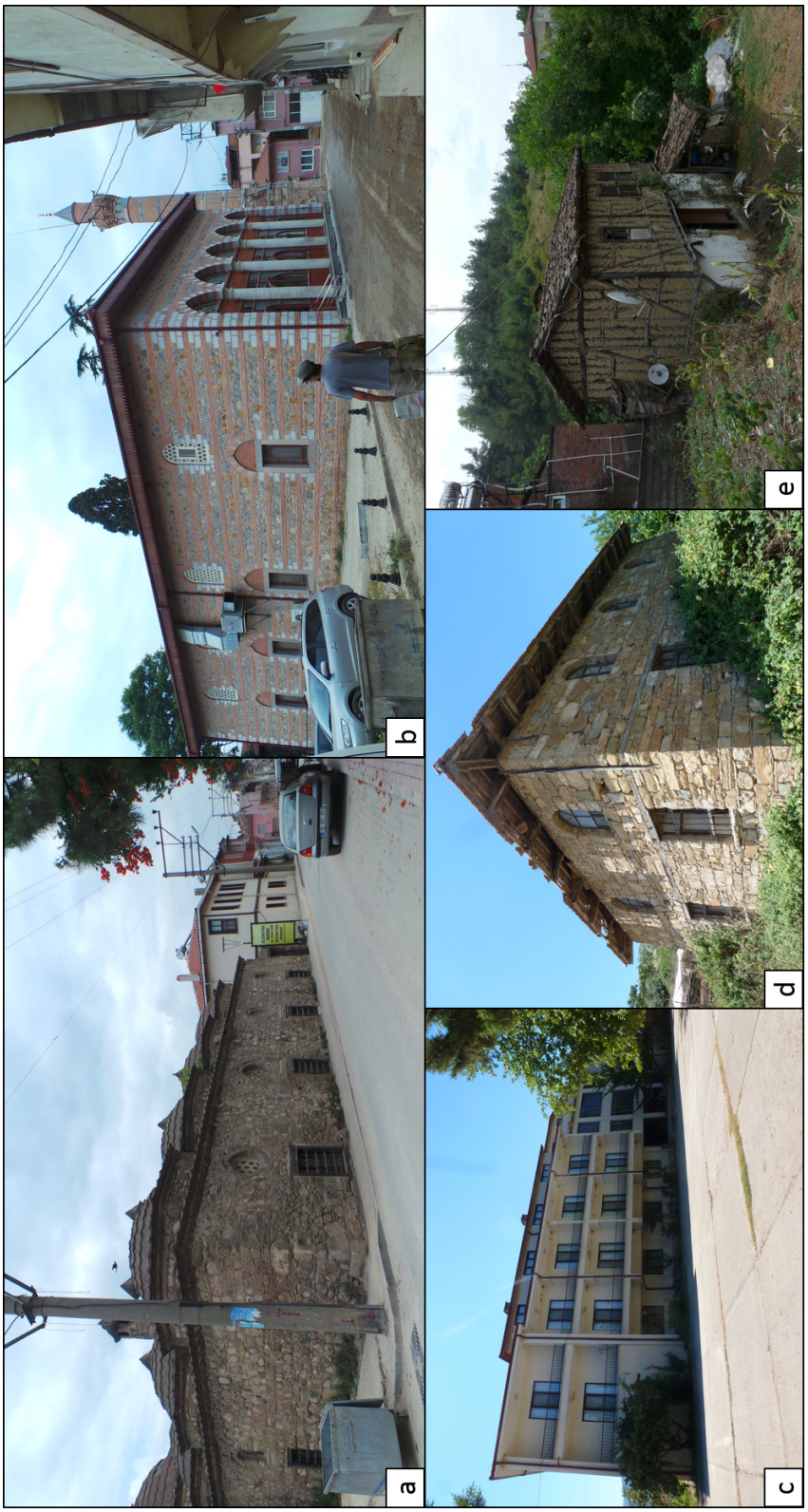

Figure D.4: Examples of Ottoman construction. (a) Süleyman Pasa Medresesi, built shortly after the Ottoman conquest. (b) Esrefzade Cami, built between the 15th and 16th centuries. (c) Iznik Earthquake Hazard Mitigation Center, a modern reinforced concrete construction. (d) A traditional village house built with a limestone rubble framework in a wooden beam structure. Lighter travertine stones were used for the windows and certain angles. (e) A traditional village house built with assembled wooden beams and adobe.

D.2 Archeological study of the aqueduct of Nicaea (Iznik, NW Turkey)

The content of this section will be submitted to the *Journal of Archaeological Science* as an article by Yacine Benjelloun, Hélène Dessales, Julia de Sigoyer, Stéphane Garambois, and Mustafa Şahin.

D.2.1 Introduction

Located in the southeast of the Marmara Sea, the ancient city of Nicaea (modern Iznik) has been an important political and cultural centre in Asia Minor since the Hellenistic period (Fig. D.5). The city came under the rule of the Roman Republic in 72 BC and has preserved several noticeable buildings from this period of time, among which a theatre, defensive walls and an aqueduct. While the walls have been the subject of several comprehensive studies (Schneider and Karnapp, 1938; Foss, 1982; Foss and Winfield, 1986; Foss, 1996), the aqueduct has never been studied in detail. Aqueducts were vital infrastructures in ancient cities and their study can therefore provide precious information on the city's history. They were generally carefully maintained and rapidly repaired when damaged, so studying their construction history can help to document the evolution of the city's wealth and political stability, as well as the occurrence of catastrophic events related to wars or natural hazards. Aqueducts are often several kilometers long, linear buildings, and their relatively simple structure makes them convenient to model, to simulate their behaviour during seismic shaking for example (Volant et al., 2009). Certain aqueducts are even cross-cut by active fault segments and can thus be used to identify past earthquakes and derive the fault slip rate (Galli and Naso, 2009; Sbeinati et al., 2010; Passchier et al., 2013). When the water running in the aqueduct is charged with dissolved carbonates, sinter deposits tend to grow on the walls of the channel and can be analyzed as paleoenvironmental archives (Passchier et al., 2016).

Most of the remains of this aqueduct visible today extend in the east of Iznik from the Lefke Gate (Fig. D.6). As the ground level elevation rises eastward, the aqueduct's height tends to decrease. The recent excavations done around Lefke Gate have revealed that the base courses of the aqueduct were partly buried, and that the ground level was lower than today when the aqueduct was built. Close to the city gate, the aqueduct's channel is enlarged on a few meters before finding its normal width again. After 600 m, the aqueduct shows a significant change in its direction associated with a peculiar terracotta structure on its northern facing. It then follows a NW-SE orientation along Abdülvahap hill and presents an underground section along the slope of a karstified carbonate massif on about 450 m. This underground section is made visible by several pits dug by man. A few built remains are again visible on 100 m at the southern tip of the hill, bordering the road

to Kaynarca. The total length of the aqueduct visible continuously on the field amounts to about 1.5 km. It is likely that the sources used at the time were located in the karstic massif east of Iznik, in the vicinity of Dereköy village, ∼6 km east of Iznik (Fig. D.6). The aqueduct is built as a large wall, pierced by several arches. The wall is composed of two masonry facings with inbetween the "nucleus", a mixture of various materials and mortar. This wall supports the channel ("specus") of the aqueduct where the water used to run. The lateral walls of the specus are covered on the inside by a special, hydraulic mortar. At some points, it is possible to observe the remains of a vault originally covering the specus. Several deformations of different kinds are visible along the aqueduct's walls, such as cracks, partial collapse of the facing. On some cracks, carbonate concretions have developed against the wall during the leakage of water. Some other deformations are more characteristic of coseismic shaking: some sections of wall show warping, the upper part of some walls are deformed and "pushed" outward.

Several phases of construction and restoration can be observed. The building visible today was built during the reign of Hadrian (117-138; Sahin, 1979) and restored at the time of Justinian (525-565) according to Procopius (*De aedificiis*, V, 3). According to Foss (1996), restorations were also done by Theodore I Lascaris (1205-1222) in the 13th century. It is difficult to know precisely when the aqueduct stopped working. Around 1335, the traveller Ibn Battuta (2.452f, cf. Defremery and Sanguinetti (1968)) visited the city a few years after the Ottoman conquest and related that the water supply came from wells, without mentioning the aqueduct, from which we could infer that it had already stopped working at that time. However, later witnesses describe an aqueduct in use (Raby, 1976). The clergyman John Covel, who visited Iznik in 1677, tells that the aqueduct brings a "very good" water, "run[ning] plentifully". Richard Pococke mentions in the 18th century the existence of an irrigation system going inside the city walls and supplying basins. The aqueduct may have even functioned until the 19th century before being interrupted with explosives if we believe oral accounts gathered during our field works.

We present here the results of a stratigraphical study of the aqueduct on the 600 m long section close to the city (Fig. D.7), conducted mainly in June and July 2015. An additional geophysical survey was carried out on the undergound section in July 2016.

Figure D.5: (a) General location map, with active faults drawn in red (Emre et al., 2011). (b) Satellite view of Iznik on the left, with the visible remains of the aqueduct in yellow. The Elbeyli normal fault is drawn in red.

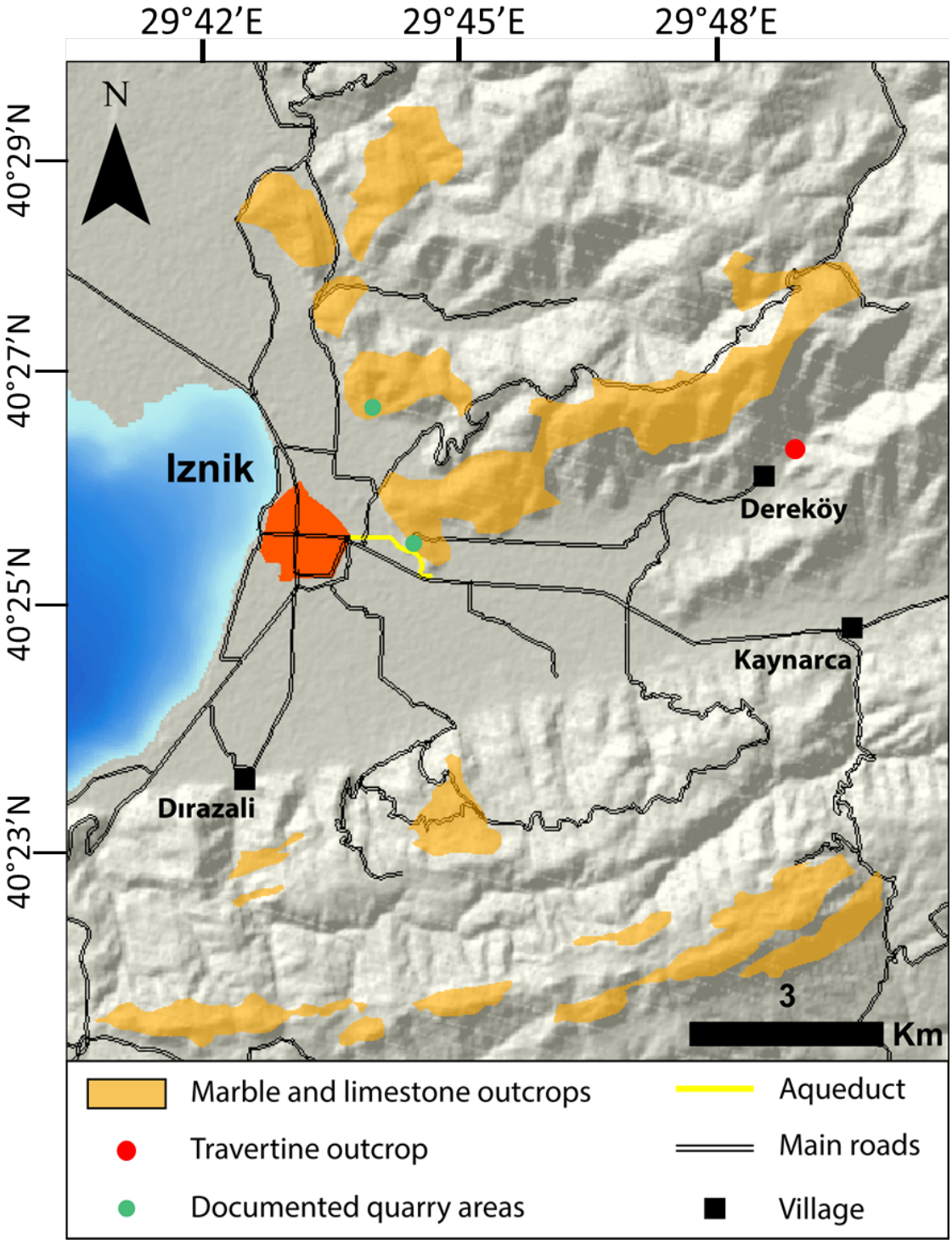

Figure D.6: Map of the possible extraction zones for the materials used in the aqueduct. The ancient quarries were visited during the field missions. The topographic isolines are spaced every 200 m. The lake shore is 83 m asl.

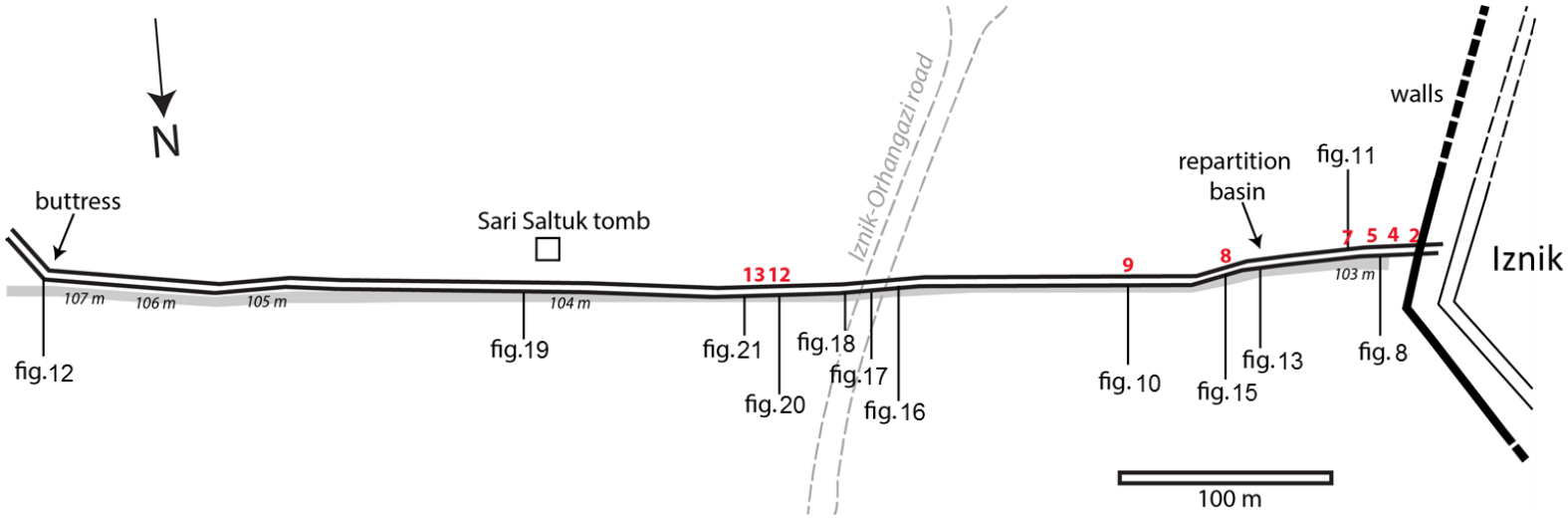

Figure D.7: Simplified sketch of the studied section of the aqueduct with the location of the main observations mentioned in the text. In grey are drawn the roads from Iznik to Abdülvahap hill following the aqueduct and from Iznik to Orhangazi (broken lines). The arches mentioned in the text are located with red numbers. The ground topography along the aqueduct is precised with a few elevations asl.

D.2.2 Methods

We focused our study on the northern facing, the southern side being largely inaccessible due to vegetation and private ownership. To study the construction, we used a method developed and implemented especially for several Roman hydraulic buildings in France and Italy (see Bukowiecki et al. (2008) for an example in Ostia). The studied sections were thoroughly described in terms of construction techniques and materials. These criteria allowed us to individualize 43 stratigraphical units (US). Each of these units was identified and registered thanks to a US number. On these units we also measured characteristic architectural features such as joints and construction stones dimensions. At the scale of the whole building, we used a second registering system to group together the construction techniques encountered which showed strong similarities with each other. These technical groups were also given specific numbers (eg. MR-0028) and registered in a database (ACoR) through synthetic forms including detailed characteristics (morphology, materials, stone dimensions and arrangement...) and photographs. The ACoR base has been developed since 2014 as a part of an atlas of the construction techniques in the Roman world (see http://www.transfers.ens.fr/atlas-des-techniques-de-construction-dans-le-monde-romain). This base currently includes techniques from several sites in Italy, Turkey and Morocco. Each technique number is composed of two letters that indicate the type of structure (MR for a wall, AR for an arch, CF for a buttress) and four digits related to its creation rank in the whole database. Finally the stratigraphical units were grouped into several main building stages showing a technical and/or structural coherence, which allowed us to propose a chronology of the construction.

D.2.3 Description of the techniques of construction observed

We were able to distinguish from our detailed survey of the northern facing of the aqueduct fifteen different techniques on ten walls, four arches and one buttress, mostly irregular rubble, regular frameworks of quadrangular rubble stones sometimes alternating with courses of terracottas, and regular frameworks of terracottas. In addition of terracottas, the masonries use in general limestone, travertine rubble, and spoil materials from other buildings. The complete descriptions of the techniques, including detail photos, can be found in appendix E. It is to be noted that the origin of these materials is locally found in the environment surrounding the city. Marble and travertine deposits are easily found in the carbonate massif located east of Iznik in the vicinity of Dereköy village, while several limestone outcrops exist in the south and east of the city between Dirazali and Kaynarca (Fig. D.6).

D.2.3.1 Techniques MR-0028 and AR-0004

The arches and walls close to the fortifications of Nicaea present a clean, regular framework of alternating bands of 1-3 courses of 4 cm thick terracotta and one course of rubble limestone, travertine and marble spoil (MR-0028, Fig. D.8). The terracottas have a bright red matrix and a homogeneous quality (Fig. D.9a). The terracotta bands are generally composed of only one course but occasionally show two or three layers using smaller or pieces of terracottas. A few dressed terracottas were also found between some rubble stones. The stones are of various sizes, with average dimensions of 20x30 cm, and rather poorly carved.

The same terracottas are used in the arches associated with these walls (AR-0004), with a maximum length of 35 cm.

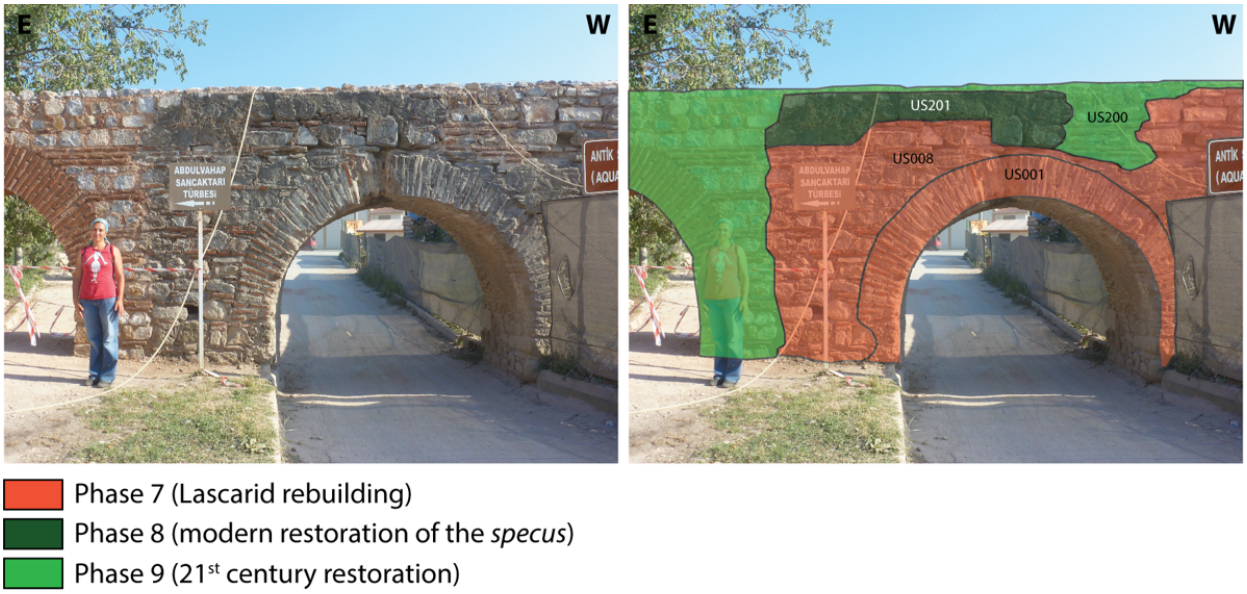

Figure D.8: Stratigraphy of arch 5 and surrounding facings, showing phase 7 (US001 and US008, AR-0004 and MR-0028) and modern restorations (US201 and US200).

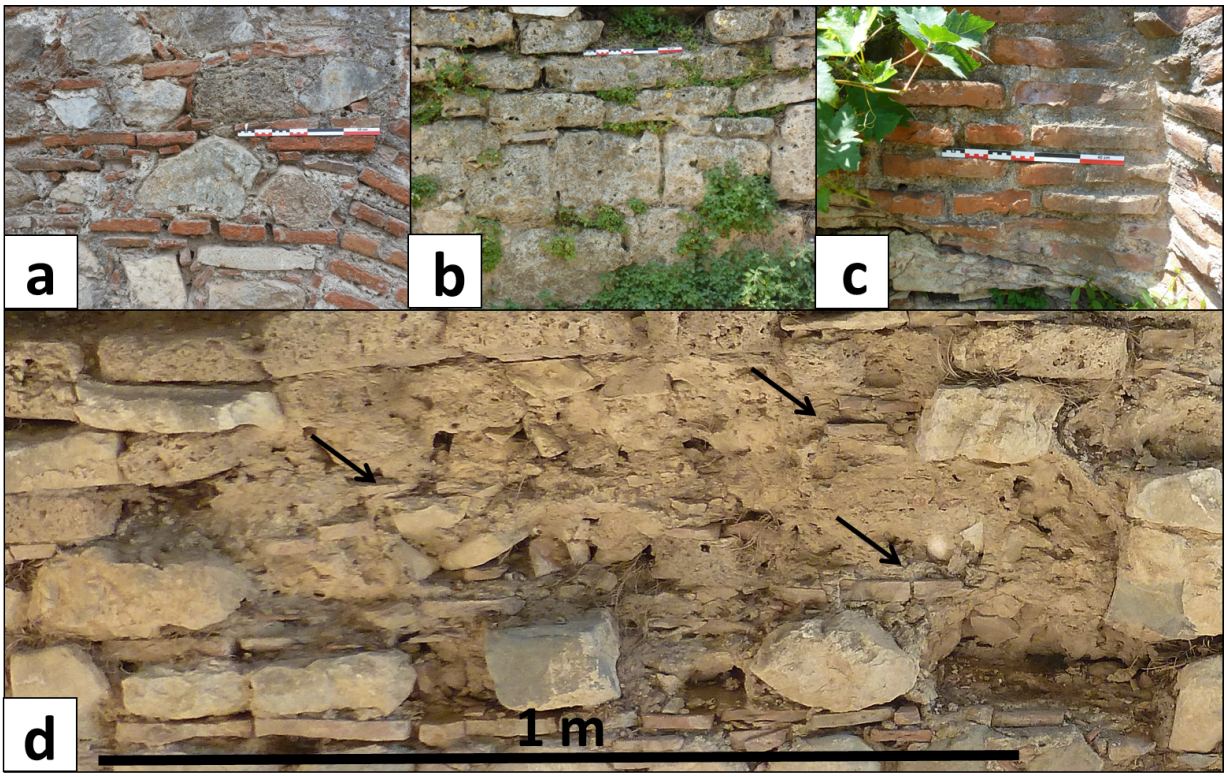

Figure D.9: Detail photos of some construction techniques. (a) Terracottas of MR-0028 close to the city gates, on the left of arch 5. (b) Travertines of MR-0034. (c) Terracottas of the buttress (CF-0006). (d) Nucleus of the aqueduct visible under the bridge of Iznik-Orhangazi road, showing alternations of terracottas (arrows) and rubble (MR-0041).

D.2.3.2 Techniques MR-0034 and AR-0002

A significant length of the section studied is made of a regular framework of quadrangular travertine stones (MR-0034, Fig. D.10). The stones were carefully cut into parallelepipeds, about 40 cm long (Fig. D.9b). The distribution of their short modulus shows that they can be divided into two batches, arranged vertically most of the time. The upper courses use 12 cm thick flat rubble while the base of the elevation is made of larger, square or rectangular stones. This technique is especially characterized by the homogeneity of the materials used which are mainly travertines.

A resembling technique was used for the facings of arches 4 and 7 (Fig. D.11) which use exclusively very well carved travertine rubble stones of homogeneous dimensions (AR-0002).



Figure D.10: Stratigraphy of arch 9 and surrounding wall. The whole travertine masonry belongs to phase 5 (MR-0034 and AR-0002). A small modern restoration is visible on the specus (US206, MR0144).

Figure D.11: Stratigraphy of southern facing of arch 7 and surrounding wall. A terracotta arch from phase 1 is visible in the nucleus (US002, AR-0003) and was later covered by a new travertine facing (US003, US203, AR-0002 and MR-0034) in phase 5. The adjacent wall was much rebuilt in phase 7 (US205, MR-0028) and the specus visible today is the result of modern restoration (US204).

D.2.3.3 Techniques CF-0006 and MR-0033

At the eastern end of the section studied, the aqueduct's direction changes to the southeast. This change is associated to a likely reinforcement structure added against the channel on its northern side (Fig. D.12). This structure is entirely made of all similar, finely crafted, 5 cm thick and 28 cm long terracottas, of red-orange colour and containing few visible temper (CF-0006, Fig. D.9c).

The same terracottas are found in another peculiar structure located closer to the city gate and interpreted as a repartition basin. The upper part of this structure is made of a regular framework composed of an alternation of 2-3 terracotta courses with a course of rubble dark marly limestone (MR-0033, Fig. D.13). The stones have rather homogeneous dimensions, around 10x25 cm.

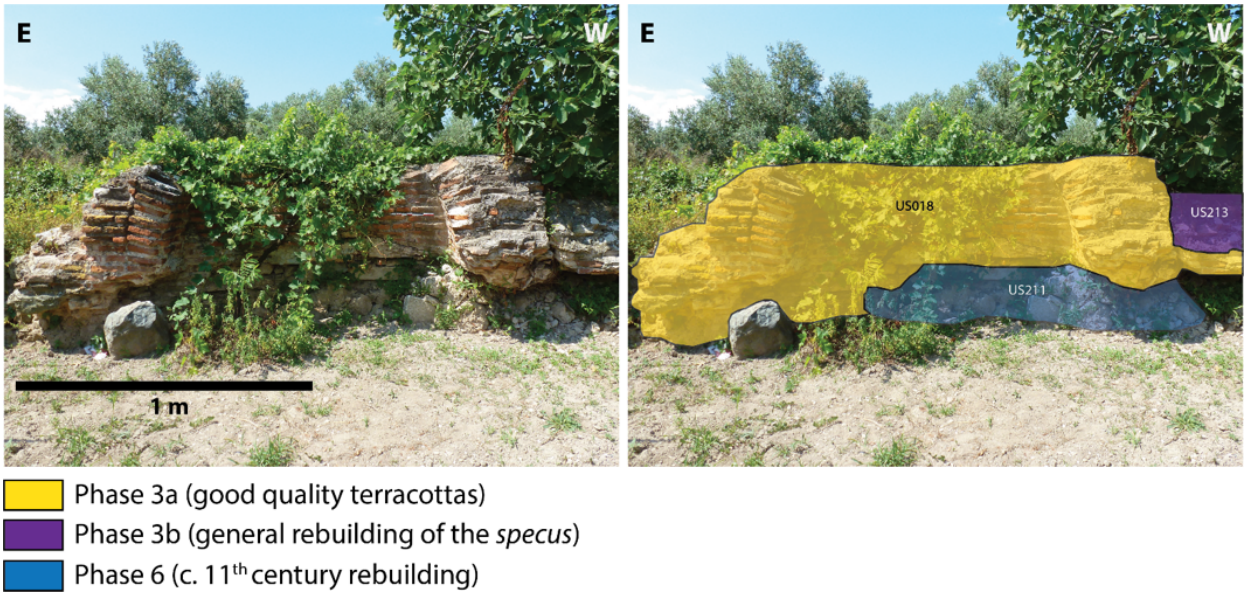

Figure D.12: Stratigraphy of the buttress located at the eastern end of the section studied. The buttress (US018, CF-006) was built in phase 3a and predates part of the base's facing (US211, MR-0036) belonging to phase 6. On the right, the specus rebuilt in phase 3b (US213, MR-0142) lies on the terracottas of phase 3a. Note that the aqueduct's height here is significantly lower than on the western portions (see for example Fig. D.8 for comparison).

Figure D.13: Stratigraphy of the repartition basin. A remnant of phase 1 masonry is visible at the base (US212, MR-0041). Most of the superstructure's facing is interpreted as a work of phase 6b (US022, MR-0036), while the top courses forming the basin belong to the preceding phase 3a (US021,MR-0033). The adjacent specus was restored during modern times (US204).

D.2.3.4 Techniques MR-0041 and AR-0003

The section located between arch 7 and the repartition basin is made of a loosely assembled regular framework composed of an alternation of terracotta courses and limestone rubble (MR-0041). The terracotta courses are often hardly visible, especially in the western section, but are obvious in some parts where the collapse of the facing makes the nucleus visible (Fig. D.9d). The rubble stones have average dimensions of 17x31 cm and are quite poorly carved in general. The few terracottas measured present an average thickness of 4.5 cm.

In the present state of the aqueduct, it is possible to see in places terracotta arches in the nucleus of the building, covered by a stone facing possibly during a same construction stage (Fig. D.14c). These inner arches are all very similar to each other and use 5.5 cm thick and 26 cm long red-orange terracottas, which are therefore restricted to this technique, assembled with a rather fine, white mortar (AR-0003).

D.2.3.5 Techniques MR-0036, AR-0005 and MR-0143

A significant length of the section studied uses a regular framework of quadrangular limestone and travertine rubble with a few marble spoils (MR-0036, Fig. D.15). The stones are quite carefully cut, especially the travertines, with average dimensions of 12x31 cm, which makes it close to MR-0034. A peculiarity of this technique is the presence of two very neat flat levels underlined by a course of flat travertine stones (Fig. D.14a). It seems that the limestones were almost exclusively used for the lower courses while the travertines are restricted to the upper courses. This technique is found closely associated with the travertine arch 8 (AR-0005).

Under the bridge of Iznik-Orhangazi road, the aqueduct presents a loosely assembled, regular framework of limestone and travertine quadrangular rubble, with a significant amount of spoils (Fig. D.16 and D.17). The overall technique has some similarity with MR-0036 but uses overall poorly cut stones of various dimensions (MR-0143). The facing of the specus, made of limestone rubble, is likely to be linked to another intervention.

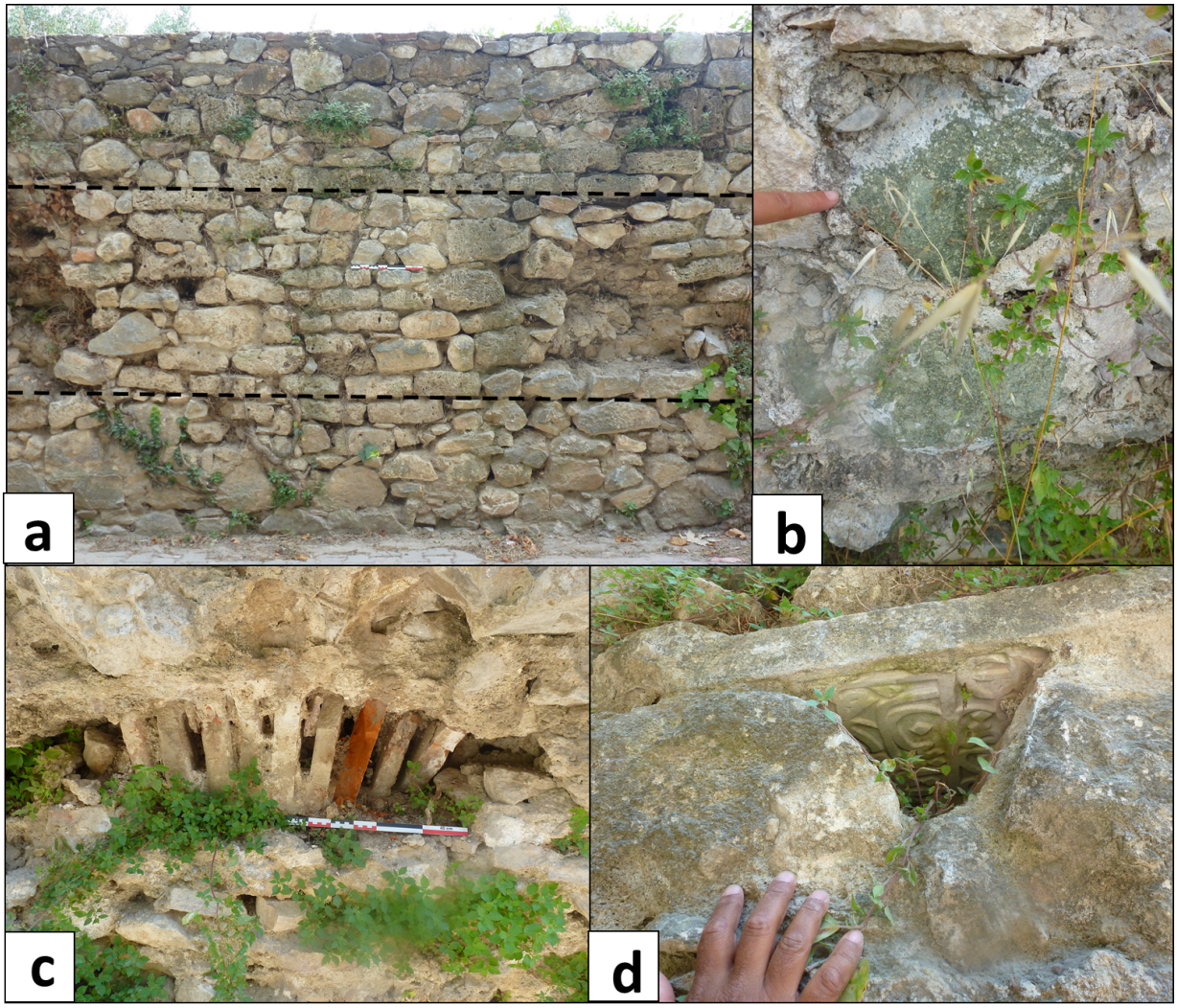

Figure D.14: Detail photos of some construction techniques. (a) Wall built with MR-0036, with two flat levels indicated by broken lines. (b) Green rocks found in MR-0142. (c) Zoomed view on an terracotta arch masked by later rebuildings. (d) Turk gravestone reused in the masonry east of arch 8.

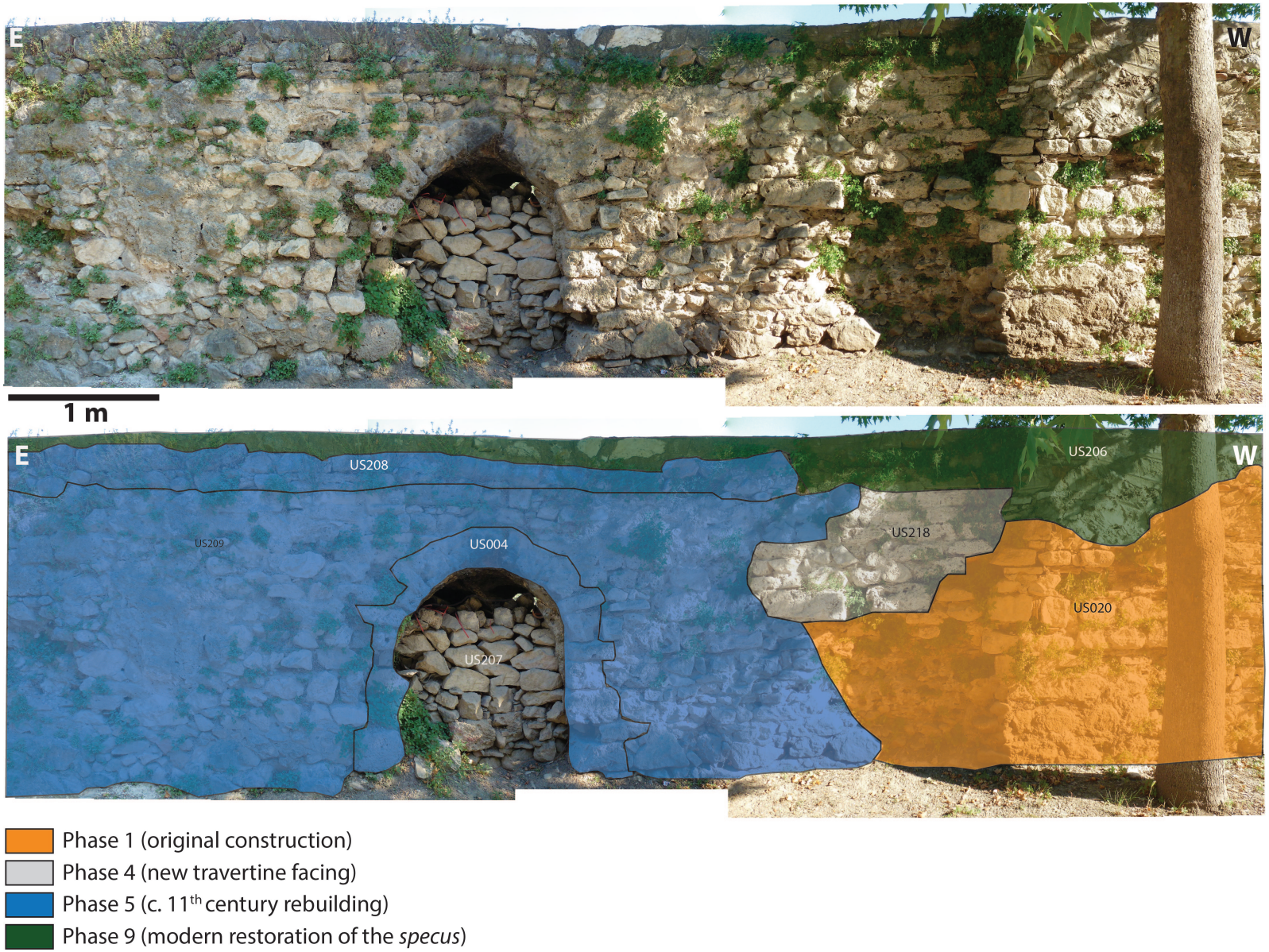

Figure D.15: Stratigraphy of arch 8 and surrounding walls. Early phases 1 and 5 are visible on the right (US020, US218 respectively). They were replaced on the left by the reconstructions of phase 6b (US004, US209 and US208). The specus have here been restored during modern times (US206). The filling of the arch (US207) is difficult to date precisely but is probably very late.

Figure D.16: Stratigraphy of the section located west of the Iznik-Orhangazi road bridge. The base courses (US019, MR-0041) belong to phase 1. The specus was almost entirely rebuilt in phase 3b (US012, MR-0142). The intermediate courses of the wall's facing (US216, MR-0143) were later added in phase 6a.

Figure D.17: Stratigraphy of the section located west of the Iznik-Orhangazi road. The base courses (US019, MR-041) belong to phase 1. Phase 2 is visible on the left (US215, MR-0035). The specus was almost entirely rebuilt in phase 3b (US012, MR-0142). Most of the intermediate courses of the wall are collapsed or covered by a new facing on the right (US216, MR-0143, phase 6a).

D.2.3.6 Techniques MR-0035

This technique is a regular framework of quadrangular rubble characterised by the exclusive use of rather well-cut limestone rubble. It is found at limited locations along the aqueduct, especially east of the Iznik-Orhangazi road bridge, in the low and middle parts of the facing (US215 and US217, Fig. D.17, D.18 and D.19). Similar stones are found in several other techniques and may have been reused from this technique.

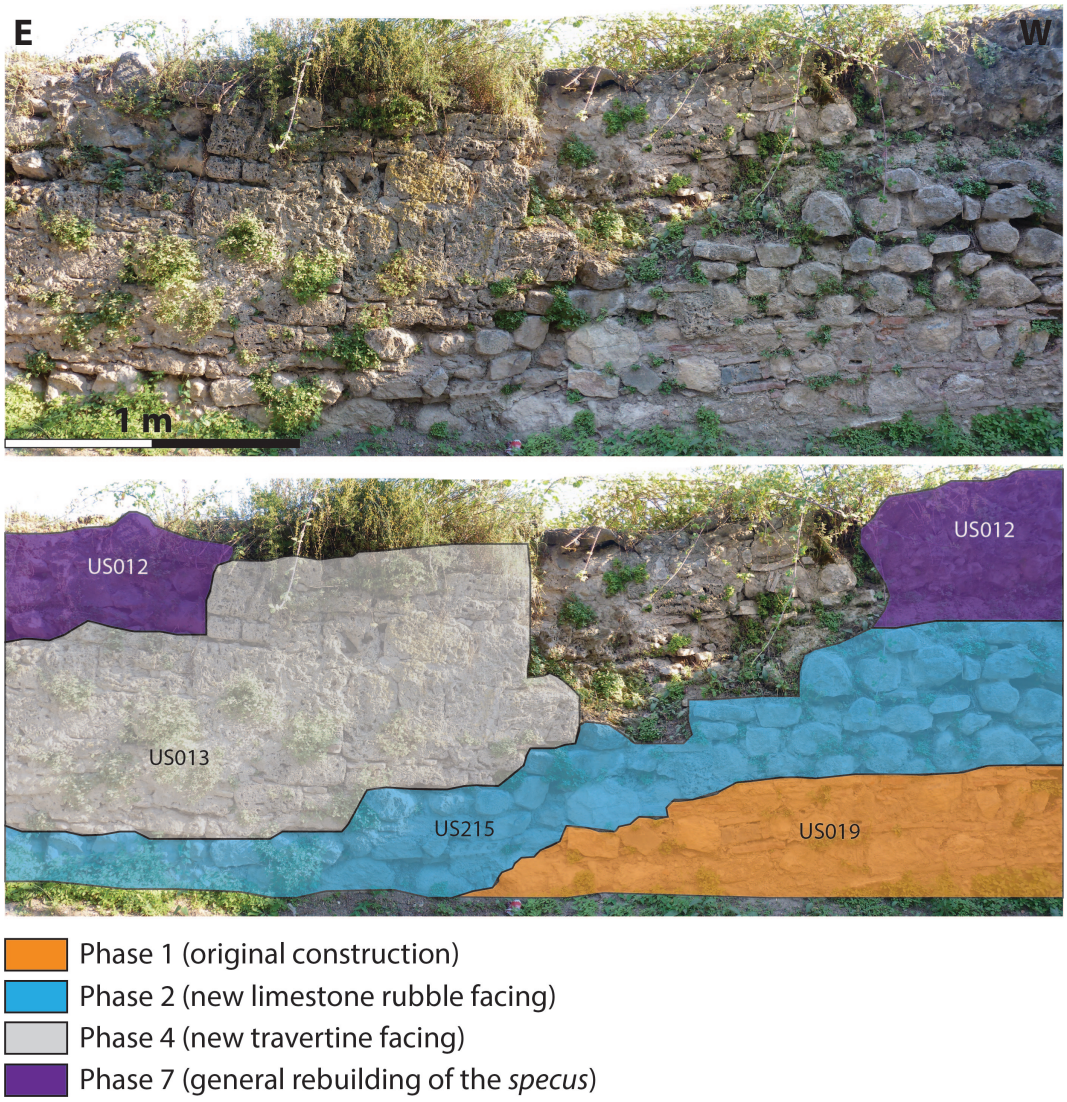

Figure D.18: Stratigraphy of the section east of the Iznik-Orhangazi road bridge. Phases 1 and 2 are present in the right-hand corner (US019 and US215 respectively). The specus visible on the sides (US012, MR-0142) is a reconstruction from phase 3b. A great part of the facing above (US013, MR0034) was rebuilt in phase 5.

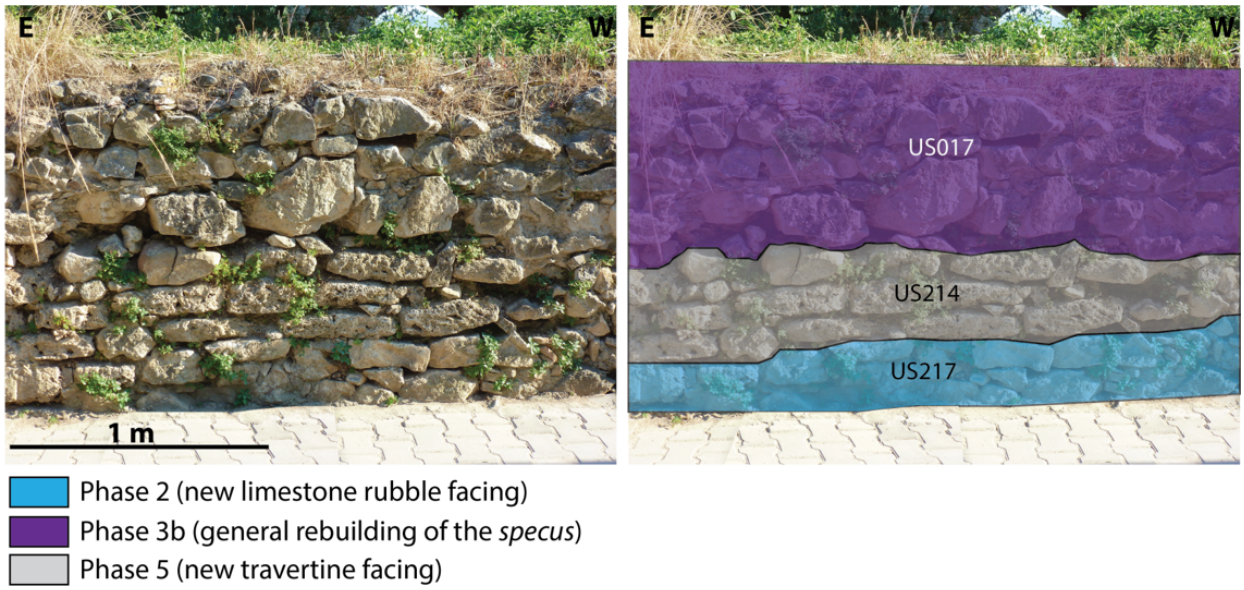

Figure D.19: Stratigraphy of the section located east of Sari Saltuk's tomb, showing from base to top phases 2, 5 and 3b (US217, US214 and US017 respectively).

D.2.3.7 Techniques MR-0142

This technique is mainly restricted to the specus facing and is made of irregular small limestone rubble including a green rock which is only found here (Fig. D.9b). The rubble stones are not cut as parallelepipeds but present homogeneous dimensions, about 10x15 cm (Fig. D.20). A similar technique is also found in the facing supporting the specus in the easternmost part of the section studied, with occasional use of travertines.

D.2.3.8 Techniques MR-0038

On a limited length, in the middle of our studied section is found a very peculiar technique using terracottas, and large travertine and limestone rubble (Fig. D.21). The technique is made of alternations of one rubble course and one terracotta course. What makes it very different from all the other techniques visible on the aqueduct is that each rubble stone of the same course is separated by a dressed terracotta. The rubble stones have quite homogeneous dimensions, about 30x40 cm. The travertine stones are well cut in parallelepipeds contrary to the limestones. The terracottas are 4 cm thick and present a red matrix. Their quality and dimensions seem rather homogeneous, especially for the dressed terracottas. We also noticed that this technique uses a mortar rich in coarse grains (from 5 mm to several cm). This technique was clearly recognized on the southern facing as well.

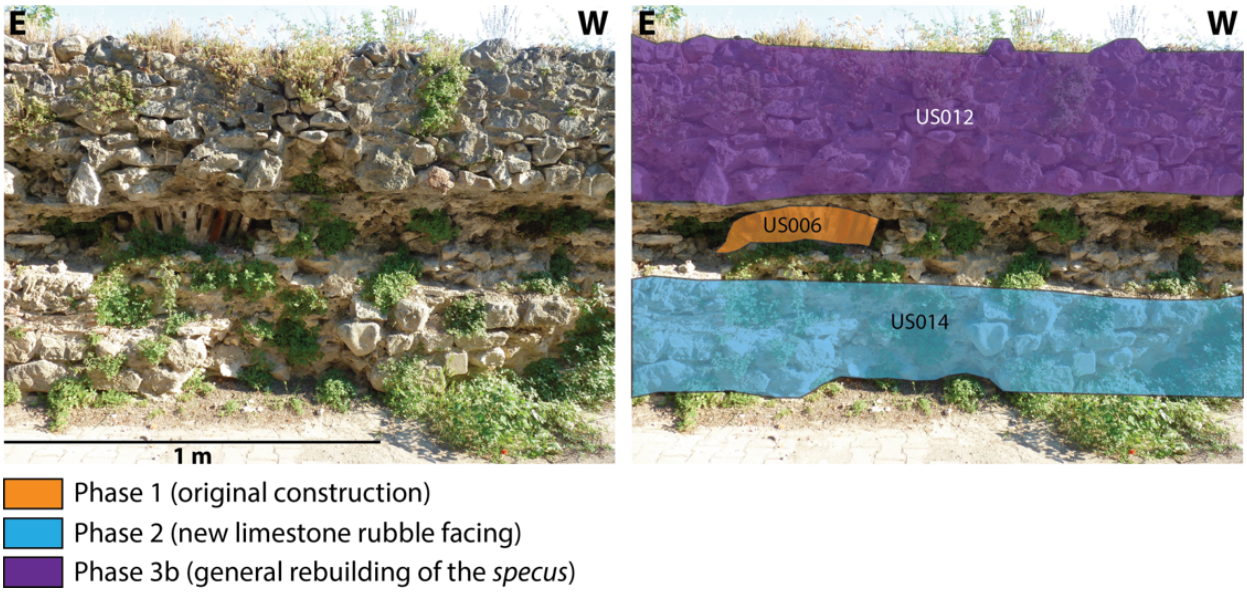

Figure D.20: Stratigraphy of arch 12 and surrounding wall, showing phases 1 (US006, AR-003) and 2 (US0014, MR-0035). The specus (US012, MR-0142) was rebuilt in phase 3b.

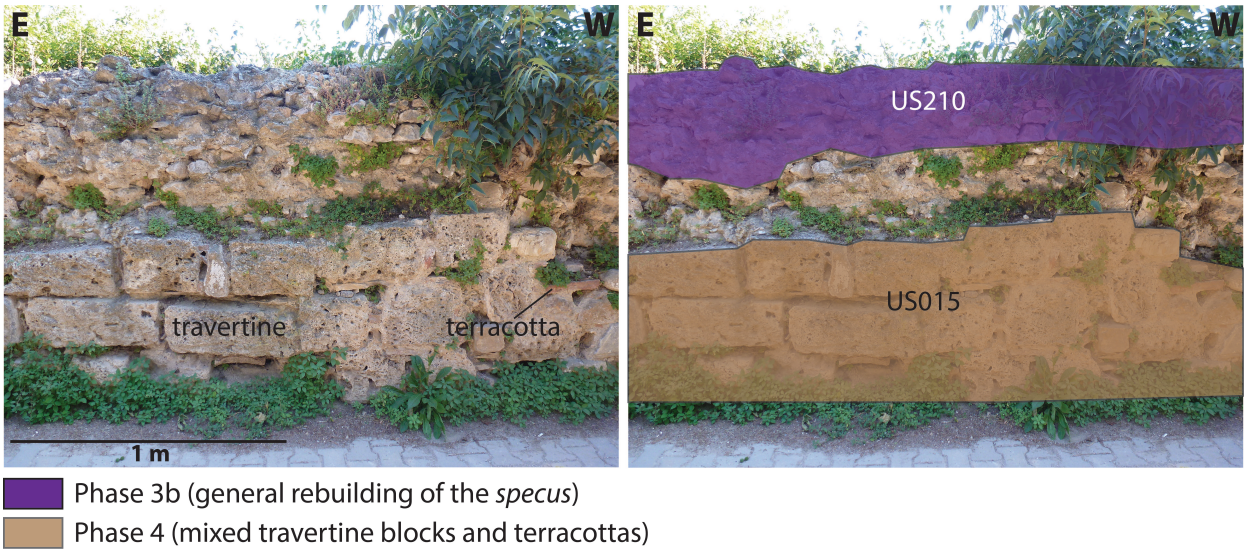

Figure D.21: Stratigraphy of the section east of arch 13, showing the rebuilt specus of phase 3b (US210, MR-0142) and phase 4 at the base (US015, MR-0038).

D.2.3.9 Techniques MR-0144

This technique corresponds to modern restoration of the top of the specus present on a significant length of the section studied (Fig. D.8, D.11, D.15). The restoration uses a very dark cement of granular aspect and mainly poorly cut marble stones of various dimensions.

D.2.4 Chronological bounds

In US209, 1 m east of arch 8 we could find a flat Turk gravestone used in the masonry, which indicates that it was built after the first arrival of the Turks in the region during the 11th century (Fig. D.14d). Such a reuse of Turk gravestones in public buildings has been well documented on the defensive walls and is exclusively found in the reconstructions by Alexios I Komnenos shortly after 1097 (Foss and Winfield, 1986). We could then infer a late 11th-early 12th age for this part.

We have also seen that several techniques reuse architectural elements from former buildings, especially the theatre. These spoils are found a lot in the walls for the reconstructions of the 8th and 9th century during Leo III and Michael III's reigns.

Another more solid technical analogy can be done between the mixed regular framework visible close to the city gate (MR-0028) and several similar techniques found in the inner and outer walls, classified by Foss and Winfield (1986) as D1, D2 for the former and D4 for the latter. In general, these techniques are dated to the Komnenoi (1097-1185) and Lascarid periods (1208-1258). It can be noted that this is the only real possible analogy with the walls in terms of construction techniques. Apart from these late works, it seems that most of the aqueduct's construction was undertaken during distinct operations unrelated to the walls.

In order to get absolute time constraints, pieces of mortar and terracottas were also sampled in different units, but no charcoal was found in the mortars and the terracottas could not be dated by archeomagnetism because of their alteration. A sample of carbonate concretion was also dated by ^{14}C but provided a very recent age (see section D.3.3.2.5).

D.2.5 Relative chronology of the building phases

Using the stratigraphic and typological evidence collected, we propose a construction history in nine phases, summarized on Fig. D.22 and D.23.

D.2.5.1 Phase 1

The masonries interpreted as the earliest construction phase visible today are composed of regular alternating courses of terracottas and quadrangular limestone rubble (MR-0041). It is visible on limited sections east of arch 7 (US100) as it was obviously extensively replaced by later phases. It is then visible again east of the repartition basin identically (US020, Fig. D.15), and the few terracottas visible at the very base of this basin (US212, Fig. D.13) are likely to be a remnant of the same phase as well. The base courses visible under the bridge and eastward use the same mixed regular framework and are remnants of the same phase (US019, Fig. D.16, D.17, D.18). The terracottas used in these units show

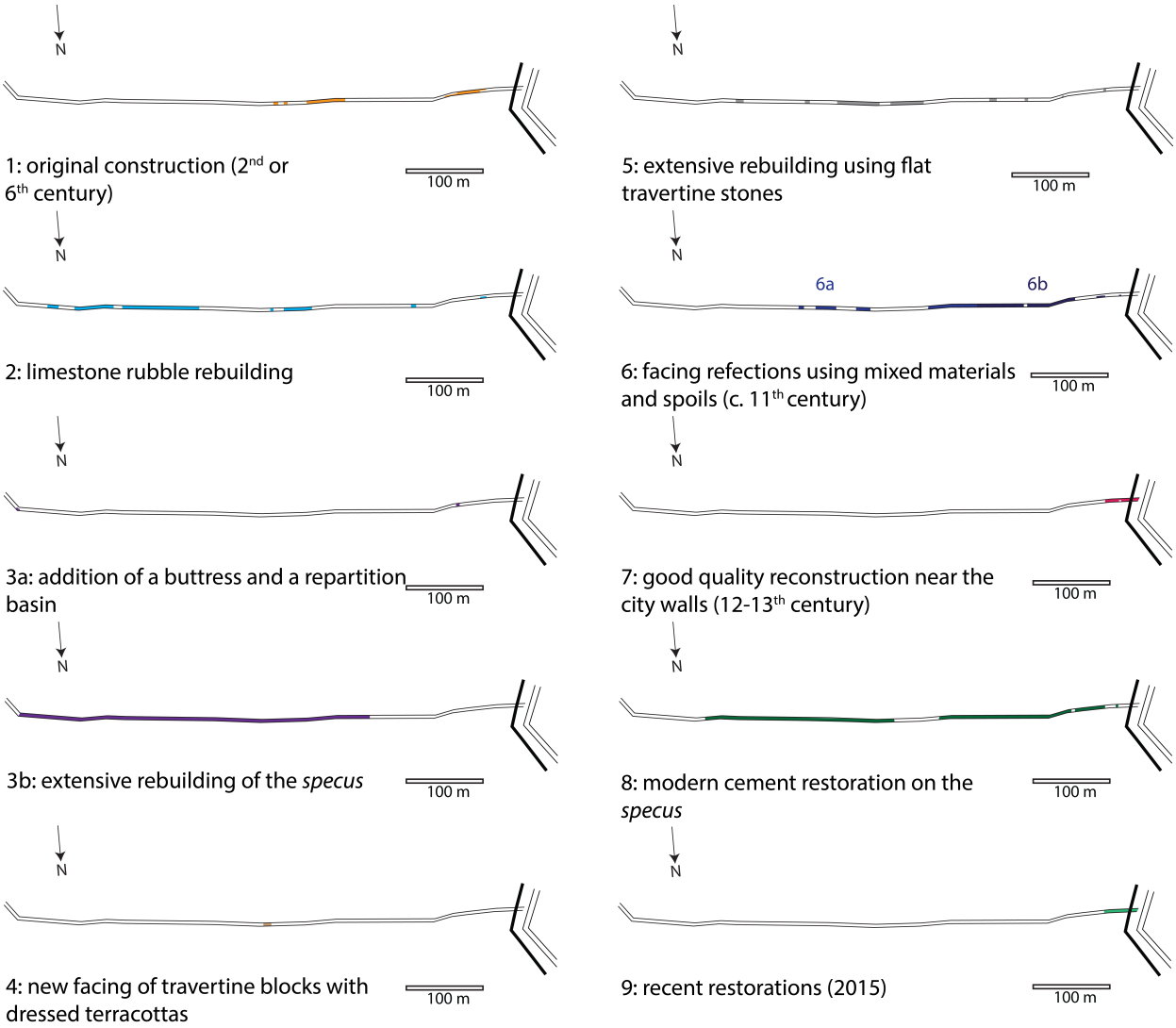

Figure D.22: Location of the different construction phases visible on the aqueduct.

very specific dimensions, about 5x30 cm. The fact that these same dimensions are found for the inner arches (US002, US006 and US007, AR-0003, Fig. D.20) suggests that we can relate these arches to the same early phase. US020 and US100 show that this technique was used on the whole height of the aqueduct, probably including the specus. As the earliest phase found, we could associate it with Hadrian's original construction or the rebuilding of Justinian mentioned by Procopius.

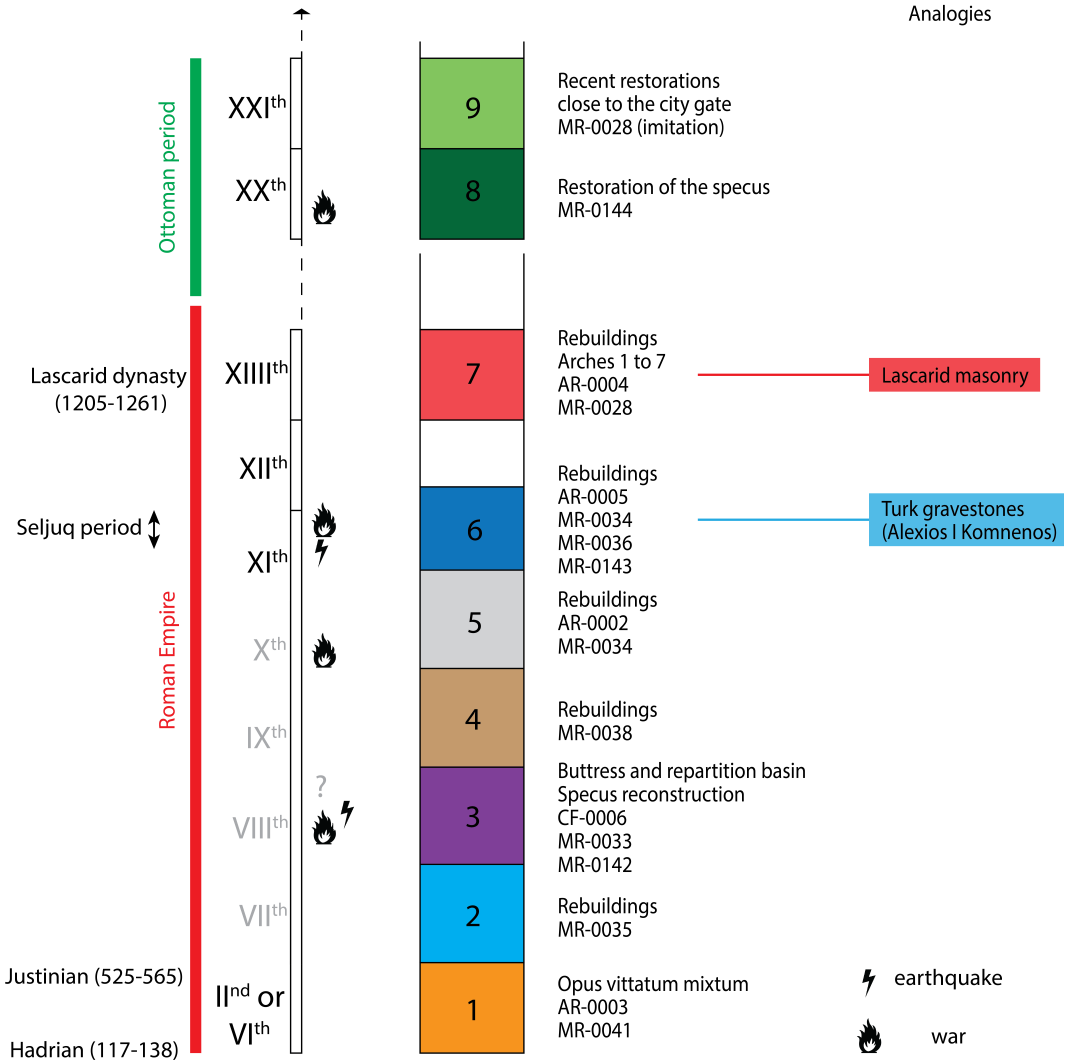

Figure D.23: Hypothetical relative chronology of the construction for Iznik aqueduct, replaced in a timeline thanks to several arguments. On the right are precised possible technical analogies with the walls. Note that the absolute chronology is more uncertain for phases 2 to 5 because precise dating and analogy are missing.

D.2.5.2 Phase 2

This phase is preferentially found in the western part of the section studied and includes lower and intermediate courses using a regular framework of quadrangular limestone rubble (MR-0035). It was seen east of the Iznik-Orhangazi road bridge, apparently replacing phase 1 (US215, Fig. D.18) and also as a new facing for arch 12 (US014, Fig. D.20). It is difficult to determine whether this phase constitutes occasional local repairs of the facing or if it was a more extensive rebuilding which was then replaced by later phases.

D.2.5.3 Phase 3

We have chosen to group in the following phase two different kinds of work. The first one (phase 3a, fig. D.22) is characterized by a specific, good quality, type of terracottas and corresponds to particular functional elements: a buttress at the eastern end of the section studied (US018, CF-0006, Fig. D.12) and a probable repartition basin closer to the city gate (US021, MR-0033, Fig. D.13). The wall supporting the specus visible today, which bypasses the buttress on the south, may be the result of later interventions and reconstructions. The second work (phase 3b) regroups several extensive reconstructions carried out especially on the specus east of the bridge (US012, US017, US210, US213, Fig. D.16, D.17, D.18, D.19, D.20) and on some parts of the supporting courses. It is characterized for the specus by a specific technique MR-0142 using smaller stones. Stratigraphically it lies directly on the terracottas of phase 3a. This is clearly visible at the junction between the buttress and the specus, where there is no apparent discontinuity between the similar mortars of both frameworks. It can thus be deduced that they were probably built during one or two successive projects at the same period of time. It is remarkable that phase 3b is today totally absent in the western part of the aqueduct (fig. D.21), as it was replaced by later works.

D.2.5.4 Phase 4

On several portions of the aqueduct, the limestone framework of the specus from phase 3b is heavily damaged and sometimes entirely replaced by travertines. Among the travertine works, the earliest phase is very limited in length, especially visible in the centre of the section studied (US015, Fig. D.21) and characterized by the use of technique MR-0038. It seems that these masonries reuse the limestone rubble of phase 2 and the stratigraphy of the construction indicates that it predates the other phases using rectangular blocks of travertine.

D.2.5.5 Phase 5

This phase constitutes a significant part of the masonries visible on the aqueduct today and is characterized by an almost exclusive use of travertine stones (MR-0034). This phase is visible close to the city gates on the southern facing of arch 7 (Fig. D.11). This part of wall depicts a succession of several interventions. The top of the current low arch is made of travertine stones (US203) masking a terracotta arch present in the nucleus similarly to AR-0003 (phase 1). This inner arch makes then way for a lower arch with a facing composed of smaller travertine rectangular stones (US003). By analogy, we can include in this phase the northern facing of the low arch 4 (AR-0002).

The phase is also visible around arch 9 (US005, Fig. D.10) and seems to alternate with other, maybe contemporary or closely related, interventions using more limestones (US010). We may also attribute to this phase the intermediate courses of the facing of the sections located east of the Iznik-Orhangazi road bridge (US013, US214, Fig. D.18 and D.19). The technique used is characterised by an almost exclusive use of well-cut travertine stones, with a flat rectangular shape most of the time. Less frequently, bigger square travertines similar to MR-0038 were used (US023). The works of phase 4 also include a new travertine facing for the specus.

D.2.5.6 Phase 6

We have chosen to group in this phase several reconstruction works using regular frameworks of quadrangular rubble characterised by a great diversity of materials: travertines, limestones and spoils from other building. This phase is found on the section passing under the Iznik-Orhangazi road bridge, probably after a large collapse of the upper facing (Fig. D.16 and D.17). The reconstruction seems to have been quick and not really programmed because of the bad quality of the masonry and the various types of material used including many big marble spoils (US216, MR-0143) probably from the theatre. By analogy with the large use of similar spoils in the walls, we could date this reconstruction 6a to the 8-9th centuries, but it could also be a much later intervention.

To this phase we also associate arch 8 (US004, AR-0005) and the surrounding wall (US209, Fig. D.15) until the bridge (US011) with some discontinuities (MR-0036). The bases of the repartition basin (US022, Fig. D.13) and the buttress (US211, Fig. D.12) were also included in this phase. The presence of several spoils in the masonry, especially a Turk gravestone, may indicate that this phase is a reconstruction following the seizure of the city by Alexios I Komnenos in 1097. The mixture of materials used can be understood as a way to rebuild in emergency with few new materials available. It is interesting to note that while this phase includes the new northern facing of arches 4, 7 and 8, only the latter shows a very different, uncommon shape, and stone voussoirs of different sizes. These observations suggest that arch 8 was significantly more damaged and needed to be rebuilt entirely. On this section, we could also note that while the main portion of the wall use limestones, the facing of the specus is also made of travertines (US208, MR-0034), which may have been preserved or reused in imitation from phase 4.

Given the significant variations in the technique used in the different reconstructions attributed to this phase, it is likely that they were not all built in a unique chantier. In some sections, the travertines of phase 4 are predominant but associated with new materials. In some others, these new materials are predominant and the joints are better conserved, indicating a different and probably later intervention (phase 6b). However, it was generally difficult to find a clear stratigraphical rupture between all these rebuildings, which we grouped into one unique phase representing several successive works around the 11th century.

D.2.5.7 Phase 7

Phase 7 is limited to the section closer to the city walls between arches 2 and 8 (Fig. D.8 and D.11). While the arches are made of terracottas (US001, AR-0004), the surrounding wall facing is a mixed regular framework using the same type of terracottas (US008 and US205, MR-0028), alternating with quadrangular rubble courses. This phase is characterized by a good quality of the construction, and was even used as a model for the very recent restoration works which sometimes overprint different techniques. The vicinity of this phase to the city walls could indicate that it is a late Byzantine intervention linked to the building of the outer wall by John Vatatzes (1222-1254) in the 13th century. Analogous techniques are also found in the walls and suggest a late date as well between the 12th and 13th centuries.

D.2.5.8 Phase 8

This phase represents a modern cement restoration (MR-0144) on parts of the specus (US016, US024 US201, US204, US206; Fig. D.15) and is probably one of the last interventions realised on the aqueduct. It is also to be noted that some arches, namely arch 7 and arch 8 were filled with stones at unknown periods. However these two late interventions are distinct: while arch 7 was filled with irregular rubble using similar materials to phase 5 (US202), arch 8's filling is made of large limestones without mortar (US207).

D.2.5.9 Phase 9

From 2015, new restorations were made on the sections of the aqueduct closer to the city gates, imitating the technique MR-0028 of phase 8 (US200, Fig. D.8).

D.2.6 On-fault displacement of the aqueduct east of Iznik

The western border of the carbonate massif east of Iznik is delimited by a normal fault, the Elbeyli fault, which clearly separates it from the flat alluvial plain of the lake. This structure can be understood as a normal fault accommodating a part of the subsidence of Iznik Lake basin linked to the transtension on the middle strand of the North Anatolian fault (MNAF, see chapter C). The trace of this fault is expected at its southern termination to cross the aqueduct.

All along its visible remains, a precise topographic survey of the aqueduct's channel was done with GPS RTK (Fig. D.24) and coupled with shallow geophysical imaging using a ground-penetrating radar with a 250 MHz shielded antenna, in order to better locate the path of the underground section (Fig. D.25). Fig. D.24b shows the result of the topographic

survey superimposed on the local topography obtained from the Pleiades DEM. On the sides of the massif, both sections of the aqueduct show a gentle slope progressively decreasing from ∼0.4 to 0.15% westward. A higher slope is visible on the western border of the massif, where the aqueduct seems to follow the topography. At this point, a basin was built to drop the water pressure caused by this locally higher gradient. The central section of the aqueduct looks clearly upthrown relatively to the sides. Considering the gap at both ends of the underground section, we obtain a similar maximum vertical offset of about 2 m. It can be noticed that while the end points of the central section define a similar slope to the built sections, several measurements in the central section fall below. This could be an original "default" of construction or result from progressive collapse of the central parts which were dug in a more altered and instable substratum.

Fig. D.25 presents the GPR profiles where the undergound channel is the most visible (the other profiles are displayed in appendix D). This is especially the case in the southeast where a shallow terracotta construction is accessible by two successive holes in the ground (Fig. D.26b, profiles 1 to 6 on Fig. D.25). In the central part along the slope of the massif, the structure is much more difficult to see (i.e. profiles 10 and 15) and is invisible on some profiles. This could imply that it has been destroyed or that the channel is filled with the surrounding soil and cannot be distinguished by GPR. It is interesting to note that the structure is more visible on the tips of the undergound section, where the carbonate substratum is closer to the surface and sometimes outcropping. This may explain why the GPR better images the structure in these areas offering a higher resistivity and a lowest attenuation. In the northern tip of the underground section, the channel is evidently dug into the carbonate rock (Fig. D.26a). The GPR data do not enable us to detect significant depth variations for the channel in the central section.

The two profiles 15 and 14 are respectively on the footwall and hanging wall of the fault. On profile 14, it is possible to see a bell-shaped anomaly below 60 ns which can be interpreted as the channel. It appears here deeper than on the other profiles on the south where similar anomalies appear at 15-20 ns. As the local topography decreases westward, the channel here should instead appear at a smaller depth. Given that the nature of the surrounding material is not significantly different between the profiles, probably with an intermediate resistivity between limestone and clay, this implies that the channel is downthrown west of profile 15. We can qualitatively estimate the depth difference associated. Taking a velocity of 10 cm/ns for carbonates, this 40 ns difference corresponds to 2 m, which is of the same order as the vertical offset observed with the topographic survey. However, profile 13 located west of profile 14 shows a small anomaly at 15-20 ns, which indicates a shallower channel here. Fig. D.27 presents hypotheses to explain these variations of the channel's depth across the fault. The local topography, decreasing westward, has to be considered (Fig. D.27b). A stronger deformation occurring near the fault can also be invoked (Fig. D.27c). The latter has been observed on the aqueduct of Venafrum in southern Italy (Galli et al., 2010). A precise topographic survey of this area would be required to quantify both effects.

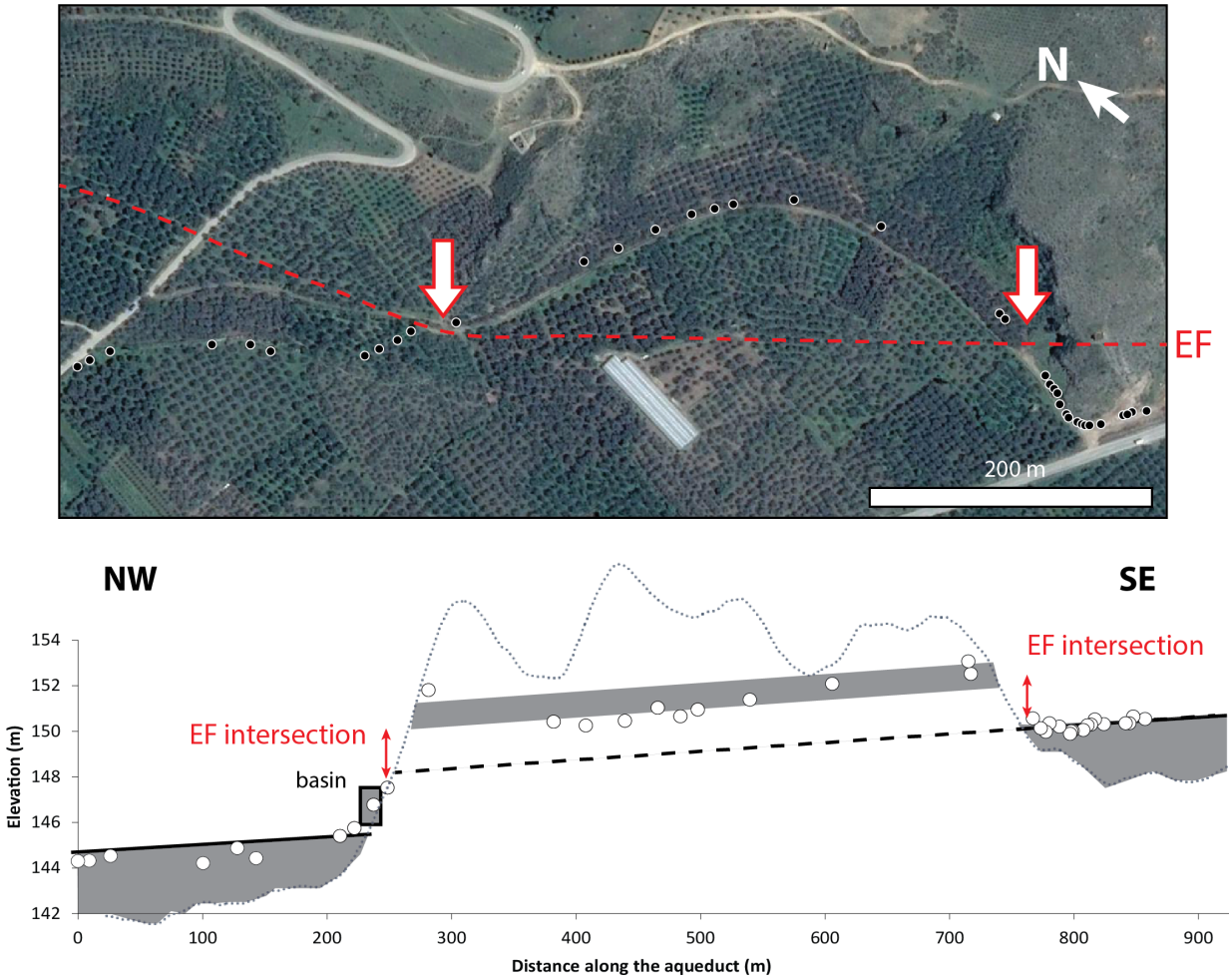

Figure D.24: Topographic survey along the aqueduct on Abdülvahap hill (see Fig D.6 for the location). On the top are localized the GPS measurement points on a Google Earth image. The Elbeyli fault (EF) trace is drawn as a red broken line and its intersections with the aqueduct are indicated with arrows. On the bottom is shown the measured elevations of the aqueduct's channel superimposed on the Pleiades surface topography (black dotted line). The aqueduct is reconstructed in grey. The black broken line represents the original undergound channel before its relative uplift. A ∼2 m vertical offset is visible at both ends of the undergound channel.

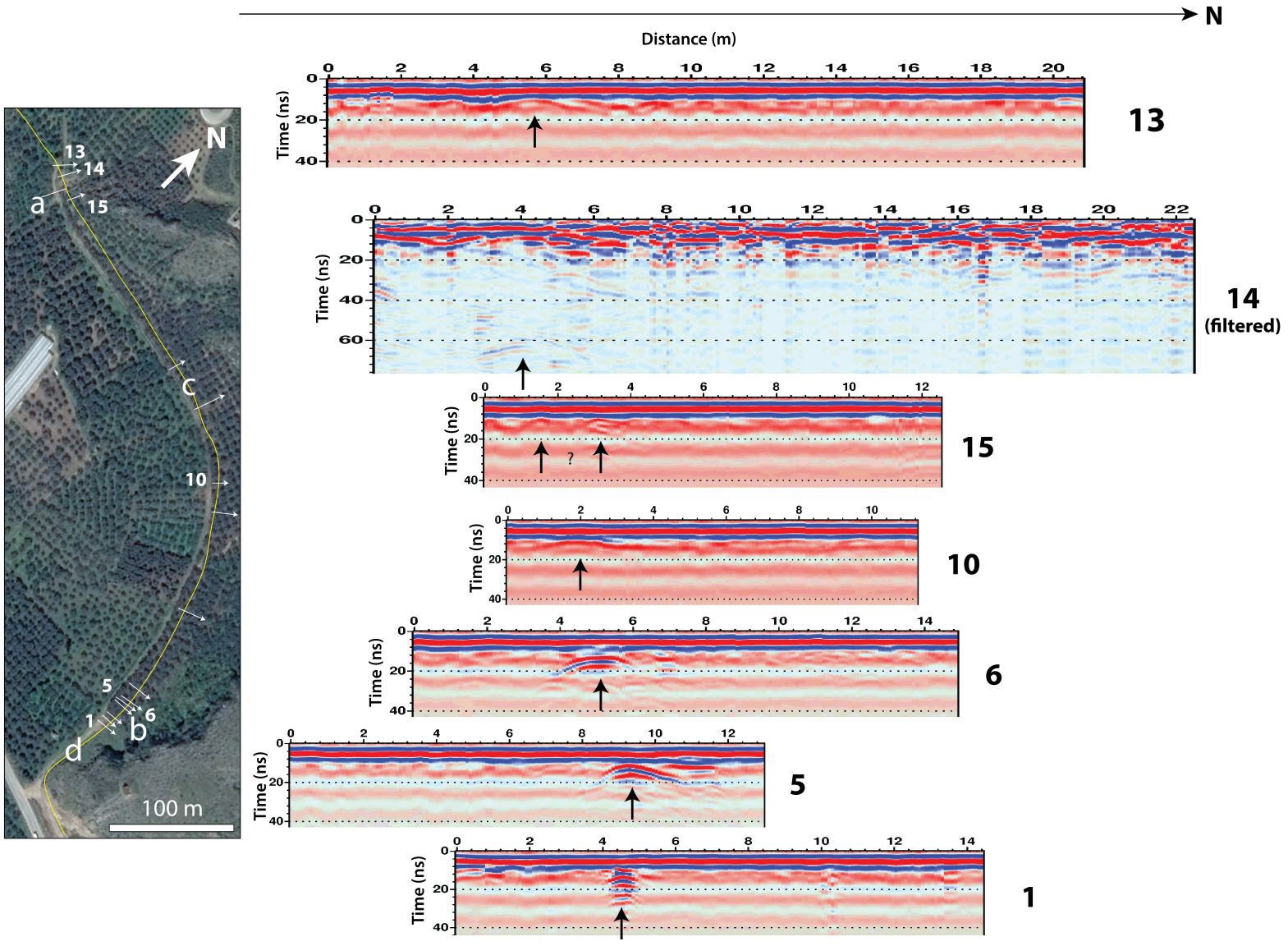

Figure D.25: GPR survey on the undergound aqueduct. The map on the left locates the aqueduct's channel in yellow and the transversal GPR acquisitions drawn as white arrows. The numbers correspond to different GPR profiles. The features photographed in Fig. D.26 are also located with letters. On the right are shown the GPR images on which the aqueduct is most visible (black arrows). To improve the visibility of deeper arrivals on profile 14, a different gain was applied and the plane wave arrivals were suppressed.

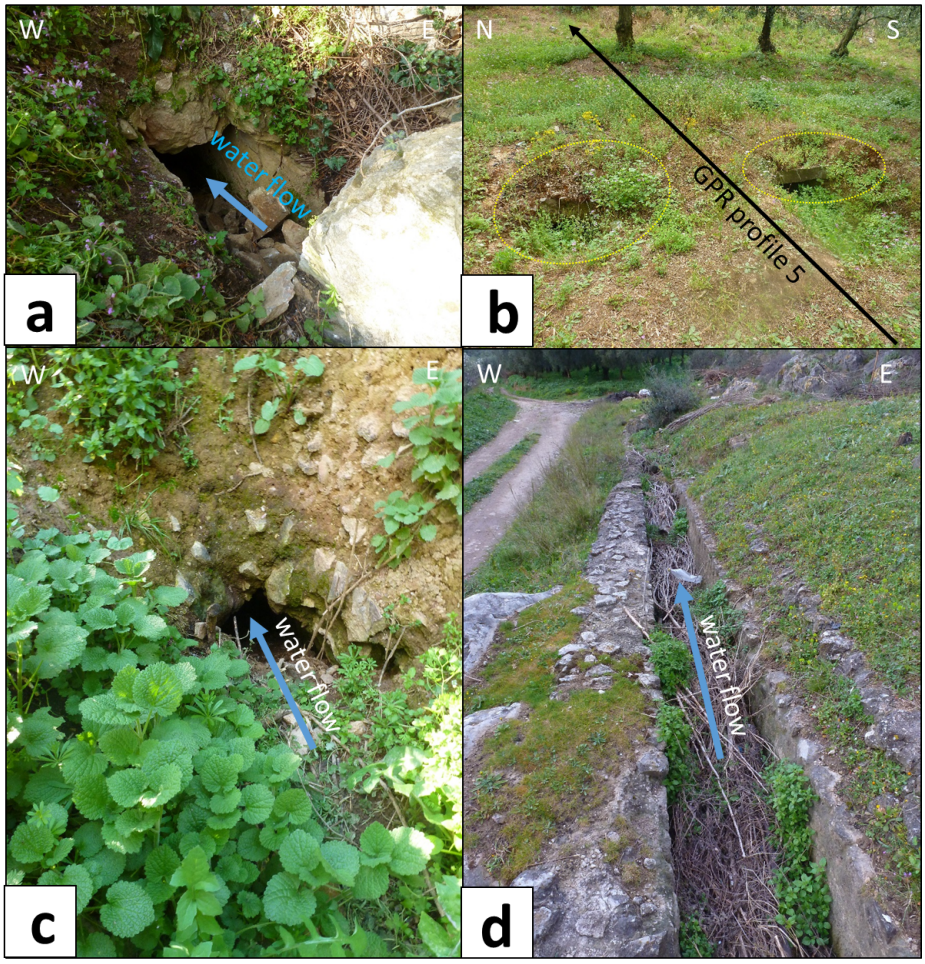

Figure D.26: Field photographs of the aqueduct east of Iznik. (a) Undergound channel dug in the carbonate massif. (b) Terracotta structure visible at the eastern end of the undergound section. (c) Undergound channel made visible by a hole in the ground. (d) The aqueduct upstream of the undergound section.

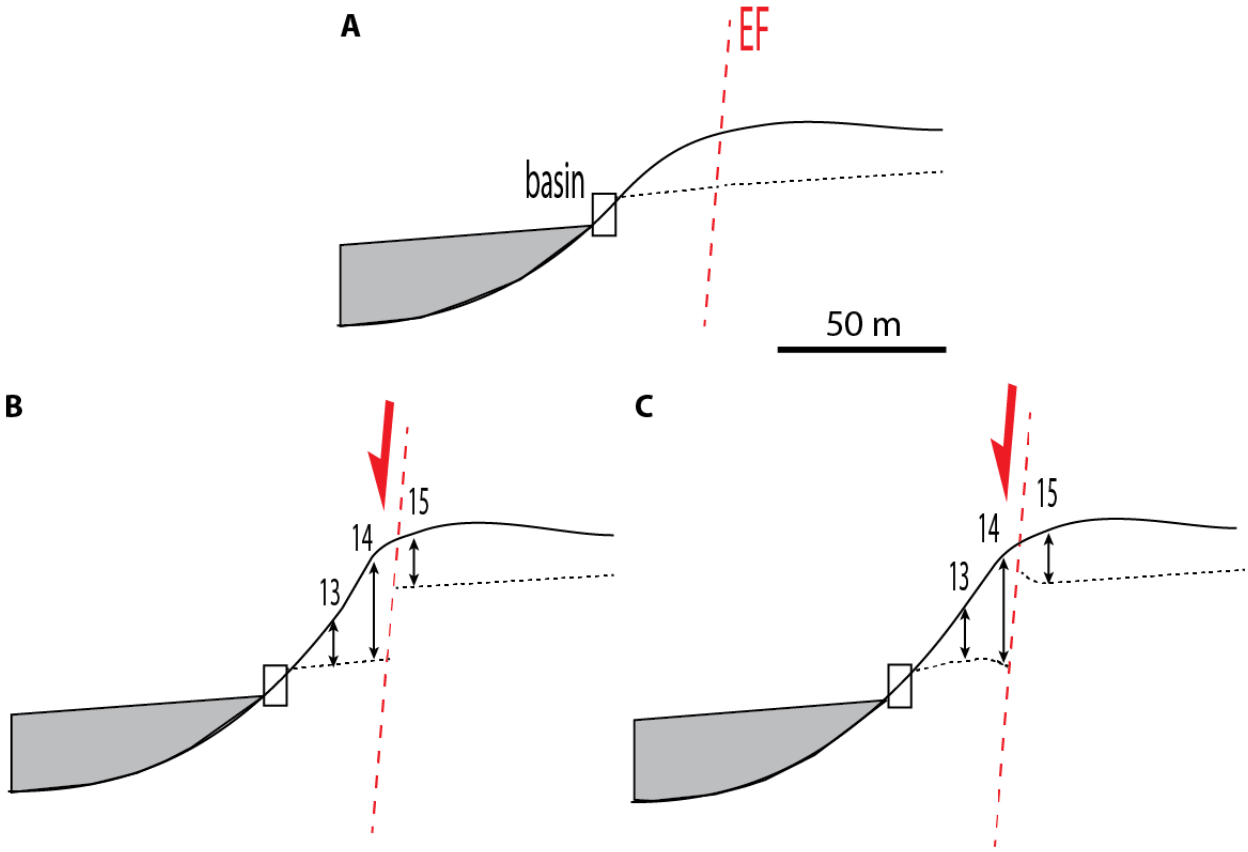

Figure D.27: Evolution of the aqueduct's geometry across the Elbeyli fault (EF) (a) Reconstructed geometry of the aqueduct before its vertical displacement on fault. The section of aqueduct built above the ground level is drawn in grey. The undergound channel is indicated with a broken line. The fault is drawn in red. The current geometry of the aqueduct is presented at the bottom (b,c). The GPR profiles located with their numbers. The larger depth of the channel observed on profile 14 can be explained by the local topography (b) but also by a bigger vertical deformation near the fault (c). The vertical scale is exaggerated.

The two vertical offsets mentioned above correlate with the supposed fault trace. At these two points of intersection, no remain of the aqueduct is visible today. The total length of the fault is about 7 km. An earthquake rupturing the whole fault length is expected to produce no more than 50 cm of displacement, with a maximum magnitude of Mw 6 (Wells and Coppersmith, 1994). This suggests that the ∼2 m offsets result from coseismic displacements on the Elbeyli fault during several historical earthquakes. The Elbeyli fault has never been documented as a significantly active structure and there is actually few clear evidence of recent faulting along-track, but the archeological markers presented here might indicate that this fault has the ability to slip conjointly with the MNAF during big ruptures or independently during smaller earthquakes.

D.2.7 Conclusions

Thanks to a stratigraphical study, we were able to propose a construction history for Iznik aqueduct, extending from the Roman period to modern times. The oldest masonries remaining may date back from Hadrian or Justinian's reign. In a later project, two specific structures, interpreted as a buttress and a repartition basin, were added and the specus was extensively rebuilt. A second period of construction is marked by a major shift in the materials used, abandoning limestones for well-cut travertines (phase 4). Around the 11th century, much of the facing of the aqueduct was rebuilt, probably after important damages, through several interventions reusing a significant amount of the former materials, theatre spoils and Turk gravestones. These reconstructions interestingly postpone a major earthquake in 1065 and the fights of the First Crusade in 1097. The last historical works date back from the Lascarid period with the use of a new regular framework with alternating courses of terracottas and quadrangular rubble close to the city gates. Modern restorations affected almost the whole length of the specus, and the portion close to the city was very recently restored in a Lascarid imitation style. The vertical deformation of the eastern section of the aqueduct evidenced the presence of an active normal fault bounding the carbonate massif east of Iznik. The center of the underground part of the building was uplifted by 2 m during several historical earthquakes.

D.2.8 Résumé

L'aqueduc d'Iznik fait ici pour la première fois l'objet d'une étude architecturale détaillée. Nombreux autour de la Méditerranée, les aqueducs étaient des infrastructures vitales dont l'étude peut fournir de précieuses informations sur l'histoire politique et économique des villes qu'ils alimentaient en eau, mais aussi sur la survenue de certains événements extrêmes comme les guerres et les catastrophes naturelles. Les vestiges de l'aqueduc d'Iznik, visibles sur presque 1,5 km de long, sont situés à l'est de la ville, entre la porte Lefke et la pointe sud-ouest du massif carbonaté qui entoure le village de Dereköy, où se situent probablement les sources de l'aqueduc. De manière générale, le chenal de l'aqueduc est aérien et soutenu par un mur en maçonnerie, constitué d'un noyau enserré entre deux parements. Le long de la pente du massif carbonaté, il présente une portion souterraine sur 450 m. Les informations historiques sur la constructions de l'édifice sont assez minces : il aurait été construit pendant le règne d'Hadrien au 2ème siècle ap. J.-C. et restauré sous Justinien au 6ème siècle, puis par Théodore I Lascaris au début du 13ème siècle. L'aqueduc semble avoir fonctionné jusqu'à la période contemporaine, possiblement au 19ème siècle.

La construction des murs de l'aqueduc a été analysée en suivant une approche stratigraphique développée et appliquée sur plusieurs bâtiments hydrauliques romains de France et d'Italie. En se basant sur les différents matériaux utilisés et leur mode d'assemblage, les murs ont été divisés en 43 unités stratigraphiques différentes. A l'échelle du bâtiment, nous avons aussi identifié 15 techniques de construction différentes, décrites et enregistrées dans une base de données. La plupart de ces techniques utilisent des moellons de calcaire massif et de travertin, des éléments architecturaux spoliés sur d'autres bâtiments de la ville, ainsi que des terres cuites. Les matières premières dont sont issus ces matériaux sont toutes présentes dans la géologie locale. Les différentes interventions identifiées n'ont pas pu être datées de façon absolue in situ mais des analogies avec les murs défensifs de la ville sont possibles pour les plus récentes. Les plus vieilles maçonneries visibles correspondent probablement aux constructions d'Hadrien ou de Justinien. Postérieurement, deux structures particulières, un contrefort et un bassin de répartition, furent ajoutées et le chenal fut complètement reconstruit. Un changement majeur est ensuite observé dans les matériaux utilisés avec une transition du calcaire massif vers le travertin. Une grande partie du parement fut restauré vers le 11ème siècle. Les reconstructions des Lascarides ont aussi été identifiées près des murs de la ville.

Les parties de l'aqueduc situées plus à l'est ont fait l'objet d'un relevé topographique précis par GPS RTK, couplé à plusieurs acquisitions au géoradar en profils transversaux sur la partie souterraine. Le chenal mesuré au GPS et visible sur plusieurs profils radar présente un décalage vertical d'environ 2 m en deux points de l'aqueduc. Ces décalages correspondent aux intersections de l'aqueduc avec une faille normale bordant le massif carbonaté et pourraient donc résulter du glissement sur cette faille lors d'un ou plusieurs séismes historiques.

D.3 3 historical earthquakes revealed on the middle strand of the NAFZ by an archeoseismological study in Iznik

D.3.1 Introduction

Documenting the calendar of the past earthquakes in tectonically active regions is an important step to determine their seismic hazard (Guidoboni and Stucchi, 1993; Bilham et al., 2001). In certain contexts, the knowledge of Holocene earthquakes is the only way to estimate the magnitude range expectable in a given area and the recurrence times between big earthquakes. It can be the case in poorly instrumented areas, when the deformation rate is too low to produce frequent earthquakes, or when no big rupture has occurred during the instrumental period. The most common tool to investigate past ruptures at these time scales is paleoseismological trenching, which allows to identify the last ruptures in the stratigraphy at a given point of the fault (McCalpin, 2009). However, one trench can only give local information, and the segmented character of many faults and the slip variability along-strike often makes it necessary to open several trenches in order to derive a significant earthquake catalog, which is expensive and time-consuming. In some contexts, trenching is hampered by the fact that the fault is not directly accessible (e. g. submarine faults) or that no single fault controls the earthquake pattern of the region studied.

Another complementary discipline, historical seismology, has been developed to build earthquake catalogs using written descriptions of seismic events (Ambraseys, 2000, 2002). Whereas paleoseismology is primarily concerned with the source of earthquakes (i. e. deformation localized along fault zones), historical seismology interprets the observable consequences (earthquake shaking) in the form of intensities felt at given locations, whatever the responsible fault and its mechanism. The compilation of several intensities dispersed on wide areas sometimes allows to derive the location of the epicenter and the magnitude using empirical laws (Gutenberg and Richter, 1956; Ambraseys, 1985; D'Amico et al., 1999; Hetényi et al., 2016). Historical seismology obviously relies on the existence of written documents for the region considered, which implies a certain degree of urbanization, cultural and political development, and is therefore limited for certain time periods and in certain places.

In the last decades of the 20th century, evidence of coseismic deformation found in the stratigraphy of archeological survey sites and on ancient buildings have been increasingly described and used to complement earthquake catalogs and even in some cases quantitatively constrain earthquakes thanks to numerical modeling (Korzhenkov and Mazor, 1999; Mazor and Korzhenkov, 2001; Hinzen, 2005). Even if no proper common methodology has been clearly defined for this kind of studies, this approach is generally called "archeoseismology". Although the interpretation of archeological evidence is delicate because possible traces

of earthquake are rarely unambiguous, it allows to document past earthquakes in regions without written archives, which extends the time scale of the catalog (Karcz and Kafri, 1978). The archeological record may also preserve smaller events that are hardly found in classical trenches (Rapp, 1986).

In this study, we apply this archeoseimological approach to the city of Iznik (ancient Nicaea), located 3 km north of the active fault segments of the middle strand of the North Anatolian fault (MNAF, Fig. D.28). Since the beginning of the instrumental period, this fault strand has been characterized by a very poor seismicity (Öztürk et al., 2009) and the small GPS network installed across the fault segment south of Iznik has not recorded any relative motion very close to the fault (Ozener et al., 2013b). However, the various available datasets documenting the pre-instrumental seismic activity strongly contrast with this modern quiescence. The historical record of ancient earthquakes having affected Iznik since 2000 years, as well as the few paleoseismological studies done along the MNAF in the vicinity of Iznik attest the occurrence of several major earthquakes on this fault strand during the last two millennia (Ambraseys and Finkel, 1991; Barka, 1992, 1993; Ambraseys and Jackson, 2000; Ambraseys, 2000, 2002; Özalp et al., 2003; Uçarkus et al., 2003; Dogan, 2010; Özalp et al., 2013). Moreover, the region presents several archeological clues suggesting past earthquake occurrence, such as the submerged basilica recently discovered in Iznik Lake, as well as the numerous traces of deformation and reconstruction on the city ancient buildings.

Despite this evidence of past earthquakes, a reliable assessment of seismic hazard for Iznik region has not been determined yet. By its close location to the MNAF and its numerous archeological remains from various periods, the city of Iznik is a promising working field for an archeoseismological study. The city was founded during the Hellenistic period and remained of great political importance during the Roman, Byzantine and Ottoman times (see Fig. D.29 for a summarized history of the city). The presence of many buildings and archeological remains from these different periods of time represents a good archive to investigate for past damage potentially linked with historical earthquakes.

The goal of this study is to use the ancient buildings in Iznik and its surroundings as records of past seismicity since ancient times. The compilation of many traces of potential earthquake damage provides a complementary dataset to historical seismology and paleoseismology in order to discuss the level of seismic activity of the MNAF during the last 2000 years. The dating of several independent buildings with their repairs having been affected confidently by earthquake shaking will allow us to complement the earthquake catalog. The archeoseismological data will also help to discuss the epicenter location and strength of the earthquakes responsible for the damage observable today in the city.

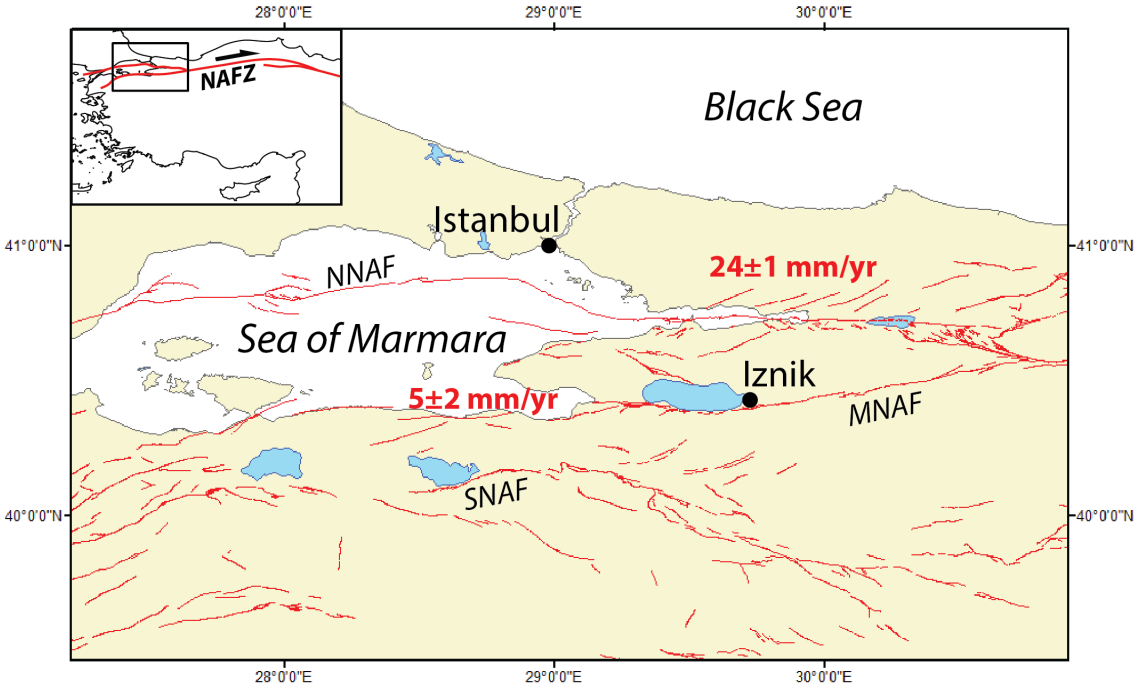

Figure D.28: General location of the study area in the Marmara region. The active faults, drawn in red, are taken from Emre et al. (2011). The slip rate values derived from GPS measurements are precised in red for the NNAF and MNAF.

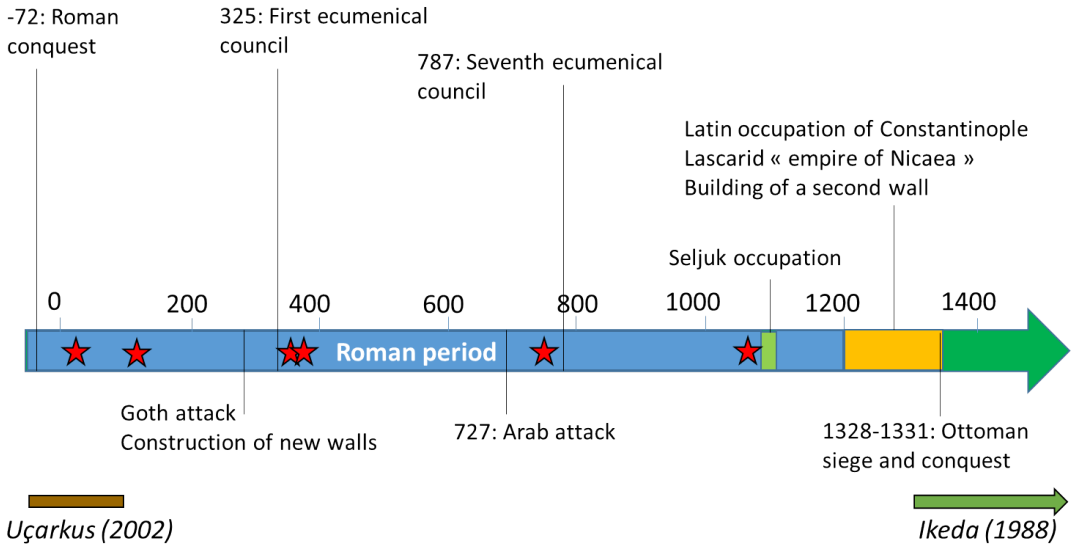

Figure D.29: Chronological frieze of Nicaea's history between 0 and 1400 AD. The red stars correspond to the historical earthquakes having damaged the city. The bars under the frieze correspond to earthquakes identified in paleoseismological trenches done on the MNAF.

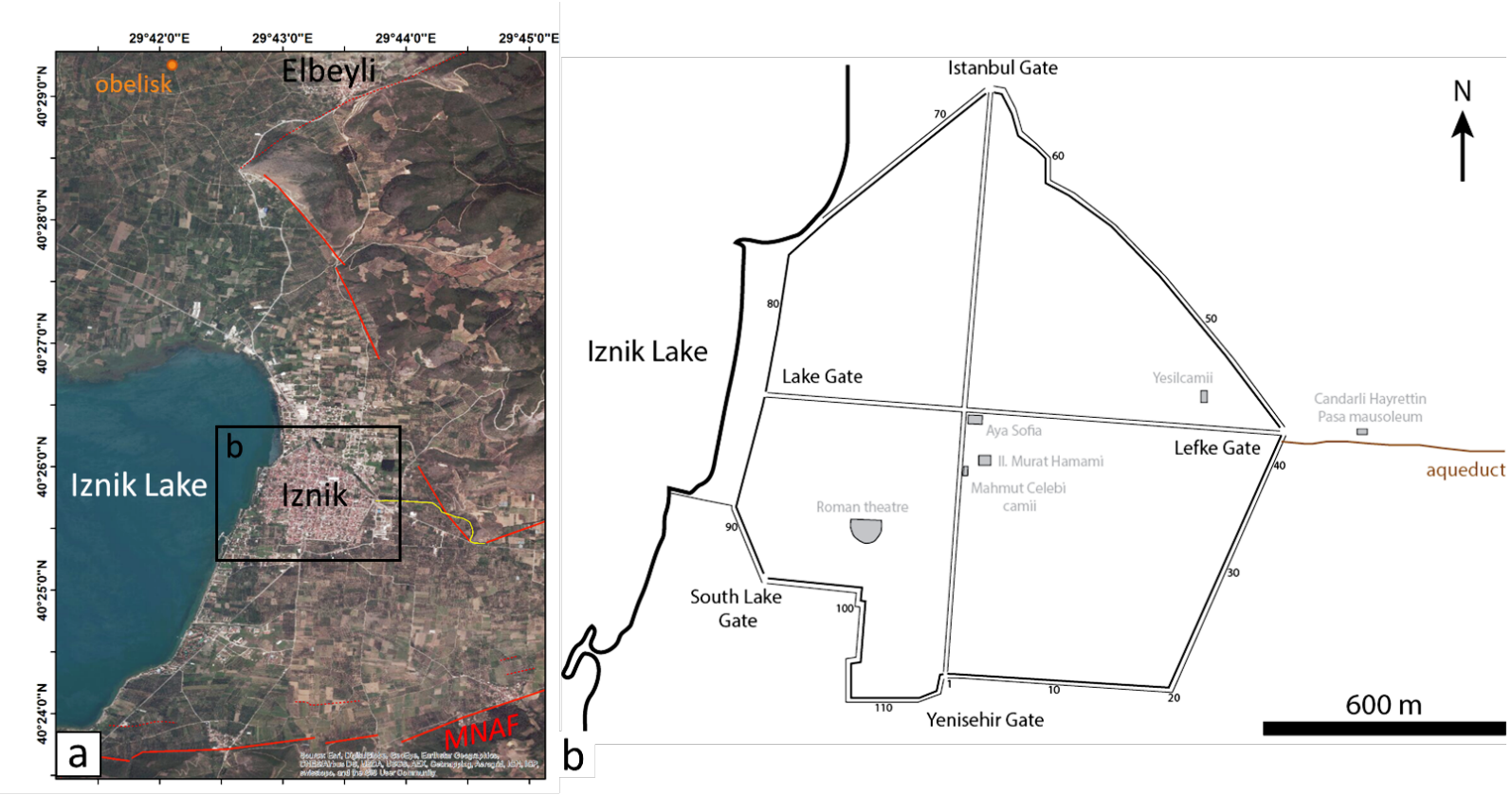

Figure D.30: (a) General location map with the active faults drawn in red and the aqueduct in yellow. (b) Simplified map of Iznik. The historical city is delimited by a double belt of defensive walls and was supplied with water by an aqueduct in the east. The other buildings investigated and mentioned in the text are drawn in grey. The numbers refer to the nomenclature of the towers used in the text, following Foss and Winfield (1986).

D.3.2 Description of the buildings studied

The selection of the buildings studied was done in a rather opportunistic way. We tried to include as many buildings as possible, but many historical remains in Iznik are either too destroyed or too much restored for the damage observations to be relevant.

D.3.2.1 The Roman obelisk at Elbeyli

6 km north of Iznik, near the village of Elbeyli, stands a Roman obelisk built during the 1st century AD in memory of C. Cassius Philiscus (Fig. D.30a). The column is made of five triangular prismatic stones lying on a rectangular pedestal (Fig. D.31a). Texier (1862) reports that a sixth decorative stone used to stand at the top of the column but presumably collapsed at an unknown period, evidently before the mid-15th century as the traveler Hans Dernschwam describes an obelisk with five stones (Grélois, 2004). Small offsets of several centimeters between the triangular stones suggest translation and rotation motions probably during seismic shaking (Fig. D.31b).

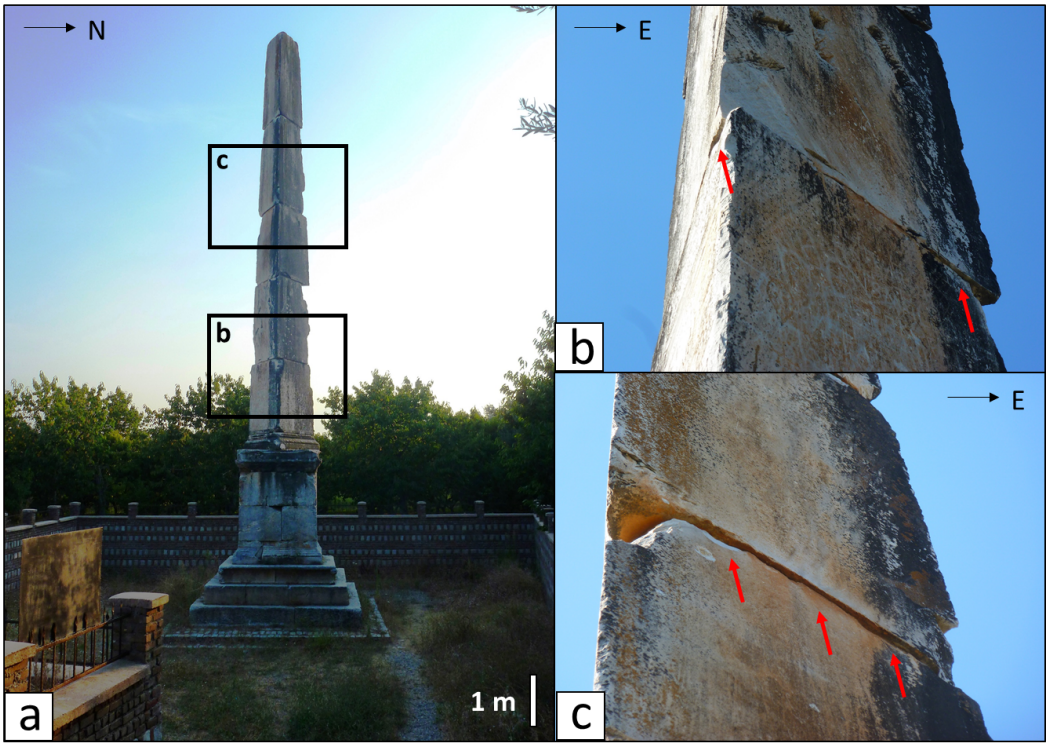

Figure D.31: (a) General view of the obelisk near Elbeyli village. (b, c) Detailed views of rotated and offset blocks. The red arrows point to the parts of the pictures where the deformation is most visible.

D.3.2.2 The aqueduct of Iznik

The remains of an aqueduct are visible in the east of Iznik, entering the city through Lefke gate (Fig. D.30). Most of the better preserved parts of this aqueduct extend from the city gate on 600 m with an E-W orientation. Further away from the city, the aqueduct runs along the southern border of a carbonate massif where its sources are located (Dereköy village). The aqueduct presents an underground section on 400 m. According to Sahin (1979), the aqueduct was built during the reign of Hadrian in the 2nd century AD. The Roman historian Procopius attests for a restoration of the building by Justinian in the 6th century (*De aedificiis*, V, 3). Later restorations were proposed by Foss (1996) and attributed to Theodore I Lascaris in the 13th century. The aqueduct of Iznik has only recently been studied in detail by Benjelloun et al. (in prep, see section D.2). Using a stratigraphical approach coupled with architectural analogies, they concluded that the earliest phases visible were likely to belong to Justinian's period and identified major restoration works around the 11th and 13th centuries (Fig. D.32).



Figure D.32: The aqueduct of Iznik close to the city's eastern gate.

D.3.2.3 The walls of Iznik

The defensive walls of Iznik are made of two belts surrounding the city (Fig. D.30b). They were quite extensively studied by Schneider and Karnapp (1938) and Foss and Winfield (1986), whose interpretations were summarized in Fig. D.33. We use here the same numerotation system to locate the towers (Fig D.30b). The numbers begin at Yenisehir Gate in the south and continue counterclockwise. The inner belt was first built during the 3rd century AD, after Gothic attacks in 256-257. The construction started under the rule of Gallienus (253-268) and ended during the reign of Claudius Gothicus (268-270). In this first configuration, the walls were 9 m high and interrupted by semi-circular brick towers each 60-70 m (Fig. D.34a). The remains of these early walls can still be seen at several points. Due to Arab attacks in 716-727 and an earthquake in 740, the walls were partly destroyed and rebuilt afterwards by Leo III (717-741, Fig. D.34b). The walls were then elevated of 1.8 m high, apparently to compensate for some rise of the circulation level, maybe due to sinking. These reconstructions mainly affected the eastern and southern parts. Another important reconstruction campaign followed in 858 under Michael III. New bricks towers with a stone base were added, especially in the eastern and southern sides (Fig. D.34c). After a period of peace, the 10th and 11th century saw the walls damaged on several opportunities: seizure of the city by the rebel Bardas Skleros in 978, destructive earthquake in 1065, seizure by the rebel Nicephorus Melissenus followed by the Turks after 1080, attack in 1097 during the first Crusade. The same year, the Turks gave the city back to the Byzantine ruler Alexios I Komnenos, who carried out a few reconstructions. Other reconstructions of the Komnenoi are dated to the late 12th century (1143-1185). The last major reconstructions occurred during the Lascarid period, during the reigns of Theodore (1205-1222) and John Vatatzes (1222-1254) who built the outer wall and elevated the inner fortifications (Fig. D.34d). Later rebuilding is known during the Palaeologue period until 1331 when the city surrendered to the Ottomans after a long siege.

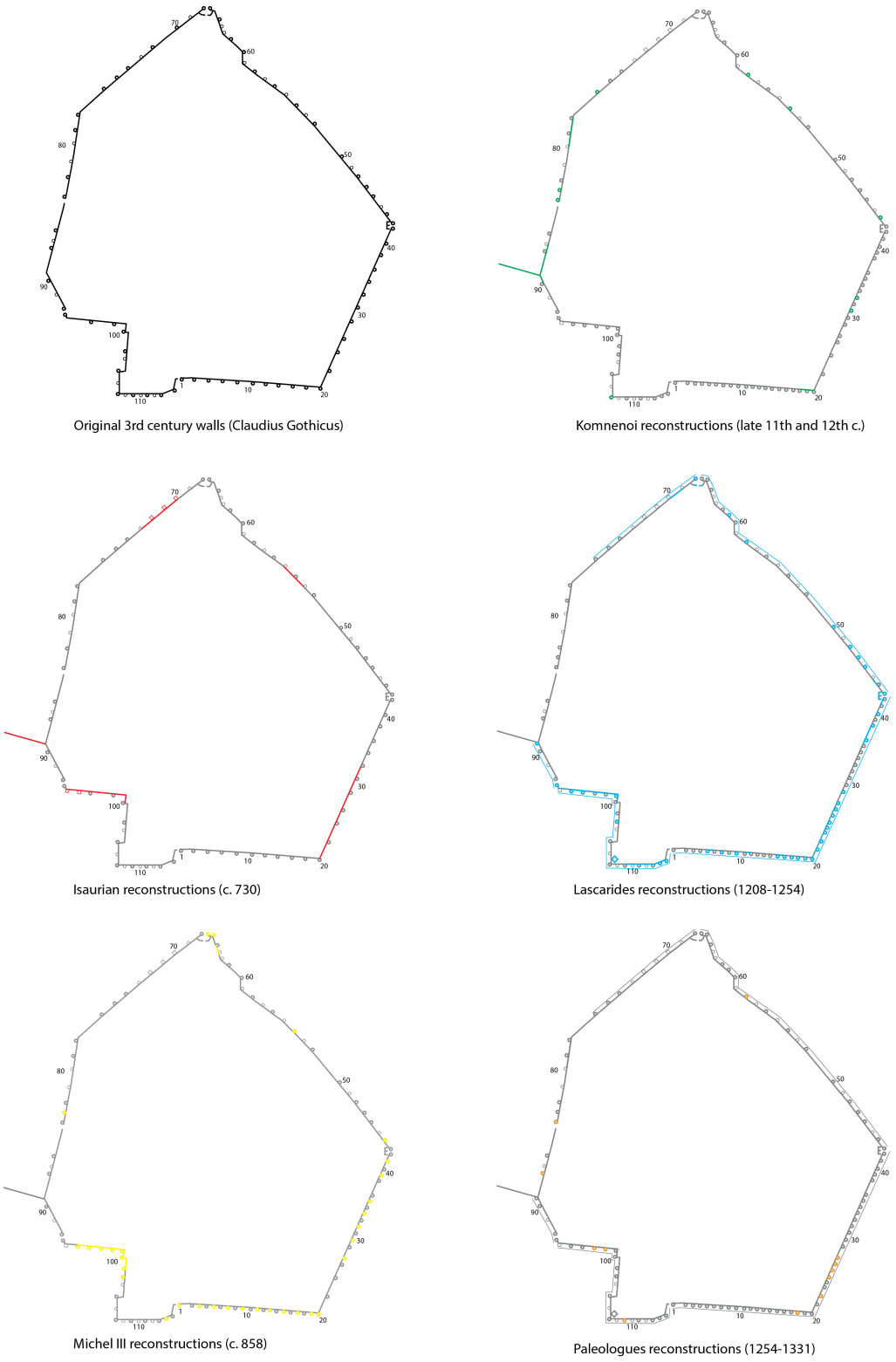

Figure D.33: Summary of the construction history of Iznik walls, after Schneider and Karnapp (1938) and Foss and Winfield (1986). After the construction of the walls in the 3rd century, the 164 successive interventions and restoration works are drawn in color. The state of the walls preceding each intervention is drawn in grey.

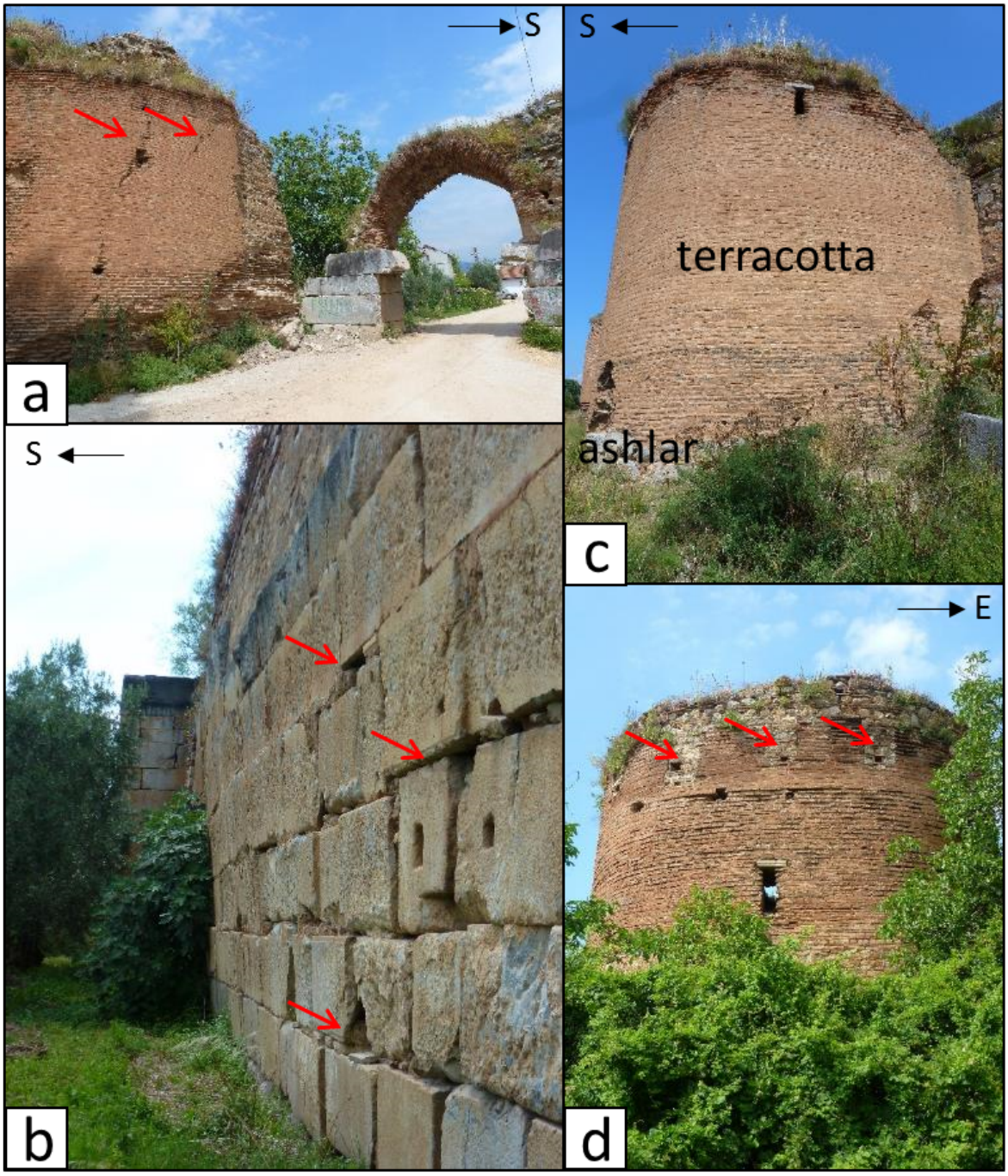

Figure D.34: Photos of Iznik inner wall. The towers are numbered according to their location (see Fig. D.30). Visible Earthquake Archeological Effects (EAE: cracks, corner expulsion...) are located with red arrows.(a) T92 and South Lake Gate, built in the 3rd century AD. (b) T94 and adjacent wall in big marble blocks, an 8th century reconstruction. (c) T17, combining a terracotta superstructure on a large block base, built in the 9th century AD. (d) T97, showing a simple terracotta superstructure from the early 13th century. The crenellations were blocked during the following reign of John Vatatzes.

D.3.2.4 Other buildings

A few observations were collected on other buildings in the city (Fig. D.30). We were able to see several deformations and possibly "paraseismic" techniques in Iznik theatre, built during the 2nd century AD when the writer Pliny served as governor of Bithynia (11-113 AD), and spoiled significantly as an open air quarry in later periods. Several deformations were also described in Aya Sofia, a former church built by Justinian, restored in the 9th, 11th, and 13th centuries, and converted into a mosque by Orhan shortly after the Ottoman conquest (Brounoff, 1925; Schneider, 1943). This church is famous for hosting the seventh Ecumenical Council in 787. We also found deformations in several ottoman buildings: Yesilcamii mosque built between 1378 and 1391, Mahmut Celebi mosque built in 1442, and Murat II (1421-1451) hamam built in the first half of the 15th century. Other traces of damage were encountered on a few ottoman tombstones located in Candarli Hayrettin Pasa mausoleum (1387). We can also include in our archeoseismic survey the Byzantine basilica which was discovered in Iznik Lake close to the shore (see section E). It was built between the 2nd and 4th centuries AD, hosted the first Ecumenical council in 325 and was probably destroyed before the seventh council in 787 which took place in Aya Sofia. The stratigraphy of the sediments on this site also suggests a disturbing event posterior to the early 15th century.

D.3.3 Inventory of the archeoseismological observations

D.3.3.1 The archeoseismological approach

Archeoseismology is the study of ancient remains as archives of past seismicity. Appeared in the last decades of the 20th century, this young discipline is still strengthening its methodological bases but has already provided interesting results in several study cases around the world. The main principle of an archeoseismological investigation is to look for traces of past earthquake deformation in archeological features, which are commonly called Earthquake Archeological Effects (EAE). A great diversity of potential EAE can be studied and interpreted as seismic evidence (Rodríguez-Pascua et al., 2011): offset buildings, rotated masonry, fallen columns, dropped ashlars... These EAE can be grouped into three big categories: on-fault, off-fault, and postseismic reconstruction. On-fault EAE happen when an archeological structure is crossed and deformed by an active fault. Once the total deformation has been precisely measured, this kind of EAE enables to directly compute a slip rate on the fault by dividing the offset measured by the age of the structure. Off-fault EAE represent the most numerous archeoseimic observations and happen when a building is not located precisely on an active fault but has been deformed or damaged because of ground motion during an earthquake. Finally, we can include in the EAE the evidence of postseismic reconstructions which intend to repair a building damaged during an earthquake and/or to make it more resistant to future earthquakes. It is to be noted that for the last two

categories, it is usually difficult to find unambiguous seismic evidence because the observed EAE may very often be the result of many other causes than earthquakes (Karcz and Kafri, 1978). Therefore, one observation at a single location can rarely prove the occurrence of an earthquake but only the gathering of many independent observations on the largest area possible can lead to a paleoearthquake scenario with a good level of confidence.

In Iznik and its surroundings, systematic archeoseismic observations were made on the remains described in Section D.3.2 (Fig. D.36, D.37 and D.38). Each EAE identified was described and quantified when possible (azimuth of the damaged structure, azimuth and strike of the deformation, amount of displacement, see Fig. D.35 for the definition of terms). For each EAE, we also indicate the probability of seismic origin using a simple quality factor between 1 and 3. Quality 1 means that the deformation observed is probably of seismic origin and that other causes (e. g. anthropic damage, natural decay, soil instability) can be reasonably discarded. Quality 2 means that the deformation potentially originates from coseismic shaking but that a few other processes might be responsible as well, though less probable. Quality 3 means either that the seismic origin is dubious or that many other processes may be invoked to explain the observed deformation. Table D.1 displays several examples of non-seismic mechanisms that can produce features similar to EAE. In practice, we attributed the quality 3 to a given EAE when more than one of these mechanisms could be invoked with a high probability. The damages were also classified on a damage scale ranging from D1 to D5. D1 corresponds to very slight damage (e.g. a few small cracks). D2 corresponds to moderate damage (e.g. cracks in many walls, facing collapse). D3 corresponds to important damage (deep fractures in walls, collapse of upper parts). D4 corresponds to very important damage (e.g. partial wall collapse). D5 corresponds to a complete destruction of the building. The buildings investigated were also classified on a vulnerability scale (Grünthal and Levret, 2001).

Many EAE observed in Iznik were constrained in time relying on the available historical and archeological information from previous works, the new chronology of the aqueduct's construction analyzed in section D.2 and the dating of samples of construction material. In general, the earliest date for the construction of the damaged structure gives the earliest year of occurrence for the EAE (*terminus post quem*). When the EAE is associated to repairs posterior to the damage, the age of the repairs gives the latest possible year of occurrence for the EAE (*terminus ante quem*).

On several EAE, construction material (brick, mortar) was sampled in the original structures and the repairs to constrain the date of damage. Carbonate concretion deposits on the aqueduct formed during potentially coseismic massive leakage episodes were also sampled to date the associated damage (Fig. D.37f).

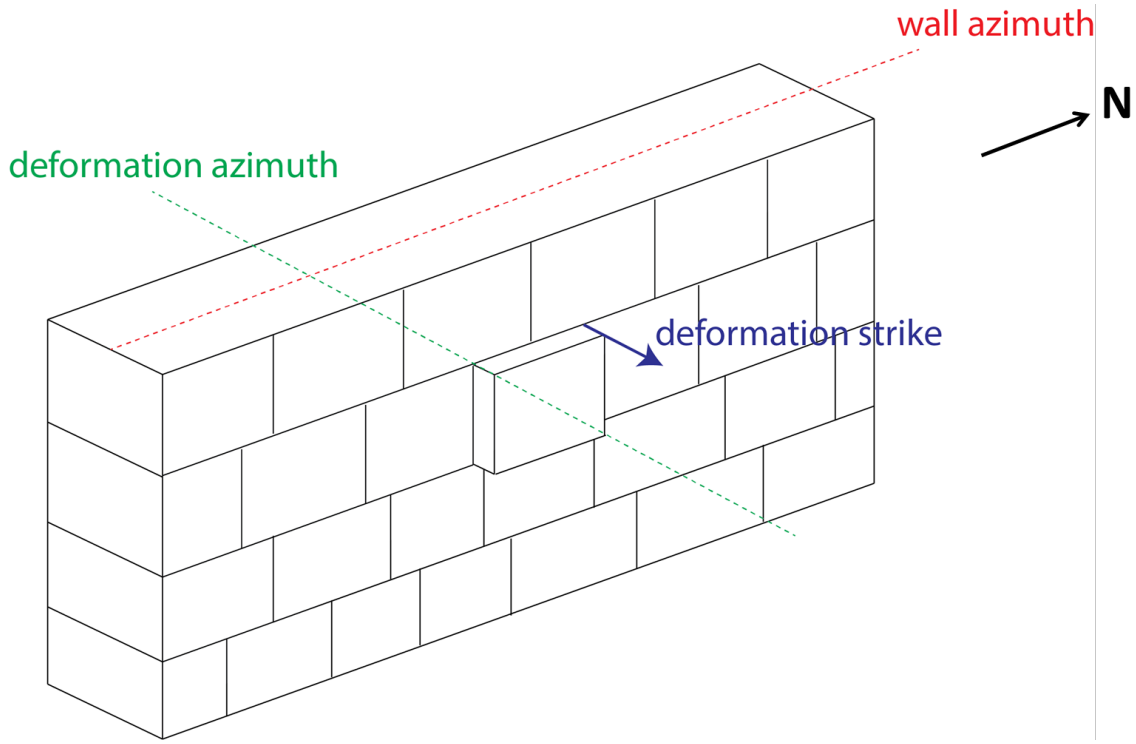

Figure D.35: Schematic representation of an ashlar wall with one expulsed block. We define the wall azimuth as the angle (0-180 ˚) between the direction of the north and the orientation of the wall (red). The deformation azimuth is the angle (0-180 ˚) between the north and the direction of the deformation (green), in the case of an oriented deformation. When possible, we also measure the strike of the deformation (0-360 ˚, blue). In this example, the wall azimuth is 0, the deformation azimuth is 90, and its strike is 90 (i.e. eastward).

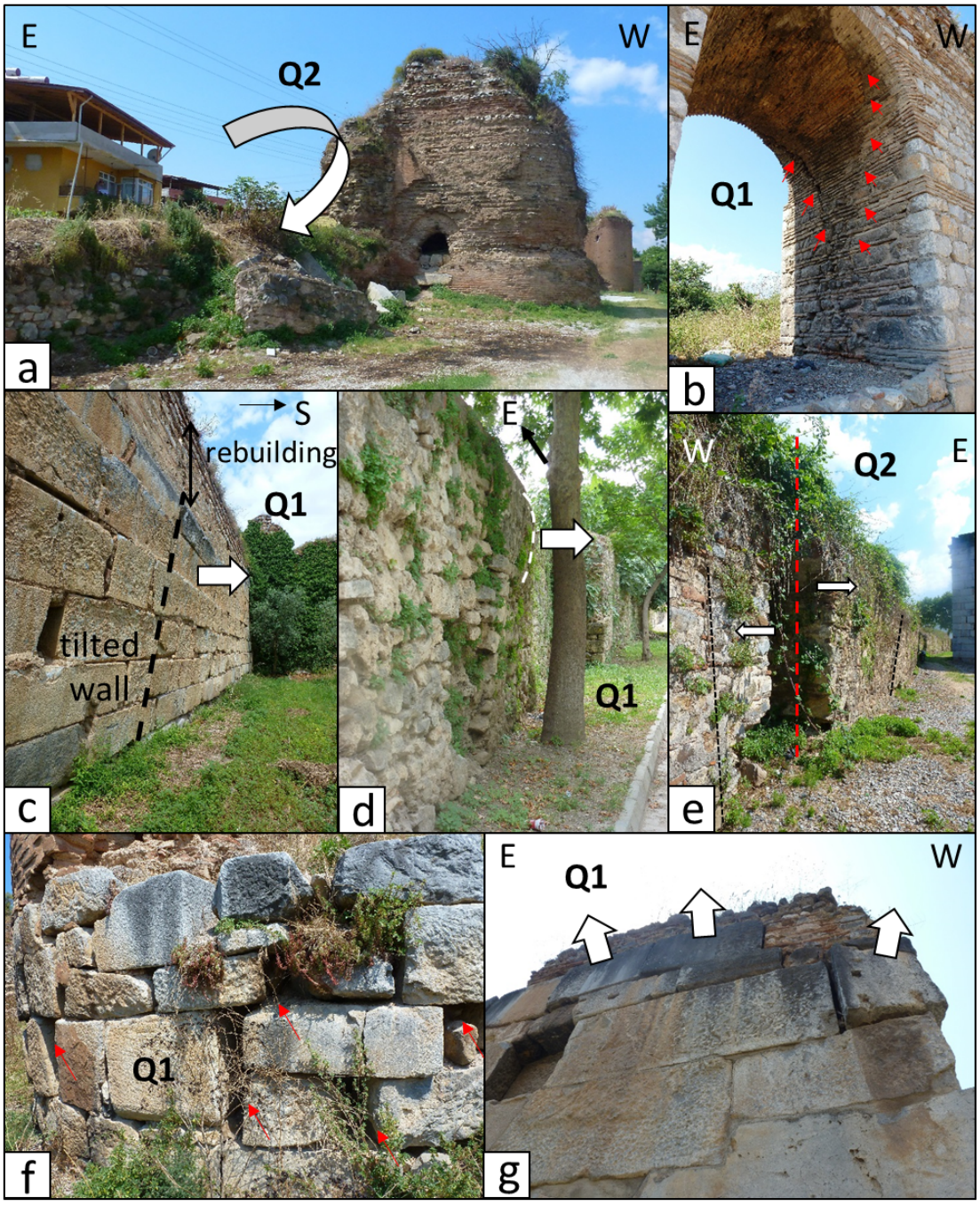

Figure D.36: Examples of EAE in Iznik. The white arrows indicate the deformation azimuth and strike. The quality category is precised on each picture. (a) Collapsed wall in the northwestern section (vulnerability B). (b) Conjugated cracks in a vaulted passage of the inner walls. (c) Tilted base of wall (vulnerability C), the upper part collapsed and was rebuilt in a very distinct masonry. (d) Warping of the upper part of the aqueduct (vulnerability A). (e) Offset walls around a vaulted door in the outer walls, both walls show tilting in opposite directions (vulnerability A). (f) Dislocated ashlars at the base of a tower; half of the tower above is collapsed (vulnerability B). (g) Pushed and rotated ashlars of the inner Istanbul Gate (vulnerability C); note the posterior rebuilding in masonry.



Figure D.37: Examples of EAE in Iznik (continued). (a) Pushed and tilted ashlar on a vaulted passage in the theatre (vulnerability B). (b) Pushed stair block in the theatre. (c) Expulsed block corner on a tower of the inner walls (vulnerability B). (d) Dropped central ashlars on an arch of Yesilcamii mosque (vulnerability C). The damaged arches were later reinforced with transversal iron bars, then wood beams. (e) Laterally displaced decorative block of Yesilcamii. (f) Massive carbonate concretions due to water leakage along cracks on the aqueduct's facing (vulnerability A).

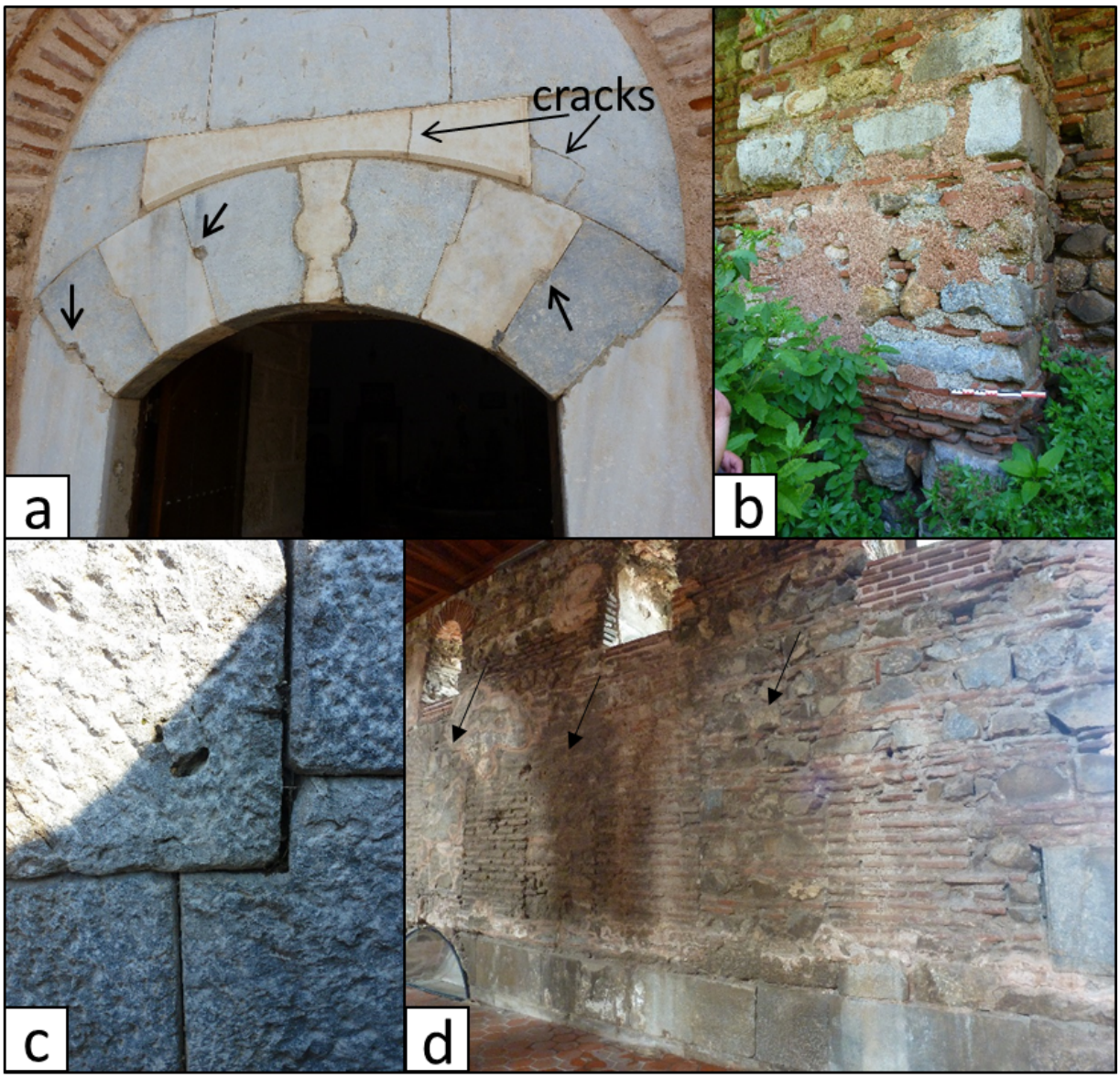

Figure D.38: Examples of potentially earthquake-related constructions. (a) Arch with imbricated ashlars, bearing traces of damage and posterior cementation on Murat II hamam. (b) Buttress built against the western wall. (c) Imbricated ashlars in a theatre wall. (d) Walled windows on the northern wall of Aya Sofia.

Type	Examples
Subsoil processes	Differential soil settlement, changes in moisture content, gravitational sliding
Natural decay	Leaching or weathering of the foundation materials over time
Other hazards	Landslide, flood, slow tectonic motion
Anthropic factors	Deliberate damage, military operations, bad quality building
Vegetation	Growing roots

Table D.1: Possible non-seismic causes for the damages typically encountered in archeoseismological studies, compiled after Karcz and Kafri (1978); Ambraseys (2006); Galadini et al. (2006); Caputo and Helly (2008).

D.3.3.2 Results

D.3.3.2.1 Location of the damage The locations of the 280 observed damages are shown in Fig. D.39. As far as the defensive walls are concerned, the observations were especially done on the inner walls (almost 4 observations every 100 m in average) and the outer walls seem much less affected (less than 1 observations every 100 m in average). The damage observed are in general regularly distributed all along the inner walls. In some areas the density of observations is much lower. This can be the case when the remains have disappeared or are too scarce today, for example west of the city. In other areas, the dense vegetation or the presence of private areas near the walls prevented the survey, as was the case in the northeastern section between towers 46 and 50, and in the southwestern section between towers 95 and 104.

D.3.3.2.2 Azimuth of the damaged walls The different walls investigated were classified according to their azimuth in Table D.2. In this table, the relative repartition of the different wall azimuths were compared to the relative number of EAE found in these different wall azimuth ranges, no matter the azimuth of the deformation. It can be noticed that the results do not change significantly when data of lower qualities are included, and we display on Fig. D.40 the result for the first quality. If all the walls were affected in the same way whatever their azimuth, the bars and the line should show the same distribution. This is the case for the E-W and NW-SE oriented walls that show a correspondence between the relative amounts of EAE and the lengths of the walls affected. In contrast, we can see that the N-S oriented walls bear much more EAE than what could be expected from their length: they locate a third of the walls' EAE whereas they represent only 12.7% of the total wall length. Inversely, the NE-SW oriented walls are underrepresented in terms of EAE.

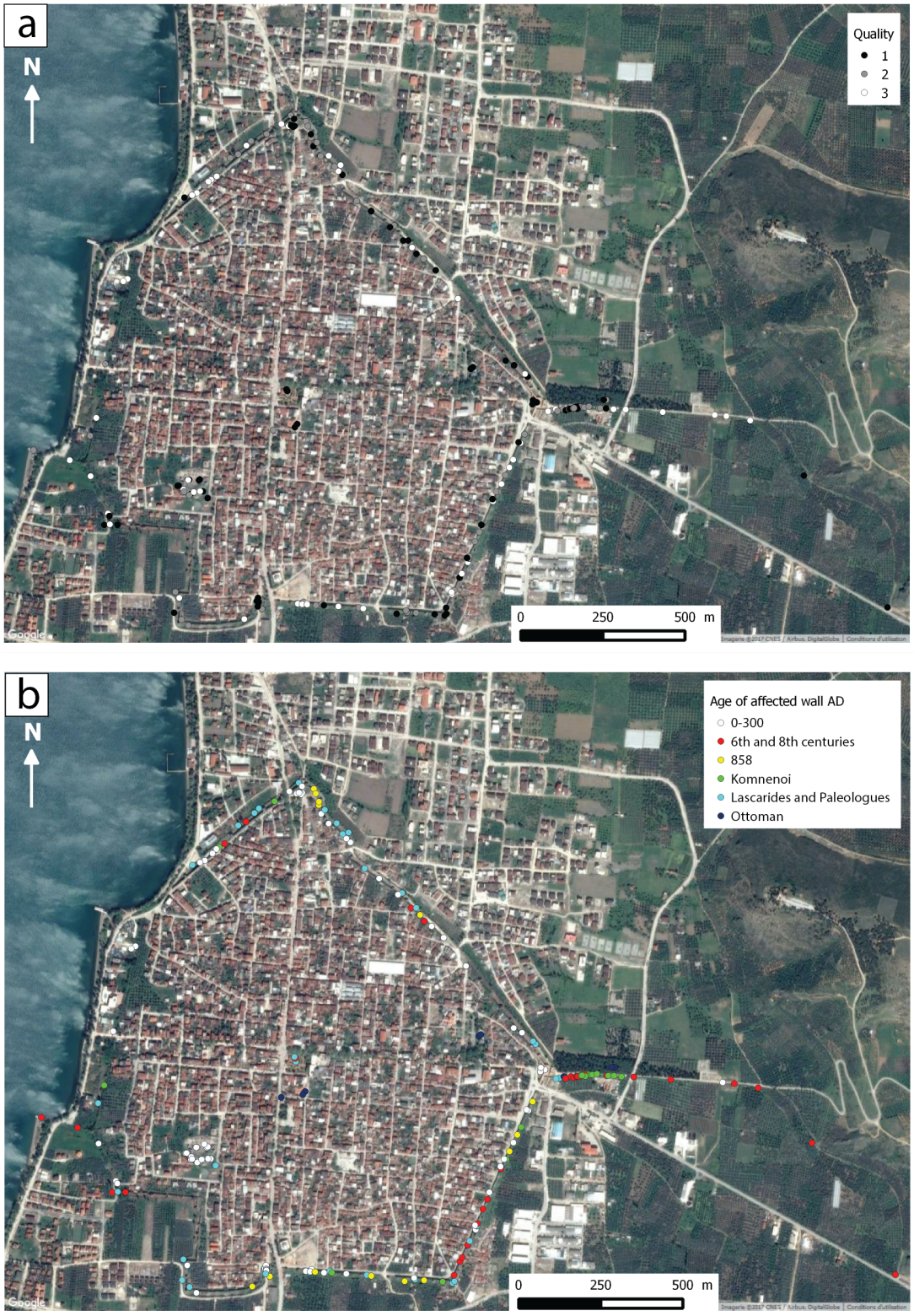

Figure D.39: Inventory of the EAE in Iznik, classified by quality (a) and by age of the wall affected (b).

Azimuth	**Length (m)**	**%Length**	**Q1**	**%Q1**	**Q1+Q2**	**%Q1+Q2**	**Q1+Q2+Q3**	**%Q1+Q2+Q3**
N-S	1124	12.7	40	31.7	63	30.9	72	26.9
NE-SW	2478	28.1	14	11.1	25	12.3	41	15.3
E-W	3319	37.6	52	41.3	82	40.2	111	41.4
NW-SE	1912	21.6	20	15.9	34	16.7	44	16.4

Table D.2: Length of walls and EAE of different qualities for each wall azimuth range. The percentages in length and EAE were computed on the total wall length and total number of EAE in each quality class respectively.

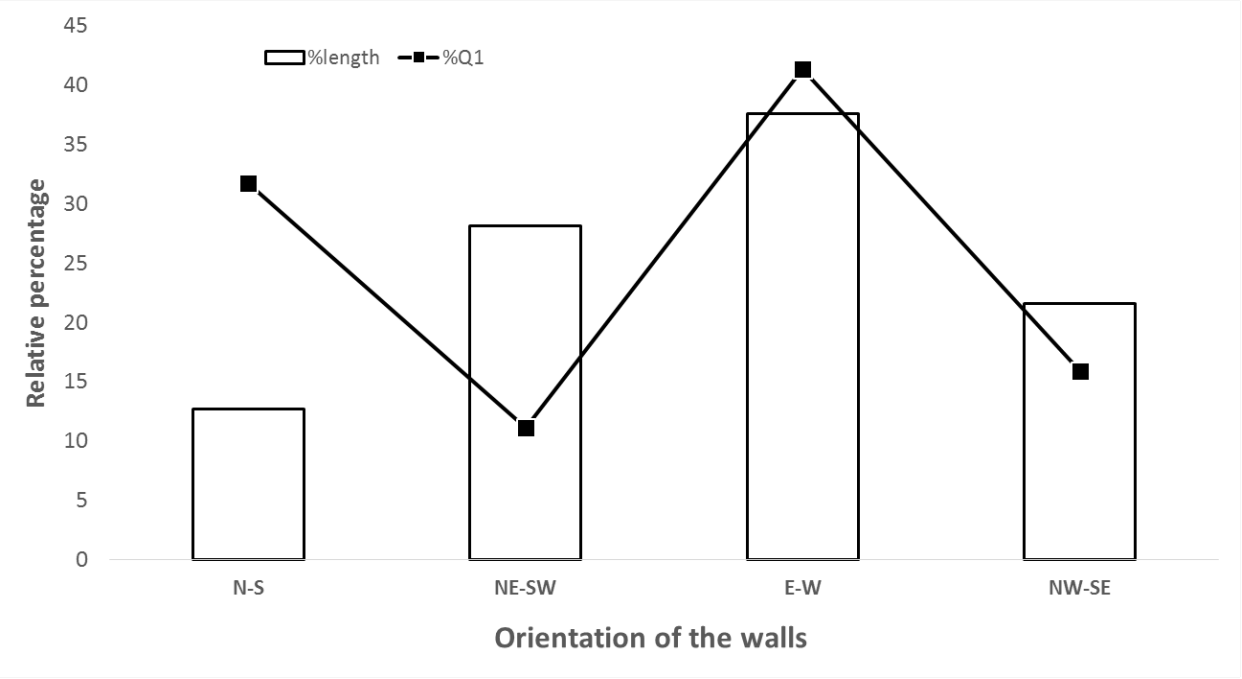

Figure D.40: Comparison between the relative distribution of wall length (bars) and quality 1 EAE (line) for different azimuths of walls. The percentages in length and EAE were computed on the total wall length and total number of EAE in each quality class respectively.

D.3.3.2.3 Oriented deformations 118 of our observations present an oriented pattern (e. g. direction of collapse or expulsion). Fig. D.41a shows the distribution of these azimuths. A clear, dominant, N-S azimuth appears, representing 30% of the observations. This actually mirrors the larger amount of walls oriented E-W mentioned in section D.3.3.2.2 When the strike of the damage is considered (Fig. D.41b), we can see that for almost all the azimuth ranges, deformations exist in both directions, but the deformation oriented NE-SW are characterized by an exclusive NE strike. We present in Fig. D.42 the relationships between the azimuths of the walls and the damage. Most of the oriented deformations show a strong correlation with the wall azimuth: they are either perpendicular to the wall (out-of-plane) or parallel (in-plane).

D.3.3.2.4 Age of the damaged walls The earliest dates of construction of the walls affected for each EAE are indicated on Fig. D.39b. The earliest EAE are found almost all around the inner wall and in the theatre. Logically, these early EAE are absent in the sections which were extensively rebuilt in the 8th century (Fig. D.33). These sections were still affected by several later deformations, as well as the other reconstructions until the 13th century. The aqueduct also shows a significant number of EAE from all periods. EAE from

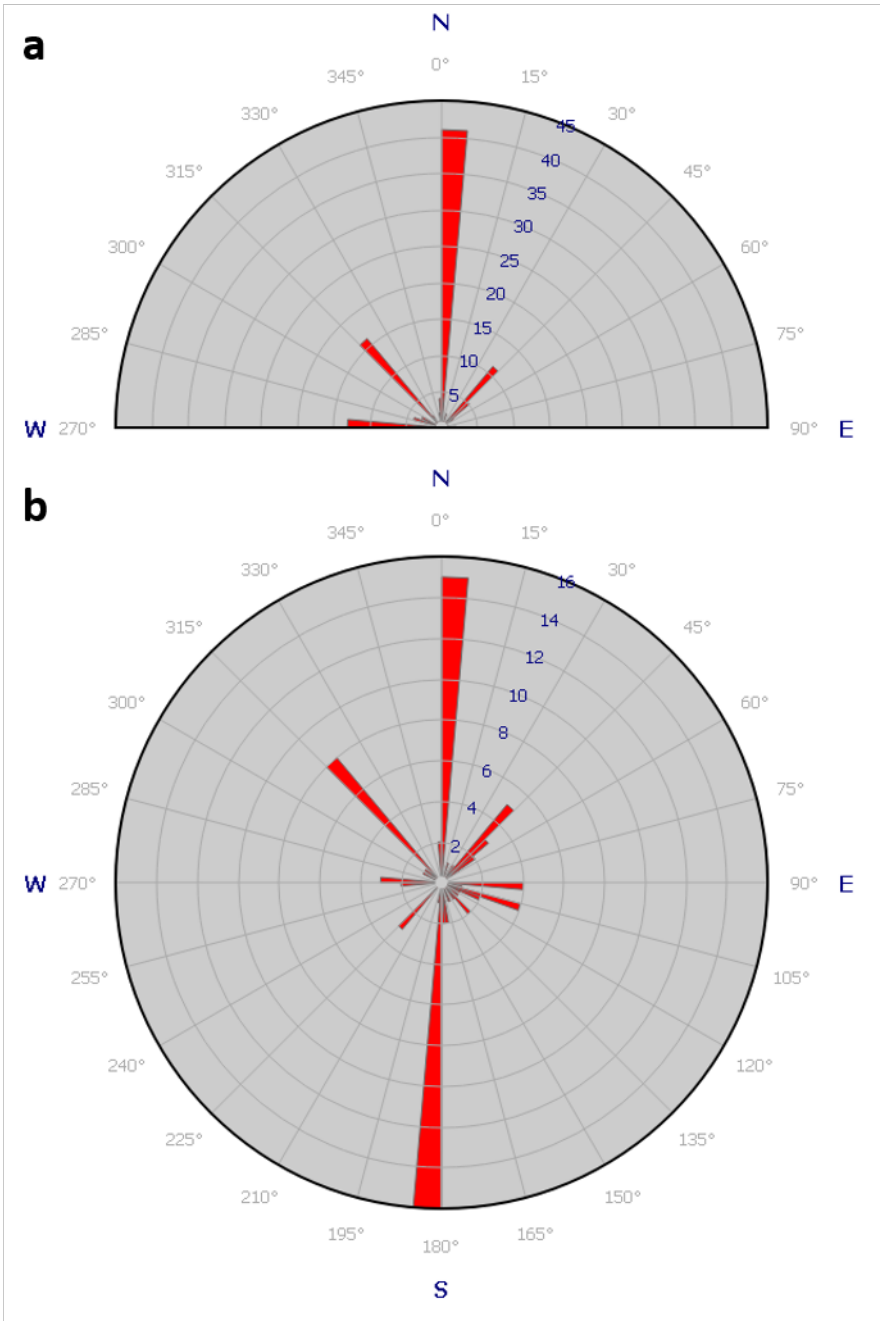

Figure D.41: Rose diagrams of the azimuths of damage observed in Iznik (a, 118 EAE) and the strikes measured (b, 85 EAE). Note the prominent N-S azimuths.

the ottoman period were found especially intra muros on the mosques and the bathhouse. As mentioned in the preceding section, the amount of EAE seems much smaller on the outer wall, which seems coherent with the fact that it is one of the latest buildings of the

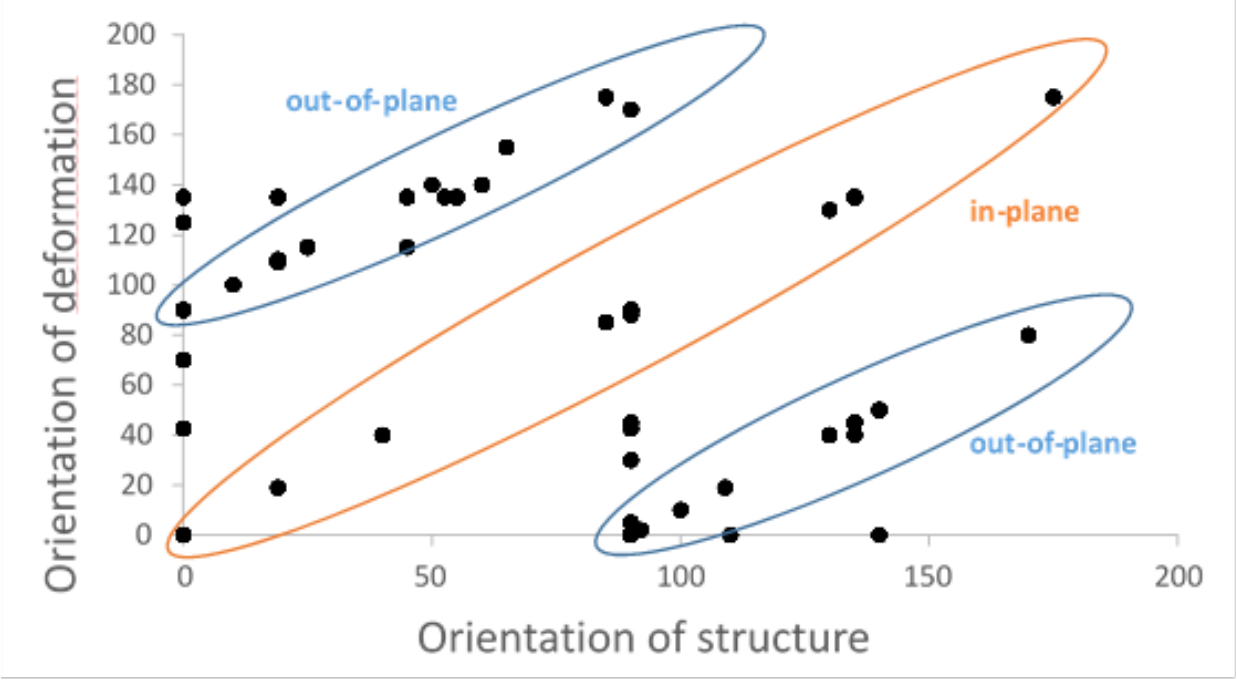

Figure D.42: Azimuths of the damage plotted against the azimuth of the wall affected. Note the general correlations between the two values. This correlation is linear for the in-plane deformations (i.e. they are parallel to the wall) and affine with a ±90 shift for the out-of-plane deformations (i.e. they are perpendicular to the wall).

Byzantine period.

D.3.3.2.5 Repairs and time constraints on deformation episodes The repairs identified in Iznik are shown in Fig. D.43 according to their date. The repairs were mainly dated relying on the age of the repaired structure and the technique used in the repair. We could find repairs in all the major construction periods of the city from the 9th century to the ottoman times. For the earlier periods, we could only find possible seismoresistant techniques of construction in the theatre with the use of polygonal imbricated ashlars (Fig. D.38c, Hinzen and Montabert, 2017). Analogous techniques, called "interlocking" or "clamp structures" have been documented in other Mediterranean sites and also in pre-Columbian buildings in Peru and Mexico (Garduño-Monroy et al., 2012; Fig. D.44). Most of the repairs, dating back from the Komnenoi (late 11th and 12th century) and the Lascarides or Paleologues (13th century) can be found on the inner walls and the aqueduct. It can be assumed that the repairs concerned especially buildings of public importance, while other damaged buildings were likely to be abandoned or entirely rebuilt. This could explain the scarcity of repairs from earlier periods. For the ottoman and modern times, several repairs were made on buildings in the city and some towers and parts of the walls have been

restored, probably quite recently.

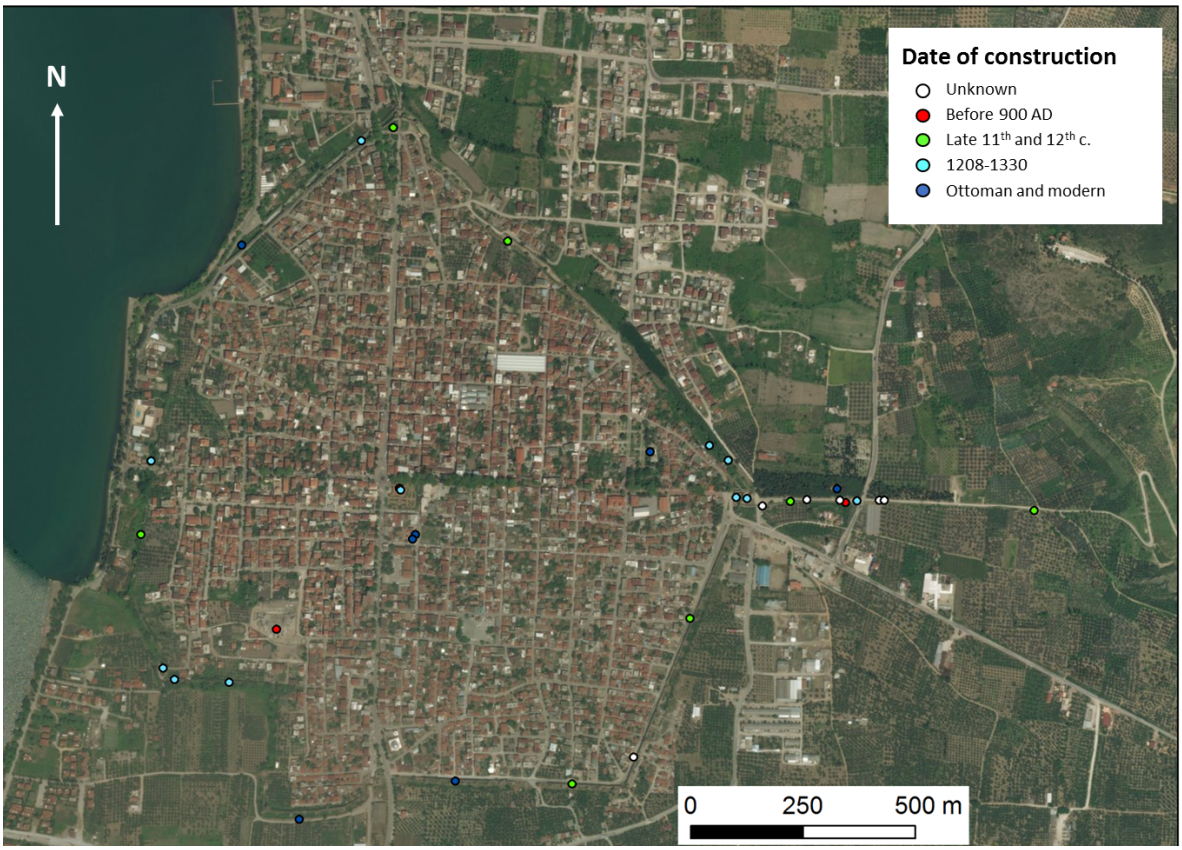

Figure D.43: Inventory of the potentially postseismic repairs and reconstructions in Iznik, classified by date of construction.

We were also able to date with ^{14}C four charcoal samples from mortar filling the dismantled ashlars of T57 base and one sample from the new masonry covering the rotated blocks of Istanbul Gate (Fig. D.36g, see Fig. D.30 for locations). The ages obtained (Table D.3) are all very coherent and point toward repairs following a deformation episode in the late 11th or early 12th centuries. One earlier age from T57 might be used to propose another episode before the 11th century, but this sample was taken from the same stratigraphical unit as the others and presents a very low carbon content, which leads us to consider this different age range rather unlikely. Finally, we tried to date the organic fraction of carbonate concretions sampled on the aqueduct wall but we obtained a very recent age. This may imply that most, if not all, the concretions of the aqueduct were formed during modern times, probably due to poor maintenance or man-made damage. These external concretions were logically given a bad quality rating as EAE.



Figure D.44: Examples of "clamp structures" (a) in Butrint walls, Albania (courtesy of Riccardo Vassallo) and (b) in Tzintzuntzan pyramid, Mexico (from Rodríguez-Pascua et al., 2010).

Name	Location	Type	Carbon analyzed (mg)	%modern carbon	^{14}C date (yr BP)	^{14}C calibrated age AD
W5a1	Repair mortar on T57	charcoal	1.38	88.84716	950±30	1024-1155
W5b1	Repair mortar on T57	charcoal	1.25	89.00717	935±30	1026-1162
W5b2	Repair mortar on T57	charcoal	1.33	89.42842	900±30	1039-1210
W5a2	Repair mortar on T57	charcoal	0.09	87.31807	1090±70	769-1046
IZAQC2	Aqueduct concretion	tufa	0.79	102.37583	Posterior to 1950	
W61b	Reconstruction Istanbul Kapi	charcoal	1.51	89.36830	905±30	1037-1207

Table D.3: Sample list and radiocarbon dating in Iznik. The dating was done by the LMC14/LSCE. The ages were calibrated with the Oxcal 4.2 program (Bronk Ramsey, 2009) using the IntCal13 calibration (Reimer et al., 2013).

D.3.3.2.6 Vulnerability analysis The investigated buildings were classified into three vulnerability classes A, B and C. Class A includes the most vulnerable buildings, which use rough rubble stones and a mortar of average quality. Class B includes the buildings using carefully cut stones or terracottas and a mortar of good quality. Class C includes more resistant buildings using large ashlar. When the building presented visible defaults or weaknesses in its construction, we shifted its vulnerability class by one rank (e.g. A instead of B). For each vulnerability class, we computed the ratio of the total number of damage of a given grade observed over the length of the walls considered (Fig. D.45). The damage repartition is quite similar for classes B and C with a maximum for grade 2 (moderate) but the buildings of class B are more affected and present more damage of higher grades whereas class C buildings show very limited damage higher than grade 2. The buildings of class A appear globally less affected by individual damages on their total length, but are characterized by a higher severity of the damage, with a maximum for grade 3 (important non-structural damage and moderate structural damage).

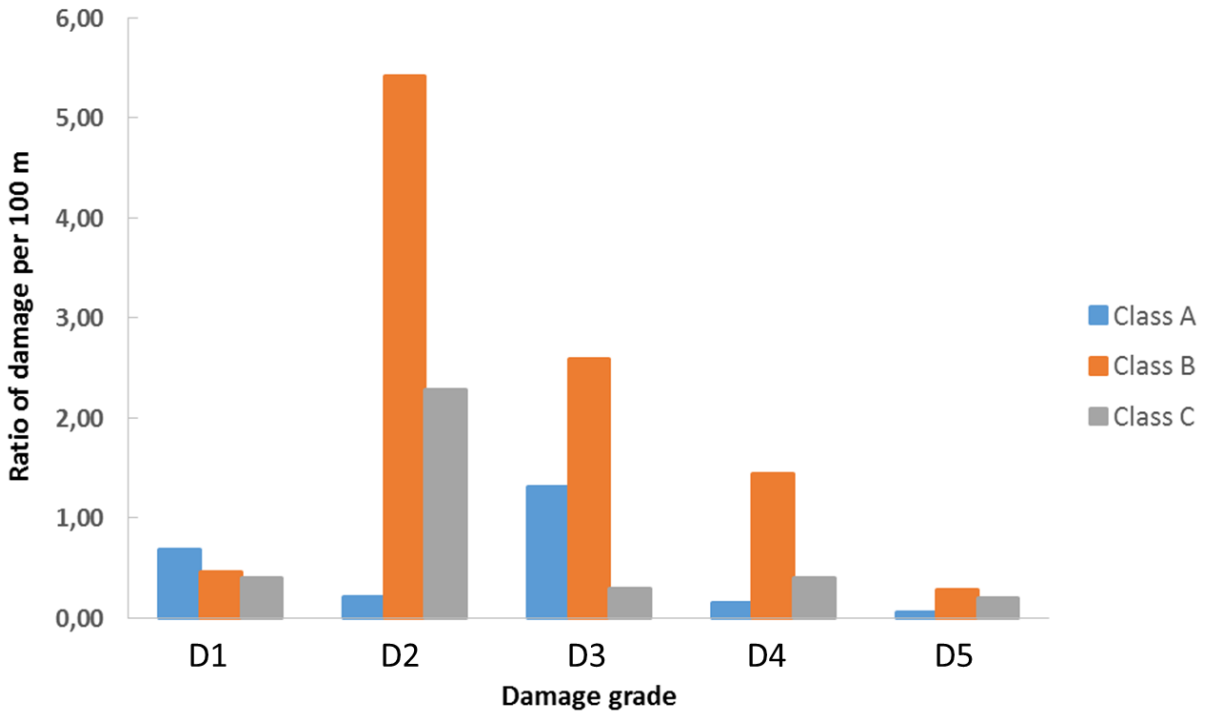

Figure D.45: Distribution of the damages of various grades for the three vulnerability classes of buildings in Iznik.

D.3.4 Modeling of the deformation of the obelisk

The obelisk located north of Iznik is a simple structure that can be easily modeled. It is then possible to test whether an earthquake rupturing the MNAF is able to cause the displacement of the blocks that is observed today. The constituting elements of the obelisk mentioned in section D.3.2.1 were measured in order to build simplified models in two dimensions (Fig. D.46) for an obelisk composed of five and six stones. The numerical model was built in collaboration with Laurent Baillet, using the Plast2 finite-element code (Baillet et al., 2005). For the mechanical properties of the marble blocks, typical values were chosen, with a Young's modulus of 50 GPa, a Poisson's ratio of 0.2 and a density of 2.7. To simulate the obelisk response to seismic shaking, we used as input signals five 3 components acceleration signals measured during real strike-slip earthquakes (Table D.4), provided by Philippe Guéguen. We selected the signals so that the distance between the recording station and the epicenter was in the same range as the distance between the obelisk and the closest MNAF segments. We also selected only stations located on a ground of similar type to Iznik obelisk. The acceleration signals were converted into displacement signals with two integrations. Before each integration, the signals were filtered with a mean substraction, a detrending and a 4 order bandpass Butterworth filtering between 0.1 and 20 Hz. The signals were also smoothed with a spline function and resampled at $0.5.10^{-5}$ s. The simulations were launched with different, realistic values of friction (0.5 and 0.7) and with a dumping factor of 0.1.

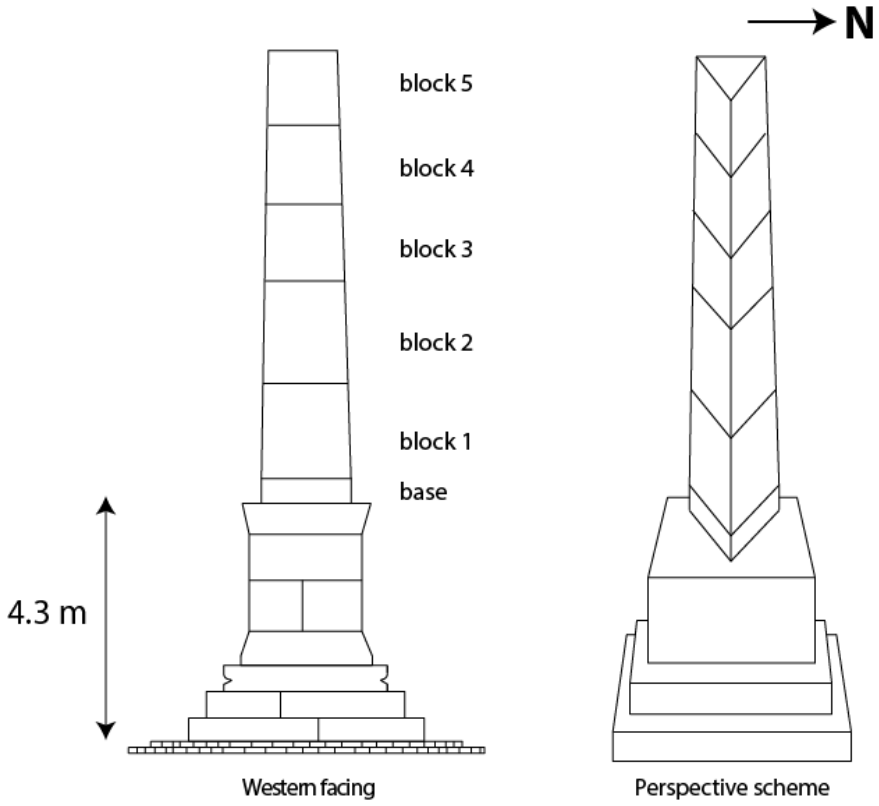

Figure D.46: Drawing of Iznik obelisk with the dimensions and arrangement of the different blocks as measured on the field. The western face is given as an example on the left. A simplified perspective sketch, which was used to design the numerical model, is shown on the right.

Name	Date	Event location (lat;lon)	Event depth (km)	Moment magnitude	Station code	Station location (lat;lon)	Epicentral distance (km)
Düzce	1999-11-12	40.81;31.19	10.4	7.3	8101	40.84;31.15	5.3
Azores Islands	1998-07-09	38.61;-28.57	10	6.1	HOR	38.53;-28.63	10.7
Patti Gulf	1978-04-15	38.27;15.11	22	6.0	MLZ	38.23;15.24	12.5
Patti Gulf	1978-04-15	38.27;15.11	22	6.0	PTT1	38.15;14.97	18.3
Kyllini	1988-10-16	37.93;20.92	25	5.9	ZAK1	37.79;20.90	15.7

Table D.4: Characteristics of the earthquakes used for the simulations on the obelisk.

	Düzce (8101)	**Azores Islands (HOR)**	**Patti Gulf (PTT1)**
Friction=0.7	5.61	11.8	0.253
Friction=0.5	32.11	13.7	0.04

Table D.5: Maximum displacements in mm obtained between adjacent blocks (5 blocks model) for the Düzce, Patti Gulf and Azores Islands earthquakes (the recording station is precised between parentheses) and different values of friction.

For the five earthquakes simulated and for the 5 and 6 blocks models, the obelisk do not collapse, but it shows irreversible relative displacement between blocks (Table D.5 and Fig. D.47). The obelisk also remains stable when a number of 7 blocks is tested with the strongest Düzce earthquake. This can be explained by the fact that the frequency content of the seismic signals is significantly different from the natural frequency of the obelisk. The first frequencies of the obelisk are 13.2 and 57 Hz, much higher than the dominant frequencies of the seismic signals which do not exceed 3 Hz. At this small frequency, very large ground displacements would be required for the obelisk to collapse. For this reason, the fact that the obelisk is still standing today does not imply that the region was never affected by strong earthquakes. The maximum displacements between adjacent blocks at the end of the simulation were measured for Düzce, Azores Islands and Patti Gulf earthquakes (Table D.5). Significant displacements between adjacent blocks are found for the Düzce and Azores Islands earthquakes, with lateral offsets between 5 mm and 3 cm. These results match our field observations with offset values high enough to be perceptible to the naked eye on site. The biggest displacement is obtained for Düzce earthquake with a friction parameter of 0.5. For the Azores Islands earthquake, smaller displacements of 1 cm are found, which seem slightly lower than those observed on the obelisk. The relative displacements obtained for the Patti earthquake can be considered negligible with offsets lower than the millimeter.

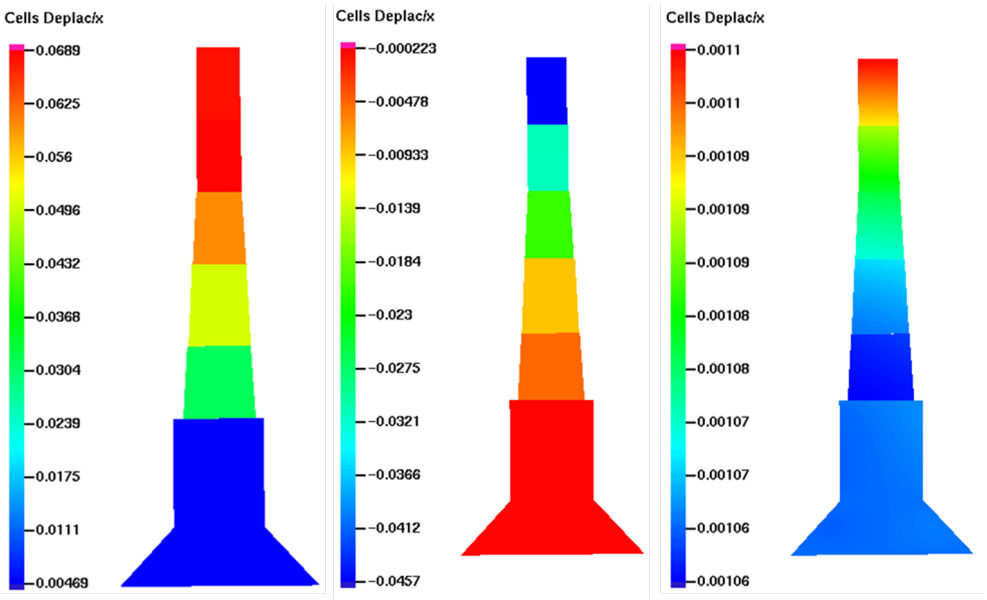

Figure D.47: Final states of the column simulation for Düzce (left), Azores Islands (centre), and Patti Gulf (right) earthquakes, with a friction coefficient of 0.5. The horizontal displacement relatively to the initial position is indicated on a colour scale, in meters.

D.3.5 Discussion

D.3.5.1 Identification of deformation episodes

Our archeoseismological investigation revealed that buildings of all periods in Iznik are affected by EAE typical of earthquake shaking. This demonstrates that the city was struck by at least one major historical earthquake since the 15th century, given the damages found on Ottoman buildings. It is generally considered that the damages of successive earthquakes tend to replace each other rather than cumulate, because the rebuilding of the heavily damaged buildings erase the former traces of deformation (Caputo and Helly, 2008). Therefore, separating the effects of different earthquake in the EAE dataset is not straightforward. The city of Iznik presents the advantage of having preserved a significant amount of walls from the older construction periods, making it possible to analyze chronological subsets of EAE (Fig. D.48). Some of these subsets should be considered with caution because they include limited lengths of walls, such as 0-200 AD, the Ottoman period, and the 9th century to a lesser extent, which include a few hundreds of meters. This may introduce a bias towards big values of the EAE over wall length ratio. In that regard, the Ottoman ratio is surprisingly high. Other factors of perturbation should be considered. The amount of repairs and reconstructions during a given period of time will erase some of the EAE. The building vulnerability may not be homogeneous among the various subsets compared, in which case similar earthquakes may produce different types and repartitions of EAE.

We can see that for the Byzantine period (5th-14th centuries), if we only consider the best quality EAE, the ratio clearly decreases over time and is quite stable between the 6th and 12th centuries with values of ∼1 EAE per 100 m (Fig. D.48). It seems that we are thus able to detect an increase of damage as the wall gets older and that the EAE are not erased over time. This interpretation would lead to propose at least one early deformation event between the 3rd and 8th centuries, and with less confidence another one between the 11th and 13th centuries, as the ratio is reduced by half for the latter period. The relative stability of the damage ratio between the 6th and 12th centuries is not easy to interpret. It might mean an absence of big earthquake or also reflect intensive rebuilding work during this period of time. Another interesting feature of Fig. D.48 comes from the comparison of the lower quality EAE ratios. While they do not fundamentally modify the tendency for most periods, they appear much greater between the 9th and 12th centuries. As these type of EAE may be related to non-seismic causes, this could indicate the occurrence of other particularly destructive events, most probably wars. It is known that between the 10th and 12th centuries, the city was besieged and taken several times by the Seljuk Turks, the Byzantine imperial army as well as rebel generals (Cahen, 1948; Foss, 1996).

Stronger evidence comes from repairs and reconstructions directly associated to EAE, which enable to give an age that is likely to closely follow the occurrence of damage. Combining the ages of the affected walls and their repairs, we obtain many time ranges of different widths constraining one or several events (Table D.6, Fig. D.49). The narrower, distinct time intervals obtained for possible earthquakes are 527-787, which corresponds to several quality 1 EAE in Aya Sofia, and 858-1097, which corresponds to EAE of lower qualities in the walls. Interestingly, this time interval includes the ^{14}C ages of the sampled postseismic repairs (Table D.3 and section D.3.3.2.5) Fig. D.49 sums up these data and enables to point out the periods chararacterized both by a significant amount of damage and fast, well dated repairs. The Ottoman deformations, which were already commented on above, appear again on this figure. The Roman and Byzantine periods until the 12th century are overall marked by relatively intense damage. The higher amounts of EAE span from the early 8th century with a "peak" before ∼850 AD, which may match the interval found with the observations in Aya Sofia. When interpreting this graph, one should however consider the total length of walls built through time. For example, the early 8th century indeed corresponds to a period of new constructions (Fig. D.33), and it seems logical to see an increase in the EAE because of these new damageable volumes. But the relationship between new walls and additional EAE does not seem so clear, as the intense Lascarid building works of the 13th century is on the contrary associated to a clearly lower amount of EAE, in spite of the later Ottoman earthquake.

In conclusion, the damage and repair datasets suggest the occurrence of at least three major earthquakes, two before the Ottoman conquest and one after. For the former, the most narrow intervals are between the 6th and late 8th centuries and between the 9th and late 11th centuries.

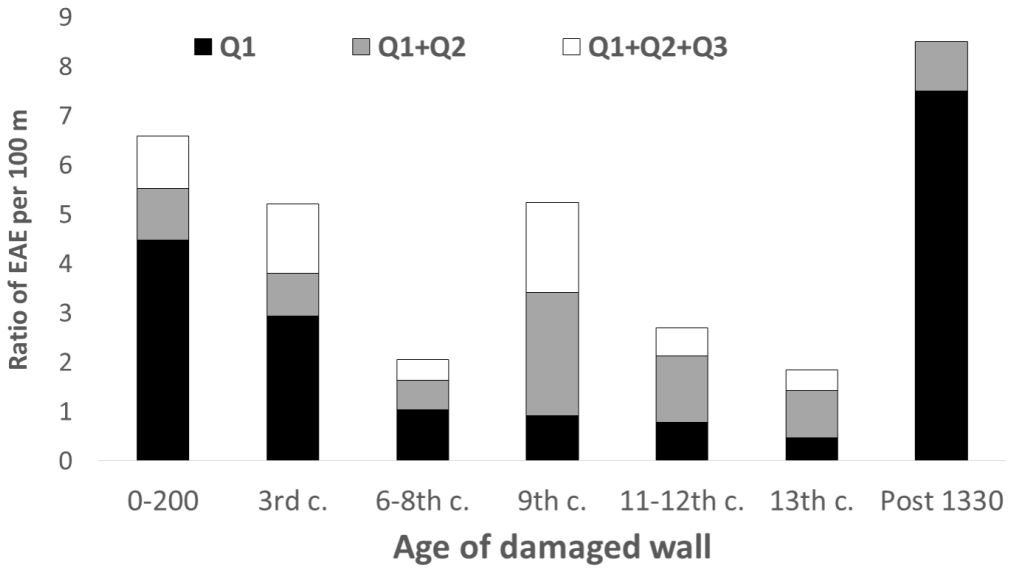

Figure D.48: Ratios of damage per linear meter of wall for the main construction periods of Iznik.

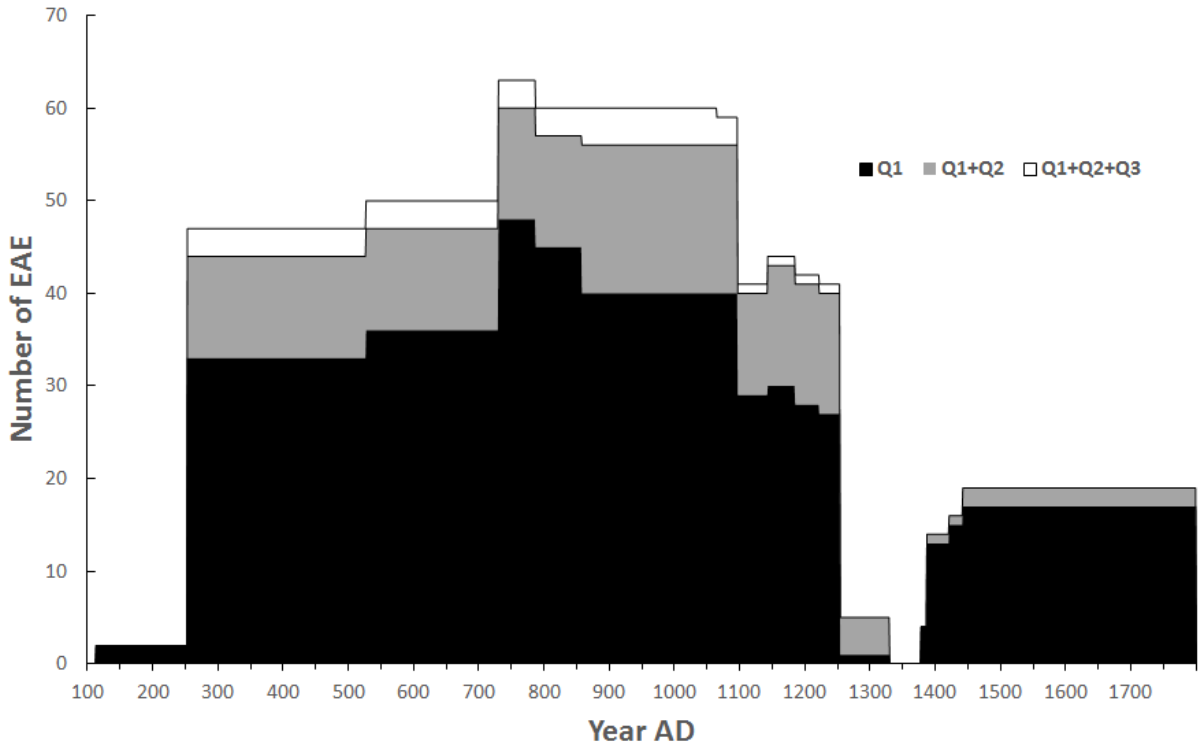

Figure D.49: Chronological constraints on the EAE. The dataset is composed of the EAE constrained by both minimum (age of the wall) and maximum (age of repair) ages during the Byzantine period until 1330 (Table D.6). For each year, we sum the number of EAE that may have occurred this year. The result represents the summation of the number of EAE on each interval, assuming the same probability for all the years of the interval. For the ottoman period after 1330, note that the EAE are only constrained by a *terminus post quem* (earliest year of occurrence).

Terminus post quem	Terminus ante quem	Q1	Q1+Q2	Q1+Q2+Q3
113	858	1	1	1
113	1330	1	1	1
253	858	5	5	5
253	1065	0	0	1
253	1097	11	15	16
253	1185	2	2	2
253	1254	13	18	19
253	1330	0	2	2
527	787	3	3	3
730	1254	12	13	13
858	1097	0	1	2
858	1222	1	1	1
858	1254	0	1	1
858	1330	0	2	2
1143	1254	1	3	3
1378	1800	4	4	4
1387	1800	9	10	10
1421	1800	2	2	2
1442	1800	2	3	3

Table D.6: EAE constrained by postseismic repairs, separated by quality categories. In general, the terminus post quem corresponds to the construction of the walls while the terminus ante quem is the date of the repair. We use 787 as the latest date for a reconstruction in Aya Sofia that preceded the 2nd council of Nicaea. 1330 corresponds to the Ottoman conquest. The other dates, which correspond to the construction of the different buildings studied and major reconstructions of the defensive walls, are exposed in section D.3.2.

D.3.5.2 Estimation of local intensity

The assessment of building damage following an earthquake generally enables to derive a local intensity reflecting the severity of ground shaking. This is possible by comparing the obtained damage distribution for given vulnerability classes with damage probability matrices (DPM). These matrices contain, for each intensity, the most probable amount of buildings affected by the different damage grades (Fig. D.50). Typically, weak (<VI) and strong (>X) intensities will result in monotone, respectively decreasing and increasing, damage distributions, while intermediate intensities will produce bell-shaped distributions centered around an average damage grade. Originally, the EMS98 scale uses qualitative terms such as "few", many" and "most" for the frequency of expected damage, but is incomplete because the frequency is precised for one or two damage grades only. Complete, quantitative translations of these terms were later proposed by Lagomarsino and Giovinazzi (2006), leading to damage matrices giving the occurrence probability distribution for each damage grade and for each intensity (Fig. D.50). The use of our vulnerability analysis to estimate a local intensity is delicate for several reasons. First, it is obvious that our damage dataset results from several successive earthquakes. Therefore, we have to assume that these damaging earthquakes were associated to similar intensities in Iznik, and that for instance the slight damage potentially produced by smaller or farther events were erased by repairs or posterior, bigger damage. In this case, the damage distributions caused by the successive earthquakes are relatively similar and we will obtain an "averaged" intensity. Given that the damage distributions obtained in Iznik (Fig. D.45) for all the vulnerability classes do not present unexpected shapes (i.e. flat or bimodal distributions), this assumption may be reasonable. The other difficulty rises from the way of counting the damages. Damage probability matrices are defined for damage grades assigned by building, meaning that each building is given one damage grade. In our case, it was not possible to do so because the number of buildings investigated is too small and also because long and linear structures like the defensive walls or the aqueduct are better suited for a count by linear meter. This way of counting the damage obviously leads to rather low ratios, not exceeding 10 damages per 100 m, and it is difficult to directly compare our damage ratios with the probabilities given by the DPM. While the calibration of our approach with modern earthquakes remains to be done, we can qualitatively compare our damage curves with the distributions of the DPM. By comparison with the quantitative DPMs (Riedel, 2015), our damages repartition for class A suggest an intensity VII while the results in classes B and C are more compatible with a minimal intensity VIII.

This result can be also discussed in regards to the numerical simulations done on the obelisk. To produce intensities VII or VIII in Iznik, with an epicenter located on the fault segments 3 km south of the city, magnitude ∼6 earthquakes are sufficient (Erdik et al., 1985). The deformations observed on the obelisk suggest magnitudes above 6, most probably between 6 and 7, in the case of events rupturing the same segments south of Iznik. Our vulnerability analysis is likely to underestimate the maximum intensity felt in Iznik during

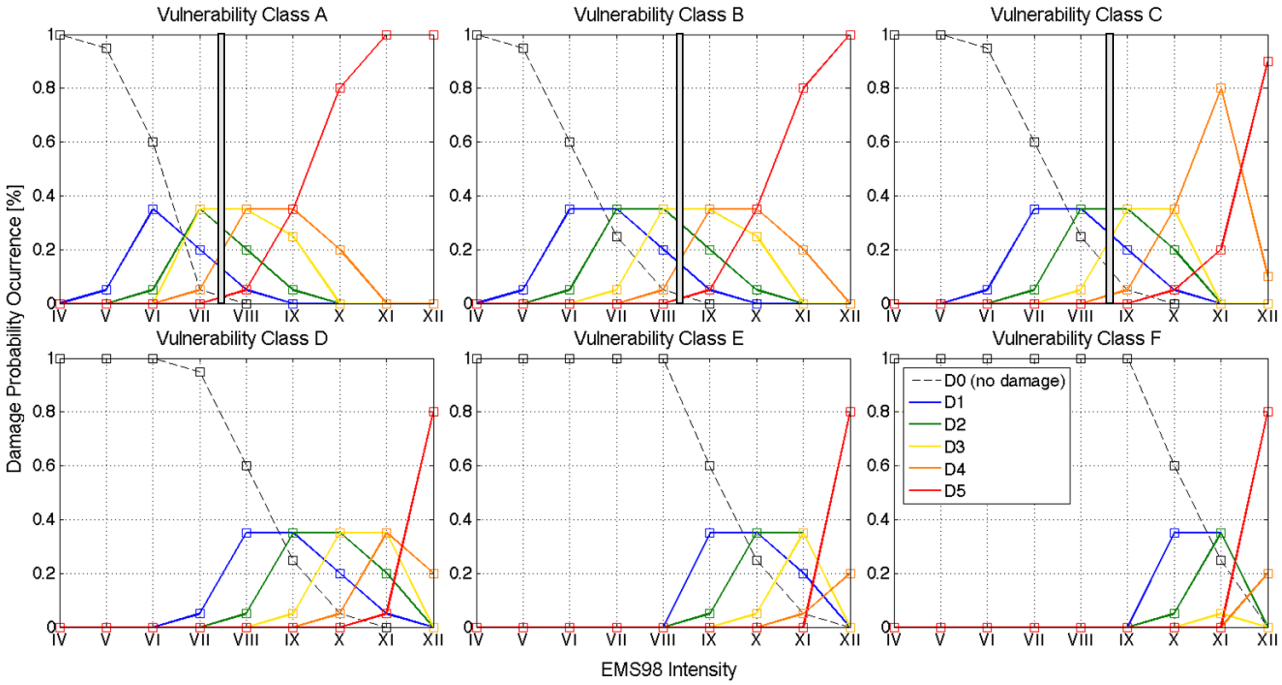

Figure D.50: Quantitative translations of the EMS98 damage classification according to vulnerability class and macroseismic intensity, taken from Riedel (2015). The vulnerability class A to C correspond to the buildings studied in Iznik that use terra cotta, rubble and ashlar. The classes D to F correspond to more resistant buildings using reinforced concrete, steel and wood. The probability distributions of the different damage grades are shown with different colours. For each vulnerability class, we try to find the intensity which best replicates our observed damage distribution (reported on the graphs as vertical bars). For example, for our vulnerability B buildings, we observe a majority of D2 damage. This is compatible with an intensity VII or VIII. Then, the fact that we have much more D3 than D1 damage rather suggests an intensity VIII.

the historical period, because of the limitations explained above, but also for other biases mentioned in the previous section. The repairs following earthquakes tend to erase the most serious damage, and it is probable that the most affected buildings have disappeared or have been entirely rebuilt. As we said, our survey was limited to a small number of ancient buildings because the vast majority of Iznik area is covered by very recent constructions.

Date AD	Areas affected	Effect	Ms	References
29-32	Nicaea	Destroyed houses	7 or more	1,2,3
121	Nicomedia, Nicaea	Complete destruction	7.4	1,2,3,4
362	Nicomedia, Nicaea, Constantinople	Complete destruction	6.8 or more	1,2,4
368	Nicaea	Complete destruction	6.8	1,2,3,4
740	Nicomedia, Praenetos, Nicaea, Constantinople, Thrace	Big damage on the walls of the three cities, almost complete destruction in Nicaea, serious damage in Constantinople and Thrace	7.1	1,2,3,4
1065	Nicaea	Widespread damage on several buildings	6.8	1,2
1419	Prusa	Widespread damage on walls and houses	7.2	1,2,4
June 1860	Iznik, Bursa, Istanbul	Collapse of a few walls, no serious damage, strongly felt in Istanbul		2
November 1860	Bursa, Iznik	Felt		2
1878	Esme, Labinia, Sapanca, Adapazari, Akyazi, Bursa, Izmit, Istanbul, Thrace, Geyve, Iznik	Slight damage in Geyve and Iznik	5.9-6.1	1,4,5
March 1893	Iznik, Yenisehir, Istanbul	Small damage on a few old houses, felt in Yenisehir, perceptible in Istanbul		2

Table D.7: Catalog of earthquakes with effects in Iznik and neighbouring areas. When not precised, the effects concern the first area mentioned. Ms=surface wave magnitude. References: 1=Ambraseys (2002), 2=Ambraseys (2009), 3=Guidoboni et al. (1994), 4=Ambraseys and Finkel (1991), 5=Ambraseys (2000).

D.3.5.3 Comparison with paleoseismological and historical seismicity data

Thanks to its numerous remains and the abundant documentation relating its history, Iznik is a great site to discuss the complementarity of the archeological and historical records of past seismicity and their relevance in a context where fault trenching is difficult. It is important to bear in mind that the former types of study may document more events than trenching on a single fault because it can record earthquakes nucleated on other nearby faults, as well as smallest damaging ruptures which do not show up in a trench stratigraphy. Besides, these methods have their own intrinsic biases, some of which were discussed above. Historical documents are especially prone to intensity exaggerations, events amalgamation, but also gaps of information for lesser known periods (Guidoboni et al., 1994; Ambraseys, 2009).

So far, the different trench studies done on the MNAF have evidenced only three main ruptures in the last 2000 years (Ikeda, 1988; Uçarkus, 2002; Özalp et al., 2013; see Chapter C for a comprehensive review): one around 0 AD west of Iznik Lake, one between the late 13th and ∼1750 AD in the west and in the east of the lake, and one or several smaller events along the lake in the late 19th century. The buildings studied may not be old enough to document the earliest rupture, apart from the obelisk, and the only archeological scenario compatible with this trench age, assuming typical ^{14}C dating uncertainties of ∼300 years, would be an earthquake shortly after the construction of the 3rd walls, as proposed from Fig. D.48 (section D.3.5.1). The events identified between the 8th and 13th centuries have no equivalent in the trench data, which may indicate that these earthquakes happened on other fault segments. Finally, the Ottoman damage seems to match the second rupture mentioned. This earthquake, found by Özalp et al. (2013) in a trench in Gemlik, is linked by the authors to the 1419 earthquake which damaged Bursa and probably other towns west of the lake (Ambraseys, 2009). Given that damage in Iznik is not explicitly described in the texts and that our dataset rather support an event after 1442 (construction of Mahmut Celebi mosque), we cannot exclude that the rupture identified in this trench happened at a different time or that Iznik was damaged by a different earthquake.

The direct comparison of archeological and historical records of seismicity often raises a few major issues (Niemi, 2008; Rucker and Niemi, 2010). In particular, it is tempting to attribute the date of a historical event to an observed damage. Proceeding so actually overestimates the real accuracy of historical sources and eventually leads to circular reasoning where the uncertain date of an earthquake is transformed into a fact and used to confirm the date of the proposed archeological destruction. Many earthquakes may be missing from the written records and a given archeological damage episode can be linked to the summed effects of several successive earthquakes. In that case, attributing the archeological damage to a single historical rupture will enlarge the perceived destruction and lead to overestimate the size of the event. The same problems apply to careless comparison with paleoseismological data. That is why the three methods should be used as independent sources of

information. That said, the comparison of our archeological deformation episodes with the historical record (Table D.7) leads to interesting remarks. We pointed out in section D.3.5.1 a possible damage period between the 3rd and 8th centuries. This seems compatible with the historical record which includes two earthquakes in 362 and 368. While the former affects several areas in Marmara region, the latter presents focused damage in Nicaea, which suggests that each rupture occurred on a distinct branch of the NAF. The following episode identified has only one historical counterpart, the 740 earthquake, a major event which affected a huge area around the Marmara Sea. No contemporary event was found in the fault trenches on the NNAF (Pavlides et al., 2006; Rockwell et al., 2009; Dikbas and Akyüz, 2011) and we can therefore suspect an epicenter located on the submarine segments. However, the episode in Iznik includes the destruction and submersion of the basilica (see Chapter E) resulting from vertical slip on the MNAF, and we can thus propose another rupture on this fault branch which is absent from the historical record or has been amalgamated with the 740 event. The last archeological episode including a historical earthquake spans between the 9th and the 11th centuries. During this interval, Nicaea was damaged by the local 1065 earthquake. Afterwards, the city disappears from the historical seismicity record until the late 19th century. It is not certain whether this absence has a tectonic significance and could be interpreted as a quiescence period. In the meantime, other cities like Gemlik and Bursa continued to suffer damage from repeated earthquakes. Another possible interpretation relies on historical considerations. From the end of the 13th century, the city suffered significant emigration because of the growing Turkish power and just after the conquest in 1331, it is described as a ruined city only inhabited by few people (Defremery and Sanguinetti, 1968). The city then loses its political and strategical importance compared to others like Izmit, Gemlik or Bursa, and all the travelers still describe Iznik as a poor village by the 18th-19th centuries (Raby, 1976). This may explain why Iznik is no more mentioned during the Ottoman period, but could still have been affected by some of the earthquakes described for the bigger neighbouring cities or by other events missing in the record. There is no particular reason to attribute the Ottoman deformation episode in Iznik to the 1419 earthquake and, as commented earlier, we favor a scenario including a later earthquake. This last case illustrates that archeoseismology can bring useful complements to historical seismology.

The fact that several earthquakes in the historical catalog apparently damaged cities located near the northern and middle strands of the NAF, like Izmit and Iznik, in the same event, raises the question of the source location of the archeological earthquakes identified. For several events, especially in the beginning of the first millennium AD, the historical descriptions mention damaging earthquake in Nicomedia (Izmit) with partial destruction of Nicaea, like in 121 and 362. Though, it is difficult to know precisely the extent of damage corresponding to these terms. The posterior descriptions are probably more accurate and show in several instances that the areas around both cities are generally not affected the same way. For example, the 1063 earthquake clearly destroyed the surroundings of the NNAF whereas the 1065 earthquake affected more severely the MNAF region. The major events

related to the NNAF during the last 500 years, such as the 1509, 1754 and 1894 earthquakes, either do not mention Iznik or describe only slight damage. This corresponds to the kind of damage reported in Iznik during the 1999 Izmit earthquake: the chimneys of some houses fell down or remained bending and only a tiny part of the defensive walls collapsed (pers. comm. Cengiz Celik). The intensity in Iznik area was estimated around V or VI (Fig. D.51). In a similar way, it seems that the earthquakes on the SNAF did not damaged Iznik significantly, but this is much more questionable for localities further west like Gemlik. We cannot exclude that some minor damages present in our dataset might have been caused by ruptures on the other NAF strands, but it is very likely that the significant damage investigated in this study and the associated earthquakes found correspond to ruptures on the MNAF segments. Another possible source of damaging earthquakes is the Elbeyli fault evidenced on the aqueduct east of Iznik (section D.2.6). Damaging ruptures on this normal fault could explain some discrepancies between the trenching results and the historical catalogue.

D.3.6 Conclusions

Using an archeoseismological approach, we identified almost 300 individual traces of possible earthquake damage in Iznik, and more than 100 of them can be reasonably attributed to seismic shaking with high confidence. The different walls of the cities, depending on their orientation or their age, were not affected similarly. The damage was more severe for N-S oriented walls, while NE-SW walls show less deformation. The inner walls bear significantly more damage than the later outer walls. Three separate episodes of earthquake damage were identified, two during the Roman period between the 3rd and 13th centuries AD and one after the mid-15th century. The dating of several repairs associated to earthquake damage enabled us to better constrain the time of occurrence of two individual events, between 527 and 787 AD and between 858 and 1097 AD. While the latter event may correspond to the 1065 earthquake described in ancient texts, the two others really complement the historical catalog because they can be related to events without any previously known damage in Iznik or even to earthquakes absent from the catalogue. Taking into account the vulnerability of the different buildings investigated, we have estimated that the damage observed correspond to a minimal intensity VIII, most compatible with ruptures on the MNAF segments of magnitudes above Mw 6. The modeling of the deformation of an obelisk a few kilometers north of Iznik suggest magnitudes between 6 and 7 or more. Our study confirms on the field the historical and paleoseismological evidence that Iznik has been repeatedly struck in the last 2000 years by strong, damaging earthquakes, with a recurrence of several centuries. Our results are also in agreement with results from tectonic geomorphology indicating that the MNAF has generated high magnitude earthquakes during the Holocene.

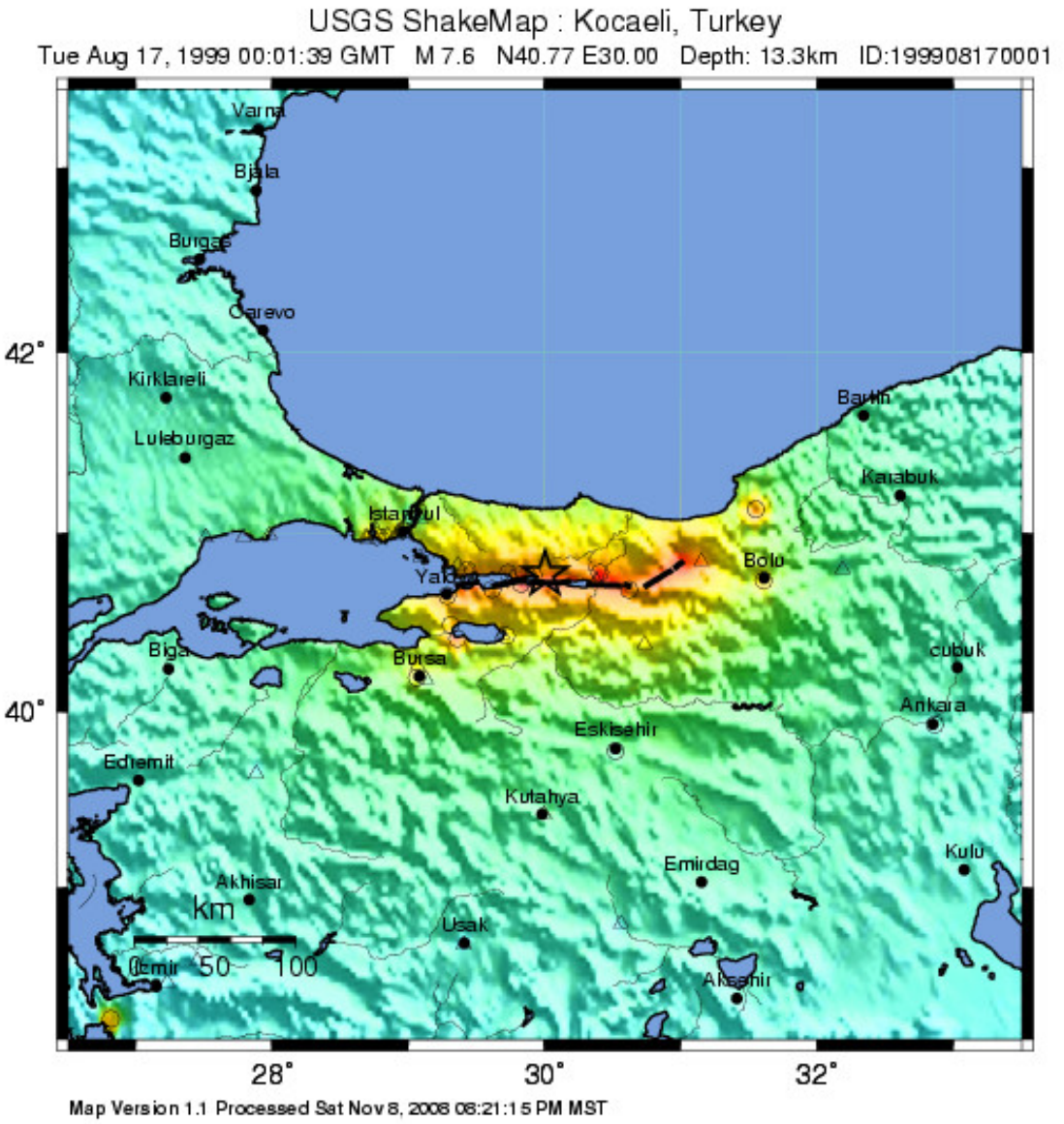

PERCEIVED SHAKING	Not felt	Weak	Light	Moderate	Strong	Very strong	Severe	Violent	Extreme
POTENTIAL DAMAGE	none	none	none	Very light	Light	Moderate	Moderate/Heavy	Heavy	Very Heavy
PEAK ACC.(%g)	*<.17*	*.17-1.4*	*1.4-3.9*	*3.9-9.2*	*9.2-18*	18-34	34-65	65-124	>124
PEAK VEL.(cm/s)	<0.1	0.1-1.1	1.1-3.4	3.4-8.1	*8.1-16*	*16-31*	*31-60*	*60-116*	*>116*
INSTRUMENTAL INTENSITY	I	II-III	IV	V	VI	VII	VIII	IX	X+

Figure D.51: Intensity map of the 1999 Izmit earthquake, provided by the USGS.

D.3.7 Résumé

La ville d'Iznik présente plusieurs monuments préservés des époques romaines, byzantines et ottomanes, et porteurs de déformations qui peuvent être reliés à des secousses sismiques. Nous utilisons une approche archéosismologique sur ces bâtiments afin d'identifier les séismes historiques ayant impacté la ville d'Iznik sur les deux derniers millénaires, et de contraindre leur date ainsi que l'intensité ressentie à Iznik. L'archéosismologie est un champ d'étude apparu à la fin du 20ème siècle, qui consiste à analyser les traces de déformations cosismiques dans la stratigraphie des sites archéologiques et sur les bâtiments anciens. Cette approche permet d'enrichir les catalogues de sismicité sur une plus grande échelle de temps, de façon complémentaire à la sismologie historique et à la paléosismologie.

Les bâtiments étudiés incluent un obélisque du 1er siècle ap. J.-C. situé 6 km au nord de la ville, l'aqueduc étudié dans la section précédente, les murs défensifs entourant la ville, le théâtre, et plusieurs mosquées. Des observations systématiques ont été réalisées sur ces bâtiments afin d'identifier les traces d'endommagement sismique (Earthquake Archeological Effects, EAE). Chaque EAE est décrit précisément et classé sur une échelle de qualité de 1 à 3. Les dommages sont aussi classés par degré sur une échelle de 1 à 5. 280 traces ont été trouvées au total, sur des bâtiments de toute époque. Il apparaît que les murs orientés N-S ont été préférentiellement endommagés tandis que les murs NE-SW sont sous-représentés. La plupart des déformations orientées sont logiquement perpendiculaires à l'axe du mur.

Lorsque des réparations sont associées aux dommages, l'âge de ces derniers a pu être contraint grâce aux datations archéologiques déjà réalisées et à de nouvelles datations sur des charbons prélevés dans le mortier des murs défensifs. Au moins trois séismes ont pu être identifiés entre le 6ème et la fin du 8ème siècle, entre 9ème et la fin du 11ème siècle et pendant la période ottomane à partir de la deuxième moitié du 15ème siècle. Les deux premiers événements identifiés n'ont pas d'équivalents dans les tranchées réalisées sur la MNAF, ce qui indique que ces ruptures ont eu lieu sur des segments différents de la faille. Le séisme ottoman est compatible avec des ruptures trouvées dans des tranchées à Gemlik mais aussi à l'est d'Iznik. Celle de Gemlik a été associée au séisme de 1419, mais aucun dommage n'est mentionné à Iznik à cette date et nos données indiquent une date postérieure à 1442. Il est donc possible que le séisme identifié à Gemlik soit plus tardif ou différent de celui ayant impacté Iznik.

La répartition des dommages de différents degrés en fonction de la vulnérabilité des bâtiments indique une intensité "globale" de VIII sur l'échelle EMS98, qui peut être produite par des séismes de magnitude 6 sur les segments de la MNAF situés au sud de la ville. Cependant, la modélisation numérique des déformations observées sur l'obélisque suggère une magnitude plus importante, entre 6 et 7. Notre étude archéosismologique complète ainsi le catalogue de la sismicité historique et confirme les données de paléosismologie et de morphotectonique indiquant que la MNAF a produit plusieurs séismes de forte magnitude durant les derniers millénaires.

Chapter E

Evolution of coastal environments since the Quaternary: impacts of climate and tectonics

After addressing the active faults segmentation, the offsets associated to these segments, and the last major earthquakes that ruptured them, we will show here evidence of variations of the ground and of Iznik lake levels at different time scales. The historical relative lake level variations were previously studied by Geyer et al. (2001). These data are completed by the study of a Roman basilica recently discovered a few meters away from the shore west of Iznik, submerged at a 2 m depth. The analysis of sediment cores sampled in the basilica area also provides preliminary information about the historical earthquakes. Variations of the ground level are observed at different places in Iznik, especially between the different construction phases of the defensive walls and along the aqueduct. At the scale of the Quaternary, the morphology of the lacustrine terraces developed north of Iznik Lake and described in Chapter B shows evidence of tectonic deformation. The comparison of the historical levels with those derived from the terraces enables to discuss the impact of tectonics and climate on the relative lake level since the Pleistocene.

E.1 Basilica study

E.1.1 Historical and archaeological context

The city of Nicaea is an important place in the history of Christianity as it held two ecumenical councils : the first one in 325, which expressed the divine nature of the Christ against the Arianist doctrine, and the seventh one in 787, which condemned iconoclasm. It is known that the latter took place in Aya Sofia. Given that the building dates from the

6th century AD, the first council obviously occurred in a different, older building, which is not precisely mentioned in the texts. In 2014, the remains of a church were discovered in Iznik Lake (Fig. E.1) and were associated by the archeologists to the location of the 325 council (personal comm. Mustafa Sahin). The building presents an organization similar to Aya Sofia and rests on the remains of an older temple with columns dating from the 1st century AD. The construction of the church was estimated to the 4th century. In the building, more than 80 graves were uncovered, containing coins from the reigns of Antoninus Pius (138-161), Constantine I (306-337) and Theodosius I (379-395). This constrains the period of use of the building at least until the late 4th century AD. The presence of graves inside religious buildings is not uncommon in the Roman world and is found in other well documented French sites like Nîmes and the Saint-Laurent church in Grenoble (Colardelle, 2013; Fournié, 2016). Another small building was found 125 m far from the shore, at a 5 m depth (Fig. E.2).

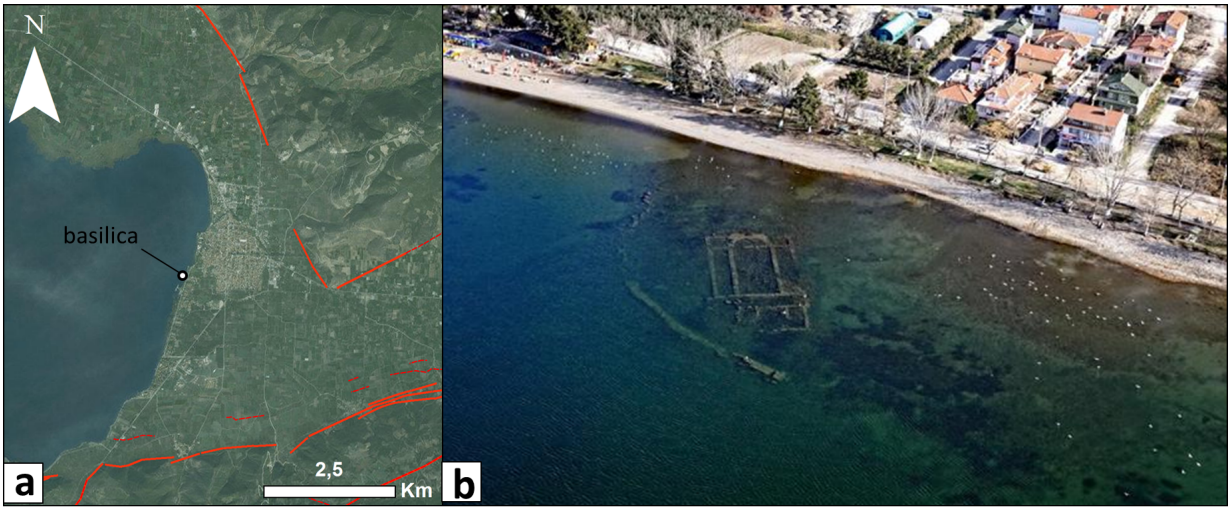

Figure E.1: (a) Location map of the basilica. (b) Aerial view of the site (courtesy of M. Sahin).

E.1.2 Study of sediment logs

To date the sinking of the basilica and identify the earthquakes posterior to this sinking, five sediment logs were sampled in the basilica area in collaboration with the archeologists from Bursa Uludag University. The logs (BA16-1 to BA16-5) were sampled in the basilica between April and September 2016 and studied during the Master's internship of Catherine Py-Circan that I partly supervised (Py-Circan, 2017). Three logs (BA16-1, BA16-4 and BA16-5) are located in the basilica's nave, one (BA16-2) at the foot of a curved wall protecting the basilica (BA16-3), and a last one in the small farther building (Fig. E.2). BA16-1 and BA16-4 were sampled at the same point to have a longer sequence. Stratigraphically,

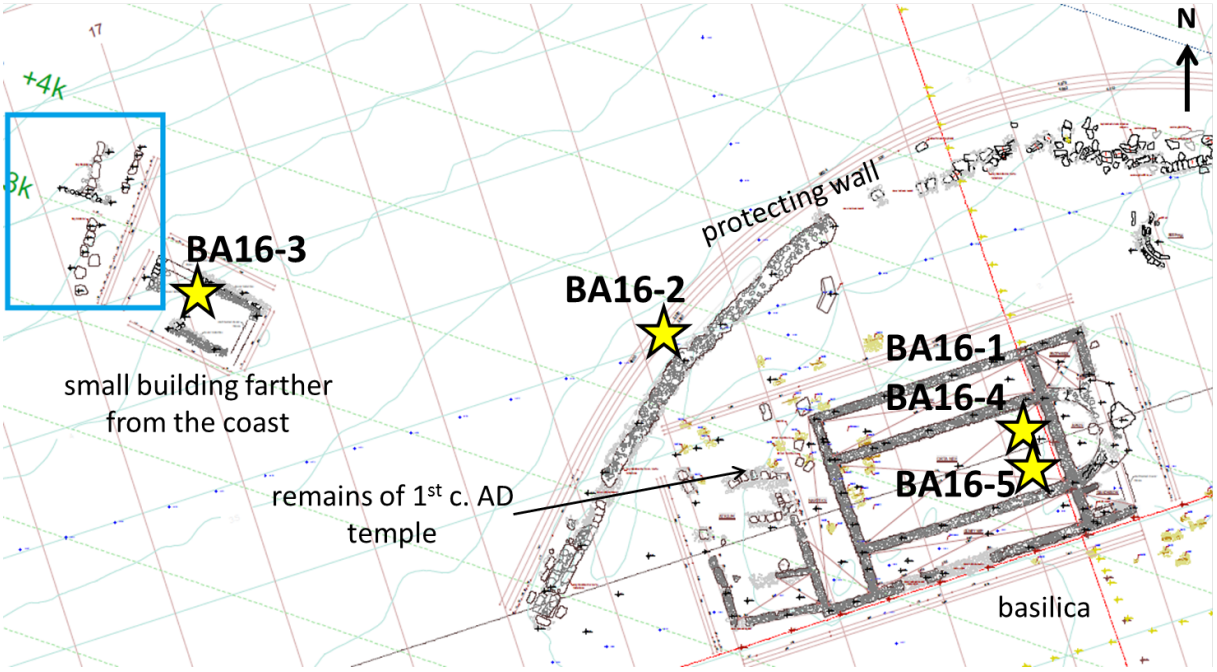

Figure E.2: Archeological plan of the basilica area. The sediment logs sampled are located with yellow stars. BA16-4 was sampled under BA16-1 at the same point. Modified from Py-Circan (2017).

BA16-1 overlays BA16-4 with a ∼140 cm gap between the two cores. The sedimentological and geochemical analysis of the cores was done in the laboratories of EDYTEM and ISTerre in Chambéry (France).

The logs are mostly composed of sandy material. BA16-2 and BA16-3 are short and mainly contain very coarse sand, gravels and pebbles. These two logs were sampled farther from the coast at the foot of walls. The lower half of BA16-4 is also composed of similar coarse material. These coarse units are overlain by a 10 cm thick silty-sandy unit. BA16-5 and BA16-1 contain finer sediments and display more significant grain size variations with depth. They are mainly composed of silt, very fine, and fine sands.

The absence of very small grains in BA16-2 and BA16-3 could be due to the refraction of waves on the walls that generates currents bringing away the finer elements. However, the presence of big pebbles implies a much greater energy, such as a tsunami wave, to explain their transport from the coast. The log pebbles are rounded and polygenic, and cannot originate from the abrasion of the adjacent walls. The other logs were taken within the basilica and were protected from the currents. They logically contain finer sediments and do not display any specific deposit of a seismic event. The fact that they were relatively short and close to the coast may make it difficult to register the earthquakes posterior to the sinking of the basilica due to the too small amount of sediments. The surface sediments

of the logs show elevated Pb/Rb ratios that indicate modern contamination (Py-Circan, 2017).

Only BA16-1 and BA16-4 contained organic fragments dated by ^{14}C (Fig. E.3). The ages obtained present some chronological inversions, which made the building of an age model impossible. Modern ages found deep in BA16-4 indicate contamination, possibly during the sampling. They are followed by a normal succession with sediments from around 300 AD which matches the assumed construction period of the basilica. The upper layers of BA16-4 and lower layers from BA16-1 provided similar ages between 1483 and 1610 AD, with an overall decreasing grain size. In BA16-1, these recent sediments from the 15th-17th centuries are covered by sediments older than the assumed age of the basilica. This suggests a remobilization posterior to the early 15th century, maybe during a seismic event. Interestingly, the age range of these recent sediments matches that of the archeoseismic evidence found in the city that suggests an Ottoman earthquake on the MNAF (section D.3).

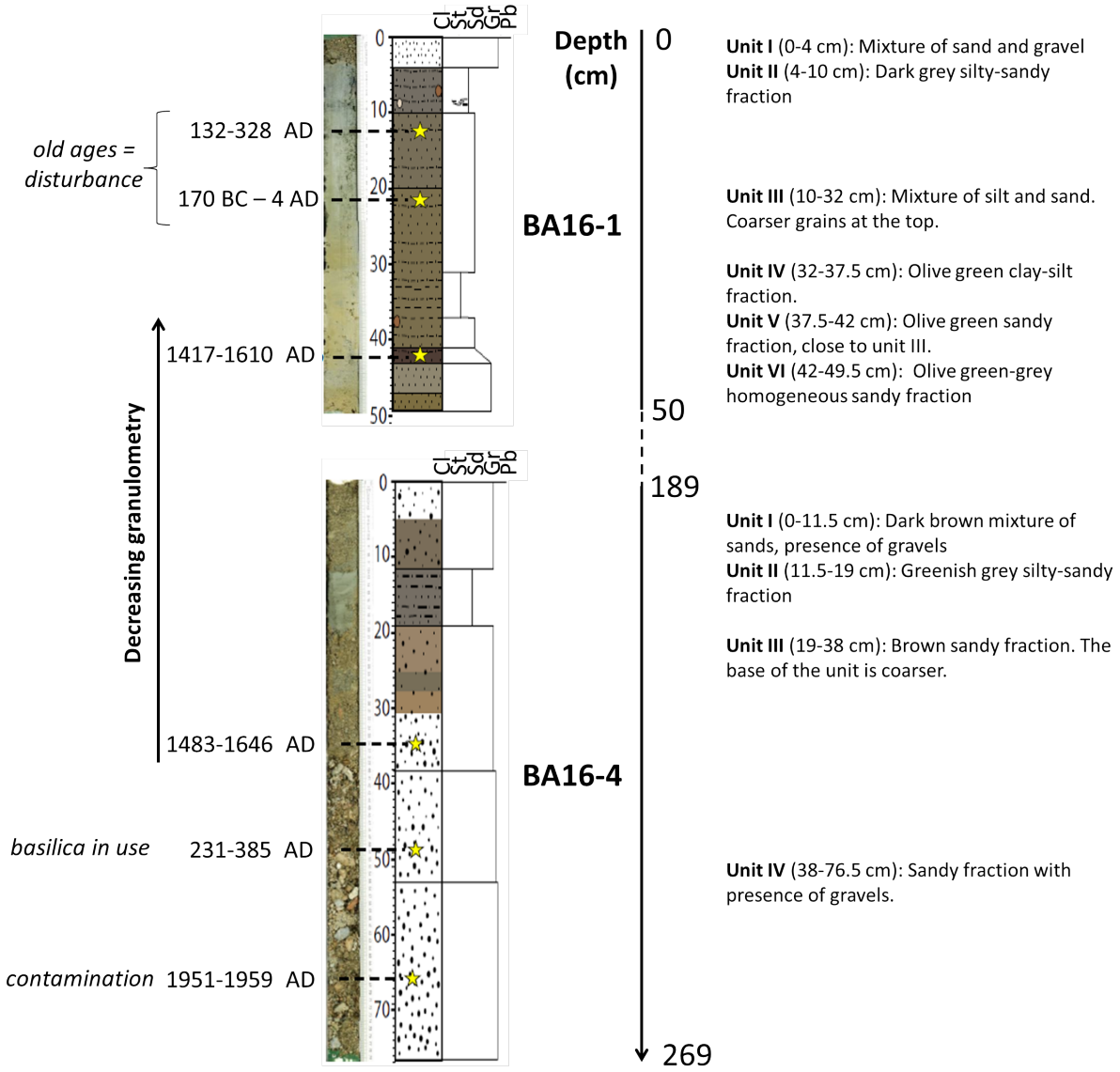

Figure E.3: Photos (left), interpretative scheme (center) and granulometry (right, Cl = clay, St = silt, Sd = sand, Gr = gravel, Pb =pebble) of sediment cores BA16-1 and BA16-4. The dated samples are located with stars and the radiocarbon ages are precised with their interpretation. Modified from Py-Circan (2017). The photos of the other cores can be found in appendix F

E.1.3 Implications for past earthquakes

Although the study of the sediment cores provided rather limited results, the observations realized, coupled with elements from other studies, can lead to interesting complements about the historical earthquakes having affected Iznik and their effects. The anomalous sediment succession in BA16-1, with older ages lying on younger ages, indicates a disturbing event potentially of seismic origin, posterior to the 15th. This hypothesis is supported by the archeoseismological study. The coarse pebbles dated at 300 AD at the base of the core BA16-4 suggest very high energy environments or could have been remobilized as sediments dykes during a liquefaction phenomena. The alternations of fine and coarse layers in the soft, saturated alluvium surrounding the lake favor the occurrence of liquefaction during earthquakes (pers. comm. Brady Cox). This might have caused sliding and sinking of certain parts of the city like the basilica (pers. comm. Brady Cox).

Another interesting question is raised by the possible trace of tsunami in BA16-2 and BA16-3 that contain coarse rounded material. The occurrence of strong sea waves is mentionned for several historical earthquakes in Nicaea. John of Nikiu tells that in October 368, "there was an earthquake [...] where the holy council had been held. For the sea rose against it and overwhelmed it". For the earthquake of 478, a later source also describes the submersion of the city by the lake. These description were considered by Ambraseys (2009) as exaggerations, but the geometrical features of the lake and the MNAF segments that pass along its southern coast make credible the hypothesis of massive floods in Iznik triggered either by vertical motion of the lake floor on the MNAF or by associated landslides. Such flash floods are known for several Swiss lakes with waves as high as 5 m (Schnellman et al., 2002; Hilbe and Anselmetti, 2014).

The sediment cores previously sampled in Iznik Lake have not been yet studied for paleoseismological purposes but they evidently contain valuable information in this regard. A core sampled by Ülgen et al. (2012) in the deep, southern sub-basin of Iznik Lake present a disturbed layer dated between 1000 and 850 BP that ends with an anomalous old age of 1329 BP. This succession is then sealed by an age of 841 BP. This suggest a disturbing event around the early 12th century AD that is quite close to some earthquakes found in the archeoseismological study. Finally, the chronology of use of the basilica, constrained by the sediment core ages, the coins and the dates of the two Councils, shows that a major event happened between the end of the 4th century when the basilica was still in use, and 787 when the second Nicaea Council was transferred to Aya Sofia. We can propose that this transfer was due to the destruction, and especially the sinking of the first basilica during this interval. We also note that this is synchronous to another earthquake deduced from archeoseismology between the 6th and late 8th centuries.

E.2 Historical variations of lake and ground levels in Iznik

E.2.1 Lake level variations

The amplitude of the lake level variations for the historical period can be retrieved from different observations (Fig. E.4). The variations of the Iznik Lake during the Middle Ages were thoroughly studied by Geyer et al. (2001). They used the stratigraphy and dating of beachrocks and bacterial carbonate concretions present on some rocky cliffs and ancient walls close to the lake waters, and several archeological remains in Iznik and its surroundings located today very close to the shore. The archeological remains mainly constrain three periods of low lake level (Fig. E.4).

1. Some Roman remains south of the lake, today partly immersed, indicate a lower level than today during the five first century AD (Geyer et al., 2001). The recent subaqueous excavations show that the inhabited area around Iznik during the Roman period was significantly larger than today and that the coast was located about 5 m under the present level, probably in the first centuries AD. The basilica is nowadays located at a 2 m depth, so the lake surface was below this level at the end of the 4th century.
2. In two archeological sites northeast of the lake, established when the lake level was lower, ceramics dated from the 13th century were found. A submerged beachrock is also present at the base of one of Iznik's towers that reaches the lake (Geyer et al., 2001). These findings indicate a lower lake level at least from the 9th century, until the 13th century.
3. The archeological sites mentioned above have also revealed ceramics from the 15th-16th centuries, which indicates another low lake level during the Ottoman period (Geyer et al., 2001).

High level stages are placed by Geyer et al. (2001) between the low level periods, relying on less certain dating of the carbonate deposits (Fig. E.4). Their observations suggest that after the sinking of the basilica, the lake level never went below again and so this part of the city remained under water. This is corroborated by the fact that no coins of later periods were found on the site and that the community had to transfer the 787 council to a church located farther from the lake shore. For the contemporary period, we know from photographs that in the 1930's the lake waters reached the base of the western towers of the city (Schneider and Karnapp, 1938). This corresponds to the highest levels found by Geyer et al. (2001), with a raise to about 3 m above the present level. Since the 1950s, the lake level has been regulated by a pumping facility located on the outlet, and varies between 84 and 85 m (Fig. E.4).

These relatively short oscillations are hard to explain with climatic factors, as the

palynological studies do not evidence similar changes in the vegetation (Argant, 2004). According to Geyer et al. (2001), these variations are mainly linked to the degree of obstruction of the outlet west of the lake. With time, sediment bars tend to develop along the western shore and block the outlet, causing a progressive increase of the lake level. The three low level stages are correlated to periods of political stability and economical wealth, when the outlet is maintained and kept clean to enable the drainage of the lake waters. Inversely, when the outlet gets blocked, for example during periods of trouble and/or decline, the lake level rises. We can add several other factors to these hypotheses. The areas in the southern part of Iznik Lake basin can be affected by tectonic subsidence during earthquakes rupturing the fault segments bordering the southern shore. Earthquakes can also trigger liquefaction phenomena, possibly identified in the sediment cores of the basilica. These can cause the sliding and sinking of some parts of Iznik, which may partly explain the depth of the remains found underwater.

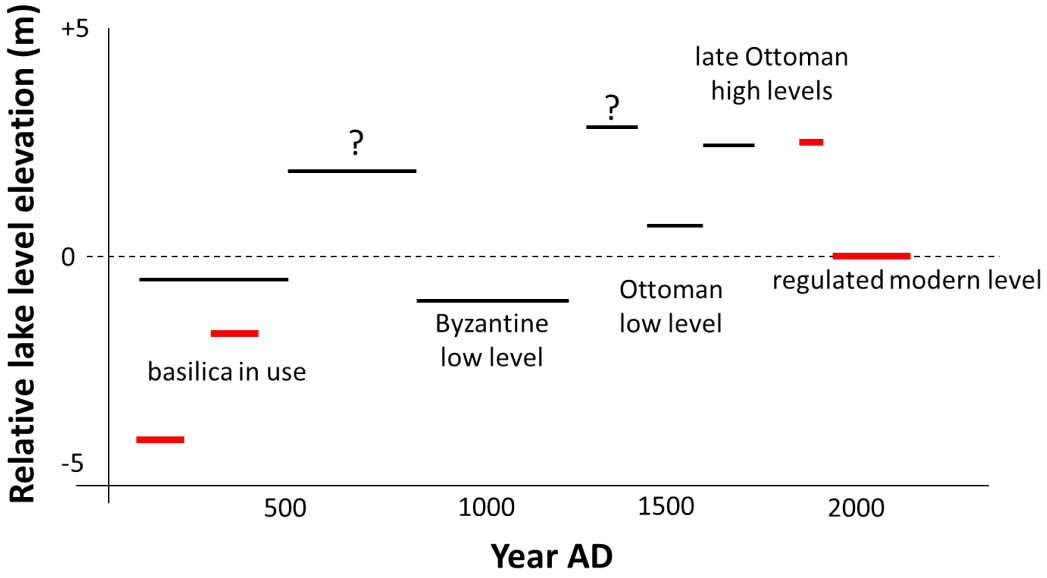

Figure E.4: Approximate reconstruction of the historical lake level variation, modified after Geyer et al. (2001). The current lake level is used as reference. We added to the data of Geyer et al. (2001) (in black) other levels deduced from the basilica study and for the 20th (in red). Note that the two high level periods before 1500 AD are less well constrained.

E.2.2 Markers of ground level change

At several places in Iznik, it was possible to observe evidence of significant changes in the ground (or "circulation") level. Successive episodes of general raising of the circulation

level were already documented for the defensive walls (Foss and Winfield, 1986). The height of the 8th century walls were raised to compensate for an increased ground level. The base of the 9th century towers is thus about 2 m higher than the original ground of the 3rd century AD (Fig. E.5a). Another episode is evidenced by the new fortifications of the early 13th century that were raised by 3-4 m (Fig. E.5b). This ground level difference is very clear behind the eastern gate (Fig. E.5e). It is also possible to see these ground level variations along the city aqueduct. The excavations of the last years have made visible the original foundations of the aqueduct close to the city walls (Fig. E.5c). It is obvious that along most of its length until 600 m east of Iznik, the lower courses of the aqueduct are buried beneath the current ground (Fig. E.5d). This shows again a significant raise of the circulation level. In the last construction stages, probably during the building of the outer walls, the part of the aqueduct that penetrates through the walls was set above an already raised ground, similarly to the reconstructions mentioned behind the gate.

Phenomena of progressive ground level raise are well known in archeology. Especially in urban context, the accumulation of waste materials and the tendency to rebuild over the debris of the older constructions lead to a significant increase of the ground's elevation over time. This is likely the case in Iznik for several ancient buildings like Aya Sofia, which lies a few meters below the modern street level. By contrast, the ground level changes observed on the walls and along the aqueduct suggest rather fast episodes on a larger scale as they are observed outside the city. The need to raise the height of the fortifications is probably not motivated by the higher ground level inside the walls but logically because the ground outside had risen, making the defensive walls less efficient. This relative ground level raise on a wider area around the city is confirmed by the partial burial of the aqueduct. The factors controlling these level changes are hard to precise without a finer study of the nature and stratigraphy of the deposits surrounding Iznik. We can at this point propose hypothetical scenarios. Recurrent floods from the lake, linked to climate or earthquake driven extreme events, can transport sediments over the western part of the city. Landslides on the instable slopes of the carbonate massif east of Iznik, along the Elbeyli normal fault, are another possible source of sediments.

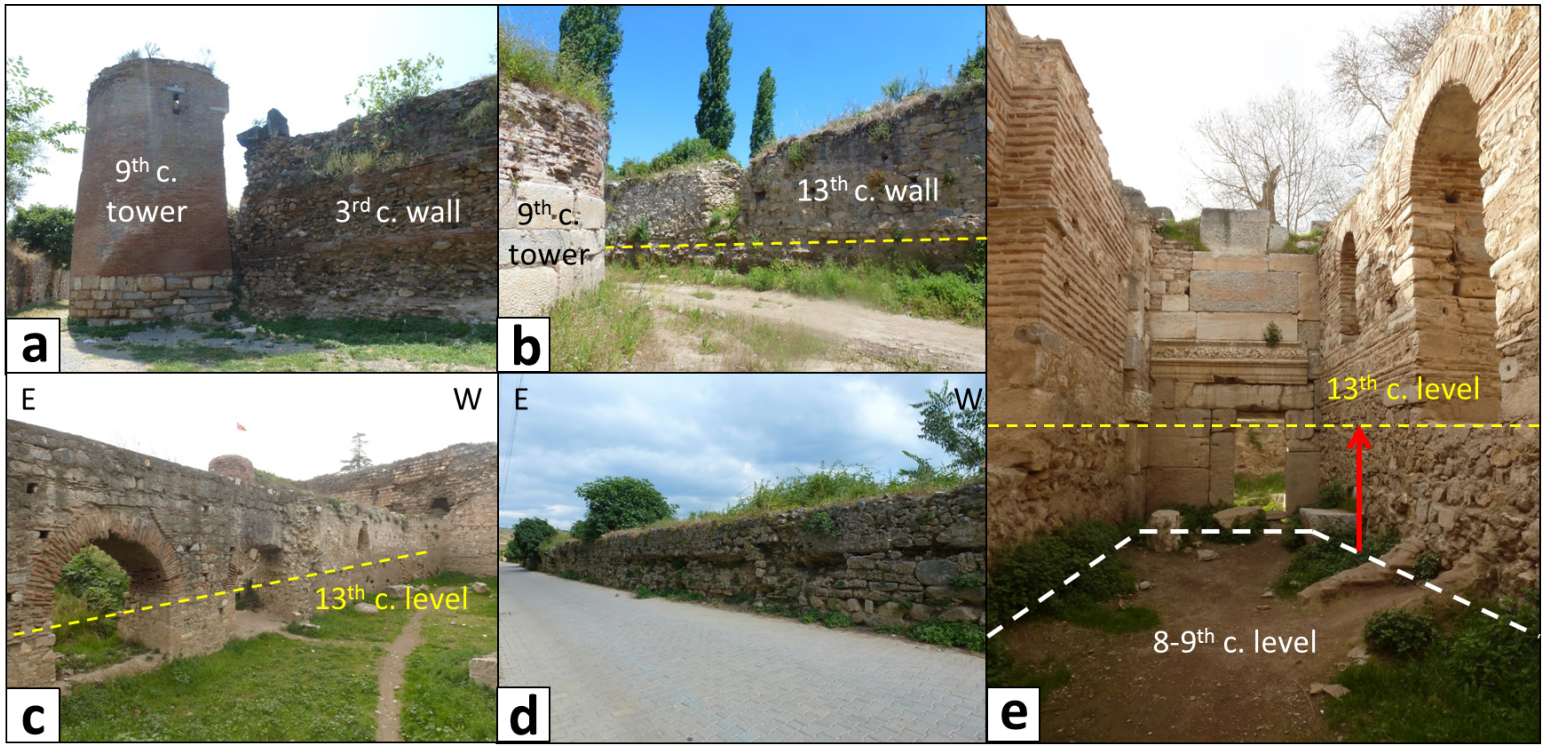

Figure E.5: Evidence of historical circulation level changes in Iznik and its surroundings. (a) Southern section of the inner walls. The ashlar base of the 9th tower appears above the base of the earlier wall which is today buried. (b) Eastern section of the walls. The outer wall was set on a higher foundation than the 9th century towers. (c) Junction of the aqueduct with the walls near Lefke Gate. The westernmost part of the aqueduct was rebuilt on a higher foundation. The color difference between the high and low courses of the aqueduct on the left shows that the latter were buried beneath this higher ground. (d) Eastern section of the aqueduct. Farther from the city, the height of the building seems significantly smaller as the higher ground hides the lowest courses. (e) Inner part of Lefke Gate. Two successive levels of circulation have been evidenced by the recent excavations.

E.3 Quaternary shorelines

Several markers of Iznik lake relative level changes during the Quaternary are observed around the lake (Fig. E.6). The lacustrine terraces of Iznik Lake (see chapter B) have been known and described since the early 20th century. Chaput (1936) identified them as old coastal deposits of the lake, and Tanoglu and Erinc (1956) consider that they represent the coast of the paleo-lake at its maximum extension during the Pleistocene. Other impressive markers are the submerged deltas of the Karadere river, which represent a paleo-coast line when the lake level was 35-40 m lower than today (Fig. E.6d). More recent coastal deposits include a series of postglacial beach ridges visible on the western coast of the lake around the outlet (Fig. E.6b), precisely described by Ikeda et al. (1991). Other deposits largely present all around the lake are beachrocks (Fig. E.6c), which are sedimentary formations hardened by a carbonate cementation, especially visible along the southern and eastern shores (Geyer et al., 2001; Erginal et al., 2012; Öztürk et al., 2016).

E.3.1 General morphology of the terraces and measurement of the deformation

Three levels of lacustrine terraces lie on the northern shore of Iznik Lake. These terraces were described by Ikeda et al. (1991) as markers of previous major high lake stands, preserved by a relative uplift of the northern part of the basin. The terraces were supposedly deposited with a small slope close to the horizontal. The terraces are separated by scarps that result from the wave erosion during the lake high stands. This erosion creates a notch at the base of the scarp, called shoreline angle. When the lake level drops, the erosion of the head of the scarp and the deposition of colluvia at its base buries the shoreline angle. If the scarp is preserved enough, it can still present a slope break called "inner edge", that gives an approximate elevation of the shoreline angle (Fig. E.7). Terrace inner edges can thus be used to retrieve paleoshorelines.

The lowest terrace Tl3 is the clearest all along the coast and presents an inner edge about 20 m high above the present lake level. The intermediate terrace Tl2 can also be followed relatively easily in the west but is hardly visible in the central part around Boyalica village (Fig. E.6). Its scarp reappears in the wider alluvial plain northeast of the lake, with an inner edge 60 m high above the present lake level. The highest and oldest terrace is much more degraded but can still be followed almost continuously in the west with a 110 m high inner edge. In the east, some wave-cut scarp morphologies are also visible though less certain. The formation of the three terraces was dated in chapter B with radiocarbon and *in-situ* produced ^{10}Be, at $20.9^{+6.0}_{-3.5}$ ka, $13.1^{+3.5}_{3.8}$ ka and $4.1^{+2.4}_{-2.9}$ ka BP respectively for Tl1, Tl2 and Tl3.

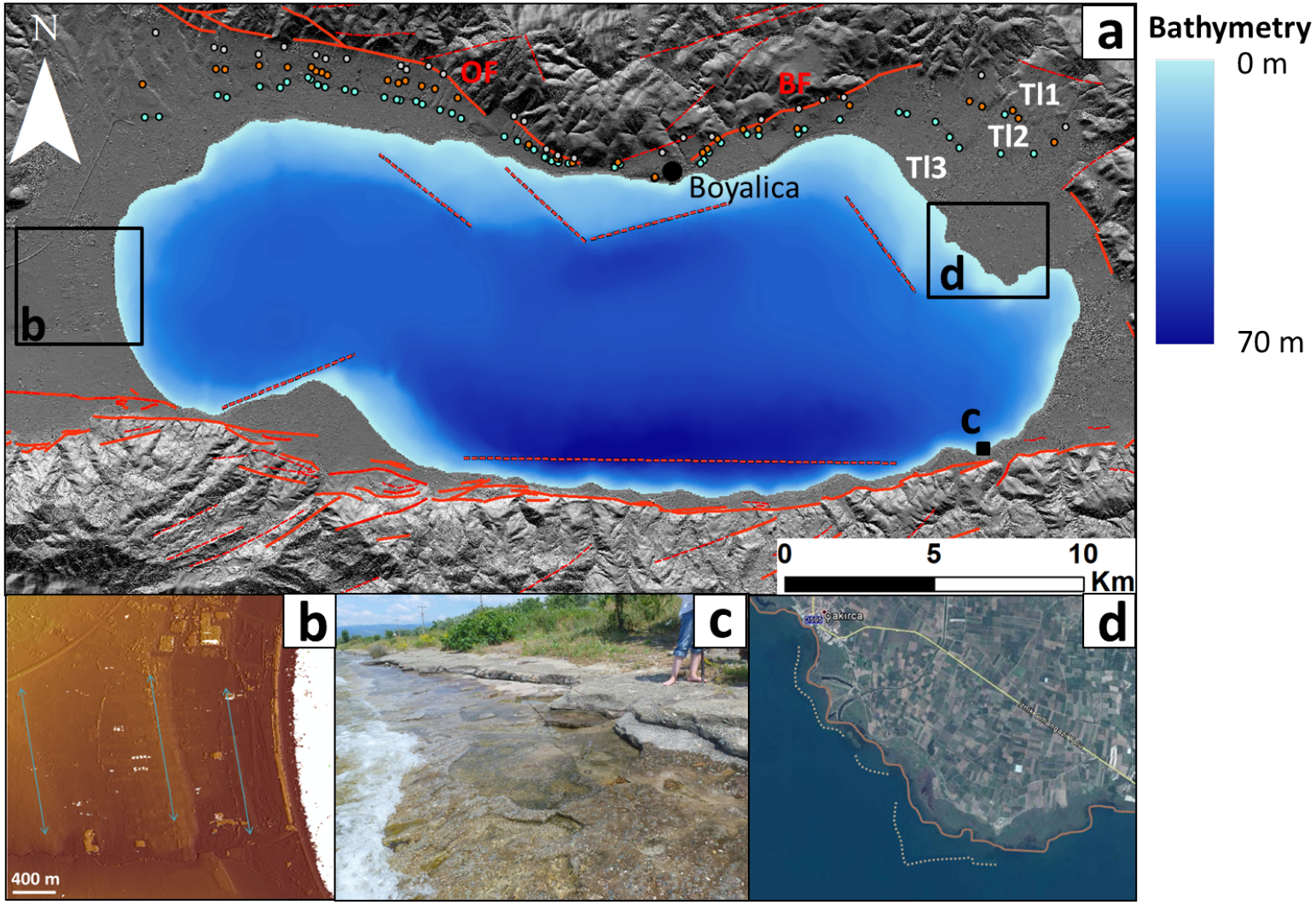

Figure E.6: Examples of past lake level markers. (a) General shaded DEM of Iznik Lake region. Faults are drawn in red (BF = Boyalica fault, OF = Orhangazi fault). The bathymetry is courtesy of DSI. The measured paleoshorelines inner edges are located as color dots (grey: Tl1, orange: Tl2, blue: Tl1). (b) Shaded DEM showing the postglacial beachridges on the eastern shore. (c) Field photograph of beachrocks southeast of the lake. (d) Satellite view of the Karadere river delta, with a submerged shoreline delimited with a broken line.

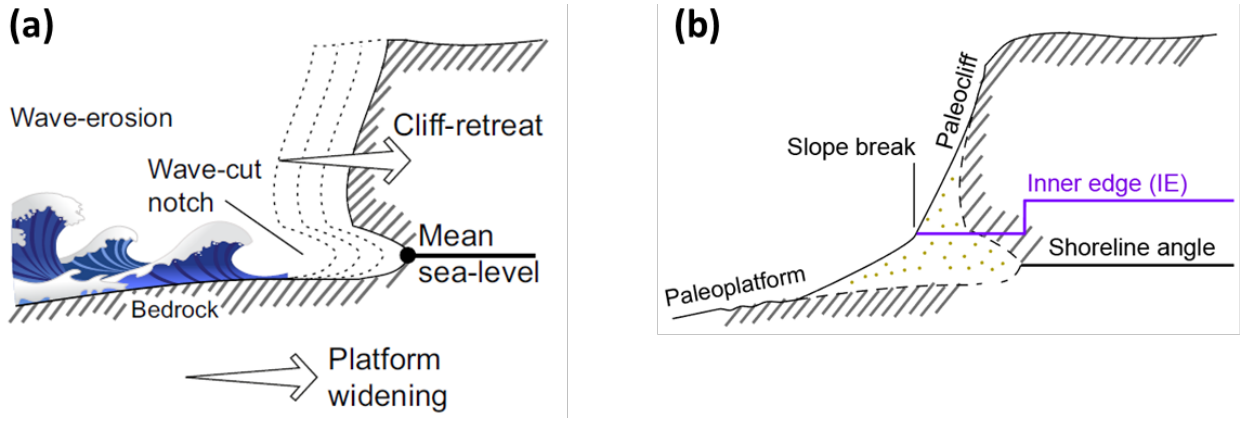

Figure E.7: Formation and preservation of paleoshoreline markers. (a) During lake level highstands, wave erosion may incise a notch at the base of the cliff that marks the position of the mean lake level. (b) The different geomorphic markers used to estimate the terrace elevation. The shoreline angle is covered by sediments but can be approximated by the inner edge, located at the slope break between the eroded paleocliff and the paleoplatform (modified from Jara-Muñoz et al., 2016).

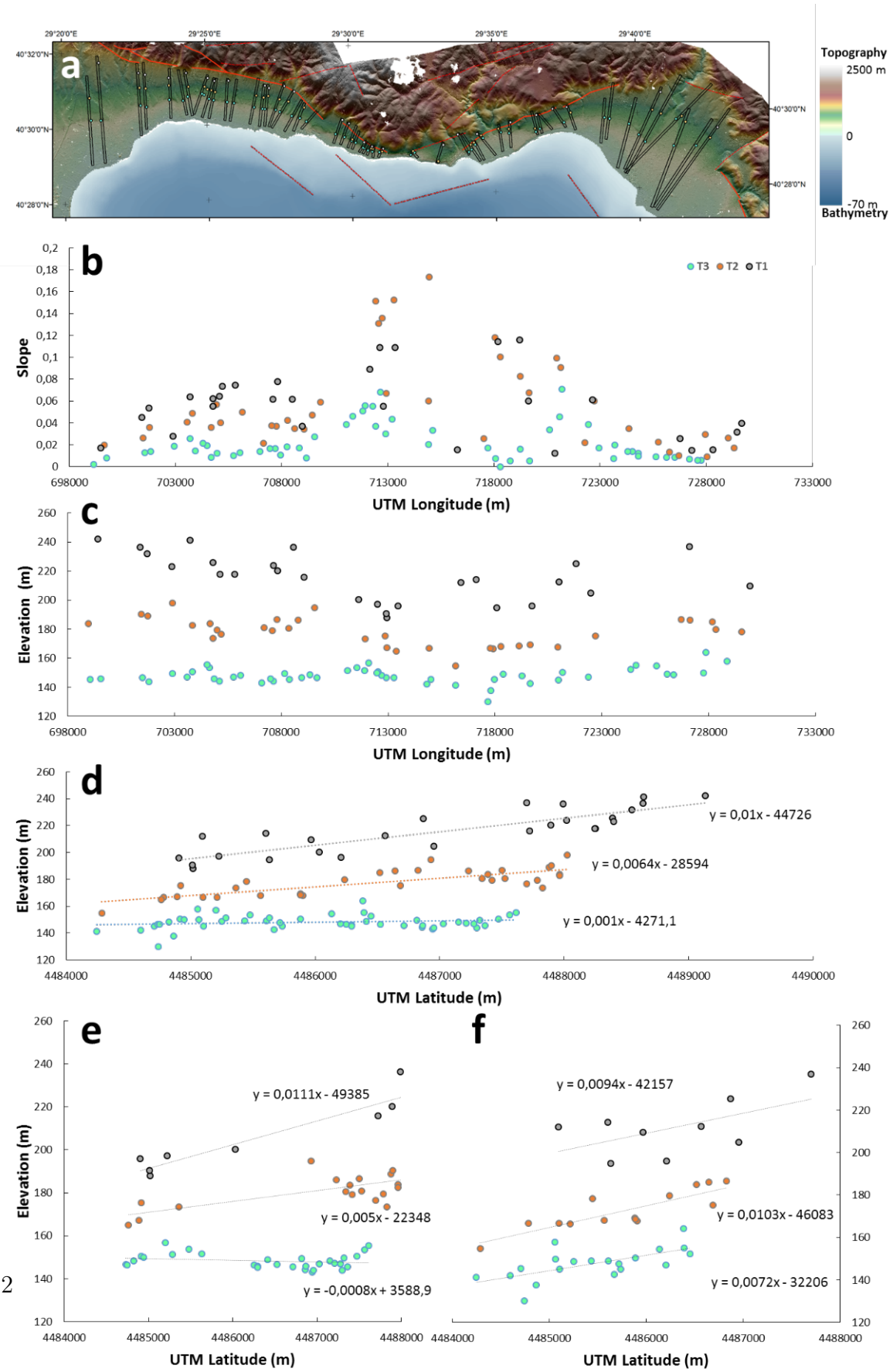
a
29°20'0"E
29°25'0"E
29°30'0"E
29°35'0"E
29°40'0"E
40°32'0"N
40°30'0"N
40°28'0"N
Topography
2500 m
0
-70 m
Bathymetry
b
T3 T2 T1
Slope
UTM Longitude (m)
c
Elevation (m)
UTM Longitude (m)
d
y = 0,01x - 44726
y = 0,0064x - 28594
y = 0,001x - 4271,1
Elevation (m)
UTM Latitude (m)
e
y = 0,0111x - 49385
y = 0,005x - 22348
y = -0,0008x + 3588,9
Elevation (m)
UTM Latitude (m)
f
y = 0,0094x - 42157
y = 0,0103x - 46083
y = 0,0072x - 32206
UTM Latitude (m)

Figure E.8 *(previous page)*: Morphology of the lacustrine terraces north of Iznik Lake. (a) Shaded DEM of the area north of the lake with the main faults mapped on land and inferred from the lake bathymetry in red. The swaths used in TerraceM to extract the terraces profiles are drawn in black and the corresponding inner edges measured are located with color dots. (b) Surface slope evolution along the terraces. The slopes where measured only where the terraces are well developed and at least 100-m large. (c) Inner edges elevations above the present lake level, from west to east. (d) N-S projection of the inner edges elevations, showing increasing tilting with terrace age. (e) N-S projection of the western subset. (f) N-S projection of the eastern subset.

In order to precisely measure the elevation of the inner edges of each terrace along the coast, we used the TerraceM Matlab® GUI developed by Jara-Muñoz et al. (2016) on the Pleiades-derived DEM. With TerraceM a total of 52 ∼100 m large swath profiles were drawn across the terraces and the maximum topography was extracted for further analysis. On each swath, we measured the inner edge elevation and average surface slope of the different terraces when they were visible (Fig. E.8b and c).

	Whole dataset	**Western subset**	**Eastern subset**
Tl3	$9.85.10^{-4}$±$7.88.10^{-4}$	-$7.67.10^{-4}$±0.0014	0.0072±0.0043
Tl2	0.0064±$9.29.10^{-4}$	0.005±0.0029	0.0103±0.0040
Tl1	0.0100±0.0012	0.0111±0.0022	0.0094±0.0119

Table E.1: Tilting values of the lake paleoshorelines. For each terrace, we projected the measured elevations of the inner edges along a N-S axis. To obtain an amount of tilting, we compute the slope of the line obtained by linear regression.

When the entire dataset is considered, we can see that the paleoshorelines, as reconstructed with the inner edges, are not horizontal but tilted toward the south when projected along a N-S axis. The amount of tilt increases with the elevation and therefore the age of the terrace (Fig. E.8c, Table E.1). This confirms the hypotheses of Ikeda et al. (1991) that the terraces were uplifted and preserved thanks to a progressive tilting of the lake basin floor associated to vertical slip on the MNAF south of the lake. It is interpreted as the result of a tectonic deformation accumulated after the formation of each terrace (Fig. E.9). In order to check the spatial homogeneity of this observed deformation, we divided our dataset into two western and eastern subsets (Fig. E.8e,f). The western subset reproduces well the trends of the whole dataset. It is more difficult to find these similar trends on the eastern subset. The data points are more scattered, especially for the Tl1 terrace, which leads to large uncertainties on the slope. It seems that Tl3 inner edges display a more significant southward trend than in the west (Table E.1). Differences between the western and eastern parts of the lake can be expected from their different structural features. In the west, the main faults visible in the morphology are the MNAF in the south and the Orhangazi fault in the north (Fig. E.6a). In the east, several additional, active NE-SW oblique faults cut

the massifs northeast of Iznik and may produce minor deformation components (chapter C, Fig. C.4).

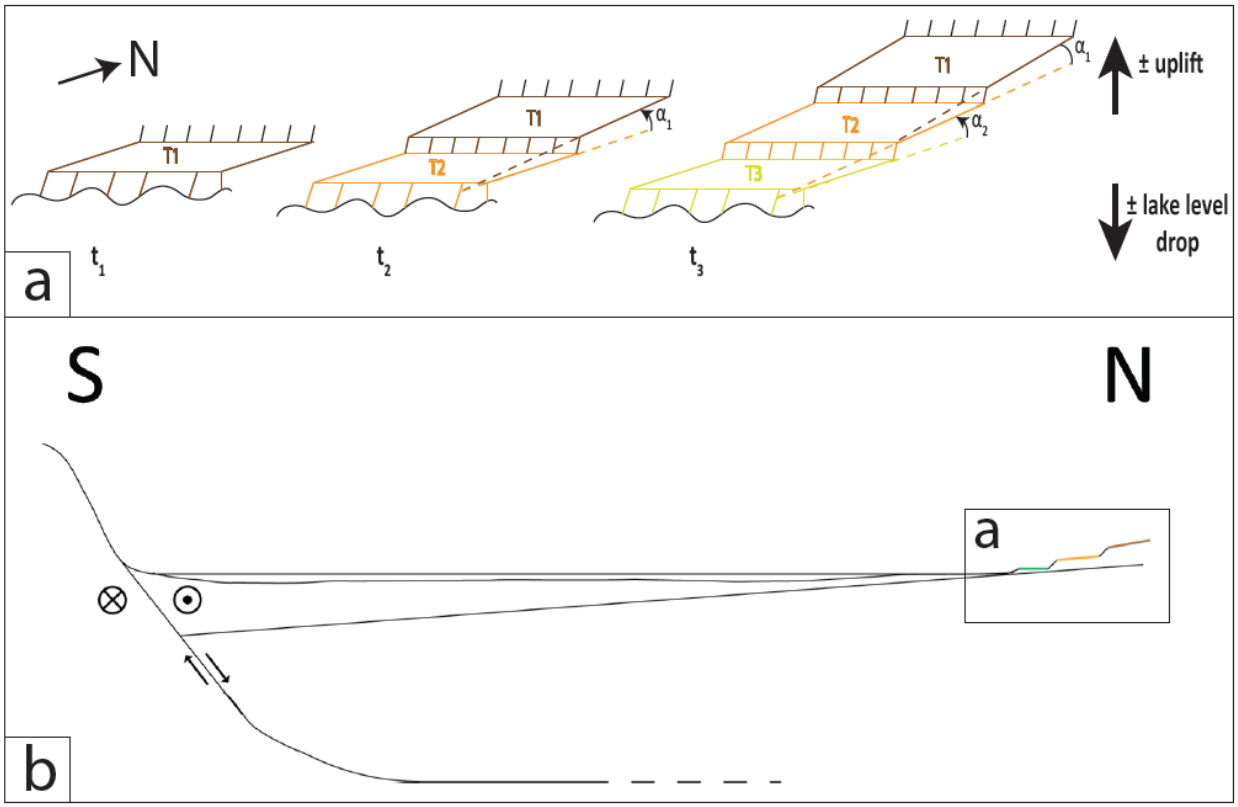

Figure E.9: Conceptual model explaining the terraces uplift and tilting by vertical slip on the MNAF south of the lake. After the terrace is formed during low or high stands of the lake, it is preserved by tectonic uplift. The curved geometry of the fault at depth produces a progressive tilting of the basin that is also observed on the paleoshorelines.

The surface slope values (Fig. E.8b) display a significant dispersion, especially in the central part, close to Orhangazi and Boyalica faults, where all the terraces show higher slopes. In average, the older terraces have a higher slope than the youngest, as was seen for the inner edges. Despite the scarcity of the data for the older terraces in the east, it can be seen that the slope values show a rather convex distribution with higher values at the centre of the lake and lower ones on both sides.

E.3.2 Tectonic and climatic components of the lake level variations observed

We have evidenced that the lacustrine terraces morphology showed evidence of tectonic deformation related to vertical slip on the MNAF. We can then discuss if the current high elevations of these paleoshorelines can be attributed to fault slip, and if these elevations also reflect significant variations of the absolute lake level during the Postglacial period. In a first stage, we assume that the terraces were formed at the present lake level elevation, and that their uplift and tilting is only caused by vertical slip on the MNAF (Fig. E.9). We use the measured tilt of the paleoshorelines to derive a value of uplift following these assumptions, by multiplying the tilting angle by the distance between the MNAF and the terrace scarp. We finally compare these computed terrace elevations to the current ones (Fig. E.10). In average, the computed elevations of Tl1 and Tl2 are higher than the real ones. This suggests that the terraces were not formed at the present lake level but a few tens of meters below. This result is compatible with the proposition of Öztürk et al. (2009) that the lake level was ∼40 m lower than today in the end of the last glacial period (24-12 ka BP) and the dating of beachrocks showing lower lake levels during dry stages around 20 ka BP (Erginal et al., 2012) and 15-9 ka BP (Öztürk et al., 2016). It is also in agreement with other proxies from sediment cores sampled in the lake that indicate low lake levels at 31-17 ka and also around 12 ka BP (Roeser et al., 2012). The theoretical elevation obtained for Tl1 is lower than the current one. This suggests that the terrace was formed at a level higher than today. This might be correlated to humid periods identified in lake sediment cores at 4.72-3.65 ka and 3.3-2.6 ka BP (Ülgen et al., 2012). Beachrocks dating by Öztürk et al. (2016) rather contradict these findings and rather support a dry period between 4.9 and 2.8 ka BP. We emphasize that if we consider the rather large uncertainties on both elevation values, the differences obtained are less significant for Tl1 and Tl2. For Tl3, variations in a similar range to the historical lake level variations (i.e. less than 10 m) may be sufficient to explain the difference obtained.

Keeping the assumption of small lake level variations relatively to the tectonic uplift, the ages of the three terraces presented in chapter B were used to compute tectonic uplift rates. The establishment of each paleoshoreline is constrained in time by the respective ages of the terraces located above and below. Thus, dividing the shoreline elevation by the age of the upper terrace will give a minimum uplift rate. Reciprocally, dividing the shoreline elevation by the age of the lower terrace will give a maximum uplift rate. The results of these calculations are presented in Table E.2. The two minimum rates obtained are relatively similar and around 2 mm/yr. The maximum rates of 11.6 mm/yr has a very large uncertainty because it was computed with the age of the youngest terrace Tl3, which has a larger relative uncertainty. The other maximum rate of 6.09±2.87 is more reliable.

We can then translate this uplift rate in terms of fault slip on the MNAF (Fig. E.11, Table E.2). We use a simple geometrical approach, by reporting the amount of vertical

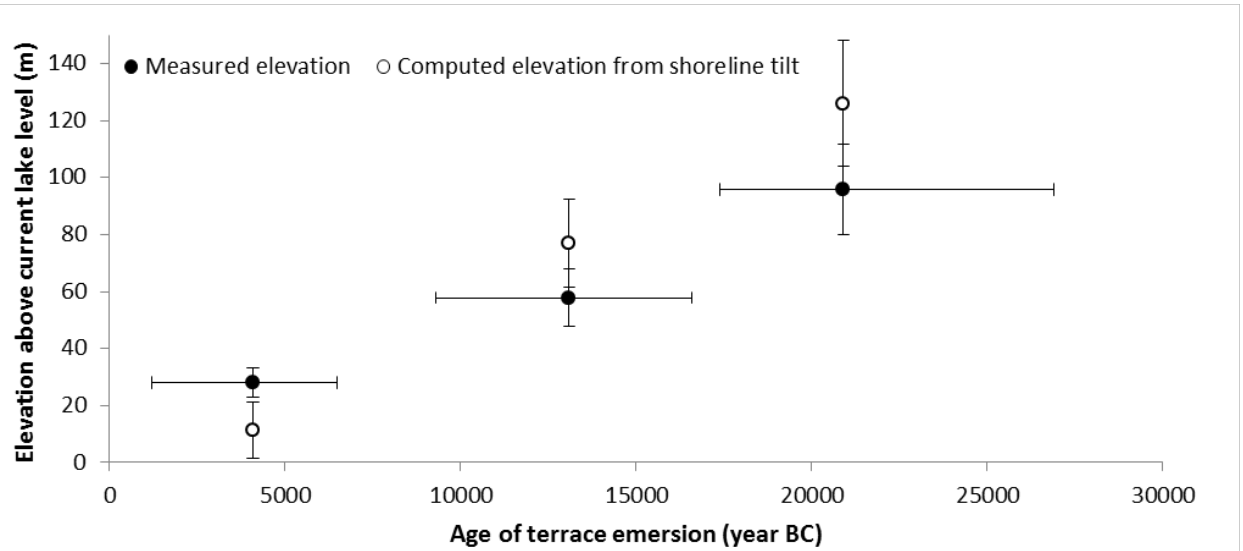

Figure E.10: Comparison between the observed elevation of lacustrine terraces with their reconstructed elevations from the tectonic tilt of the associated paleoshorelines. Using a simple geometric relationship, we multiplied the shoreline tilting angle by the distance to the MNAF to obtain theoretical elevations of the terraces. We assume that after their formation at the current lake level, the terraces are uplifted by vertical slip on the MNAF. We added on the measured points the uncertainties on the ages of the terraces.

uplift on the fault scarp. The corresponding value of slip on fault then depends on the fault dip. For a given value of uplift, a steeper fault will give a smaller slip. We used a value of 70 ° for the fault dip angle, which is an intermediate value between the typical angles of normal and strike-slip faults. The minimum values obtained are around 2 mm/yr. The age of Tl1 constrains a maximal slip rate of 6.48±3.06 mm/yr. Overall, they are in the same range as the horizontal slip rates estimated before on geomorphic markers and by GPS. This suggests that the MNAF segments located south of Iznik Lake present a significant vertical slip component. This can produce oblique slip, as observed on certain segments on shore. We can also suspect that a part of this vertical slip is located on different segments, like the subaqueous faults visible in the bathymetry south of the lake.

The minimum values obtained for the slip rate are larger than the previous estimate of Ikeda et al. (1991) who computed a 1.4 mm/yr minimum slip rate on the MNAF from tilted postglacial beachridges on the western shore of Iznik Lake. However, he used an age of 11 ka, which is obviously too old because these beachridges are younger than the terrace Tl3. Using younger ages, the tilting of these beachridges leads to slip rates in the same range as those presented above. We can also note that the slip rates obtained for the late Pleistocene and Holocene are larger than the vertical slip rate of 0.7 mm/yr derived from the triangular facet slope (chapter C).

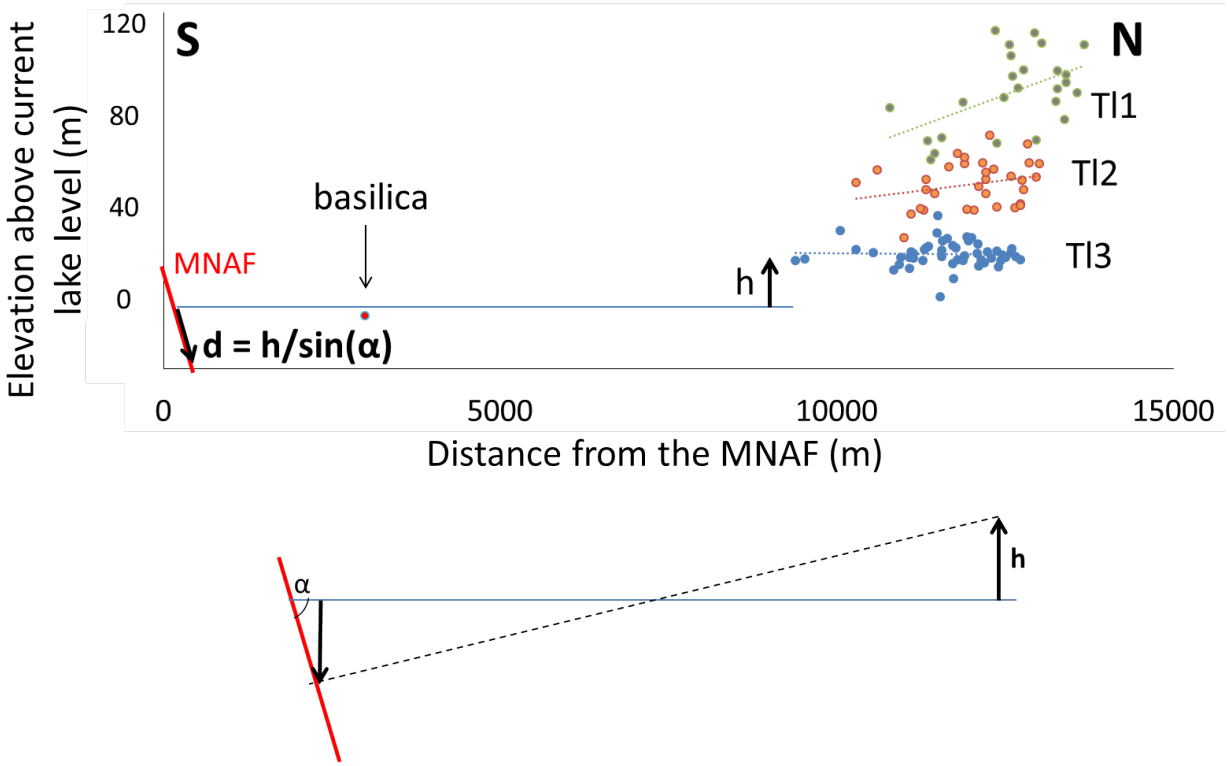

Figure E.11: N-S simplified cross section of Iznik Lake basin (top). The basilica and the lacustrine terraces are placed relatively to the MNAF scarp in the south of the lake. A simple geometrical relationship (bottom) is used to derive a vertical displacement d on the fault from the uplift h measured north of the lake. α is the dip angle of the fault.

	Tl3	Tl2	Tl1
Elevation above the current lake level (m)	28.1±5.3	57.7±9.7	95.8±16.3
Age of terrace (ka BP)	4.1±2.4	13.1±3.5	20.9±3.5
Min uplift rate (mm/yr)	1.76±0.88	2.28±0.85	
Max uplift rate (mm/yr)		11.6±9.18	6.09±2.87
Min vertical slip rate on MNAF (mm/yr)	1.88±0.94	2.43±0.90	
Max vertical slip rate on MNAF (mm/yr)		12.4±9.77	6.48±3.06

Table E.2: Estimation of uplift rates and vertical slip rates on the MNAF from the terraces elevations. For a given paleoshoreline, the minimum and maximum uplift rates are constrained by the upper and lower terraces respectively. The uplift rate is then reported on the MNAF. The fault slip rate is derived from the uplift rate as a function of the fault dip angle.

E.4 Résumé

Ce chapitre traite des marqueurs des variations relatives du niveau du lac d'Iznik, mais aussi du niveau du sol de la ville d'Iznik, à différentes échelles de temps et leurs causes, climatiques ou tectoniques. Dans un premier temps sont présentés les premiers résultats obtenus grâce à l'étude de carottes sédimentaires prélevées sur le site d'une basilique romaine enfouie, découverte en 2014. Cette basilique est considérée par les archéologues comme le lieu où se serait tenu le premier concile de Nicée en 325. Trois carottes ont été prélevées dans la nef de la basilique, une au pied d'un mur courbe protégeant l'édifice, et une dans un petit bâtiment plus éloigné de la côte actuelle. Ces deux dernière carottes contiennent des éléments très grossiers qui suggèrent des courants de très haute énergie, possiblement des tsunamis. Dans les autres carottes, une séquence datée entre les 15ème et et 17ème siècles, est surmontée d'âges antérieurs à la construction de la basilique. Cette inversion chronologique suggère une remobilisation postérieure au 15ème siècle, possiblement lors d'un épisode de liquéfaction lié à un séisme.

Les variations du lac d'Iznik au Moyen-Age ont été étudiées précédemment par Geyer et al. (2001). Cette étude a mis en évidence des variations rapides du niveau du lac, liées selon les auteurs au degré d'obstruction de l'exutoire du lac par la sédimentation naturelle. Des photographies des années 30 montrent un niveau du lac 3 m au-dessus du niveau actuel. A partir des années 50, le niveau du lac est régulé par une station de pompage située à l'exutoire et varie entre 84 et 85 m au-dessus du niveau de la mer. Des variations significatives du niveau du sol sont aussi visibles à Iznik. Les fortifications ont été surélevées au 8ème siècle et au début du 13ème siècle pour compenser ce sol plus haut. L'aqueduc a été partiellement enterré et, à la jonction avec les murs défensifs, reconstruit en s'appuyant sur ce niveau plus élevé de sol. Ceci suggère des événements plutôt rapides et à l'échelle de la ville et ses environs, liés à des crues importantes du lac ou des glissements de terrain sur les pentes du massif carbonaté à l'est d'Iznik.

A l'échelle du Quaternaire, plusieurs marqueurs des variations de niveau sont visibles autour du lac d'Iznik. Trois terrasses lacustres formées à la fin du Pléistocène et à l'Holocène sont notamment visibles au nord du lac. Ces terrasses correspondent à d'anciens hauts niveaux de lac, préservés par la surrection tectonique. Les paléolignes de rivage associées à ces terrasses ont été mesurées sur le MNT haute-résolution en plusieurs points. La projection N-S de ces points fait apparaître un basculement vers le sud, croissant avec l'âge de la terrasse. Ce basculement progressif est interprété comme résultant du glissement vertical sur la faille bordant la rive sud du lac. Ce mécanisme semble suffisant pour expliquer l'élévation des terrasses, en plus de variations du niveau du lac relativement faibles. En utilisant une relation géométrique simple, la surrection des terrasses permet d'estimer le déplacement vertical correspondant sur la MNAF. Les âges des terrasses déterminés au chapitre B donnent des valeurs de glissement entre 2 et 6.5 mm/an, ce qui est du même ordre que le glissement horizontal estimé aussi bien par la géomorphologie que par le GPS.

Conclusions and perspectives

The primary goal of this thesis was to complement the catalogue of the seismicity of the last millennia on the middle strand of the NAF between Mekece and Gemlik using a multidisciplinary approach. The combined results of our geomorphological and archeological studies evidence that this fault strand is capable of producing high magnitude earthquakes, repeated over a millennial time scale. This fault behaviour confirms and explains the historical record of the seismicity that already suggested a significant earthquake hazard for Iznik region. The population of this area seems indeed more at risk from the deformation occuring on the middle strand of the NAF than from the earthquakes rupturing the northern strand, though more active.

A **minimal horizontal slip rate** on the MNAF for the Holocene was estimated on the **Mekece-Sölöz** segment at **5.4±3.4 mm/yr**. This value with its uncertainties is in a similar range to the rate computed by Gasperini et al. (2011), at 3 mm/yr in Gemlik Gulf. Both slip rates are relatively close to the GPS estimate of 5 mm/yr, and it thus seems that the fault slip rate did not vary significantly over the Holocene.

The analysis of cumulated offsets preserved on geomorphic markers led to the identification of the **six last major ruptures** between Gemlik and Mekece. Some of these earthquakes may have propagated on different adjacent segments across the Sölöz releasing stepover. The occurrence of big earthquakes in the vicinity of Iznik was also shown by our archeological study. Several reconstruction stages at the scale of the whole city enabled us to identify three earthquakes: (1) between the **6th and 8th** century AD, (2) between the **9th and late 11th** century AD, and (3) after the **mid-15th** century. The coseismic deformations observed and measured in the city and its surroundings indicate local intensities of **at least VIII** on the EMS98 scale and strong magnitudes **until Mw 7 or more**. Our archeological study has also shown that the MNAF is not the only fault characterized by surface displacement during the historical period. The normal Elbeyli fault has vertically offset Iznik aqueduct by 2 m. More detailed investigations, including trenching, would be required along this fault to find other evidence of recent motion and precise the timing of the measured historical offset.

At the scale of the Mekece-Sölöz fault segment, the fact that the last five ruptures preserved have displaced markers of 22 m on the youngest, 4.1±2.5 ka old terrace of Iznik

Lake provides a very rough idea of the average recurrence of these big, **Mw ∼7 events**, around **1000 years**. This is in agreement with the paleoseismological work of Barka (1993) who only identified three ruptures in the last 4000 years on the same segment. However, the earthquake catalog known from historical seismology and completed by our archeoseismological study support shorter time intervals between successive earthquakes. This apparent discrepancy actually brings interesting information on the fault behavior and its segmentation (Fig. E.12). For instance, Iznik was destroyed by earthquakes in ∼30 AD, 368 AD, around 650 AD and in 1065 AD. The recurrence times between these events is too short to accumulate enough stress on the studied segment and produce the coseismic displacement obtained in the geomorphological study. We can thus propose that these earthquakes did not rupture the same segments of the MNAF. Some of them may have been centered in the west of the fault strand while others were focused on the eastern segments. It is interesting to note that Iznik occupies a rather central position in the fault strand, so earthquakes rupturing various segments are all likely to cause high intensities in the city.

A possible scenario that reconciles the historical catalog with higher recurrence times on individual segments is proposed on Fig. E.12. Some previous paleoseismological studies enable us to better locate two past earthquakes. An ottoman rupture (posterior to 1300) was identified in two trenches in Gemlik and west of Mekece. The trench findings of Uçarkus (2002) indicate a 2000 years old rupture west of Iznik Lake. We note that this time frame includes the 30 AD earthquake. Finally, the 6-8th century event supported by archeological data seems associated with a significant vertical component (chapter E) and possibly ruptured the segments bordering the south of Iznik Lake.

Smaller magnitude events can also be expected. Such earthquakes are documented for the 19th with magnitudes between 4.5 and 6.5. Even if they do not change significantly the balance of stress accumulated along the fault, we have seen in the case of Iznik that they can cause some damage in the areas closer to the fault. These events can rupture parts of the MNAF but also other secondary faults unsuspected before, like the Elbeyli fault as evidenced on the aqueduct. The seismicity of this smaller fault might also partly explain the discrepancies observed between the historical seismicity catalog and the paleoseismological data.

Replacing our scenario at the larger scale of the whole NAF system enables to compare the historical behaviour of the northern and middle strands. Our pluridisciplinary study does not support the occurrence of fast successions of big ruptures along strike, like those observed on the NNAF in the last 800 years (Fig. A.9). This can be linked to the smaller total length of the middle strand and its slower slip rate. Though, possible stress interactions between the two strands in the Marmara region would be worth studying more specifically in stress models. The rupture identified after the 15th century can be integrated in the earthquake sequence that started in 1254 from Erzincan in eastern Anatolia to the Marmara region with earthquakes on the NNAF in 1509 and 1754 (Fig. A.9). Other ruptures in 600-800 and 1065 are more difficult to link with the 967-1050 series of ruptures that propagated eastward in

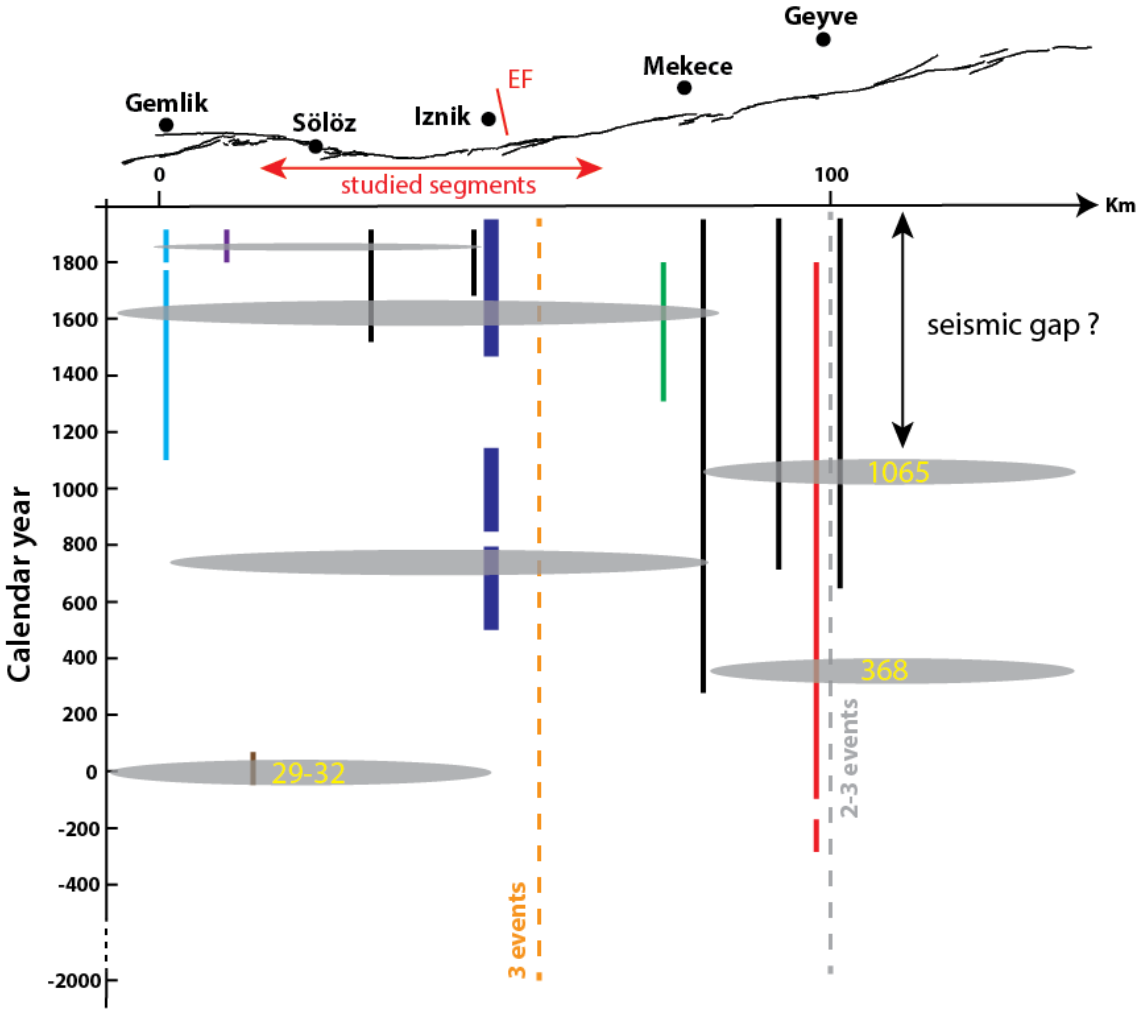

Figure E.12: Geometry of the MNAF (top) with the Elbeyli fault added in red, and synthetic diagram (bottom) presenting the available paleoseismological data (thin color lines, see chapter C for details) and the archeological earthquakes found in Iznik (thick blue line). We draw in grey the possible rupture lengths of the major historical earthquakes known from historical seismology (yellow dates AD) and archeoseismology. This scenario leaves sufficient time between successive earthquakes on individual fault segments to accumulate the stress required for Mw∼7 events. The approximate lengths of the historical events have been derived from the surface magnitudes estimated in the literature. The length of the 500-800 AD event is less constrained. The length of the last major event (around 1600 AD) was extended on the compatible ruptures found in trenches. Finally, the recent rupture drawn thinner may correspond to several small earthquakes described after 1800.

central Anatolia. Our study evidenced a possible seismic gap on the Geyve-Mekece segment,

with no major ruptures since almost 1000 years. This has serious implications for the seismic hazard in this area, and there is a possibility that the next big earthquake in the Marmara region may happen on this segment, before the one expected in the Marmara Sea south of Istanbul. It would thus be interesting to extend our study to the eastern segments of the MNAF to complete the slip rate data along the strand and validate our assumptions about the spatial distribution of past earthquakes and the current stress state.

In the last chapter, we focused on Iznik Lake and the impacts of climate and tectonics on its relative level at various time scales. A significant vertical slip has occurred at least since the late Pleistocene, as shown by the uplift of the lacustrine terraces north of the lake. It is not necessary to invoke large postglacial variations of the lake level, exceeding the historical variations, to explain the observed elevation of the terraces. The study of the terraces show that the tilting and elevation of the corresponding paleoshorelines can be explained by vertical fault slip on the MNAF with rates between **2 and 6.5 mm/yr**. This value is higher than the minimal previous estimate of 1.4 mm/yr (Ikeda et al., 1991). It is also much higher than the 0.7 mm/yr rate derived from the slope of the triangular facets south of the lake. This raises interesting questions about the distribution of the vertical slip across the different fault segments bordering the lake and its evolution in time. Following Öztürk et al. (2009), the triangular facets may represent an older tectonic stage linked to the development of Iznik Lake basin. In this case, the steep subaqueous segment of the MNAF south of the lake may have accommodated most of the vertical deformation in a later period.

The current landscape of Iznik region has been strongly shaped by the MNAF tectonics. This is illustrated by the southern sub-basin of Iznik Lake and the relative high elevation of the mountain ranges that constitute the footwall of the fault. Many markers used in this study to constrain the tectonic activity of the MNAF were formed in the postglacial period. I have also inventoried many features (perched valleys, erratic striated blocks, moraines, elevated lake deposits) suggesting the presence of glaciers that developped at an unusually low elevation. These glaciers were dated in fluvio-glacial deposits to the Last Glacial Maximum and possibly earlier. The end of this glaciation is bounded by the age of the oldest lake terrace preserved around 23 ka. These unexpected findings should lead to revisit the effects of the past climatic variation and the previous extent of glaciers in northwestern Turkey.

It is also very likely that the landscape includes elements inherited from older tectonic stages. The million year time scale is not covered by this thesis and would be worth investigating in future works. During its formation, the MNAF has evidently reactivated previous faults with different anterior kinematics. A better knowledge of the large scale geometry of these structures at depth and their interactions might help to understand the development of Iznik Lake basin and the transition towards the neotectonic stage. This would also require to investigate the role of Orhangazi and Boyalica faults north of the lake, as well as other parallel structures seen in the bathymetry. A particularly intriguing NE-SW structure

seems to cross the lake, passing along the northern borders of Sölöz delta and the northern sub-basin (Fig E.13). It is associated with left-lateral offsets of the lake shore, and could be interpreted as an R' anti-Riedel fault that was rotated by the dextral deformation.

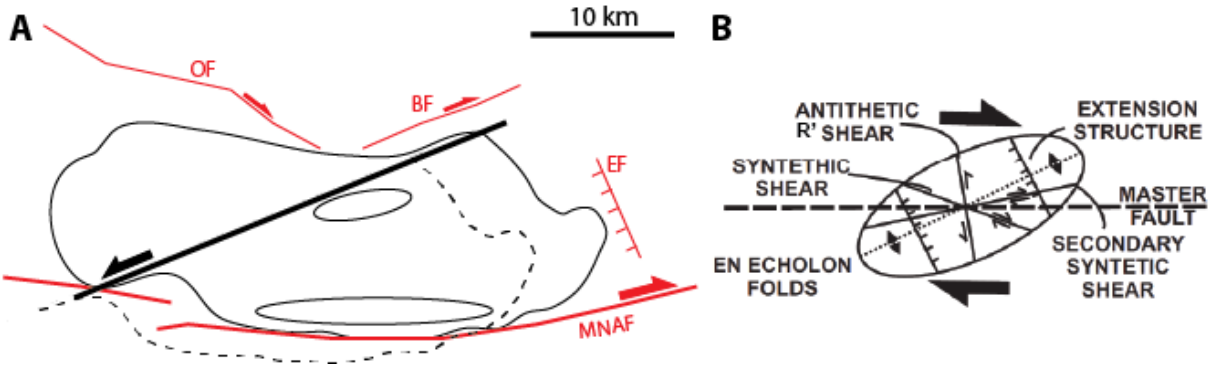

Figure E.13: (A) Simplified sketch of the structural setting of Iznik Lake basin. The main active faults are drawn in red (BF = Boyalica fault, EF = Elbeyli fault, OF = Orhangazi fault). The thick black line is a transversal structure with a left-lateral component visible on its intersection with the lake shores. A retrodeformation of the lake along this structure is proposed as a black broken line. (B) Strain ellipse for a dextral strike-slip deformation (from Wilcox et al., 1973). This transversal structure is compatible with an antithetic R' fault that was rotated clockwise.

From a methodological aspect, we are now able to point out certain limitations and recommandations for the archeoseismological approach. We have commented in section D.3 that in cities affected by repeated earthquakes, the systematic repairs and the removal of the most damaged buildings was likely to produce a bias towards lower intensities when the damaged are surveyed several centuries later. The ideal case where to perform this kind of study would be a "petrified" or abandonned city following the last earthquake. In continuously inhabited cities like Iznik, the archeological damage surveys can still be interesting to study the small deformations, especially in areas of moderate seismicity. They are less relevant to estimate intensities for the bigger events as many buildings may have been totally destroyed. That is where the numerical modeling of selected buildings stands as a good tool because it allows to test ground motion scenarios and deduce semi-quantitative constrains on the possible earthquakes investigated. Another point that we are not the first to make is that archeoseismology gets more powerful when it is used in combination with other more conventional approaches of paleoseismology. This is necessary to replace the archeological observations and interpretations in a wider and more precise seismotectonic context.

The discovery of the submerged basilica at the very beginning of my PhD project enabled to discuss other possible consequences of the earthquakes, like lake tsunamis and liquefaction. Thanks to our study, the history of this emblematic site have been precised. From our perspective, the most enticing prospects to pursue the study of the recent activity of the MNAF, as part of a future thesis, lie under the lake surface. High-resolution

bathymetrical and seismic data on the subaqueous faults in Iznik Lake may reveal very well preserved markers of Quaternary deformation. The study of a long sediment core sampled in the deepest sub-basin close to the MNAF could also provide a continuous archive of past earthquakes, possibly over ∼35 kyr, that could be compared to the present catalogue and shed light on the behavior of the MNAF over a bigger number of earthquake cycles. This could for example evidence if at longer time scales, the MNAF is characterized by periods of strong activity alternating with periods of relative quiescence.

Bibliography

Abbasoglu, H. and Delemen, I. (2003). Remains from Ancient Nicaea. In Akbaygil, I., Inalcik, H., and Aslanapa, O. (Eds.), *Iznik Throughout History*, pp. 189–197. Türkiye Is Bankasi, Istanbul.

Adams, F. D. (1912). An Experimental Contribution to the Question of the Depth of the Zone of Flow in the Earth's Crust. *The Journal of Geology*, 20(2):97–118.

Akçar, N., Yavuz, V., Ivy-Ochs, S., Reber, R., Kubik, P. W., Zahno, C., and Schlüchter, C. (2014). Glacier response to the change in atmospheric circulation in the eastern Mediterranean during the Last Glacial Maximum. *Quaternary Geochronology*, 19:27 – 41.

Akay, G. and Ozener, H. (2009). Investigation of long period crustal deformation on the inactive branch of the North Anatolian Fault Zone. *Natural Hazards and Earth System Sciences*, 9(3):663–671.

Akbulak, C. (2009). Human and Economic Geographical Investigation of Iznik Basin. Technical report, Eurasia Ethnography Foundation Publications, Ankara.

Aki, K. (1984). Asperities, barriers, characteristic earthquakes and strong motion prediction. *Journal of Geophysical Research: Solid Earth*, 89(B7):5867–5872.

Akkoyunlu, A. (2003). Evaluation of eutrophication process in Lake Iznik. *Fresenius Environmental Bulletin*, 12(7):801–807.

Aksu, A., Hiscott, R., and Yaşar, D. (1999). Oscillating Quaternary water levels of the Marmara Sea and vigorous outflow into the Aegean Sea from the Marmara Sea–Black Sea drainage corridor. *Marine Geology*, 153(1):275 – 302.

Akyüz, S., Dogan, B., Aksoy, M. E., Tigli, O., and Zabci, C. (2014). Preliminary Paleoseismological results of the Middle Strand of the North Anatolian Fault (NAF) in the Marmara Region, NW Turkey. In *Geophysical Research Abstracts*, volume 16. EGU2014-5451.

Allen, C. R. (1969). Active faulting in northern Turkey. Division Geol. Sci. Contr. 1577, California Institute of Technology.

Alpar, B. and Yaltırak, C. (2002). Characteristic features of the North Anatolian Fault in the eastern Marmara region and its tectonic evolution. *Marine Geology*, 190(1):329 – 350.

Alpar, B., Öztürk, K., Adatepe, F., Demirel, S., and Balkis, N. (2003). Sparker in lakes; reflection data from Lake Iznik. *Turkish J. Marine Science*, 9 (3):195–206.

Ambraseys, N. (1970). Some characteristic features of the North Anatolian fault zone. *Tectonophysics*, 9(2):143 – 165.

Ambraseys, N. (1985). Intensity-attenuation and magnitude-intensity relationships for Northwest European earthquakes. *Earthquake Engineering & Structural Dynamics*, 13(6):733–778.

Ambraseys, N. (2000). The Seismicity of the Marmara Sea Area 1800-1899. *Journal of Earthquake Engineering*, 4(3):377–401.

Ambraseys, N. (2002). The Seismic Activity of the Marmara Sea Region over the Last 2000 Years. *Bulletin of the Seismological Society of America*, 92(1):1–18.

Ambraseys, N. (2006). Earthquakes and archaeology. *Journal of Archaeological Science*, 33(7):1008 – 1016.

Ambraseys, N. (2009). *Earthquakes in the Mediterranean and Middle East. A multidisciplinary study of seismicity up to 1900*. Cambridge University Press, Cambridge.

Ambraseys, N. and Finkel, C. (1991). Long-term seismicity of Istanbul and of the Marmara Sea region. *Terra Nova*, 3(5):527–539.

Ambraseys, N. and Jackson, J. A. (2000). Seismicity of the Sea of Marmara (Turkey) since 1500. *Geophysical Journal International*, 141(3):F1.

Angold, M. J. (1991). Empire of Nicaea (1204-61). In Kazhdan, A. (Ed.), *Ofxford Dictionary of Byzantium*. Oxford University Press.

Ansberque, C., Bellier, O., Godard, V., Lasserre, C., Wang, M., Braucher, R., Talon, B., de Sigoyer, J., Xu, X., and Bourlès, D. L. (2016). The Longriqu fault zone, eastern Tibetan Plateau: Segmentation and Holocene behavior. *Tectonics*, 35(3):565–585. 2015TC004070.

Argant, J. (2004). Données palynologiques. In Geyer, B. and Lefort, J. (Eds.), *La Bithynie au Moyen Âge*, pp. 175–200. Lethielleux, Paris.

Armijo, R., Meyer, B., Hubert, A., and Barka, A. A. (1999). Westward propagation of the North Anatolian fault into the northern Aegean: Timing and kinematics. *Geology*, 27:267–270.

Armijo, R., Meyer, B., King, G. C. P., Rigo, A., and Papanastassiou, D. (1996). Quaternary evolution of the Corinth Rift and its implications for the Late Cenozoic evolution of the Aegean. *Geophysical Journal International*, 126(1):11–53.

Armijo, R., Meyer, B., Navarro, S., King, G., and Barka, A. (2002). Asymmetric slip partitioning in the Sea of Marmara pull-apart: a clue to propagation processes of the North Anatolian Fault? *Terra Nova*, 14(2):80–86.

Baillet, L., Linck, V., D'Errico, S., Laulagnet, B., and Berthier, Y. (2005). Finite element simulation of dynamic instabilities in frictional sliding contact. *Journal of Tribology*, 127 (3):652–657.

Balco, G., Stone, J. O., Lifton, N. A., and Dunai, T. J. (2008). A complete and easily accessible means of calculating surface exposure ages or erosion rates from ^{10}Be and ^{26}Al measurements. *Quaternary Geochronology*, 3(3):174 – 195.

Bargu, S. (1982). The Geology of Iznik-Yenisehir (Bursa) Osmaneli (Bilecik) Area. *Istanbul Earth Science Review*, 3(1-2):191–234.

Bariş, Ş., Ito, A., Üçer, S. B., Honkura, Y., Kafadar, N., Pektaş, R., Komut, T., and Işikara, A. M. (2002). Microearthquake Activity before the İzmit Earthquake in the Eastern Marmara Region, Turkey (1 January 1993-17 August 1999). *Bulletin of the Seismological Society of America*, 92(1):394–405.

Barka, A. (1992). The North Anatolian fault zone. *Annales Tectonicae*, 6:164–195.

Barka, A. (1993). Kuzey Anadolu Fayı'nın Sapanca-Izmit ve Geyve-Iznik Kolları üzerinde Paleosismik Arastırmalar. Technical report, TÜBITAK, Istanbul. Proje No:YBAG-4/7551.

Barka, A. (1996). Slip distribution along the North Anatolian fault associated with the large earthquakes of the period 1939 to 1967. *Bulletin of the Seismological Society of America*, 86(5):1238–1254.

Barka, A. (1999). The 17 August 1999 Izmit Earthquake. *Science*, 285(5435):1858–1859.

Barka, A. and Kadinsky-Cade, K. (1988). Strike-slip fault geometry in Turkey and its influence on earthquake activity. *Tectonics*, 7(3):663–684.

Bellier, O., Över, S., Poisson, A., and Andrieux, J. (1997). Recent temporal change in the stress state and modern stress field along the North Anatolian Fault Zone (turkey). *Geophysical Journal International*, 131(1):61–86.

Berthier, E., Vincent, C., Magnússon, E., Gunnlaugsson, A. ., Pitte, P., Le Meur, E., Masiokas, M., Ruiz, L., Pálsson, F., Belart, J. M. C., and Wagnon, P. (2014). Glacier topography and elevation changes derived from Pléiades sub-meter stereo images. *The Cryosphere*, 8(6):2275–2291.

Bilham, R., Gaur, V. K., and Molnar, P. (2001). Himalayan seismic hazard. *Science*, 293(5534):1442–1444.

Bilham, R., Ozener, H., Mencin, D., Dogru, A., Ergintav, S., Cakir, Z., Aytun, A., Aktug, B., Yilmaz, O., Johnson, W., and Mattioli, G. (2016). Surface creep on the North

Anatolian Fault at Ismetpasa, Turkey, 1944–2016. *Journal of Geophysical Research: Solid Earth*, 121(10):7409–7431.

Birman, J. H. (1968). Glacial reconnaissance in Turkey. *Geological Society of America Bulletin*, 79:1009–1026.

Bridgman, P. W. (1936). Shearing phenomena at high pressure of possible importance for geology. *The Journal of Geology*, 44(6):653–669.

Bridgman, P. W. (1945). Polymorphic transitions and geological phenomena. *Am. J. Sci.*, 243a:90–97.

Bronk Ramsey, C. (2009). Bayesian analysis of radiocarbon dates. *Radiocarbon*, 51(1):337–360.

Brounoff, N. (1925). L'église de Sainte-Sophie de Nicée. *Echos d'Orient*, 24:471–481.

Broxton, M. J. and Edwards, L. J. (2008). The Ames Stereo Pipeline: Automated 3D Surface Reconstruction from Orbital Imagery. In *Lunar and Planetary Science Conference*, volume 39. abstract 2419.

Bukowiecki, E., Dessales, H., and Dubouloz, J. (2008). *Ostie, l'eau dans la ville : châteaux d'eau et réseau d'adduction*. Ecole Française de Rome, Rome.

Çağatay, M., Görür, N., Algan, O., Eastoe, C., Tchapalyga, A., Ongan, D., Kuhn, T., and Kuşcu, I. (2000). Late Glacial–Holocene palaeoceanography of the Sea of Marmara: timing of connections with the Mediterranean and the Black Seas. *Marine Geology*, 167(3):191–206.

Çağatay, M., Görür, N., Polonia, A., Demirbağ, E., Sakınç, M., Cormier, M.-H., Capotondi, L., McHugh, C., Emre, Ö., and Eriş, K. (2003). Sea-level changes and depositional environments in the İzmit Gulf, eastern Marmara Sea, during the late glacial–Holocene period. *Marine Geology*, 202(3):159–173.

Cahen, C. (1948). La Première Pénétration Turque en Asie Mineure. *Byzantion*, 18:5–67.

Cakir, Z., Akoglu, A. M., Belabbes, S., Ergintav, S., and Meghraoui, M. (2005). Creeping along the Ismetpasa section of the North Anatolian fault (Western Turkey): Rate and extent from InSAR. *Earth and Planetary Science Letters*, 238(1):225–234.

Cambazoğlu, S., Koçkar, M. K., and Akgün, H. (2016). A generalized seismic source model for the Eastern Marmara Region along the segments of the North Anatolian Fault System. *Soil Dynamics and Earthquake Engineering*, 88:412–426.

Caputo, R. and Helly, B. (2008). The use of distinct disciplines to investigate past earthquakes. *Tectonophysics*, 453(1):7–19.

Chaput, E. (1936). *Voyages d'études géologiques et géomorphogéniques en Turquie*, volume 2. De Boccard.

Chmeleff, J., von Blanckenburg, F., Kossert, K., and Jakob, D. (2010). Determination of the ^{10}Be half-life by multicollector ICP-MS and liquid scintillation counting. *Nuclear Instruments and Methods in Physics Research Section B: Beam Interactions with Materials and Atoms*, 268(2):192–199.

Cilgin, Z., Bayrakdar, C., and Oliphant, J. S. (2014). An example of polygenetic geomorphologic development (Karst-Glacial-Tectonics) on Munzur Mountains: Kepir Cave-Elbala spring karstic system. *International Journal of Human Sciences*, 11 (1):89–104.

Ciner, A. (2003). Une revue de la répartition et de l'extension des glaciations pléistocènes et des glaciers actuels en Turquie. *Géographie physique et Quaternaire*, 57(2-3):205–218.

Colardelle, R. (2013). *Saint-Laurent de Grenoble - De la crypte au musée archéologique*. Presses Universitaires de Grenoble.

D'Amico, V., Albarello, D., and Mantovani, E. (1999). A distribution-free analysis of magnitude-intensity relationships: an application to the Mediterranean region. *Physics and Chemistry of the Earth, Part A: Solid Earth and Geodesy*, 24(6):517–521.

Defremery, C. and Sanguinetti, B. R. (1968). *Voyages d'Ibn Battuta*, volume IV. Anthropos, Paris.

deMenocal, P., Ortiz, J., Guilderson, T., and Sarnthein, M. (2000). Coherent High- and Low-Latitude Climate Variability During the Holocene Warm Period. *Science*, 288(5474):2198–2202.

Dikbas, A. and Akyüz, H. S. (2011). Palaeoseismological Investigations on the Karadere Fault Segment, North Anatolian Fault Zone, Turkey. *Turkish J. Earth Sci.*, 20:395–409.

Dogan, B. (2010). *Kuzey Anadolu Fay Sistemi Güney Kolunun Geyve-Gemlik Arasindaki Kesiminin Morfotektonik, Tektonostratigrafik ve Paleosismolojik Evrimi*. PhD thesis, Istanbul Teknik Üniversitesi.

Doğan, B., Tüysüz, O., and Şanlı, F. B. (2015). Tectonostratigraphic evolution of the basins on the southern branch of the North Anatolian Fault System in the SE Marmara Region, Turkey. *International Journal of Earth Sciences*, 104(2):389–418.

DSI (1974). Iznik, Orhangazi and Gemlik plains - Hydrogeological investigation report. Technical report, Ministry of Energy and Natural Resources of Turkey.

Dunai, T. J. (2010). *Cosmogenic Nuclides: Principles, Concepts and Applications in the Earth Surface Sciences*. Cambridge University Press.

Dunne, J., Elmore, D., and Muzikar, P. (1999). Scaling factors for the rates of production of cosmogenic nuclides for geometric shielding and attenuation at depth on sloped surfaces. *Geomorphology*, 27(1):3–11.

Emre, Ö., Duman, T. Y., and Özalp, S. (2011). 1:250.000 Ölçekli Türkiye Diri Fay Haritası Serisi. Technical report, Maden Tetkik ve Arama Genel Müdürlüğü, Ankara.

Emre, Ö., Erkal, T., Tchepalyga, A., Kazanci, N., Keçer, M., and Ünay, E. (1998). Neogene-Quaternary Evolution of the Eastern Marmara Region, Northwest Turkey. *Mineral Res. Expl. Bull.*, 120:116–145.

Erdik, M., Doyuran, V., Akkas, N., and Gulkan, P. (1985). A Probabilistic Assessment of the Seismic Hazard in Turkey. *Tectonophysics*, 117:295–344.

Ergin, M., Kazanci, N., Varol, B., Özden Ileri, and Karadenizli, L. (1997). Sea-level changes and related depositional environments on the southern Marmara shelf. *Marine Geology*, 140(3):391–403.

Erginal, A. E., Kiyak, N. G., Öztürk, M. Z., Avcioglu, M., Bozcu, M., and Yigitbas, E. (2012). Cementation characteristics and age of beachrocks in a fresh-water environment, Lake Iznik, NW Turkey. *Sedimentary Geology*, 243-244:148–154.

Ergintav, S., Reilinger, R. E., Çakmak, R., Floyd, M., Cakir, Z., Doğan, U., King, R. W., McClusky, S., and Özener, H. (2014). Istanbul's earthquake hot spots: Geodetic constraints on strain accumulation along faults in the Marmara seismic gap. *Geophysical Research Letters*, 41(16):5783–5788. 2014GL060985.

Eriş, K. K., Çağatay, M. N., Akçer, S., Gasperini, L., and Mart, Y. (2011). Late glacial to Holocene sea-level changes in the Sea of Marmara: new evidence from high-resolution seismics and core studies. *Geo-Marine Letters*, 31(1):1–18.

Faccenna, C., Bellier, O., Martinod, J., Piromallo, C., and Regard, V. (2006). Slab detachment beneath eastern Anatolia: A possible cause for the formation of the North Anatolian fault. *Earth and Planetary Science Letters*, 242(1):85 – 97.

Flerit, F., Armijo, R., King, G. C. P., Meyer, B., and Barka, A. (2003). Slip partitioning in the Sea of Marmara pull-apart determined from GPS velocity vectors. *Geophysical Journal International*, 154(1):1–7.

Foss, C. (1982). The defences of Asia Minor against the Turks. *Greek Orthodox Theological Review*, 27:145–205.

Foss, C. (1996). *Nicaea: A Byzantine Capital and Its Praises*. Holy Cross Orthodox Press.

Foss, C. and Winfield, D. (1986). *Byzantine Fortifications: An Introduction*. University of South Africa Press, Pretoria.

Fournié, E. (2016). La plus vieille église de Nîmes. *Archéologia*, 547:14–14.

Franz, S. O., Schwark, L., Brüchmann, C., Scharf, B., Klingel, R., Van Alstine, J. D., Çagatay, N., and Ülgen, U. B. (2006). Results from a Multi-disciplinary Sedimentary Pilot Study of Tectonic Lake Iznik (NW Turkey) – Geochemistry and Paleolimnology of the Recent Past. *Journal of Paleolimnology*, 35(4):715–736.

Fraser, C., Dial, G., and Grodecki, J. (2006). Sensor orientation via RPCs. *ISPRS Journal of Photogrammetry and Remote Sensing*, 60(3):182 – 194.

Fraser, J., Vanneste, K., and Hubert-Ferrari, A. (2010). Recent behavior of the North Anatolian Fault: Insights from an integrated paleoseismological data set. *Journal of Geophysical Research: Solid Earth*, 115(B9):B09316.

French, D. H. (1967). Prehistoric Sites in Northwest Anatolia: I. The Iznik Area. *Anatolian Studies*, 17:49–100.

Fu, B., Ninomiya, Y., Lei, X., Toda, S., and Awata, Y. (2004). Mapping active fault associated with the 2003 Mw 6.6 Bam (SE Iran) earthquake with ASTER 3D images. *Remote Sensing of Environment*, 92(2):153–157.

Galadini, F., Hinzen, K.-G., and Stiros, S. (2006). Archaeoseismology: Methodological issues and procedure. *Journal of Seismology*, 10(4):395–414.

Galli, P. A. C., Giocolli, A., Naso, J. A., Piscitelli, S., Rizzo, E., Capini, S., and Scaroina, L. (2010). Faulting of the roman aqueduct of venafrum (southern italy): Methods of investigation, results, and seismotectonic implications. *Geological Society of America Special Papers*, 471:233–242.

Galli, P. A. C. and Naso, J. A. (2009). Unmasking the 1349 earthquake source (southern Italy): paleoseismological and archaeoseismological indications from the Aquae Iuliae fault. *Journal of Structural Geology*, 31(2):128–149.

Garduño-Monroy, V. H., Benavente Escobar, C., A., O., Rodríguez-Pascua, M. A., Perez Lopez, R., and Giner, J. L. (2012). Evidence of past seisms in Cusco (Peru) and Tzintzuntzan (Mexico) : cultural relations. In *3rd INQUA-IGCP-567 International Workshop on Active Tectonics, Paleoseismology and Archaeoseismology*, Morelia, Mexico.

Gasperini, L., Polonia, A., Çağatay, M. N., Bortoluzzi, G., and Ferrante, V. (2011). Geological slip rates along the North Anatolian Fault in the Marmara region. *Tectonics*, 30(6):TC6001.

Gerritsen, F., Fokke, A., Özbal, R., and Thissen, L. C. (2013). The Earliest Neolithic Levels at Barcin Höyük, Northwestern Turkey. *Anatolica*, 39:53–92.

Geyer, B., Dalongeville, R., and Lefort, J. (2001). Les niveaux du lac de Nicée au Moyen Âge. In Martin, J. M. (Ed.), *Zones côtières littorales dans le monde méditerranéen au Moyen Âge : défense, peuplement, mise en valeur*, volume 7 of *Castrum*, pp. 77–93. Casa de Velazquez, Rome-Madrid.

Gosse, J. C. and Phillips, F. M. (2001). Terrestrial in situ cosmogenic nuclides: theory and application. *Quaternary Science Reviews*, 20(14):1475 – 1560.

Gürbüz, C., Aktar, M., Eyidogan, H., Cisternas, A., Haessler, H., Barka, A., Ergin, M., Türkelli, N., Polat, O., Üçer, S., Kuleli, S., Baris, S., Kaypak, B., Bekler, T., Zor, E., Bicmen, F., and Yoruk, A. (2000). The seismotectonics of the Marmara region (Turkey): results from a microseismic experiment. *Tectonophysics*, 316(1):1–17.

Grischott, R., Kober, F., Lupker, M., Reitner, J. M., Drescher-Schneider, R., Hajdas, I., Christl, M., and Willett, S. D. (2017). Millennial scale variability of denudation rates for the last 15 kyr inferred from the detrital 10Be record of Lake Stappitz in the Hohe Tauern massif, Austrian Alps. In *Geophysical Research Abstract*, volume 19. European Geophysical Union.

Grélois, J.-P. (1998). *Dr. John Covel : Voyages en Turquie 1675-1677*. Lethielleux.

Grélois, J.-P. (2004). Hans Dernschwam, voyage en Asie Mineure (1555). In Geyer, B. and Lefort, J. (Eds.), *La Bithynie au Moyen Âge*, pp. 120–121. Lethielleux, Paris.

Grünthal, G. and Levret, A. (2001). *L'échelle macrosismique européenne*. Conseil de l'Europe.

Guidoboni, E., Comastri, A., and Traina, G. (1994). *Catalogue of ancient earthquakes in the Mediterranean area up to the 10th century*. Istituto Nazionale di Geofisica.

Guidoboni, E. and Stucchi, M. (1993). The contribution of historical records of earthquakes to the evaluation of seismic hazard. *Annals of Geophysics*, 36(3-4).

Gutenberg, B. and Richter, C. F. (1954). *Seismicity of the Earth and Associated Phenomena*. Princeton University Press, Princeton, New Jersey.

Gutenberg, B. and Richter, C. F. (1956). Earthquake magnitude, intensity, energy, and acceleration. *Bulletin of the Seismological Society of America*, 46(2):105–145.

Heisinger, B., Lal, D., Jull, A., Kubik, P., Ivy-Ochs, S., Knie, K., and Nolte, E. (2002a). Production of selected cosmogenic radionuclides by muons: 2. capture of negative muons. *Earth and Planetary Science Letters*, 200(3):357 – 369.

Heisinger, B., Lal, D., Jull, A., Kubik, P., Ivy-Ochs, S., Neumaier, S., Knie, K., Lazarev, V., and Nolte, E. (2002b). Production of selected cosmogenic radionuclides by muons: 1. fast muons. *Earth and Planetary Science Letters*, 200(3):345 – 355.

Hetényi, G., Le Roux-Mallouf, R., Berthet, T., Cattin, R., Cauzzi, C., Phuntsho, K., and Grolimund, R. (2016). Joint approach combining damage and paleoseismology observations constrains the 1714 A.D. Bhutan earthquake at magnitude 8±0.5. *Geophysical Research Letters*, 43(20):10,695–10,702.

Hidy, A. J., Gosse, J. C., Pederson, J. L., Mattern, J. P., and Finkel, R. C. (2010). A geologically constrained Monte Carlo approach to modeling exposure ages from profiles of cosmogenic nuclides: An example from Lees Ferry, Arizona. *Geochemistry, Geophysics, Geosystems*, 11(9):Q0AA10.

Hilbe, M. and Anselmetti, F. S. (2014). Signatures of slope failures and river-delta collapses in a perialpine lake (Lake Lucerne, Switzerland). *Sedimentology*, 61(7):1883–1907.

Hinzen, K.-G. (2005). The Use of Engineering Seismological Models to Interpret Archaeoseismological Findings in Tolbiacum, Germany: A Case Study. *Bulletin of the Seismological Society of America*, 95(2):521–539.

Hinzen, K.-G. and Montabert, A. (2017). Rectangular blocks vs polygonal walls in archaeoseismology. *Annals of Geophysics*, 60(4):0443.

Hoelzle, M., Chinn, T., Stumm, D., Paul, F., Zemp, M., and Haeberli, W. (2007). The application of glacier inventory data for estimating past climate change effects on mountain glaciers: A comparison between the European Alps and the Southern Alps of New Zealand. *Global and Planetary Change*, 56(1):69–82.

Hoernes, R. (1878). Erdeben Studien. *Jahrb. Geol. Reichsanst.*, 28:387–448.

Holmes, C. (2005). *Basil II and the Governance of Empire, 976-1025*. Oxford University Press, Oxford.

Honkura, Y. and Işikara, A. (1991). Multidisciplinary research on fault activity in the western part of the North Anatolian Fault Zone. *Tectonophysics*, 193(4):347–357.

Honkura, Y. and Isikara, A. M. (1988). Multidisciplinary Research on Fault Activity in the Western Part of the North Anatolian Fault Zone. Technical report.

Honkura, Y. and Isikara, A. M. (1989). Multidisciplinary Research on Fault Activity in the Western Part of the North Anatolian Fault Zone (2). Technical report.

Honkura, Y. and Isikara, A. M. (1990). Multidisciplinary Research on Fault Activity in the Western Part of the North Anatolian Fault Zone (3). Technical report.

Hubert-Ferrari, A., Barka, A., Jacques, E., Nalbant, S. S., Meyer, B., Armijo, R., Tapponnier, P., and King, G. C. P. (2000). Seismic hazard in the Marmara Sea region following the 17 August 1999 Izmit earthquake. *Nature*, 404(6775):269–273.

Hugues, P. D. and Woodward, J. C. (2017). Quaternary glaciation in the mediterranean mmountain: a new synthesis. *Geological Society of America Special Publications*, 433:1–23.

Ikeda, Y. (1988). Recent activity of the Iznik-Mekece fault at Corak Stream, east of Iznik. In Honkura, Y. and Isikara, A. M. (Eds.), *Multidisciplinary research on fault activity in the western part of the North Anatolian Fault Zone*, pp. 15–27. Tokyo Institute of Technology, Tokyo.

Ikeda, Y., Herece, E., Sugai, T., and Isikara, A. M. (1991). Postglacial Crustal Deformation Associated with Slip on the Western Part of the North Anatolian Fault Zone in the Iznik Lake Basin, Turkey. *Bulletin of the Department of Geography University of Tokyo*, 23:13–23.

Ikeda, Y., Suzuki, Y., and Herece, E. (1989). Late holocene activity of the north anatolian fault zone in the orhangazi plain, northwestern turkey. In Honkura, Y. and Isikara, A. M. (Eds.), *Multidisciplinary research on fault activity in the western part of the North Anatolian fault zone (2)*, volume 2, pp. 16–30. Tokyo Institute of Technology.

Isikara, A. M. and Honkura, Y. (1986). Electric and Magnetic Research on Active Faults in the North Anatolian Fault Zone. Technical report.

İslamoğlu, Y. (2009). Middle Pleistocene bivalves of the Iznik lake basin (Eastern Marmara, NW Turkey) and a new paleobiogeographical approach. *International Journal of Earth Sciences*, 98(8):1981–1990.

Ivy-Ochs, S. and Schaller, M. (2009). Examining Processes and Rates of Landscape Change with Cosmogenic Radionuclides. *Radioactivity in the Environment*, 16:231–294.

Jara-Muñoz, J., Melnick, D., and Strecker, M. R. (2016). Terracem: A MATLAB® tool to analyze marine and lacustrine terraces using high-resolution topography. *Geosphere*, 12(1):176.

Kaneko, Y., Fialko, Y., Sandwell, D. T., Tong, X., and Furuya, M. (2013). Interseismic deformation and creep along the central section of the North Anatolian Fault (Turkey): InSAR observations and implications for rate-and-state friction properties. *Journal of Geophysical Research: Solid Earth*, 118(1):316–331.

Karabacak, V., Altunel, E., and Cakir, Z. (2011). Monitoring aseismic surface creep along the North Anatolian Fault (Turkey) using ground-based LIDAR. *Earth and Planetary Science Letters*, 304(1):64–70.

Karcz, I. and Kafri, U. (1978). Evaluation of supposed archaeoseismic damage in Israel. *Journal of Archaeological Science*, 5(3):237–253.

Ketin, I. (1968). Relations between general tectonic features and the main earthquake regions in Turkey. *Min. Res. Explor. Dir. Turk. Bull.*, 86:1238–1254.

Klinger, Y., Etchebes, M., Tapponnier, P., and Narteau, C. (2011). Characteristic slip for five great earthquakes along the Fuyun fault in China. *Nature Geosci*, 4(6):389–392.

Korzhenkov, A. M. and Mazor, E. (1999). Structural reconstruction of seismic events: ruins of ancient cities as fossil seismographs. *Science and New Technologies Special issue*, 1:62–73.

Koçyigit, A. (1988). Tectonic setting of the Geyve Basin: age and total displacement of the Geyve Fault Zone. *Journal of Pure and Applied Sciences*, 21:81–104.

Koçyigit, A. and Özacar, A. A. (2003). Extensional Neotectonic Regime through the NE edge of the outer Isparta Angle, SW Turkey: new field and seismic data. *Turkish Journal of Earth Sciences*, 12(1):67–90.

Kravari, V. (2004). Evocations médiévales. In Geyer, B. and Lefort, J. (Eds.), *La Bithynie au Moyen Âge*, pp. 65–98. Lethielleux, Paris.

Kürçer, A., Chatzipetros, A., Tutkun, S. Z., Pavlides, S., Özkan Ateş, and Valkaniotis, S. (2008). The Yenice–Gönen active fault (NW Turkey): Active tectonics and palaeoseismology. *Tectonophysics*, 453(1):263 – 275.

Kurtuluş, C. and Canbay, M. M. (2007). Tracing the middle strand of the North Anatolian Fault Zone through the southern Sea of Marmara based on seismic reflection studies. *Geo-Marine Letters*, 27(1):27–40.

Kuşçu, I., Okamura, M., Matsuoka, H., Yamamori, K., Awata, Y., and Özalp, S. (2009). Recognition of active faults and stepover geometry in Gemlik Bay, Sea of Marmara, NW Turkey. *Marine Geology*, 260(1):90–101.

Lacroix, P., Berthier, E., and Maquerhua, E. T. (2015). Earthquake-driven acceleration of slow-moving landslides in the Colca valley, Peru, detected from Pléiades images. *Remote Sensing of Environment*, 165:148–158.

Lagomarsino, S. and Giovinazzi, S. (2006). Macroseismic and mechanical models for the vulnerability assessment of current buildings. *Bulletin of Earthquake Engineering*, 4 (4):415–443.

Lal, D. (1991). Cosmic ray labeling of erosion surfaces: in situ nuclide production rates and erosion models. *Earth and Planetary Science Letters*, 104(2):424–439.

Langridge, R. M., Stenner, H. D., Fumal, T. E., Christofferson, S. A., Rockwell, T. K., Hartleb, R. D., Bachhuber, J., and Barka, A. A. (2002). Geometry, Slip Distribution, and Kinematics of Surface Rupture on the Sakarya Fault Segment during the 17 August 1999 İzmit, Turkey, Earthquake. *Bulletin of the Seismological Society of America*, 92(1):107–125.

Le Pichon, X., Şengör, A., Demirbağ, E., Rangin, C., İmren, C., Armijo, R., Görür, N., Çağatay, N., de Lepinay, B. M., Meyer, B., Saatçılar, R., and Tok, B. (2001). The active Main Marmara Fault. *Earth and Planetary Science Letters*, 192(4):595 – 616.

Le Pichon, X., İmren, C., Rangin, C., Şengör, A. M. C., and Siyako, M. (2014). The South Marmara Fault. *International Journal of Earth Sciences*, 103(1):219–231.

Le Pichon, X., Sengör, A. M. C., and Taymaz, T. (1999). Büyük Marmara Fayi : Nicin, nerede ve ne olabilir. *Cumhuriyet Bilim Teknik*, 661:8–11.

Louderback, G. D. (1942). Faults and earthquakes. *Bulletin of the Seismological Society of America*, 32(4):305–330.

Lowry, H. W. (2003). Ottoman Iznik (Nicaea): Through the Eyes of Travelers & as Recorded in Administrative Documents, 1331-1923. In Akbaygil, I., Inalcik, H., and Aslanapa, O. (Eds.), *Iznik Throughout History*, pp. 135–174. Türkiye Is Bankasi.

Manighetti, I., Perrin, C., Dominguez, S., Garambois, S., Gaudemer, Y., Malavieille, J., Matteo, L., Delor, E., Vitard, C., and Beauprêtre, S. (2015). Recovering paleoearthquake slip record in a highly dynamic alluvial and tectonic region (Hope Fault, New Zealand) from airborne lidar. *Journal of Geophysical Research: Solid Earth*, 120(6):4484–4509.

Mazaud, A., Laj, C., Bard, E., Arnold, M., and Tric, E. (1991). Geomagnetic field control of ^{14}C production over the last 80 ky: Implications for the radiocarbon time-scale. *Geophysical Research Letters*, 18(10):1885–1888.

Mazor, E. and Korzhenkov, A. (2001). Applied archeoseismology: decoding earthquake parameters recorded in archeological ruins. In Krasnov, B. and Mazor, E. (Eds.), *The Makhteshim Country: A Laboratory of Nature*, pp. 123–149. Pensoft Publishers, Sofia-Moscow.

McCalpin, J. P. (2009). Field techniques in paleoseismology - terrestrial environments. In McCalpin, J. P. (Ed.), *Paleoseismology*, pp. 123–149. Academic Press.

McClusky, S., Balassanian, S., Barka, A., Demir, C., Ergintav, S., Georgiev, I., Gurkan, O., Hamburger, M., Hurst, K., Kahle, H., Kastens, K., Kekelidze, G., King, R., Kotzev, V., Lenk, O., Mahmoud, S., Mishin, A., Nadariya, M., Ouzounis, A., Paradissis, D., Peter, Y., Prilepin, M., Reilinger, R., Sanli, I., Seeger, H., Tealeb, A., Toksöz, M. N., and Veis, G. (2000). Global Positioning System constraints on plate kinematics and dynamics in the eastern Mediterranean and Caucasus. *Journal of Geophysical Research: Solid Earth*, 105(B3):5695–5719.

McGill, S. F. and Rubin, C. M. (1999). Surficial slip distribution on the central Emerson fault during the June 28, 1992, Landers earthquake, California. *Journal of Geophysical Research: Solid Earth*, 104(B3):4811–4833.

McGill, S. F. and Sieh, K. (1991). Surficial offsets on the Central and Eastern Garlock Fault associated with prehistoric earthquakes. *Journal of Geophysical Research: Solid Earth*, 96(B13):21597–21621.

McKenzie, D. (1972). Active Tectonics of the Mediterranean Region. *Geophysical Journal of the Royal Astronomical Society*, 30(2):109–185.

Meade, B. J., Hager, B. H., McClusky, S. C., Reilinger, R. E., Ergintav, S., Lenk, O., Barka, A., and Özener, H. (2002). Estimates of Seismic Potential in the Marmara Sea Region from Block Models of Secular Deformation Constrained by Global Positioning System Measurements. *Bulletin of the Seismological Society of America*, 92(1):208–215.

Miebach, A., Niestrath, P., Roeser, P., and Litt, T. (2016). Impacts of climate and humans on the vegetation in northwestern Turkey: palynological insights from Lake Iznik since the Last Glacial. *Climate of the Past*, 12(2):575–593.

Migowski, C., Agnon, A., Bookman, R., Negendank, J. F., and Stein, M. (2004). Recurrence pattern of holocene earthquakes along the Dead Sea transform revealed by varve-counting and radiocarbon dating of lacustrine sediments. *Earth and Planetary Science Letters*, 222(1):301–314.

Moratto, Z. M., Broxton, M. J., Beyer, R. A., Lundy, M., and Husmann, K. (2010). Ames Stereo Pipeline, NASA's Open Source Automated StereogrammetrySoftware. In *Lunar and Planetary Science Conference*, volume 41. abstract 2364.

Murru, M., Akinci, A., Falcone, G., Pucci, S., Console, R., and Parsons, T. (2016). M $\geq$ 7 earthquake rupture forecast and time-dependent probability for the sea of Marmara region, Turkey. *Journal of Geophysical Research: Solid Earth*, 121(4):2679–2707.

Nazik, A., Meriç, E., Avsar, N., Ünlü, S., Esenli, V., and Gökasan, E. (2011). Possible waterways between the Marmara Sea and the Black Sea in the late Quaternary: evidence from ostracod and foraminifer assemblages in lakes İznik and Sapanca, Turkey. *Geo-Marine Letters*, 31 (2):75–86.

Nesje, A. (2005). Briksdalsbreen in western Norway: AD 1900-2004 frontal fluctuations as a combined effect of variations in winter precipitation and summer temperature. *The Holocene*, 15(8):1245–1252.

Nicolle, D. (2011). *The Fourth Crusade 1202-04: The betrayal of Byzantium*. Osprey Publishing.

Niemi, T. M. (2008). Historical earthquake catalogues and archaeological data: Avoiding circular reasoning. In *Seismological Society of America Annual Meeting*, Santa Fe, NM.

Norwich, J. J. (1993). *Byzantium: The Apogee*. Penguin.

Otto-Dorn, K. (1941). *Das islamische Iznik*. Deutsches Archäologisches Institut, Berlin.

Ousterhout, R. (2008). Construction of Foundations and Walls. In *Master Builders of Byzantium*, pp. 174–179. University of Pennsylvania Press.

Özalp, S., Dogan, A., and Emre, Ö. (2003). The last two faulting events on the southern strand of the North Anatolian Fault Zone, NW Turkey. In *Eos Trans. AGU Fall Meet. Suppl.*, volume 84. F1003.

Özalp, S., Emre, Ö., and Dogan, A. (2013). The segment structure of southern branch of the North Anatolian Fault and Paleoseismological behaviour of the Gemlik fault, NW Anatolia. *Bulletin of MTA*, 147:1–17.

Özcan, Z., Okay, A., Özcan, E., Hakyemez, A., and Altiner, S. (2012). Late Cretaceous-Eocene geological evolution of the Pontides based on new stratigraphic and palaeontologic data between the Black Sea coast and Bursa (NW Turkey). *Turkish Journal of Earth Sciences*, 21(6):933–960.

Ozener, H., Dogru, A., and Turgut, B. (2013a). Quantifying aseismic creep on the Ismetpasa segment of the North Anatolian Fault Zone (Turkey) by 6 years of GPS observations. *Journal of Geodynamics*, 67:72–77.

Ozener, H., Yilmaz, O., Dogru, A., Turgut, B., and Gurkan, O. (2013b). Gps-derived velocity field of the Iznik-Mekece segment of the North Anatolian Fault Zone. *Journal of Geodynamics*, 67:46–52.

Öztürk, K., Yaltirak, C., and Alpar, B. (2009). The Relationship Between the Tectonic Setting of the Lake Iznik Basin and the Middle Strand of the North Anatolian Fault. *Turkish J. Earth Sci.*, 18:209–224.

Öztürk, M. Z., Erginal, A. E., Kiyak, N. G., Demirci, A., Ekinci, Y. L., Curebal, I., Avcioglu, M., and Öztürk, T. (2016). Records of repeated drought stages during the

Holocene, Lake Iznik (Turkey) with reference to beachrocks. *Quaternary International*, 408 (A):16–24.

Page, M. and Felzer, K. (2015). Southern San Andreas Fault Seismicity is Consistent with the Gutenberg–Richter Magnitude–Frequency Distribution. *Bulletin of the Seismological Society of America*, 105(4):2070–2080.

Parsons, T., Toda, S., Stein, R. S., Barka, A., and Dieterich, J. H. (2000). Heightened Odds of Large Earthquakes near Istanbul: An Interaction-Based Probability Calculation. *Science*, 288(5466):661–665.

Passchier, C., Sürmelihindi, G., Spötl, C., Mertz-Kraus, R., and Scholz, D. (2016). Carbonate deposits from the ancient aqueduct of Béziers, France — a high-resolution palaeoenvironmental archive for the Roman Empire. *Palaeogeography, Palaeoclimatology, Palaeoecology*, 461:328 – 340.

Passchier, C. W., Wiplinger, G., Güngör, T., Kessener, P., and Sürmelihindi, G. (2013). Normal fault displacement dislocating a Roman aqueduct of Ephesos, western Turkey. *Terra Nova*, 25(4):292–297.

Pavlides, S. B., Chatzipetros, A., Tutkun, Z. S., Özaksoy, V., and Doğan, B. (2006). Evidence for late Holocene activity along the seismogenic fault of the 1999 Izmit earthquake, NW turkey. *Geological Society, London, Special Publications*, 260(1):635–647.

Pera Air (2016). Timeline and history of Asia Minor (Anatolia). http://www.peraair.com/timeline-and-history-of-asia-minor-anatolia [Accessed 13 September 2017].

Petit, C., Gunnell, Y., Gonga-Saholiariliva, N., Meyer, B., and Séguinot, J. (2009). Faceted spurs at normal fault scarps: Insights from numerical modeling. *Journal of Geophysical Research: Solid Earth*, 114(B5):B05403.

Pondard, N., Armijo, R., King, G. C. P., Meyer, B., and Flerit, F. (2007). Fault interactions in the Sea of Marmara pull-apart (North Anatolian Fault): earthquake clustering and propagating earthquake sequences. *Geophysical Journal International*, 171(3):1185–1197.

Py-Circan, C. (2017). Utilisation de l'archéo-sismicité couplée à la paléolimnologie comme nouvel outil pour améliorer l'évaluation de l'aléa sismique. Master's thesis, Université Grenoble Alpes.

Rabbel, W., Erkul, E., Stümpel, H., Wunderlich, T., Pašteka, R., Papco, J., Niewöhner, P., Bariş, ., Çakin, O., and Pekşen, E. (2015). Discovery of a Byzantine Church in Iznik/Nicaea, Turkey: an Educational Case History of Geophysical Prospecting with Combined Methods in Urban Areas. *Archaeological Prospection*, 22(1):1–20. ARP-14-0004.R1.

Raby, J. (1976). A Seventeenth Century Description of Iznik-Nicaea. *Istanbuler Mitteilungen*, 29:149–188.

Rapp, G. (1986). Assessing archaeological evidence for seismic catastrophies. *Geoarchaeology*, 1(4):365–379.

Reid, H. F. (1910). The mechanics of the earthquake. In *The California earthquake of April 18, 1906: Report of the state earthquake investigation commission, v. 2.* Carnegie Institution of Washington Publication.

Reilinger, R., McClusky, S., Vernant, P., Lawrence, S., Ergintav, S., Cakmak, R., Ozener, H., Kadirov, F., Guliev, I., Stepanyan, R., Nadariya, M., Hahubia, G., Mahmoud, S., Sakr, K., ArRajehi, A., Paradissis, D., Al-Aydrus, A., Prilepin, M., Guseva, T., Evren, E., Dmitrotsa, A., Filikov, S. V., Gomez, F., Al-Ghazzi, R., and Karam, G. (2006). GPS constraints on continental deformation in the Africa-Arabia-Eurasia continental collision zone and implications for the dynamics of plate interactions. *Journal of Geophysical Research: Solid Earth*, 111(B5):B05411.

Reilinger, R. E., McClusky, S. C., Oral, M. B., King, R. W., Toksoz, M. N., Barka, A. A., Kinik, I., Lenk, O., and Sanli, I. (1997). Global Positioning System measurements of present-day crustal movements in the Arabia-Africa-Eurasia plate collision zone. *Journal of Geophysical Research: Solid Earth*, 102(B5):9983–9999.

Reimer, P. J., Bard, E., Bayliss, A., Beck, J. W., Blackwell, P. G., Ramsey, C. B., Buck, C. E., Cheng, H., Edwards, R. L., Friedrich, M., and et al. (2013). IntCal13 and Marine13 Radiocarbon Age Calibration Curves 0–50,000 Years cal BP. *Radiocarbon*, 55(4):1869–1887.

Riedel, I. (2015). *Analyse de la vulnérabilité du bâti existant. Estimation et réduction des incertitudes dans l'estimation des dommages et des pertes pour un scénario sismique donné.* PhD thesis, Université Grenoble Alpes.

Robinson, C., Raisbeck, G. M., Yiou, F., Lehman, B., and Laj, C. (1995). The relationship between ^{10}Be and geomagnetic field strength records in central North Atlantic sediments during the last 80 ka. *Earth and Planetary Science Letters*, 136(3):551–557.

Rockwell, T., Ragona, D., Seitz, G., Langridge, R., Aksoy, M. E., Ucarkus, G., Ferry, M., Meltzner, A. J., Klinger, Y., Meghraoui, M., Satir, D., Barka, A., and Akbalik, B. (2009). Palaeoseismology of the North Anatolian Fault near the Marmara Sea: implications for fault segmentation and seismic hazard. *Geological Society, London, Special Publications*, 316(1):31–54.

Rodríguez-Pascua, M., Pérez-López, R., Giner-Robles, J., Silva, P., Garduño-Monroy, V., and Reicherter, K. (2011). A comprehensive classification of Earthquake Archaeological Effects (EAE) in archaeoseismology: Application to ancient remains of Roman and Mesoamerican cultures. *Quaternary International*, 242(1):20–30.

Rodríguez-Pascua, M. A., Pérez-López, R., Giner-Robles, J. L., Silva, P. G., Garduño-Monroy, V. H., and Reicherter, K. (2010). Nueva Tabla de Clasificacion de Efectos Arqueologicos de Terremotos. *Tierra y tecnologia*, 38:59–65.

Roeser, P. (2014). *Paleolimnology of Lake Iznik (NW Turkey) during the past ∼31 ka cal BP*. PhD thesis, Rheinische Friedrich-Wilhelms-Universität Bonn, Bonn.

Roeser, P. A., Franz, S. O., Litt, T., Ülgen, U. B., Hilgers, A., Wulf, S., Wennrich, V., Ön, S. A., Viehberg, F. A., Çağatay, M. N., and Melles, M. (2012). Lithostratigraphic and geochronological framework for the paleoenvironmental reconstruction of the last ∼36 ka cal BP from a sediment record from Lake Iznik (NW Turkey). *Quaternary International*, 274:73–87.

Roodenberg, J. and Roodenberg, S. A. (2008). *Life and Death in a Prehistoric Settlement in Northwest Anatolia: The Ilipinar Excavations*, volume 3. Nederlands Instituut voor het Nabije Oosten.

Rousset, B., Jolivet, R., Simons, M., Lasserre, C., Riel, B., Milillo, P., Çakir, Z., and Renard, F. (2016). An aseismic slip transient on the North Anatolian Fault. *Geophysical Research Letters*, 43(7):3254–3262. 2016GL068250.

Rucker, J. D. and Niemi, T. M. (2010). Historical earthquake catalogues and archaeological data: Achieving synthesis without circular reasoning. In Sintubin, M., Stewart, I. S., Niemi, T. M., and Altunel, E. (Eds.), *Ancient Earthquakes*, pp. 97–106. Geological Society of America.

Sahin, S. (1979). *Katalog der antiken Inschriften des Museums von Iznik (Nikaia)*, volume I. Habelt, Bonn.

Sahin, S. (2003). Iznik (Nicaea) in the Hellenistic and Roman Periods. In Akbaygil, I., Inalcik, H., and Aslanapa, O. (Eds.), *Iznik Throughout History*, pp. 3–23. Türkiye Is Bankasi, Istanbul.

Sarikaya, M. A. and Ciner, A. (2015). Late Pleistocene Glaciations and Paleoclimate of Turkey. *Bulletin of the Mineral Research and Exploration*, 151:107–127.

Sarikaya, M. A., Ciner, A., Haybat, H., and Zreda, M. (2014). An early advance of glaciers on Mount Akdag, SW Turkey, before the global Last Glacial Maximum; insights from cosmogenic nuclides and glacier modeling. *Quaternary Science Reviews*, 88:96–109.

Sarikaya, M. A., Ciner, A., and Zreda, M. (2011). Quaternary Glaciations of Turkey. In Ehlers, J., Gibbard, P. L., and Hughes, P. D. (Eds.), *Quaternary Glaciations - Extent and Chronology: a Closer Look*, pp. 393–403. Elsevier, Amsterdam, The Netherlands.

Savage, J. C. and Prescott, W. H. (1978). Asthenosphere readjustment and the earthquake cycle. *Journal of Geophysical Research: Solid Earth*, 83(B7):3369–3376.

Sbeinati, M. R., Meghraoui, M., Suleyman, G., Gomez, F., Grootes, P., Nadeau, M.-J., Al Najjar, H., and Al-Ghazzi, R. (2010). Timing of earthquake ruptures at the Al Harif Roman aqueduct (Dead Sea fault, Syria) from archaeoseismology and paleoseismology. *Geological Society of America Special Papers*, 471:243–267.

Schindler, C. (1997). Geology of Northwestern Turkey: Results of the MARMARA Poly-Project. In Schindler, C. and Pfister, M. (Eds.), *Active Tectonics of Northwestern Anatolia - the MARMARA Poly-Project*. vdf Hochschulverlag AG.

Schlagenhauf, A., Manighetti, I., Benedetti, L., Gaudemer, Y., Finkel, R., Malavieille, J., and Pou, K. (2011). Earthquake supercycles in Central Italy, inferred from ^{36}Cl exposure dating. *Earth and Planetary Science Letters*, 307(3):487–500.

Schneider, A. M. (1943). *Die römischen und byzantinischen Denkmäler von Iznik-Nicaea*. Deutsches Archaologisches Institut.

Schneider, A. M. and Karnapp, W. (1938). *Die Stadtmauer von Iznik (Nicaea)*. Deutsches Archaologisches Institut.

Schnellman, M., Anselmetti, F. S., Giardini, D., McKenzie, J. A., and Ward, S. N. (2002). Prehistoric earthquake history revealed by lacustrine slump deposits. *Geology*, 30:1131–1134.

Scholz, C. H. (1998). Earthquakes and friction laws. *Nature*, 391(6662):37–42.

Scholz, C. H. (2002). *The Mechanics of Earthquakes and Faulting*. Cambridge University Press, Cambridge, New York, Melbourne, 2nd edition.

Schwartz, D. P. and Coppersmith, K. J. (1984). Fault behavior and characteristic earthquakes: Examples from the Wasatch and San Andreas Fault Zones. *Journal of Geophysical Research: Solid Earth*, 89(B7):5681–5698.

Şengör, A. M. C., Görür, N., and Saroglu, F. (1985). Strike-slip faulting and related asin formation in zones of tectonic escape: Turkey as a case study. In Biddle, K. T. and Christie-Blick, N. (Eds.), *Strike-slip faulting and basin formation*, pp. 227–264. Society of Economic Paleontologists and Mineralogists.

Şengör, A., Tüysüz, O., İmren, C., Sakınç, M., Eyidoğan, H., Görür, N., Pichon, X. L., and Rangin, C. (2005). The North Anatolian Fault: a New Look. *Annual Review of Earth and Planetary Sciences*, 33(1):37–112.

Şengör, A. and Yilmaz, Y. (1981). Tethyan evolution of Turkey: A plate tectonic approach. *Tectonophysics*, 75(3):181–241.

Şengör, A. M. C., Grall, C., İmren, C., Le Pichon, X., Görür, N., Henry, P., Karabulut, H., and Siyako, M. (2014). The geometry of the North Anatolian transform fault in the Sea of Marmara and its temporal evolution: implications for the development of intracontinental transform faults. *Canadian Journal of Earth Sciences*, 51(3):222–242.

Shean, D. E., Alexandrov, O., Moratto, Z., Smith, B. E., Joughin, I. R., Porter, C. C., and Morin, P. J. (2016). An automated, open-source pipeline for mass production of digital elevation models (DEMs) from very high-resolution commercial stereo satellite imagery. *ISPRS Journal of Photogrammetry and Remote Sensing*, 116:101–117.

Siame, L., Sébrier, M., Bellier, O., Bourlès, D., Castano, J., Aurojo, M., Yiou, F., and Raisbeck, G. (1996). Segmentation and horizontal slip-rate estimation of the El Tigre fault zone, San Juan province (Argentina) from SPOT images analysis. In *Third ISAG*, St Malo, France.

Sieh, K. E. (1981). A review of geological evidence for recurrence times of large earthquakes. In Simpson, D. W. and Richards, P. G. (Eds.), *Earthquake Prediction, An International Review*, pp. 181–207. AGU, Washington, D.C.

Sieh, K. E. and Jahns, R. H. (1984). Holocene activity of the San Andreas fault at Wallace Creek, California. *Geological Society of America Bulletin*, 95(8):883–896.

Slemmons, D. B. (1957). Geological effects of the Dixie Valley-Fairview Peak, Nevada, earthquakes of December 16, 1954. *Bulletin of the Seismological Society of America*, 47(4):353–375.

Smith, A. D., Taymaz, T., Oktay, F., Yüce, H., Alpar, B., Basaran, H., Jackson, J. A., Kara, S., and Simsek, M. (1995). High-resolution seismic profiling in the Sea of Marmara (northwest Turkey): Late Quaternary sedimentation and sea-level changes. *GSA Bulletin*, 107 (8):923–936.

Stein, R. S., Barka, A. A., and Dieterich, J. H. (1997). Progressive failure on the North Anatolian fault since 1939 by earthquake stress triggering. *Geophysical Journal International*, 128(3):594–604.

Steinbrugge, K. V., Zacher, E. G., Tocher, D., Whitten, C. A., and Claire, C. N. (1960). Creep on the San Andreas fault. *Bulletin of the Seismological Society of America*, 50(3):389–415.

Stone, J. O. (2000). Air pressure and cosmogenic isotope production. *Journal of Geophysical Research: Solid Earth*, 105(B10):23753–23759.

Straub, C., Kahle, H.-G., and Schindler, C. (1997). GPS and geologic estimates of the tectonic activity in the Marmara Sea region, NW Anatolia. *Journal of Geophysical Research: Solid Earth*, 102(B12):27587–27601.

Stroeven, A. P., Heyman, J., Fabel, D., Björck, S., Caffee, M. W., Fredin, O., and Harbor, J. M. (2015). A new Scandinavian reference ^{10}be production rate. *Quaternary Geochronology*, 29:104–115.

Stuiver, M. and Braziunas, T. F. (1993). Modeling Atmosphere ^{14}C Influences and ^{14}C Ages of Marine Samples to 10,000 BC. *Radiocarbon*, 35 (01):137–189.

Tanoglu, A. and Erinc, S. (1956). Garsak boğazı ve Eski Sakarya (The Garsak gorge and the Sakarya River diversion). *İstanbul Universitesi Coğrafya Enstitusu Dergisi*, 4:17–31.

Taylor, R. E. (1997). Radiocarbon dating. In Taylor, R. E. and Aitken, M. J. (Eds.), *Chronometric Dating in Archaeology*, pp. 65–96. Springer US.

Texier, C. (1862). *Asie Mineure : description géographique, historique et archéologique des provinces et des villes de la Chersonnèse d'Asie*, pp. 109–110. Firmin Didot frères, fils et Cie, Paris.

Toksöz, M. N., Shakal, A. F., and Michael, A. J. (1979). Space-time migration of earthquakes along the North Anatolian fault zone and seismic gaps. *Pure and Applied Geophysics*, 117(6):1258–1270.

Tse, S. T. and Rice, J. R. (1986). Crustal earthquake instability in relation to the depth variation of frictional slip properties. *Journal of Geophysical Research: Solid Earth*, 91(B9):9452–9472.

Tsimi, C. and Ganas, A. (2015). Using the ASTER global DEM to derive empirical relationships among triangular facet slope, facet height and slip rates along active normal faults. *Geomorphology*, 234:171 – 181.

Tsukuda, T., Satake, K., Honkura, Y., Üçer, S. B., and Isikara, A. M. (1988). Low seismicity, low coda-Q and discontinuities of the upper crust in the vicinity of the Iznik-Mekece fault, the North Anatolian Fault Zone, Turkey. *Bull. Earthquake Res. Inst. Univ. Tokyo*, 63:327–348.

Uçarkus, G. (2002). Gemlik Fay Zonunun Aktif Tektoniği [Active Tectonics of Gemlik Fault Zone]. Msc thesis, İTÜ Avrasya Yerbilimleri Enstitüsü. [in Turkish with English abstract, unpublished].

Uçarkus, G., Akyüz, H. S., Barka, A., and Tari, U. (2003). Morphotectonics and paleoseismicity of the Gemlik fault zone, middle strand of the NAFZ in Marmara region, Turkey. In *EGS-AGU-EUG Joint Assembly*, Nice, France.

Ülgen, U. B., Franz, S. O., Biltekin, D., Çagatay, M. N., Roeser, P. A., Doner, L., and Thein, J. (2012). Climatic and environmental evolution of Lake Iznik (NW Turkey) over the last ∼4700 years. *Quaternary International*, 274:88 – 101.

Van Hise, C. R. (1904). *A treatise on metamorphism*. USGS.

Vardar, D., Öztürk, K., Yaltırak, C., Alpar, B., and Tur, H. (2014). Late Pleistocene–Holocene evolution of the southern Marmara shelf and sub-basins: middle strand of the North Anatolian fault, southern Marmara Sea, Turkey. *Marine Geophysical Research*, 35(1):69–85.

Volant, P., Levret, A., Carbon, D., Scotti, O., Combescure, D., Verdel, T., Piant, A., and Laurent, P. (2009). An archaeo-seismological study of the Nîmes Roman aqueduct, France:indirect evidence for an M > 6 seismic event? *Natural Hazards*, 49(1):53–77.

Wadati, K. (1935). On the activity of deep focus earthquakes in the Japan Islands and neighbourhoods. *Geophysical Magazine*, 8:305–325.

Wallace, R. E. (1968). Notes on Stream Channels Offset by the San Andreas Fault, SouthernCoast Ranges, California. In *Conference on Geologic Problems of the San Andreas Fault System*.

Wang, Y., Zhu, L., Shi, F., Schubnel, A., Hilairet, N., Yu, T., Rivers, M., Gasc, J., Addad, A., Deldicque, D., Li, Z., and Brunet, F. (2017). A laboratory nanoseismological study on deep-focus earthquake micromechanics. *Science Advances*, 3(7).

Wells, D. L. and Coppersmith, K. J. (1994). New empirical relationships among magnitude, rupture length, rupture width, rupture area, and surface displacement. *Bulletin of the Seismological Society of America*, 84(4):974–1002.

Wesnousky, S. G. (1994). The Gutenberg-Richter or characteristic earthquake distribution, which is it? *Bulletin of the Seismological Society of America*, 84(6):1940–1959.

Wikipedia (2017a). Battle of Dorylaeum (1097) — Wikipedia, The Free Encyclopedia. https://en.wikipedia.org/w/index.php?title=Battle_of_Dorylaeum_(1097)&oldid=799356604 [Accessed 13 September 2017].

Wikipedia (2017b). Empire of Nicaea — Wikipedia, The Free Encyclopedia. https://en.wikipedia.org/w/index.php?title=Empire_of_Nicaea&oldid=792343086 [Accessed 13 September 2017].

Wilcox, R. E., Harding, T. P., and Seely, D. R. (1973). Basic wrench tectonics. *American Association of Petroleum Geologists Bulletin*, 57:74–96.

Wu, J. E., McClay, K., Whitehouse, P., and Dooley, T. (2009). 4D analogue modelling of transtensional pull-apart basins. *Marine and Petroleum Geology*, 26 (8):1608–1623.

Yaltırak, C., Sakinç, M., and Oktay, F. Y. (2000). Westward propagation of North Anatolian fault into the northern Aegean: Timing and kinematics: Comment and Reply. *Geology*, 28(2):187–188.

Yaltırak, C., Ülgen, U. B., Zabcı, C., Franz, S. O., Ön, S. A., Sakınç, M., Çağatay, M. N., Alpar, B., Öztürk, K., Tunoğlu, C., and Ünlü, S. (2012). Discussion: a critique of Possible waterways between the Marmara Sea and the Black Sea in the late Quaternary: evidence from ostracod and foraminifer assemblages in lakes iznik and Sapanca, Turkey, Geo-Marine Letters, 2011. *Geo-Marine Letters*, 32(3):267–274.

Yaltırak, C. (2002). Tectonic evolution of the Marmara Sea and its surroundings. *Marine Geology*, 190(1):493–529.

Yaltırak, C. and Alpar, B. (2002). Evolution of the middle strand of North Anatolian Fault and shallow seismic investigation of the southeastern Marmara Sea (Gemlik Bay). *Marine Geology*, 190(1):307–327.

Yılmaz, Y., Genç, C., Yiğitbaş, E., Bozcu, M., and Yılmaz, K. (1995). Geological evolution of the late Mesozoic continental margin of NorthwesternAnatolia. *Tectonophysics*, 243(1):155–171.

Yılmaz, Y., Tüysüz, O., Yiğitbaş., E., Genç, ., and Sengör, A. M. C. (1997). Geology and tectonic evolution of the pontides. In Robinson, A. G. (Ed.), *Petroleum Geology of the Black Sea and Surrounding Region*, pp. 183–226. AAPG.

Yokoyama, Y., Lambeck, K., De Deckker, P., Johnston, P., and Fifield, L. K. (2000). Timing of the Last Glacial Maximum from observed sea-level minima. *Nature*, 406(6797):713–716.

Yoshioka, T. and Kusçu, I. (1994). Late Holocene faulting events on the İznik-Mekece fault in the western part of the North Anatolian fault zone, Turkey. *Bull. Geol. Surv. Jpn.*, 45(11):677–685.

Youngs, R. R. and Coppersmith, K. J. (1985). Implications of fault slip rates and earthquake recurrence models to probabilistic seismic hazard estimates. *Bulletin of the Seismological Society of America*, 75(4):939–964.

Zahno, C., Aksar, N., Yavuz, V., Kubik, P., and Schlüchter, C. (2010). Chronology of Late Pleistocene glacier variations at the Uludag Mountain, NW Turkey. *Quaternary Science Reviews*, 29(9):1173–1187.

Zielke, O., Klinger, Y., and Arrowsmith, J. R. (2015). Fault slip and earthquake recurrence along strike-slip faults — Contributionsof high-resolution geomorphic data. *Tectonophysics*, 638:43–62.

Zreda, M., Çiner, A., Sarıkaya, M. A., Zweck, C., and Bayarı, S. (2011). Remarkably extensive glaciation and fast deglaciation and climate change in Turkey near the Pleistocene-Holocene boundary. *Geology*, 39(11):1051.

Appendix A

Historical seismicity of the MNAF region

In this section, we only consider the earthquakes having damaged localities close to the MNAF segments (Geyve, Iznik, Mudanya, Bandirma, Cyzicus, Baris, Gemlik). We added some other earthquakes that did not specifically targeted these localities but are mentioned in the discussion. The cities and areas mentioned are located on Fig. A.1. According to Ambraseys and Finkel (1991), it is unlikely that all moderate and large magnitude shocks before the middle of the 18th century have been recorded. But it is very probable that any large or major earthquake has been noted, although not necessarily fully identified. Data about moderate and large magnitude events after ∼1770 should be complete, and all earthquakes with Ms>6.8 since 1500 have been identified (Ambraseys and Jackson 2000). For each event are precised when available the main area affected, the location and the estimated magnitude Ms. All the dates are AD.

29-32 Nicaea 40.5-30.5 Ms=7

This event affected Bithynia and destroyed many houses in Nicaea (Ambraseys 2009). Ambraseys (2009) and Guidoboni et al. (1994) diverge on the date of this event proposing 32 and 24.11.29 AD respectively. Orosius (5th century) adds that Tiberius exempted the damaged cities of Asia Minor from tribute and gave generous donations towards repairs. Appolonius Grammaticus also reported an earthquake in Pontus (southern coast of the Black Sea) at the time of Tiberius, which is likely to be the same event according to Guidoboni et al. (1994). Ambraseys and Finkel (1991) propose a magnitude over 7.

121 Nicomedia 40.5-30.1 Ms=7.4

This event destroyed completely Nicomedia, a great part of Nicaea, and probably Aoria (close to Yenisehir). The cities were rebuilt with public funding. The defensive walls of Nicomedia and Nicaea were rebuilt by the state (Ambraseys 2009). Ambraseys and Finkel

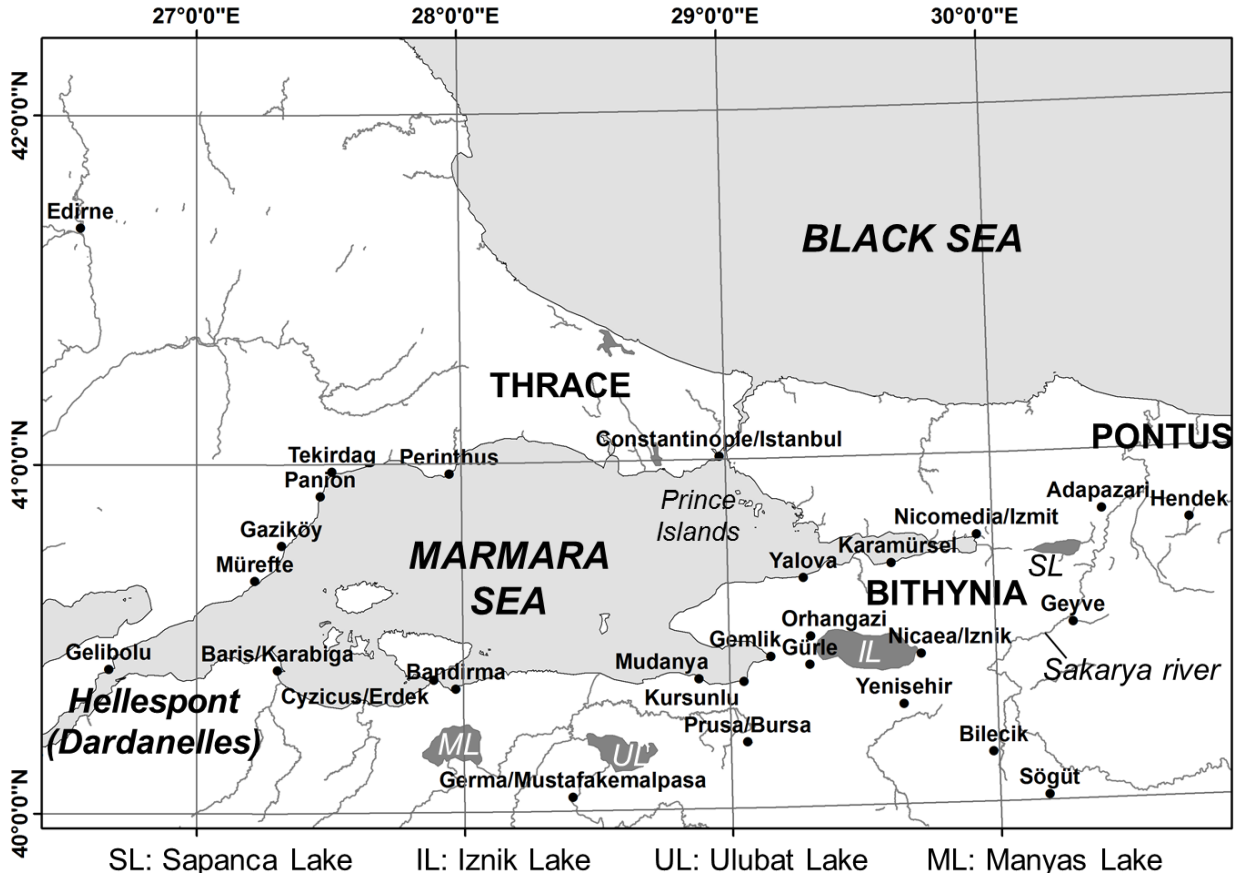

Figure A.1: General location map. When precised, the city's ancient names is followed by the modern name. The main rivers are drawn in light grey.

(1991) propose a magnitude over 7. Guidoboni et al. (1994) date it to 120/128 AD.

10 November 123 Cyzicus 40.3-27.7 Ms=7.0

The city was destroyed by a large earthquake. Imperial funds were used for its reconstruction (Ambraseys and Finkel 1991). Ambraseys (2009) suggests that about this time Baris, about 30 km west of Cyzicus, was also affected.

128 Bithynia 40.17-27.54 Ms>7

This earthquake destroyed the greater part of Aoria and Nicomedia with the region around (Ambraseys and Finkel 1991). Only one source records this event at this date, and Ambraseys (2009) does not include it and attributes this source to the 121 event.

155-160 Bithynia 40.17-27.5 Ms>7

Cyzicus was totally destroyed, together with other towns. In the interior of the Hellespont (Dardannelles), the ground deformed extensively. Cyzicus was restored with the financial assistance of Rome (Ambraseys and Finkel 1991; Guidoboni et al. 1994).

3 May 181 Mudopolis 40.6-30.6 Ms=7.3

A relatively large earthquake in Bithynia caused serious damage in Nicomedia and the surrounding region as far as the region around Mudopolis (about 100 km south of Nicomedia) and the river Sangarius (Sakarya). The imperial government provided funds for the restoration of Nicomedia. The only source is the 6th century writer Malalas (Ambraseys 2009).

24 August 358 Nicomedia 40.7-30.2 Ms=7.4

Nicomedia was almost totally destroyed. Damage in Constantinople and Perinthus (Marmara Ereglisi) is mentioned. Damage is also reported in Nicaea but is dubious (Ambraseys 2009). The event was strongly felt in Macedonia and Asia Minor. Nicomedia was restored with the help of the emperor. It appears that the effects of the earthquake were less catastrophic than individual reports seem to indicate.

2 December 362 Nicomedia 40.7-30.2 Ms=6.8

Towards the evening, Nicomedia was totally destroyed (Guidoboni et al. 1994). A great part of Nicaea and Constantinople were destroyed. The earthquake was followed by aftershocks for a few days (Ambraseys 2009). The authorities lowered the price of essentials for relief.

11 October 368 Nicaea 40.5-30.5 Ms=6.8

Nicaea was destroyed completely (Guidoboni et al. 1994), as well as other cities around. A sea wave is reported by John of Nikiu, following Malalas, but Ambraseys (2009) considers it an exaggeration. Guidoboni et al. (1994) claim it is possible that the sea wave occurred in September 367 and is separated from the 368 event. Ambraseys and Finkel (1991) locate the epicentral area around Iznik and further west in Bithynia. No other major city was affected.

November (?) 368 Germa 40.1-27.8 Ms=6.8

The greater part of Germa (Mustafakemalpasa, southwest of Ulubat Lake) was destroyed. According to Ambraseys and Finkel (1991), it was probably a large aftershock

of the former earthquake, which confirms a center of activity between Nicaea and Germa. Socrates is the only contemporary source (Ambraseys 2009).

7 April 460 Hellespont 40.1-27.6 Ms=7

Extensive damage in the province of Hellespont and in the greater part of Thrace. Cyzicus and villages in the interior were partly destroyed with great loss of life (Ambraseys and Finkel 1991; Guidoboni et al. 1994). In some places, the ground opened up (Ambraseys 2009).

24-25 September 478 Nicomedia 40.7-29.8 Ms=7.3

Nicomedia was totally destroyed, as well as Helenoupolis (Karamürsel). Constantinople was seriously damaged. Strong replicas occurred during several days. There might have been some damage in Nicaea where a later source describes submersion by the lake. According to Ambraseys (2009), this is an exaggeration referring to the Marmara Sea instead.

6 September 543 Cyzicus 40.28-27.74

Half of Cyzicus was destroyed, together with part of its wall. The rest of the city was severely damaged (Ambraseys 2009; Guidoboni et al. 1994).

15-16 August 554 Constantinople 40.7-29.8 Ms=7

Constantinople was severely affected by an earthquake during the night. Many houses, baths, churches, and parts of the city walls were damaged. A large part of Nicomedia was also destroyed. Only one source mentions partial damage in Nicaea (Ambraseys 2009; Guidoboni et al. 1994).

14/23 December 557 Constantinople 40.9-28.3 Ms=6.9

This event affected the north coast of the Marmara Sea and especially Constantinople where many houses and the city walls were destroyed (Ambraseys and Finkel 1991). One source mentions damage in Nicomedia and Nicaea, but Ambraseys (2009) argues that there is no contemporary supporting evidence that damage extended in the east. These regions were affected by earlier earthquakes and probably later amalgamated by the writer.

26 October 740 Constantinople 40.7-28.7 Ms=7.1

This is a major event in the eastern part of the Marmara Sea. The walls of Constantinople, Nicomedia, Praenetos (Karamürsel) and Nicaea were badly damaged and repaired immediately (Ambraseys and Finkel 1991; Guidoboni et al. 1994). The same authors report that the massive damage forced the emperor to impose supplementary taxation for

the reconstruction. It is said that only one church remained standing in Nicaea. Serious damage in Constantinople and villages in Thrace is reported. Probable replicas occurred during the following year (Ambraseys 2009).

23 September 1063 Marmara region 40.8-27.4 Ms=7.4

The area affected is delimited by Tekirdag, Erdek and the Dardanelles. Walls, aqueducts, churches and other public buildings were thrown down, particularly at Mürefte, Panion (near Barbaros) and Tekirdag. Some damage is also reported in Constantinople. The remains of the temple of Hadrian at Cyzicus collapsed (Ambraseys and Finkel 1991). One anonymous source mentions the destruction of the cathedral of Nicaea in this same event (Ambraseys 2009). Guidoboni et al. (1994) state that this destruction must be associated to another event in September 1065. Aftershocks continued to be felt in Constantinople for two years. Most probably, the shock originated in the Marmara Sea.

September 1065 Nicaea 40.4-30.0 Ms=6.8

This event is not so strong as the September 1063 earthquake, but bigger than its aftershocks. The Holy Wisdom church, the Shrine of the Holy Fathers and other churches, the walls and numerous houses in Nicaea were destroyed. (Ambraseys 2009) states that the two events of 1063 and 1065 originates from distinct sources as they affected separate areas.

15-17 March 1419 Prusa 40.4-29.3 Ms=7.2

A series of earthquakes happened from east to west during three days and three nights. Aftershocks were felt during 40 days and during the rest of the year with less strength (Ambraseys 2009). It destroyed the walls of Bursa together with most of its houses. Other towns in the area were possibly damaged. The shock triggered huge rock falls and the earth opened up. Rivers overflowed and new springs appeared (Ambraseys and Finkel 1991).

10 September 1509 Marmara Sea 40.9-28.7 Ms=7.2

This earthquake caused considerable damage throughout the Marmara region, from Gelibolu to Bolu, and from Edirne to Bursa. Heavy damage and casualties is reported in Istanbul with the destruction of many mosques and other buildings, part of the city walls, about 1000 houses. Many houses and public buildings sustained various degree of damage in Gelibolu and Bolu. The shock was felt within a radius of 750 km. Aftershocks, some of them destructive, continued intermittently for almost two years. Bursa is mentioned in one source as having been affected by the earthquake but information about damage from contemporary sources is lacking. A contemporary register describes repairs on the city baths in December 1510 but do not relate it to the earthquake. No evidence has been found to suggest that Iznik was damaged, except for a notice dated February 1511 mentioning

repairs to the imaret (public soup kitchen), which are not attributed to earthquake damage (Ambraseys 2009).

2 September 1754 Izmit 40.8-29.2 Ms=7

The earthquake occured at night and was preceded by a period of foreshocks. Widespread material damage is reported in Izmit and Istanbul, especially on old stone or brick buildings. The region of Izmit seems to have suffered more than Istanbul. In the regions of Iznik and Bursa, a few houses were destroyed but no casualties are reported. Geyve was also affected, which implies that the epicentral region should be sought in the eastern part of Izmit Gulf. The additional damage caused by some of the aftershocks in Istanbul suggests that seismic activity moved to the western part of the Gulf (Ambraseys 2009). The shock was felt in Izmir, possibly in Edirne and probably in Ankara.

22 May 1766 Marmara region 40.8-29.0 Ms=7.1

Damage is reported in Bursa, Gelibolu, Edirne, Izmit, and Istanbul. It extended from Tekirdag to Izmit and to the south coast from Mudanya to Karamürsel. In Istanbul, houses and public buildings of all types collapsed. Floods are reported in Mudanya (Ambraseys 2009). The shock was felt strongly at Athos, Thessaloniki, Aytos in Bulgaria and along the west coast of the Black Sea. Damaging aftershocks continued for weeks, the whole sequence lasting for over a year. The epicentral region is assumed to be offshore by Ambraseys and Finkel (1991).

5 August 1766 Marmara region 40.6-27.0 Ms=7.4

An equally large if not larger earthquake than the May event happened in August. It enlarged the affected area west of Tekirdag to the region of Ganos (Gaziköy) and Gelibolu. Damage extended to Bursa, Istanbul, throughout Thrace to Edirne and the district of Biga. Much of Ganos was destroyed by the earthquake and the following fire. In places, the ground cracked and liquefied. Half of Gelibolu was destroyed. Damage in Istanbul was not very serious. In Edirne, several minarets fell, and some baths and the city walls suffered. Damage is also reported in Izmit, Yalova and Karamürsel where the courthouse was destroyed and four people killed (Ambraseys 2009).

5 August 1794 Bursa

This earthquake caused damage on a mosque in Sögüt and probably on another one in Afyon. It is likely to have been felt in Hendek, Iznik, and Istanbul (Ambraseys 2009).

29 December 1854 Iznik 40.4-29.5 Ms=4.5

A big earthquake occurred along the southern shore of Iznik Lake. Significant damage was reported in two close villages (Mehmeçik and Pamukcik). The event was only felt in Iznik with minor damage (Ambraseys 2009). It was felt in Istanbul. Ambraseys (2000) considers it a precursor of the following bigger events.

28 February 1855 Bursa 40.1-28.9 Ms=7.1

The earthquake destroyed many villages along the south coast of Ulubat Lake and along the foothills of Uludag mountain. Bursa was almost totally destroyed as well as villages between Yenisehir and Celtikçi (Ambraseys and Finkel 1991). In Bursa, few of the 125 taller minarets collapsed completely but only two remained entire. All the 125 mosques of the town suffered damage, and 1500 houses were destroyed. A lot of damage is reported at Mudanya without casualties. The shock was strong in Gemlik and Kursunlu with few damage (Ambraseys 2000). Some slight damage was done at Canakkale and Gelibolu. Minor damage extended to Edirne and Istanbul. The shock was also felt in Rhodes, Chios, Samos, Izmir and Athens. Aftershocks continued to be felt, decreasing in number and intensity.

11 April 1855 Bursa 40.19-28.95 Ms=6.3

According to Ambraseys and Finkel (1991), it is the biggest replica of the former earthquake. The destructions were important in Bursa. It also affected the area north of Bursa, from Gemlik to Mudanya. No damage was reported around Ulubat Lake where the main shock had produce destructive effects. Ambraseys (2000) states that it was strongly felt in Mudanya and that Gemlik was not affected much. The shock was strong in Istanbul, Edirne, Lesbos, and Izmir. The government had to borrow money for the reconstruction to stop the massive emigration. This reconstruction was very slow and many of the mosques remained damaged ten years after the earthquake. Aftershocks continued to be felt in Bursa until late December.

14 December 1855 Gemlik

A damaging aftershock ruined two villages south of Gemlik. It was felt in Bursa without damage, and also in Istanbul. It was followed by weaker shocks several days long (Ambraseys 2009).

17 September 1857 Gemlik 40.40-29.15 Ms=5.3

A small, destructive earthquake occurred between Gemlik and Yalova. Destructions are reported in Gemlik on houses and public buildings, and in Yalova. In Bursa, 30 houses were destroyed and hundreds were damaged. It was strongly felt in Iznik, Izmit, and Istanbul (Ambraseys 2009).

7 March 1858 Bandirma

An earthquake shock was felt and caused no damage (Ambraseys 2009).

9 January 1859 Bandirma

A strong earthquake was felt in the evening (Ambraseys 2009).

7 June 1860 Bursa

A very strong shock occurred in Iznik and Bursa, only causing the collapse of a few walls. It was felt strongly in Istanbul and other places in Bithynia. Aftershocks continued to be felt intermittently through the year (Ambraseys 2009).

6 November 1863 Iznik Lake 40.40-29.15 Ms=5

This was a relatively small earthquake. Damage is reported in Gemlik (Ambraseys and Finkel 1991). The shock was strongly felt in Bursa with the collapse of one already damaged tomb. The shock was also felt in Istanbul, Gelibolu and Bolu. Öztürk et al. (2009) argue that the damage pattern suggests an epicenter on the fault passing along the southern coast of Iznik Lake.

17 April 1876 Mudanya

A strong earthquake was reported from Mudanya, Gemlik and the region of Bursa. The shock lasted 30 seconds and was followed by a number of aftershocks until late May. It caused no damage (Ambraseys 2009).

19 April 1878 Sapanca 40.70-30.20 Ms=6.1

This was a locally destructive earthquake in the region between Esme, Labinia, Sapanca and Adapazari which were destroyed. Damage extended to Bursa and Izmit. Slight damage also extended to Geyve and Iznik. It was strongly felt in Istanbul and perceptible through Thrace (Ambraseys 2009; 2000).

27 February 1889 Bandirma

An earthquake shock was felt (Ambraseys 2009).

17 May 1889 Marmara region

A light shock was reported from Bandirma, Istanbul, the Prince Islands and Gemlik. The shock probably originated from the sea (Ambraseys 2009).

17 May 1890 Gemlik

An earthquake was felt in Gemlik (Ambraseys 2009).

3 March 1893 Iznik

A strong earthquake occurred in Iznik region. Small damage is reported on a few old buildings in Iznik. The shock was felt in Yenisehir and perceptible in Istanbul (Ambraseys 2009).

25 May 1893 Gemlik

A shock was felt in Gemlik. It caused no damage (Ambraseys 2009).

5 May 1894 Gemlik

This earthquake was preceded and followed by many small shocks. It caused no damage. It was strongly felt at Mudanya and Gemlik (Ambraseys 2009).

10 July 1894 Izmit 40.7-29.6 Ms=7.3

The epicentral area extended from Adapazari in the east, along Izmit Gulf and into the Sea of Marmara. In Gemlik, the Greek school and houses were destroyed, and a few walls collapsed without casualties. There is no information for Iznik but it is probable that the damage was important (Ambraseys 2009). Maximum effects were reported from the region between Yalova and Sapanca, where most villages were totally destroyed. The shock caused the Sakarya River to flood its banks and the development of mud volcanoes. Liquefaction of the ground and landslides were described in the epicentral region. Widespread damage is reported in Istanbul. The shock was felt in Bucarest, Sofia and Crete. It was not followed by a significant aftershock sequence (Ambraseys 2000).

3 September 1894 Geyve

The shock happened in the morning (Ambraseys 2009).

21 January 1895 Gemlik

The shock was felt in the villages around Gemlik (Ambraseys 2009).

19 September 1895 Bilecik

A strong shock was felt at Bilecik, Karaköy and Geyve. It caused not damage (Ambraseys 2009).

25 October 1896 Iznik

A small earthquake occurred west of Iznik Lake, with damaged in Gürle and Orhangazi, and cracked walls in Gemlik. The shock was felt in Geyve (Ambraseys 2009).

24 May 1899 Gemlik

Strong shocks occurred during the night and were not felt very far away (Ambraseys 2009).

Appendix B

Protocole d'analyse du ^{10}Be in-situ

Les échantillons prélevés sur le terrain sont d'abord broyés et tamisés. La fraction 200-500 μm est utilisée de préférence pour la suite du traitement. Pour les échantillons contenant peu de quartz, on inclut les fractions plus grossières. Les grains sont ensuite passés au séparateur magnétique Franz pour isoler les minéraux magnétiques. Le matériel non magnétique conservé comprend le quartz, mélangé à des carbonates de calcium et des feldspaths en proportions variables. Les grains non magnétiques sont soumis à des attaques acides successives pour isoler le quartz. Dans un premier temps, les carbonates sont extraits par quelques bains d'acide chlorhydrique (HCl). Dans un deuxième temps, les feldspaths sont dissouts par des bains successifs dans un mélange d'acides chlorhydrique et fluorosilicique (H_2SiF_6) en proportion 2:1. La masse restante est finalement soumise à trois attaques séquentielles à l'acide fluorhydrique (HF) pour éliminer le ^{10}Be atmosphérique présent à la surface des grains.

A ce stade, chaque échantillon reçoit $\sim$300 μg d'entraineur ^{9}Be qui permet de fixer le rapport 10/9 mesuré par le spectromètre de masse. Après une dissolution totale à l'acide fluorhydique, les échantillons subissent des évaporations partielles successives. Lors de cette étape, l'HF est substitué par d'autres acides, perchlorique ($HClO_4$), nitrique (HNO_3) puis chlorhydrique. Enfin, le pH de la solution restante est neutralisé. L'extraction du béryllium est réalisée par un passage dans deux colonnes échangeuses d'ions. La première colonne utilise une résine DOWEX 1x8 à mailles 100-200 et permet d'éliminer les anions (fer et manganèse) La deuxième colonne utilise une résine DOWEX 50wx8 à mailles 100-200 et permet d'éliminer les cations (dont l'isobare du beryllium-10, le bore) Les solutions de béryllium obtenues sont oxydées à 950 $^\circ$C et transférées au laboratoire LN2C-CEREGE d'Aix-en-Provence pour la mesure du rapport 10/9 sur le spectromètre de masse par accélérateur ASTER.

Appendix C

Décalages latéraux mesurés le long de la MNAF

Distance along strike (km)	Quality	Offset value (m)	Uncertainty (m)
8.92	1	3	1
8.92	1	6	4
8.92	2	14	4
9.5	1	4	1
9.76	1	11	1
10.04	1	9.5	1
10.5	2	11.5	2
12.59	1	3.2	1
14.59	2	16	5
16.17	2	43	6
23.04	2	15	5
23.68	3	34	1
23.68	1	5	2
25.11	1	4	1
25.46	2	8	3
25.46	2	61	4
27.36	1	16	1
27.36	1	3	2
28.03	1	5	2
28.15	1	5	1
28.56	2	6	1
28.82	1	25	2
29.53	1	6	2
30.05	2	5	4
30.99	3	24	7
31.11	2	8.5	2.5
31.58	2	29	4
32.1	2	16	4
33.3	2	16	5
34.16	2	3.5	4
34.16	2	11	4
36.08	2	12	4
36.82	2	17.5	2.5
37.29	2	5	1
37.29	2	78	4

Figure C.1: Offset values measured along the MNAF between Sölöz and Mekece.

Distance along strike (km)	Quality	Offset value (m)	Uncertainty (m)
37.42	2	9	4
38.23	1	22	1
41.68	2	28	4
42.81	2	5	2
43.77	2	6	1
43.91	2	23	2
44.36	2	8	4
44.36	3	62	4
44.52	1	15	4
44.61	1	40	4
44.77	1	6	3
45.45	1	19.5	6
45.61	2	11	4
45.78	1	12	1
46.11	2	25	4
46.32	1	2.5	1
46.32	1	9	1
46.86	2	4	2
47.22	2	15	4
47.78	2	112	16
48.24	2	25	7
48.24	3	72.5	22.5
48.73	3	8.5	4
48.74	1	11.5	1
48.85	2	47.5	5
49.16	2	3	1.5
49.34	2	5.5	2
49.51	2	16.5	6
49.67	2	29.5	5
49.8	1	29.5	5
50.4	3	4	4
50.54	2	6	4
50.74	2	6	1
51.12	2	5	1
51.66	2	18	1

Figure C.2: Offset values measured along the MNAF between Sölöz and Mekece (continued).

Distance along strike (km)	Quality	Offset value (m)	Uncertainty (m)
52.08	1	12	1
52.09	2	48.5	4.5
52.44	1	6	1
52.44	2	10	2
52.44	3	22	9
52.92	1	5	1
53.11	2	14	4
53.11	2	53	4
53.62	3	4.5	1
53.95	1	10	1
54.08	1	11	1
54.25	3	12	1
54.28	1	2	1
54.35	3	2.5	1
54.55	2	12	2
54.78	1	17	4
54.83	1	15	3
54.93	2	2.6	4
54.98	3	180	25
55.09	2	20	9
55.26	2	11.5	2
55.49	1	23	5
55.76	2	7.5	4
56.08	2	48	7
56.35	1	10	1
56.41	3	10	5
56.83	1	5.5	1
56.83	1	17	1
56.83	1	17	1
56.83	3	8.5	1.5
56.83	3	12	2
58.62	1	15	1
58.78	1	15	2.5
59.18	1	8.5	0.5
59.58	1	5.7	1

Figure C.3: Offset values measured along the MNAF between Sölöz and Mekece (continued).

Appendix D

Données GPR supplémentaires

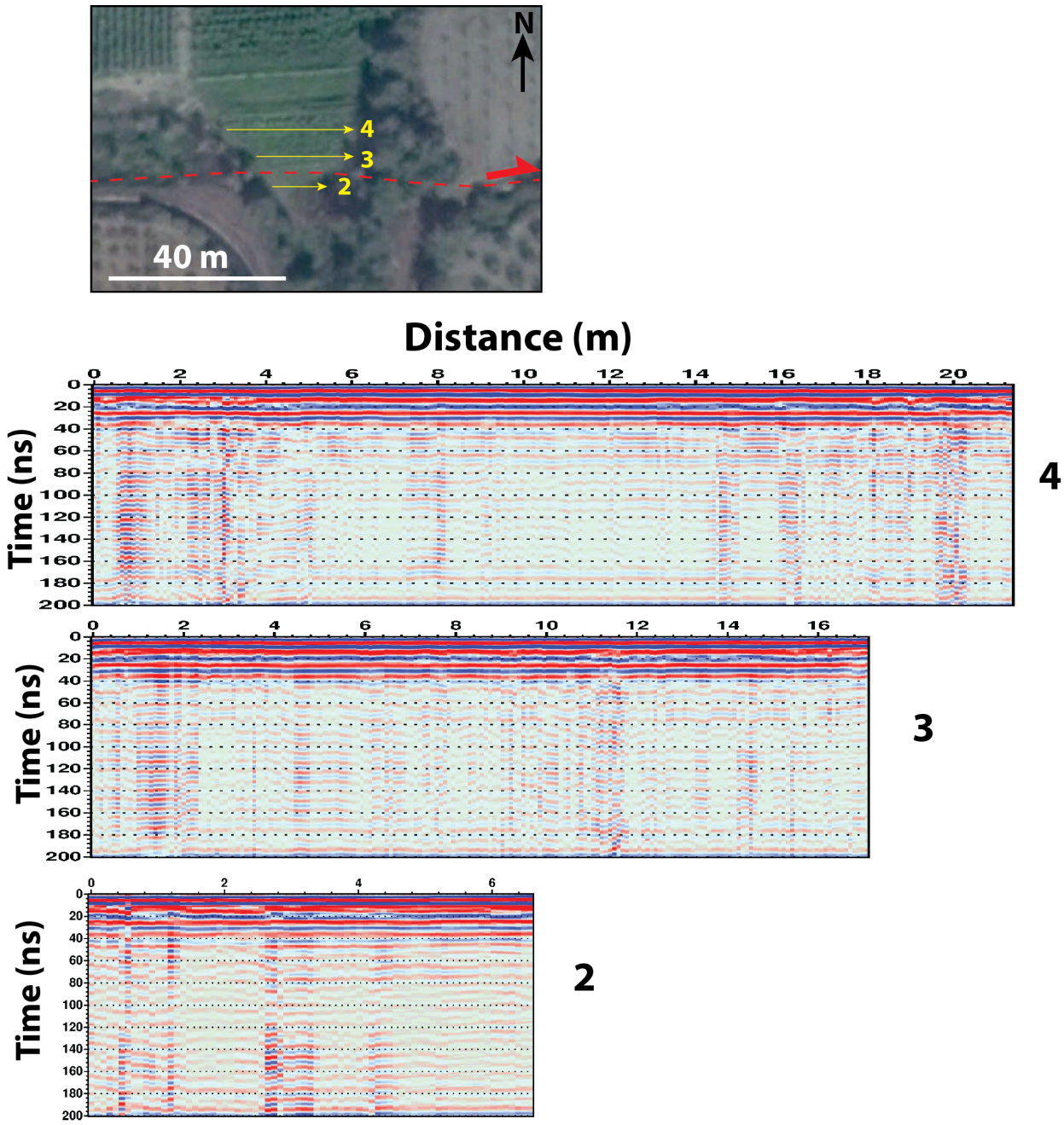

Figure D.1: GPR survey on the MNAF site 1. The map at the top locates the profiles in yellow and the fault as a red broken line. The numbers correspond to different GPR profiles. At the bottom are shown the GPR images.

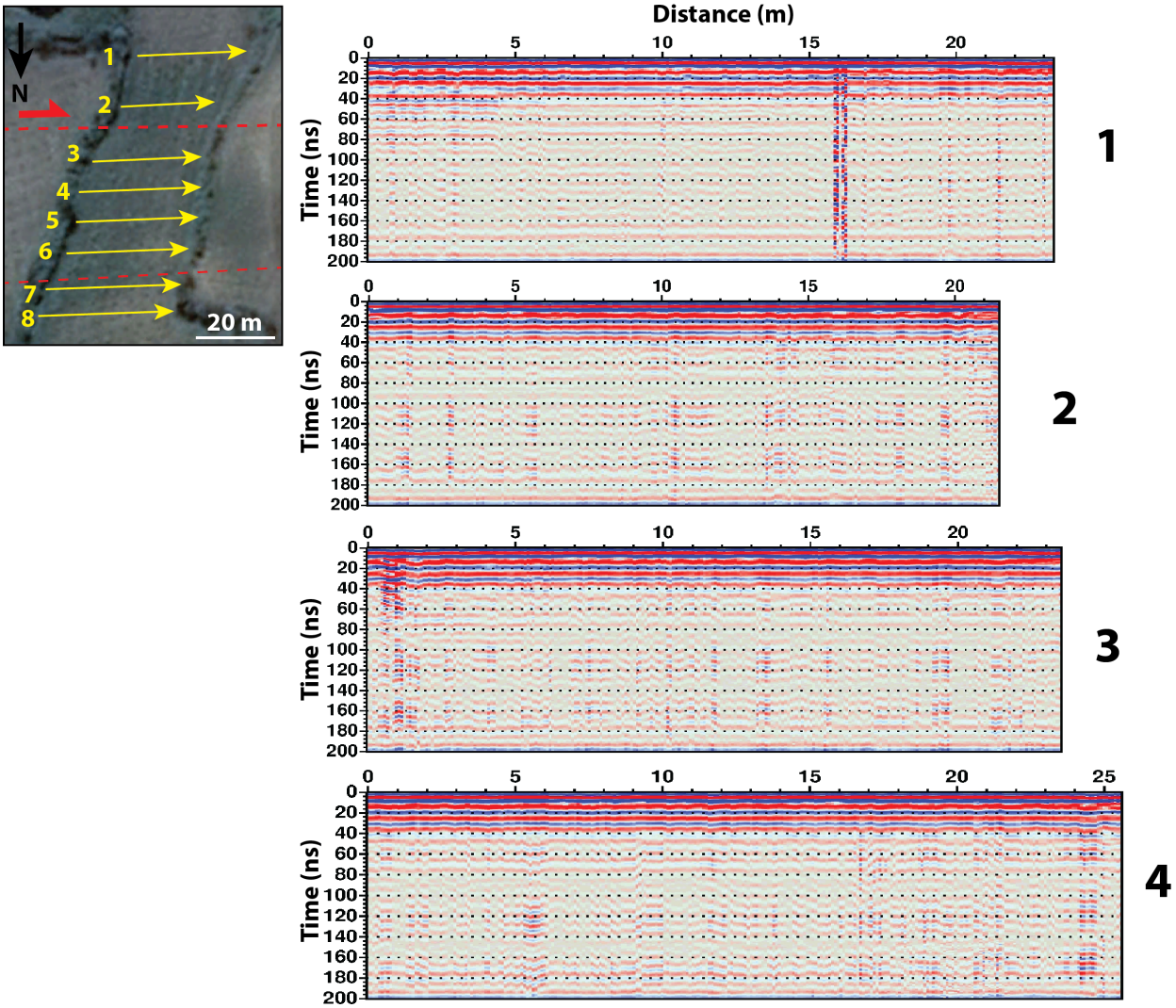

Figure D.2: GPR survey on the MNAF site 2. The map on the left locates the profiles in yellow and the faults as red broken lines. The numbers correspond to different GPR profiles. On the right are shown the GPR images.

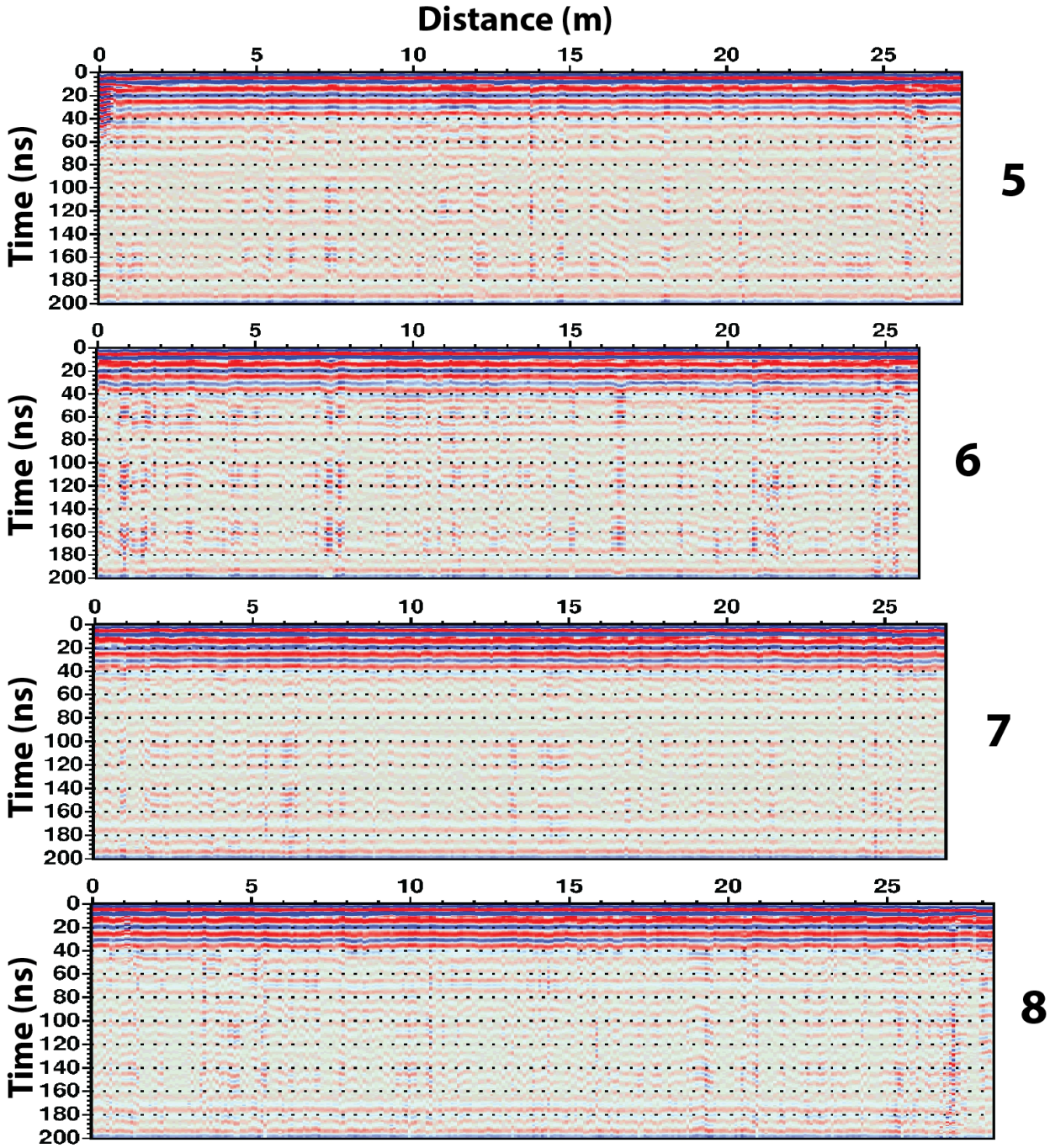

Figure D.3: GPR survey on the MNAF site 2 (continued). The numbers correspond to the different GPR profiles located on the previous figure.

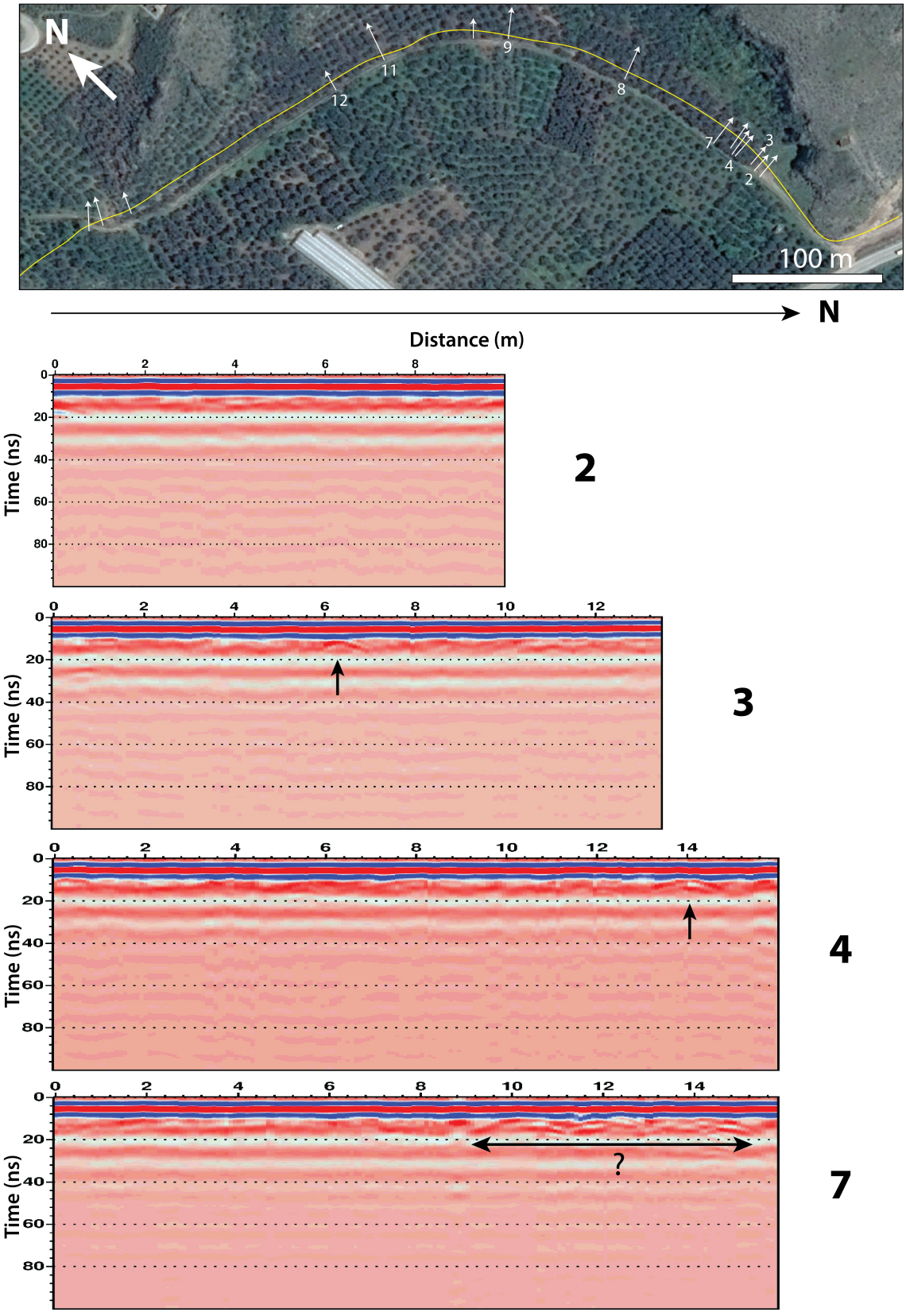

Figure D.4: GPR survey on the undergound aqueduct. The map at the top locates the aqueduct's channel in yellow and the transversal GPR aquisitions drawn as white arrows. The numbers correspond to different GPR profiles. At the bottom are shown the GPR images. When possible, visible anomalies compatible with the aqueduct's location are shown in black.

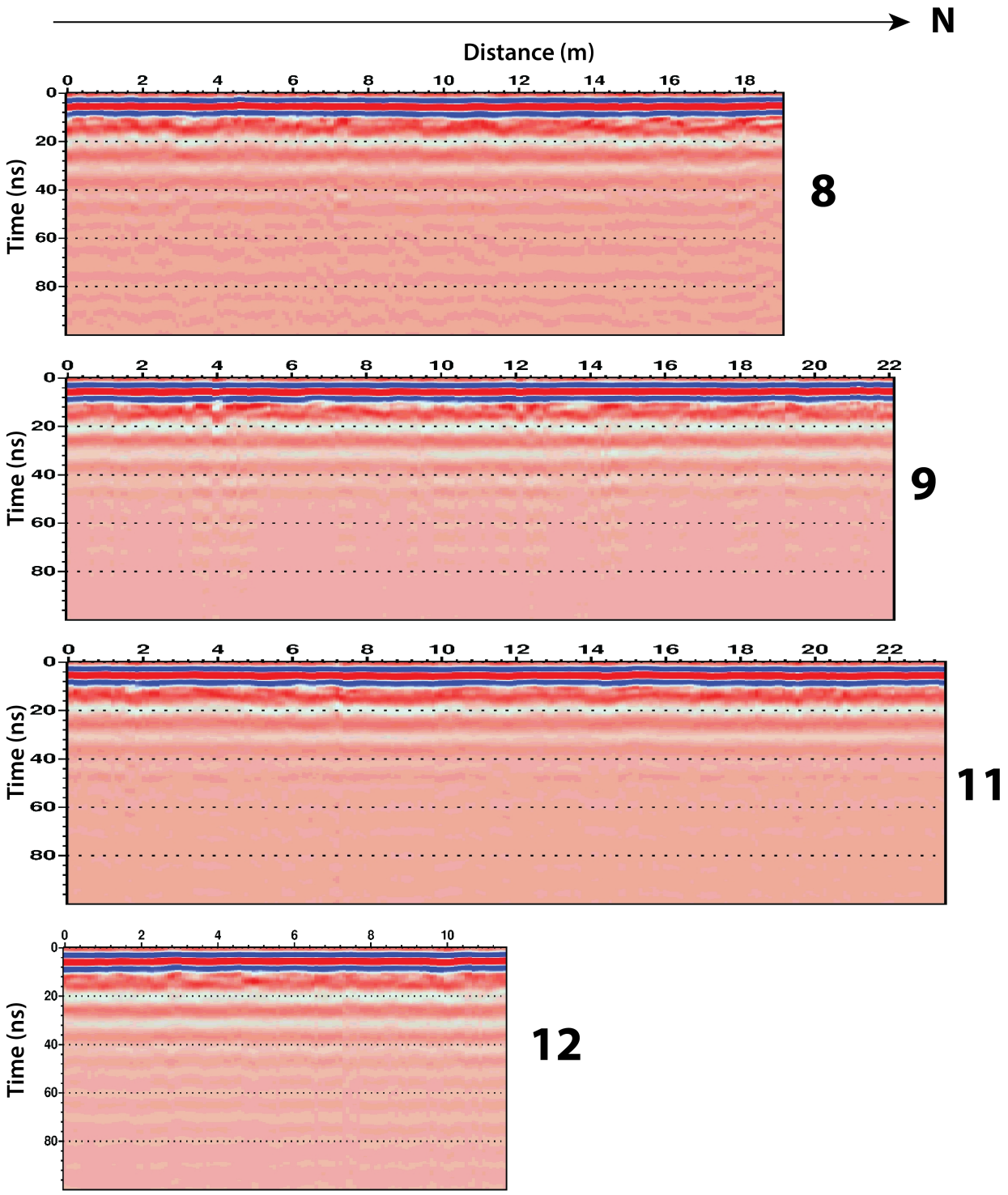

Figure D.5: GPR survey on the undergound aqueduct (continued). The numbers correspond to the different GPR profiles located on the previous figure. When possible, visible anomalies compatible with the aqueduct's location are shown in black.

Appendix E

Fiches descriptives des techniques identifiées sur l'aqueduc

Atlas des techniques de la Construction Romaine

Arc : AR-0002

Identification

Identité	Arc AR-0002 ; 2 éléments
Provenance	Nicaea, Aqueduc
Phase(s) chronologique(s)	Réaménagement 5 : Reconstruction importante en travertins
Description	Arche 7 en moellons de travertin quadrangulaires.
Technique associée	Mur MR-0034

Caractéristiques générales

Type morphologique	En plan : En plein cintre surbaissé En section : Avec noyau Forme : Extradossé
Fonction	Passage - Élévations
Position	En élévation - En série

Arc

Matériau	Pierre (travertin) - Liant (chaux)
Appareil	Clef : Matériaux homogènes avec le reste de l'arc Imposte : Matériaux identiques avec le reste de l'arc
Pierres	Finition : Absence de finition Dureté : Ferme Dimensions : Grand module ; Long. : 21 ; Haut. : 16
Commentaire	Mortier à matrice homogène blanche, granuleux, solide mais un peu friable, de granulométrie hétérogène (<1mm à 4mm). Grains noirs et bruns bien répartis.

Précisions

Notes	Arches 4 et 7.

Références

Auteur(s) de la notice	Yacine Benjelloun
Date de création	27/04/2017
Édition électronique	Agnès Tricoche
Citer cette notice	Base de données ACoR (en ligne), notice AR-0002, https://acor.huma-num.fr/AR-0002/fr. Consultée le 10/08/2017.

Images

AR-0002-2.jpg - Vue générale
Yacine Benjelloun



AR-0002-1.png - Courbe statistique / histogramme : Diagramme des modules des claveaux
Yacine Benjelloun

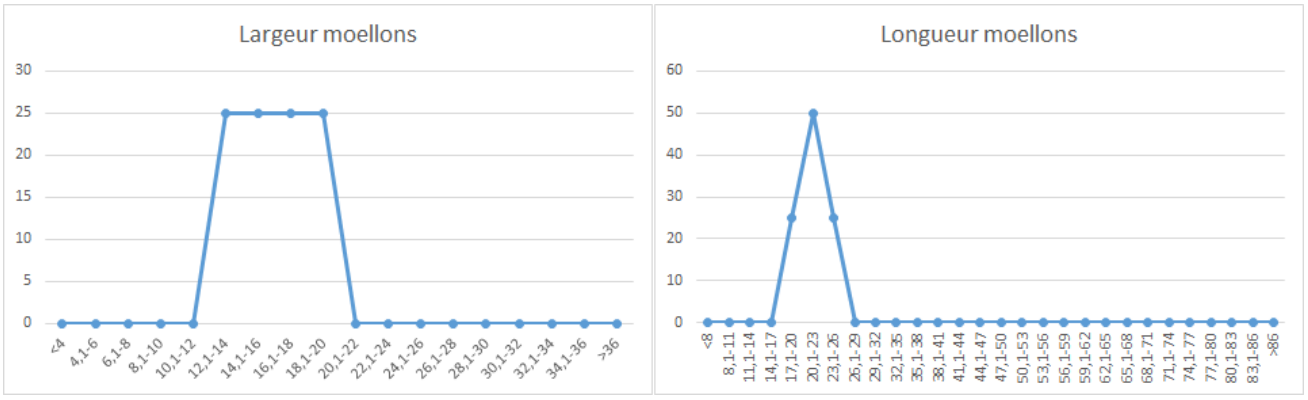

Copyright © 2016 labex TransferS | Pôle Humanités Numériques
Ce contenu est sous licence Creative Commons BY-NC-SA.

Atlas des techniques de la Construction Romaine

Arc : AR-0003

Identification

Identité	Arc AR-0003 ; 3 éléments
Provenance	Nicaea, Aqueduc
Phase(s) chronologique(s)	Projet originel (527/565)
Description	Arches en TCA de la première phase de construction de l'aqueduc, aujourd'hui masquées par un parement de travertins.
Technique associée	Mur MR-0041

Caractéristiques générales

Type morphologique	En plan : En plein cintre En section : Homogène Forme : Extradossé
Fonction	Passage - Élévations
Position	En élévation - En série

Arc

Matériau	Terre cuite - Liant (mortier de chaux et de sable)
Terres cuites architecturales	Forme : Tuiles Finition : [Non visible] Dimensions moyennes (cm) : Long. : 25 ; Haut. : 5,3
Joints	Épaisseur : > 2 cm
Commentaire	Mortier blanc à grains moyens sombres peu abondants.

Références

Auteur(s) de la notice	Yacine Benjelloun
Date de création	27/04/2017
Édition électronique	Agnès Tricoche
Citer cette notice	Base de données ACoR (en ligne), notice AR-0003, https://acor.huma-num.fr/AR-0003/fr. Consultée le 10/08/2017.

Images

AR-0003-1.jpg - Vue de détail
Yacine Benjelloun



AR-0003-2.png - Courbe statistique / histogramme : Diagramme des modules des claveaux
Yacine Benjelloun

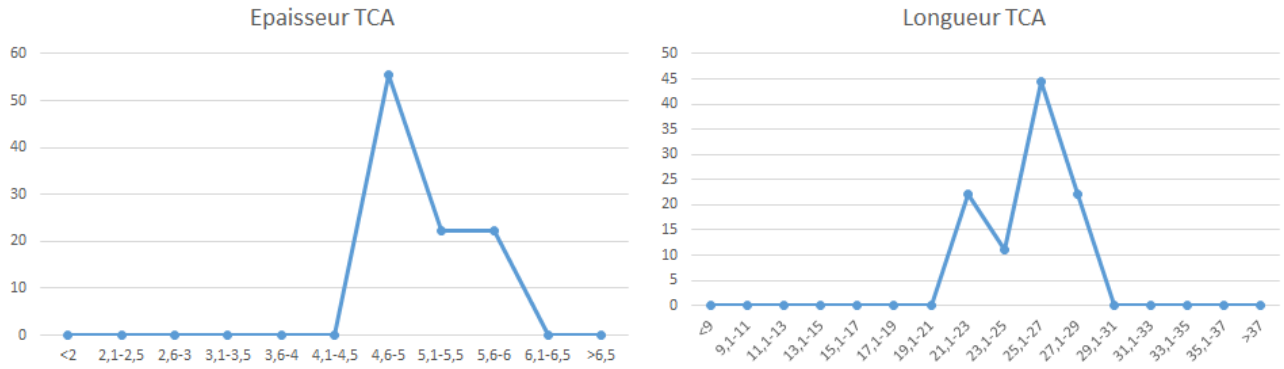

Copyright © 2016 labex TransferS | Pôle Humanités Numériques
Ce contenu est sous licence Creative Commons BY-NC-SA.

Atlas des techniques de la Construction Romaine

Arc : AR-0004

Identification

Identité	Arc AR-0004 ; 2 éléments
Provenance	Nicaea, Aqueduc
Phase(s) chronologique(s)	Réaménagement 7 (1205/1254) : Reconstruction des élévations près des portes de la ville
Description	Arche 5 en TCA homogènes.
Technique associée	Mur MR-0028

Caractéristiques générales

Type morphologique	En plan : En plein cintre En section : Homogène Forme : Extradossé
Fonction	Passage - Élévations
Position	En élévation - En série

Arc

Matériau	Terre cuite - Liant (mortier de chaux et de sable)
Terres cuites architecturales	Forme : Tuiles Finition : [Non visible] Dimensions moyennes (cm) : Long. : 23 ; Haut. : 4,3
Joints	Finition : Sans finition Épaisseur : > 2 cm
Commentaire	TCA rouge vif, pâte homogène. Qualité des TCA homogène. Mortier à matrice homogène blanc jaunâtre, solide, granuleux. Grains homogènes, noir-bruns, bien répartis. Quelques grains très grossiers.

Précisions

Notes	Arche 5. TCA identiques à MR-0028.

Références

Auteur(s) de la notice	Yacine Benjelloun
Date de création	27/04/2017
Édition électronique	Agnès Tricoche
Citer cette notice	Base de données ACoR (en ligne), notice AR-0004, https://acor.huma-num.fr/AR-0004/fr. Consultée le 10/08/2017.

Images

AR-0004-1.jpg - Vue de détail
Yacine Benjelloun



AR-0004-2.png - Courbe statistique / histogramme : Diagramme des modules des tuiles
Yacine Benjelloun

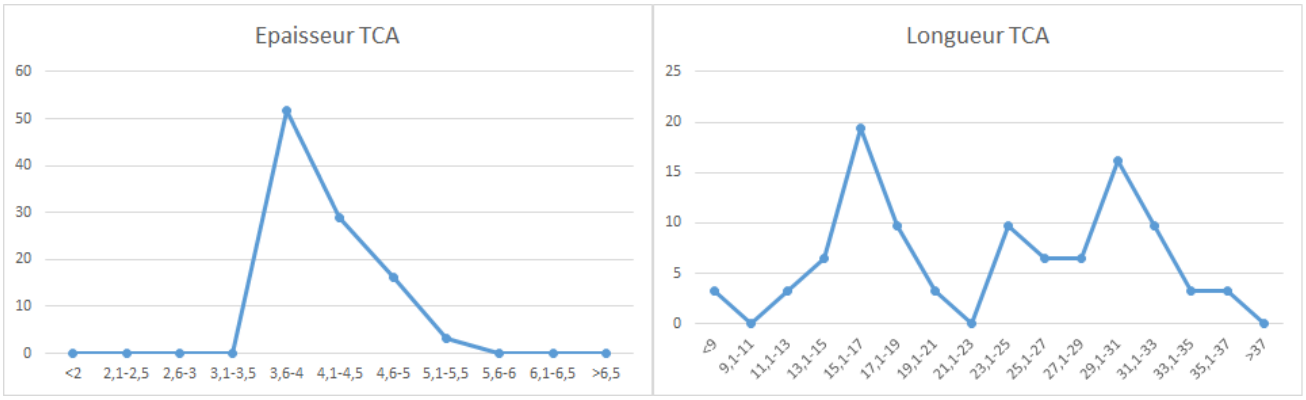

Copyright © 2016 labex TransferS | Pôle Humanités Numériques
Ce contenu est sous licence Creative Commons BY-NC-SA.

Atlas des techniques de la Construction Romaine

Arc : AR-0005

Identification

Identité	Arc AR-0005 ; 1 élément
Provenance	Nicaea, Aqueduc
Phase(s) chronologique(s)	Réaménagement 6 (800) : Reconstructions en matériaux variés
Description	Arche asymétrique en moellons quadrangulaires de travertin de tailles différentes.
Technique associée	Mur MR-0036

Caractéristiques générales

Type morphologique	En plan : En plein cintre surhaussé En section : Homogène Forme : Extradossé
Fonction	Passage - Élévations
Position	En élévation - Isolé

Arc

Matériau	Pierre (travertin) - Liant (chaux)
Appareil	Claveaux irréguliers Clef : Matériaux homogènes avec le reste de l'arc Imposte : Matériaux identiques avec le reste de l'arc
Pierres	Finition : Absence de finition Dureté : Ferme Dimensions : Grand module ; Long. : 32 ; Haut. : 15
Commentaire	Mortier blanc, extrêmement altéré en surface, recouvert de concrétions.

Précisions

Notes	Arche 8.

Références

Auteur(s) de la notice	Yacine Benjelloun
Date de création	27/04/2017
Édition électronique	Agnès Tricoche
Citer cette notice	Base de données ACoR (en ligne), notice AR-0005, https://acor.huma-num.fr/AR-0005/fr. Consultée le 10/08/2017.

Images

AR-0005-1.jpg - Vue générale
Yacine Benjelloun



AR-0005-2.png - Courbe statistique / histogramme : Diagramme des modules des claveaux
Yacine Benjelloun

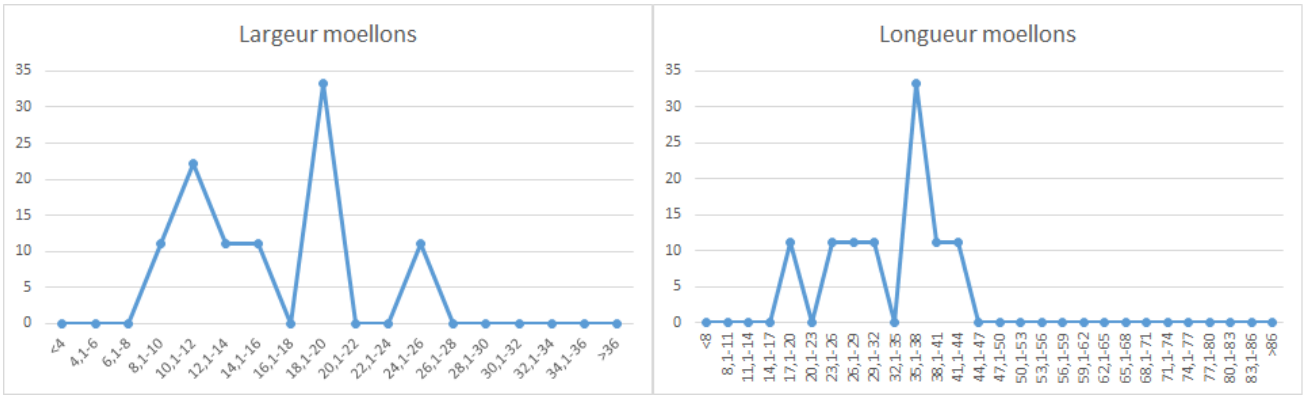

Copyright © 2016 labex TransferS | Pôle Humanités Numériques
Ce contenu est sous licence Creative Commons BY-NC-SA.

Atlas des techniques de la Construction Romaine

Contrefort : CF-0006

Identification

Identité	Elévation : Contrefort CF-0006 ; 1 élément
Provenance	Nicaea, Aqueduc
Phase(s) chronologique(s)	Réaménagement 3 : Reconstruction du chenal et ajout d'un contrefort et d'un bassin de répartition
Description	Structure de renforcement en TCA (contrefort) associée à un changement de direction de l'aqueduc.

Caractéristiques générales

Type morphologique	En plan : En arc ; Externe
Fonction	Elément non porteur, Lié
Section	Homogène

Parement

Matériau	Terre cuite - Liant
Terres cuites architecturales	**Forme** : Tuiles **Finition** : [Non visible] **Dimensions moyennes (cm)** : Long. : 28 ; Haut. : 5 ; Épaisseur des joints : 3,5
Assises	**Disposition des matériaux** : Assises horizontales **Disposition des terres cuites architecturales** : En panneresse & en boutisse, disposition irrégulière **Hauteur** : Constante (isodome)
Joints	**Finition** : Sans finition **Épaisseur** : > 2 cm
Commentaire	TCA rouge-oranges toutes identiques (peu de dégraissant grossier, excellente facture)

Précisions

Notes	Cette technique semble aussi présente dans les arches murées. Les TCA sont identiques à celles utilisées dans l'opus vittatum mixtum de l'autre bassin/contrefort plus proche des murailles.

Références

Auteur(s) de la notice	Yacine Benjelloun
Date de création	27/04/2017
Édition électronique	Agnès Tricoche
Citer cette notice	Base de données ACoR (en ligne), notice CF-0006, https://acor.huma-num.fr/CF-0006/fr. Consultée le 10/08/2017.

Images

CF-0006-1.jpg - Echantillon (photographie / relevé)
Yacine Benjelloun



CF-0006-2.png - Courbe statistique / histogramme
Yacine Benjelloun

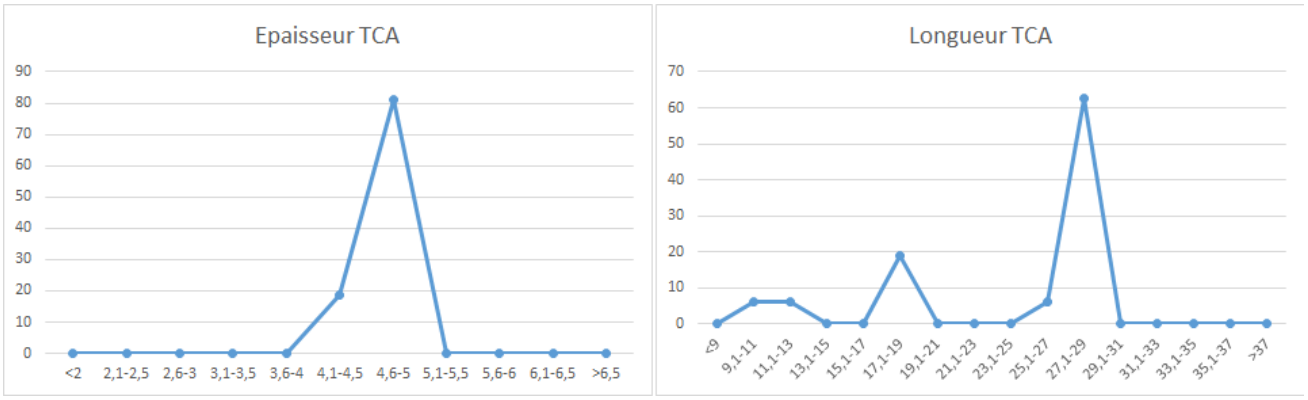

Copyright © 2016 labex TransferS | Pôle Humanités Numériques
Ce contenu est sous licence Creative Commons BY-NC-SA.

Atlas des techniques de la Construction Romaine

Mur : MR-0028

Identification

Identité	Elévation : Mur MR-0028 ; 1 élément
Provenance	Nicaea, Aqueduc
Phase(s) chronologique(s)	Réaménagement 7 (1205/1254) : Reconstruction des élévations près des portes de la ville
Description	Maçonnerie régulière faisant alterner 1 assise de moellons quadrangulaires et 1-3 assises de terres cuites.

Caractéristiques générales

Type morphologique	En plan : A faces parallèles - Linéaire continu. En coupe : A faces parallèles
Fonction	Elément non porteur
Section	Parementé (2 parements) ; Présence d'un noyau interne

Parement

Matériau	Pierre (calcaire, travertin, marbre) - Terre cuite - Liant (mortier de chaux et de sable)
Pierres	**Forme** : Quadrangulaire : rectangulaire - Polygonale **Finition** : Surface dressée **Épaisseur** : Constante **Dureté** : Ferme - Dure **Dimensions** : Petit et grand module ; Long. : 25 ; Haut. : 15 ; Module de 5 assises : 140 ; Épaisseur des joints : 3,5
Terres cuites architecturales	**Forme** : Tuiles **Finition** : [Non visible] **Dimensions moyennes (cm)** : Long. : 23 ; Haut. : 4 ; Épaisseur des joints : 3,5
Assises	**Disposition des matériaux** : Matériaux alternés par assise **Disposition des pierres** : En panneresse & en boutisse, disposition régulière (en parement) ; 1 assise (en coupe) **Disposition des terres cuites architecturales** : [autre] **Hauteur** : Irrégulière **Assises de réglage** : Terres cuites architecturales
Joints	**Finition** : Sans finition **Épaisseur** : > 2 cm
Commentaire	TCA rouge vif de qualité homogène. De façon générale, les assises sont constituées d'une épaisseur de TCA, mais ponctuellement certaines assises présentent deux ou trois épaisseurs avec des TC plus petites. Présence ponctuelle de TCA dressées entre les moellons. Présence parmi les moellons de quelques remplois de marbre. Les moellons sont de taille hétérogène et peu soignée.

Arc

Type morphologique	En plan : En plein cintre En section : Homogène Forme : Extradossé
Fonction	Passage - Élévations
Position	En élévation - En série

Précisions

Notes	Les TCA sont similaires à celles utilisées dans l'arche 5.

Références

Auteur(s) de la notice	Yacine Benjelloun
Date de création	17/06/2016
Édition électronique	Agnès Tricoche
Citer cette notice	Base de données ACoR (en ligne), notice MR-0028, https://acor.huma-num.fr/MR-0028/fr. Consultée le 10/08/2017.

Images

MR-0028-3.jpg - Echantillon (photographie / relevé)
Yacine Benjelloun



MR-0028-1.png - Courbe statistique / histogramme
Yacine Benjelloun

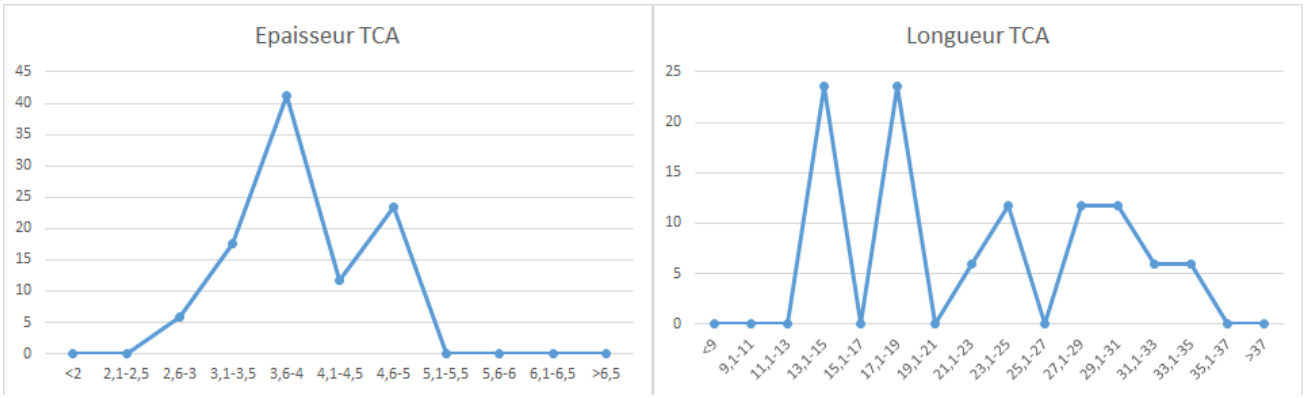

MR-0028-2.png - Courbe statistique / histogramme
Yacine Benjelloun

Atlas des techniques de la Construction Romaine

Mur : MR-0033

Identification

Identité	Elévation : Mur MR-0033 ; 1 élément
Provenance	Nicaea, Aqueduc
Phase(s) chronologique(s)	Réaménagement 3 : Reconstruction du chenal et ajout d'un contrefort et d'un bassin de répartition
Description	Maçonnerie régulière faisant alterner 1 assise de calcaire marneux sombre et 2 assises de TCA, utilisée pour le bassin de répartition situé à proximité des portes.

Caractéristiques générales

Type morphologique	En plan : Linéaire continu. En coupe : A faces parallèles
Fonction	Elément porteur
Section	Parementé (2 parements)

Parement

Matériau	Pierre (calcaire) - Terre cuite - Liant (chaux)
Pierres	**Forme** : Irrégulière **Dimensions** : Grand module ; Long. : 25 ; Haut. : 10
Terres cuites architecturales	**Forme** : Tuiles **Finition** : [Non visible] **Dimensions moyennes (cm)** : Long. : 28 ; Haut. : 5
Assises	**Disposition des matériaux** : Matériaux alternés par assise **Disposition des pierres** : En panneresse (en parement) ; 1 assise (en coupe) **Disposition des terres cuites architecturales** : En panneresse **Particularités** : A dédoublement **Hauteur** : Irrégulière **Assises de réglage** : Terres cuites architecturales
Joints	**Finition** : Lissés
Commentaire	Alternance d'1 assise de pierres et de 2-3 assises de TCA. Pierres calcaires gris foncé avec aspect d'"écorce".

Précisions

Notes	Les TCA sont identiques à MR-0029.

Références

Auteur(s) de la notice	Yacine Benjelloun
Date de création	21/06/2016
Édition électronique	Agnès Tricoche
Citer cette notice	Base de données ACoR (en ligne), notice MR-0033, https://acor.huma-num.fr/MR-0033/fr. Consultée le 10/08/2017.

Images

MR-0033-1.jpg - Echantillon (photographie / relevé)
Yacine Benjelloun



Copyright © 2016 labex TransferS | Pôle Humanités Numériques
Ce contenu est sous licence Creative Commons BY-NC-SA.

Atlas des techniques de la Construction Romaine

Mur : MR-0034

Identification

Identité	Elévation : Mur MR-0034 ; 3 éléments
Provenance	Nicaea, Aqueduc
Phase(s) chronologique(s)	Réaménagement 5 : Reconstruction importante en travertins
Description	Maçonnerie régulière de moellons quadrangulaires de travertins.

Caractéristiques générales

Type morphologique	En plan : Linéaire continu. En coupe : A faces parallèles
Fonction	Elément non porteur
Section	Parementé (2 parements) ; Présence d'un noyau interne

Noyau

Matériau	Pierre (calcaire, travertin) - Liant (chaux, mortier de chaux et de sable)
Pierres	**Dureté** : Ferme
Assises	**Disposition des matériaux** : Jeté en vrac entre les parements
Commentaire	Petits moellons. Mortier brun, granuleux, alvéolaire.

Parement

Matériau	Pierre (travertin) - Liant (chaux)
Pierres	**Forme** : Quadrangulaire : rectangulaire **Dureté** : Ferme **Dimensions** : Grand module ; Long. : 41 ; Haut. : 14 ; Module de 5 assises : 80 ; Épaisseur des joints : 3
Assises	**Disposition des matériaux** : Assises horizontales **Disposition des pierres** : En panneresse (en parement) ; [Autre] (en coupe) **Hauteur** : Irrégulière **Assises de réglage** : Pierre
Joints	**Finition** : Sans finition **Épaisseur** : > 2 cm
Commentaire	Mortier très altéré. Les travertins sont plus plats au sommet et plus gros à la base.

Arc

Type morphologique	En plan : En plein cintre surbaissé En section : Avec noyau Forme : Extradossé
Fonction	Passage - Élévations
Position	En élévation - En série

Précisions

Notes	Cette technique semble commune à l'arche 5, les assises intermédiaires des sections montrant une structure ternaire, et d'autres sections situées plus à

	l'est.

Références

Auteur(s) de la notice	Yacine Benjelloun
Date de création	21/06/2016
Édition électronique	Agnès Tricoche
Citer cette notice	Base de données ACoR (en ligne), notice MR-0034, https://acor.huma-num.fr/MR-0034/fr. Consultée le 10/08/2017.

Images

MR-0034-2.jpg - Echantillon (photographie / relevé)
Yacine Benjelloun



MR-0034-1.png - Courbe statistique / histogramme
Yacine Benjelloun

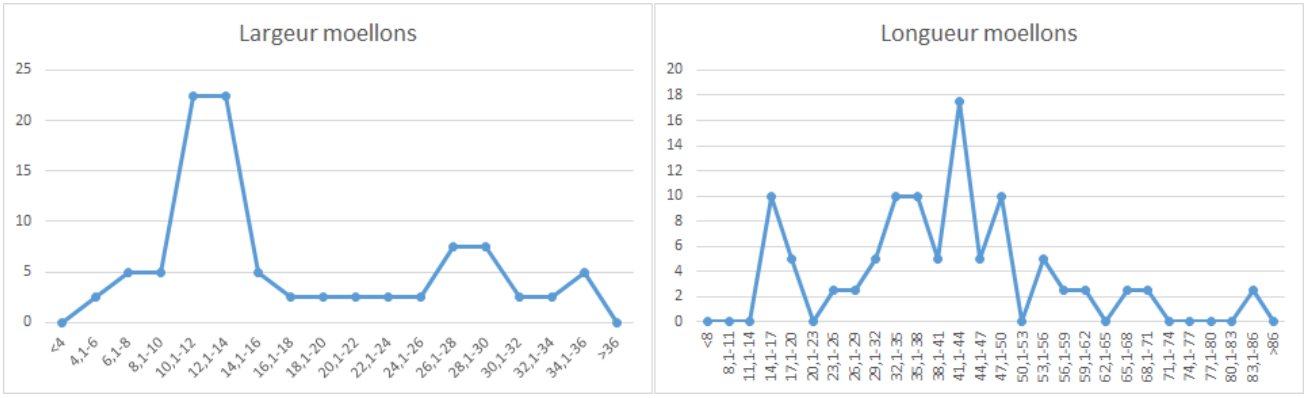

Copyright © 2016 labex TransferS | Pôle Humanités Numériques
Ce contenu est sous licence Creative Commons BY-NC-SA.

Atlas des techniques de la Construction Romaine

Mur : MR-0035

Identification

Identité	Elévation : Mur MR-0035 ; 2 éléments
Provenance	Nicaea, Aqueduc
Phase(s) chronologique(s)	Réaménagement 2 (565) : Nouveau parement en calcaires
Description	Parement régulier de moellons calcaires quadrangulaires, présent surtout à la base de l'aqueduc.

Caractéristiques générales

Type morphologique	En plan : Linéaire continu. En coupe : A faces parallèles
Fonction	Elément non porteur
Section	Parementé (2 parements) ; Présence d'un noyau interne ; Parements de même technique

Noyau

Matériau	Pierre (calcaire) - Liant (mortier de chaux et de sable)
Pierres	**Forme** : Irrégulière **Finition** : Absence de finition **Dureté** : Dure

Parement

Matériau	Pierre (calcaire) - Terre cuite - Liant (mortier de chaux et de sable)
Pierres	**Forme** : Quadrangulaire : rectangulaire **Finition** : Absence de finition **Épaisseur** : Constante **Dureté** : Dure **Dimensions** : Petit et grand module ; Long. : 26,1 ; Haut. : 17
Terres cuites architecturales	**Forme** : Fragments
Assises	**Disposition des matériaux** : Assises horizontales **Disposition des pierres** : En boutisse & en panneresse, disposition irrégulière (en parement) ; 1 assise (en coupe) **Disposition des terres cuites architecturales** : En panneresse, disposition irrégulière **Hauteur** : Constante (isodome) **Assises de réglage** : Pierre
Joints	**Finition** : Sans finition
Commentaire	Quelques TCA intercalées ponctuellement. Mortier blanc granuleux. Traces d'enduit, identique au mortier.

Précisions

Notes	Cette maçonnerie constitue la partie basale des sections à structure ternaire, et se trouve aussi à proximité des murailles.

Références

Auteur(s) de la notice	Yacine Benjelloun
Date de création	21/06/2016

Édition électronique	Agnès Tricoche
Citer cette notice	Base de données ACoR (en ligne), notice MR-0035, https://acor.huma-num.fr/MR-0035/fr. Consultée le 10/08/2017.

Images

MR-0035-2.jpg - Echantillon (photographie / relevé)
Yacine Benjelloun



MR-0035-1.png - Courbe statistique / histogramme
Yacine Benjelloun

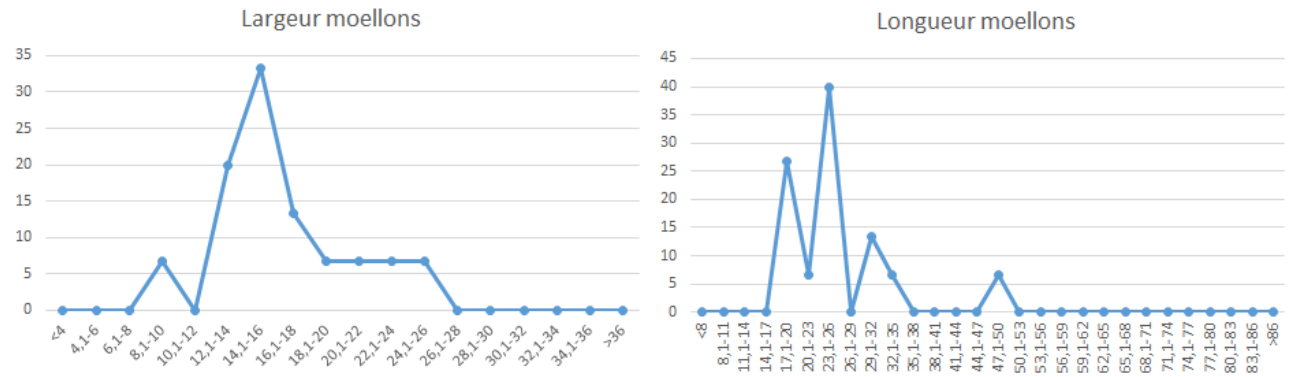

Copyright © 2016 labex TransferS | Pôle Humanités Numériques
Ce contenu est sous licence Creative Commons BY-NC-SA.

Atlas des techniques de la Construction Romaine

Mur : MR-0036

Identification

Identité	Elévation : Mur MR-0036 ; 2 éléments
Provenance	Nicaea, Aqueduc
Phase(s) chronologique(s)	Réaménagement 6 (800) : Reconstructions en matériaux variés
Description	Maçonnerie régulière de moellons quadrangulaires en matériaux variés.

Caractéristiques générales

Type morphologique	En plan : Linéaire continu. En coupe : A faces parallèles
Fonction	Elément non porteur
Section	Parementé (2 parements) ; Présence d'un noyau interne

Parement

Matériau	Pierre (calcaire, travertin) - Liant (mortier de chaux et de sable) - Autre
Pierres	**Forme** : Quadrangulaire : rectangulaire **Finition** : Surface dressée **Épaisseur** : Constante **Dureté** : Dure - Ferme **Dimensions** : Petit et grand module ; Long. : 31 ; Haut. : 12 ; Module de 5 assises : 80 ; Épaisseur des joints : 4
Assises	**Disposition des matériaux** : Assises horizontales **Disposition des pierres** : En boutisse & en panneresse, disposition irrégulière (en parement) ; [Autre] (en coupe) **Hauteur** : Irrégulière **Assises de réglage** : Pierre
Joints	**Épaisseur** : > 2 cm
Commentaire	Présence de remplois (marbre). Taille soignée, surtout pour le travertin. Joints très altérés. Mortier blanc, granuleux, riche en grains (nature et granulométrie hétérogènes, 1-2 mm ou plus), solide. Deux assises de réglages soulignée par des travertins plats.

Arc

Type morphologique	En plan : En plein cintre surhaussé En section : Homogène Forme : Extradossé
Fonction	Passage - Élévations
Position	En élévation - Isolé

Références

Auteur(s) de la notice	Yacine Benjelloun
Date de création	21/06/2016
Édition électronique	Agnès Tricoche
Citer cette notice	Base de données ACoR (en ligne), notice MR-0036, https://acor.huma-num.fr/MR-0036/fr. Consultée le 10/08/2017.

Images

MR-0036-2.jpg - Echantillon (photographie / relevé)
Yacine Benjelloun



MR-0036-1.png - Courbe statistique / histogramme
Yacine Benjelloun

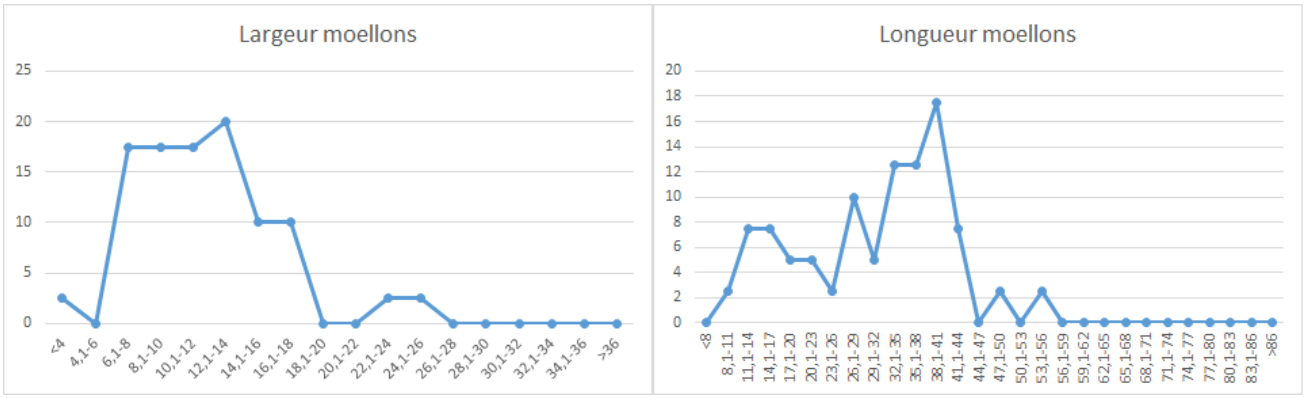

Copyright © 2016 labex TransferS | Pôle Humanités Numériques
Ce contenu est sous licence Creative Commons BY-NC-SA.

Atlas des techniques de la Construction Romaine

Mur : MR-0038

Identification

Identité	Elévation : Mur MR-0038 ; 1 élément
Provenance	Nicaea, Aqueduc
Phase(s) chronologique(s)	Réaménagement 4 : Nouveau parement en blocs de travertin et TCA
Description	Maçonnerie régulière faisant alterner 1 assise de moellons séparés par des TCA dressées et 1 assise de TCA.

Caractéristiques générales

Type morphologique	En plan : Linéaire continu. En coupe : A faces parallèles
Fonction	Elément porteur
Section	Parementé

Parement

Matériau	Pierre (calcaire, travertin) - Terre cuite - Liant (mortier de chaux et de sable)
Pierres	**Forme** : Quadrangulaire : rectangulaire **Finition** : Surface dressée **Épaisseur** : Constante **Dureté** : Ferme **Dimensions** : Grand module ; Long. : 42 ; Haut. : 30 ; Épaisseur des joints : 5
Terres cuites architecturales	**Forme** : Tuiles **Dimensions moyennes (cm)** : Long. : 22 ; Haut. : 4 ; Épaisseur des joints : 5
Assises	**Disposition des matériaux** : Assises en damiers **Disposition des pierres** : En panneresse (en parement) **Disposition des terres cuites architecturales** : En boutisse & en panneresse, disposition irrégulière **Hauteur** : Irrégulière **Assises de réglage** : Pierre
Joints	**Épaisseur** : > 2 cm
Commentaire	Le parement fait alterner 1 assise de TCA, et 1 assise de pierres alternées avec des TCA dressées. Présence d'1 assise de calcaire sans TCA. Les TCA sont rouges et épaisses, de qualité et de forme hétérogènes. Le travertin est bien taillé contrairement au calcaire massif. Le mortier est riche en grains assez grossiers (5 mm- plusieurs cm).

Références

Auteur(s) de la notice	Yacine Benjelloun
Date de création	22/06/2016
Édition électronique	Agnès Tricoche
Citer cette notice	Base de données ACoR (en ligne), notice MR-0038, https://acor.huma-num.fr/MR-0038/fr. Consultée le 10/08/2017.

Images

MR-0038-4.jpg - Echantillon (photographie / relevé)

Yacine Benjelloun



MR-0038-1.png - Courbe statistique / histogramme
Yacine Benjelloun

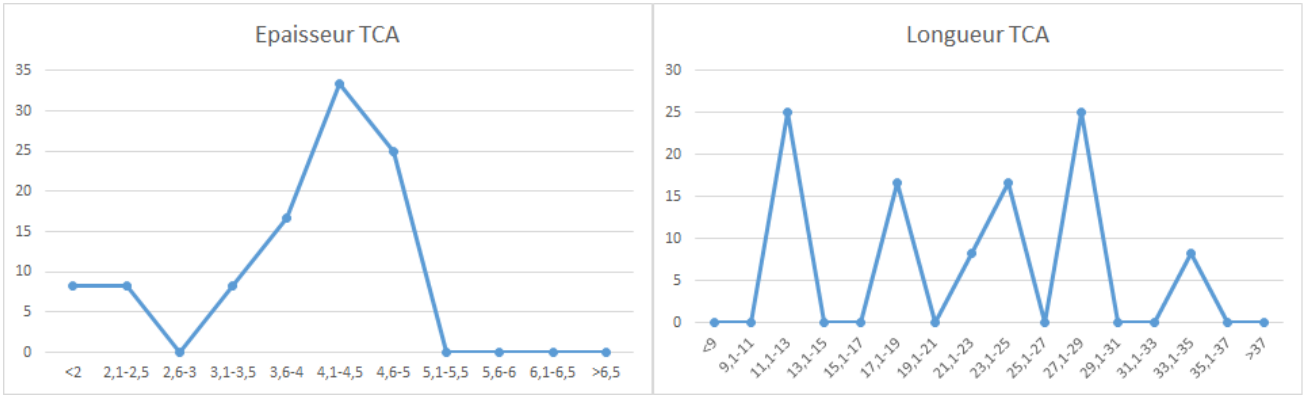

MR-0038-2.png - Courbe statistique / histogramme

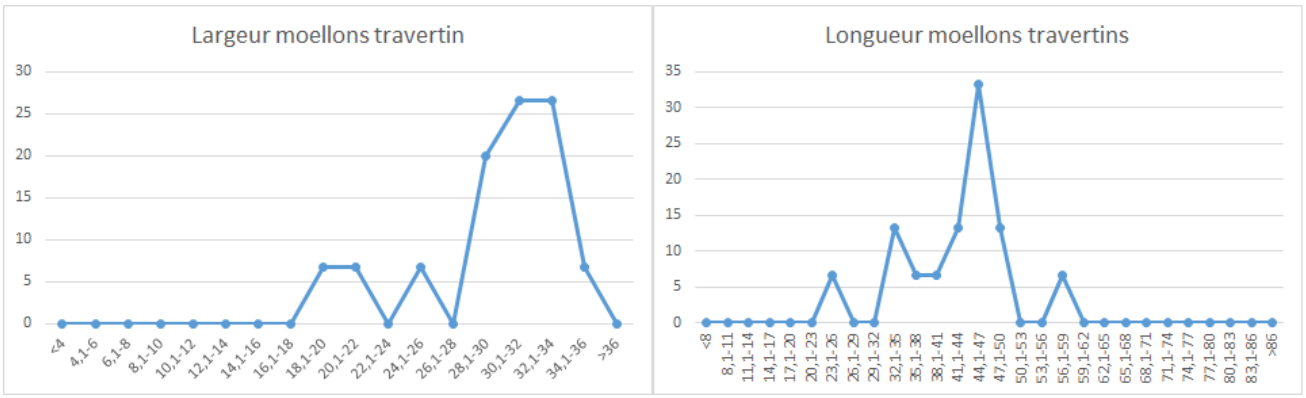

Copyright © 2016 labex TransferS | Pôle Humanités Numériques
Ce contenu est sous licence Creative Commons BY-NC-SA.

Atlas des techniques de la Construction Romaine

Mur : MR-0041

Identification

Identité	Elévation : Mur MR-0041 ; 1 élément
Provenance	Nicaea, Aqueduc
Phase(s) chronologique(s)	Projet originel (527/565)
Description	Maçonnerie la plus précoce de l'aqueduc composée d'une alternance régulière de TCA et de moellons calcaires.

Caractéristiques générales

Type morphologique	En plan : Linéaire interrompu. En coupe : A faces parallèles
Fonction	Elément porteur
Section	[Non visible]

Parement

Matériau	Pierre (calcaire) - Terre cuite - Liant
Pierres	**Forme** : Polygonale **Finition** : Absence de finition **Dureté** : Dure
Terres cuites architecturales	**Forme** : Tuiles ; Haut. : 4,5
Assises	**Disposition des matériaux** : Assises horizontales **Disposition des pierres** : En panneresse (en parement) ; 1 assise (en coupe) **Disposition des terres cuites architecturales** : En panneresse, disposition irrégulière **Particularités** : Irrégulières avec interruptions **Hauteur** : Régulièrement alternée (pseudo-isodome) **Assises de réglage** : Terres cuites architecturales
Commentaire	Mortier granulaire, terreux, à gros grains (>cm, ou agrégats).

Arc

Type morphologique	En plan : En plein cintre En section : Homogène Forme : Extradossé
Fonction	Passage - Élévations
Position	En élévation - En série

Références

Auteur(s) de la notice	Yacine Benjelloun
Date de création	22/06/2016
Édition électronique	Agnès Tricoche
Citer cette notice	Base de données ACoR (en ligne), notice MR-0041, https://acor.huma-num.fr/MR-0041/fr. Consultée le 10/08/2017.

Images

MR-0041-1.jpg - Echantillon (photographie / relevé)

Yacine Benjelloun



MR-0041-2.png - Courbe statistique / histogramme
Yacine Benjelloun

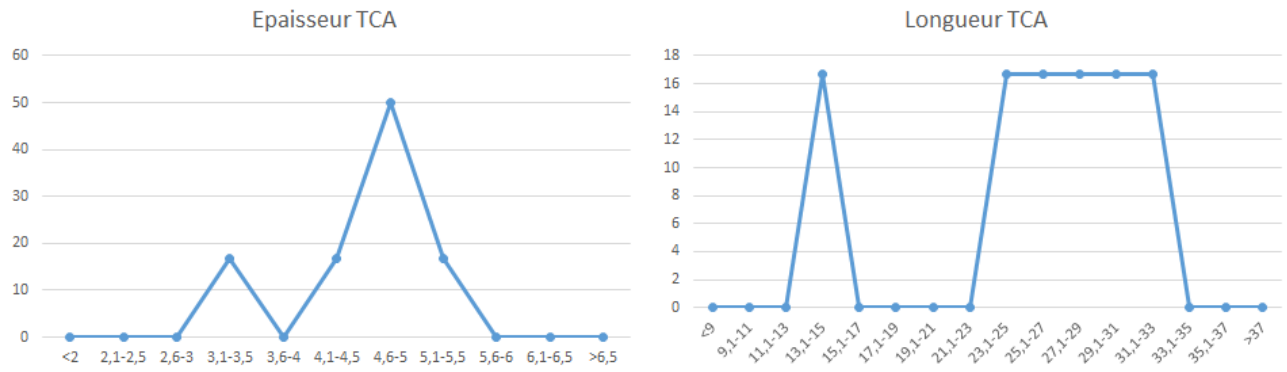

Copyright © 2016 labex TransferS | Pôle Humanités Numériques
Ce contenu est sous licence Creative Commons BY-NC-SA.

Atlas des techniques de la Construction Romaine

Mur : MR-0142

Identification

Identité	Elévation : Mur MR-0142 ; 1 élément
Provenance	Nicaea, Aqueduc
Phase(s) chronologique(s)	Réaménagement 3 : Reconstruction du chenal et ajout d'un contrefort et d'un bassin de répartition
Description	Appareil irrégulier de petits moellons calcaires situé au niveau du chenal.

Caractéristiques générales

Type morphologique	En plan : A faces parallèles - Linéaire continu. En coupe : A faces parallèles
Fonction	Elément non porteur
Section	Parementé (2 parements) ; Parements de même technique

Parement

Matériau	Pierre (calcaire) - Liant (mortier de chaux et de sable)
Pierres	**Forme** : Irrégulière - Polygonale **Finition** : Absence de finition **Épaisseur** : Constante **Dureté** : Dure **Dimensions** : Petit et grand module ; Long. : 18 ; Haut. : 11
Assises	**Disposition des matériaux** : Sans assises **Disposition des pierres** : En boutisse & en panneresse, disposition irrégulière (en parement) ; [Autre] (en coupe) **Hauteur** : Constante (isodome)
Commentaire	Mortier blanc très riche en grains assez grossiers (3 mm-2 cm), très dur.

Références

Auteur(s) de la notice	Yacine Benjelloun
Date de création	31/03/2017
Édition électronique	Agnès Tricoche
Citer cette notice	Base de données ACoR (en ligne), notice MR-0142, https://acor.huma-num.fr/MR-0142/fr. Consultée le 10/08/2017.

Images

MR-0142-2.jpg - Echantillon (photographie / relevé)
Yacine Benjelloun



MR-0142-1.png - Courbe statistique / histogramme
Yacine Benjelloun

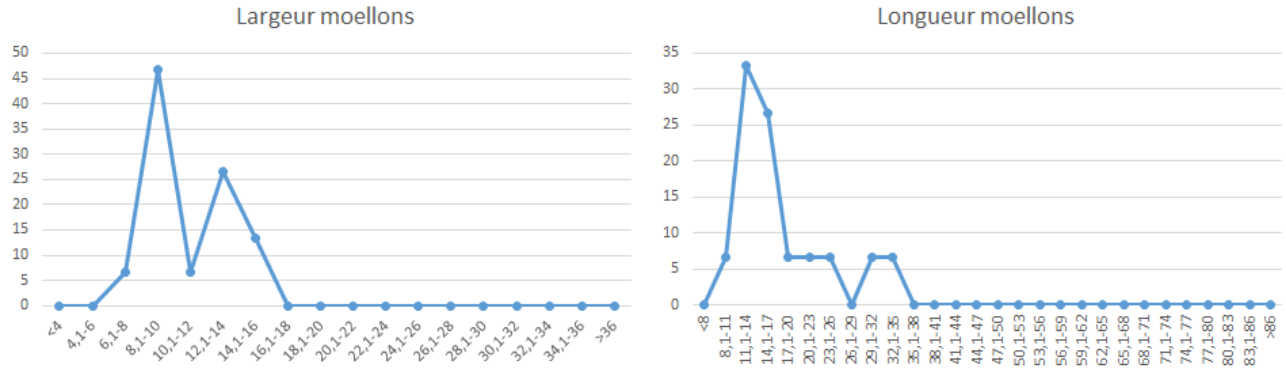

Copyright © 2016 labex TransferS | Pôle Humanités Numériques
Ce contenu est sous licence Creative Commons BY-NC-SA.

Atlas des techniques de la Construction Romaine

Mur : MR-0143

Identification

Identité	Elévation : Mur MR-0143 ; 1 élément
Provenance	Nicaea, Aqueduc
Phase(s) chronologique(s)	Réaménagement 6 (800) : Reconstructions en matériaux variés
Description	Maçonnerie peu soignée à assises régulières de moellons de tailles et matériaux variés.

Caractéristiques générales

Type morphologique	En plan : A faces parallèles - Linéaire continu. En coupe : A faces parallèles
Fonction	Elément non porteur
Section	Parementé (2 parements) ; Présence d'un noyau interne ; Parements de même technique

Parement

Matériau	Pierre (calcaire, travertin, marbre) - Liant (mortier de chaux et de sable)
Pierres	**Forme** : Quadrangulaire : rectangulaire **Finition** : Absence de finition **Dureté** : Ferme - Dure
Assises	**Disposition des matériaux** : Assises horizontales **Disposition des pierres** : En panneresse (en parement) ; 1 assise (en coupe)
Joints	**Finition** : Sans finition

Précisions

Notes	Maçonnerie surtout visible sous le pont de la route Iznik-Orhangazi.

Références

Auteur(s) de la notice	Yacine Benjelloun
Date de création	26/04/2017
Édition électronique	Agnès Tricoche
Citer cette notice	Base de données ACoR (en ligne), notice MR-0143, https://acor.huma-num.fr/MR-0143/fr. Consultée le 10/08/2017.

Images

MR-0143-1.jpg - Echantillon (photographie / relevé)
Yacine Benjelloun



Copyright © 2016 labex TransferS | Pôle Humanités Numériques
Ce contenu est sous licence Creative Commons BY-NC-SA.

Atlas des techniques de la Construction Romaine

Mur : MR-0144

Identification

Identité	Elévation : Mur MR-0144 ; 3 éléments
Provenance	Nicaea, Aqueduc
Phase(s) chronologique(s)	Réaménagement 8 (1900) : Restauration moderne du chenal en ciment
Description	Restauration moderne à assises plus ou moins régulières de moellons de marbre et calcaire, partiellement recouverts de ciment.

Caractéristiques générales

Type morphologique	En plan : A faces parallèles - Linéaire continu. En coupe : A faces parallèles
Fonction	Elément non porteur
Section	Parementé (2 parements) ; Présence d'un noyau interne ; Parements de même technique

Parement

Matériau	Pierre (calcaire, marbre) - Liant (plâtre et autres composants)
Pierres	**Forme** : Polygonale **Finition** : Absence de finition **Dureté** : Dure
Assises	**Disposition des matériaux** : Assises ondulées **Disposition des pierres** : En panneresse (en parement) ; 1 assise (en coupe)
Commentaire	Les moellons sont joints par du ciment, qui les recouvre partiellement. Les joints entre moellons ont été retracés à la pointe de la truelle.

Références

Auteur(s) de la notice	Yacine Benjelloun
Date de création	26/04/2017
Édition électronique	Agnès Tricoche
Citer cette notice	Base de données ACoR (en ligne), notice MR-0144, https://acor.huma-num.fr/MR-0144/fr. Consultée le 10/08/2017.

Images

MR-0144-1.jpg - Echantillon (photographie / relevé)
Yacine Benjelloun



Copyright © 2016 labex TransferS | Pôle Humanités Numériques
Ce contenu est sous licence Creative Commons BY-NC-SA.

Appendix F

Sediment cores sampled on the basilica site

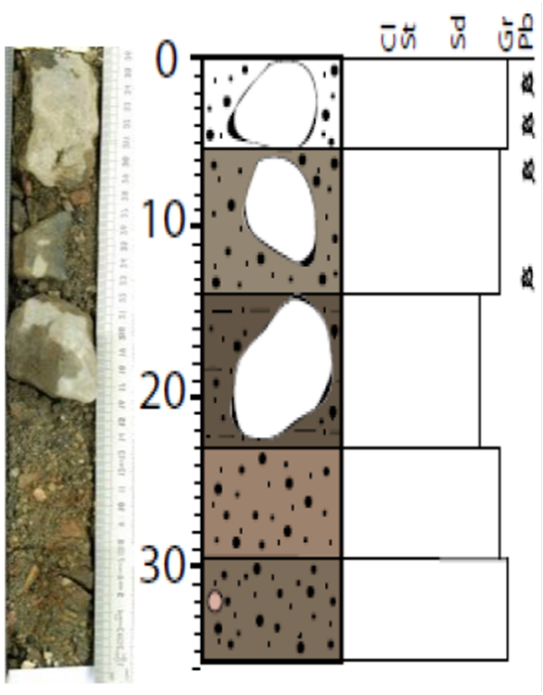

Unit I (0-14 cm): Brown layer of coarse sand and gravels. Presence of 10 cm thick pebbles .

Unit II (14-23 cm): Dark brown mixture of silt and coarse sand. Presence of a 10 cm thick pebble.

Unit III (23-35.5 cm): Brown sandy fraction. Presence of gravels.

Figure F.1: Photos (left), interpretative scheme (center) and granulometry (right) of sediment cores BA16-2, modified from Py-Circan (2017).

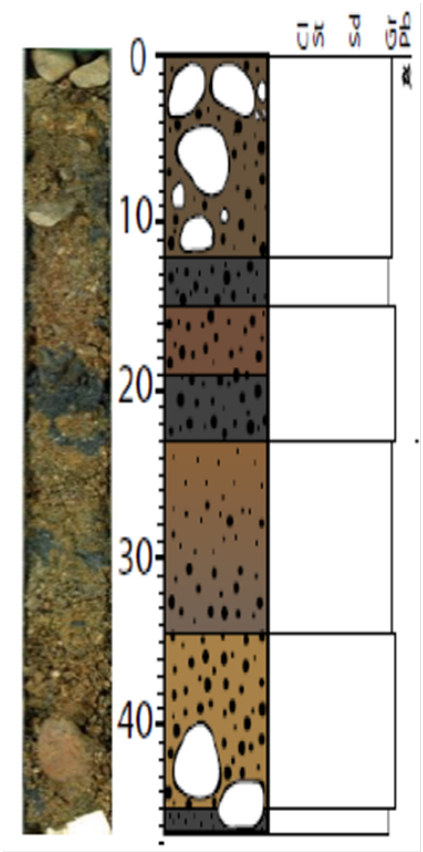

Unit I (0-12 cm): Dark brown mixture of coarse sand and gravels. Presence of several pebbles and one organic remain .

Unit II (13-23 cm): Black mixture of sand and gravels.

Unit III (23-34.5 cm): Yellowish brown sandy fraction. Finer material at the top of the unit.
Unit IV (34.5-45 cm): Yellowish brown layer of very coarse sand. Presence of gravels and pebbles.
Unit V (45-46.5 cm): Black sandy fraction.

Figure F.2: Photos (left), interpretative scheme (center) and granulometry (right) of sediment cores BA16-3, modified from Py-Circan (2017).

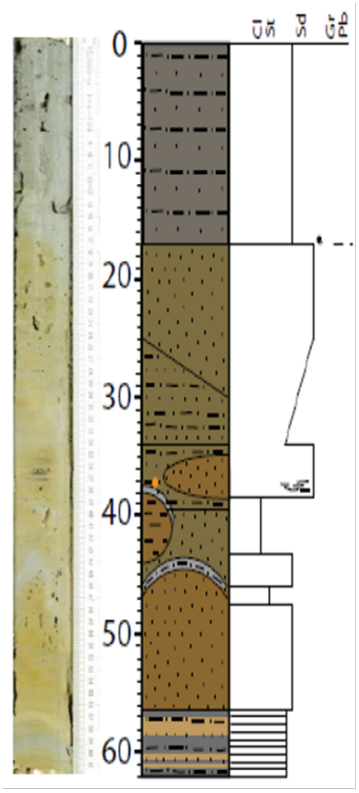

Unit I (0-15 cm): Dark grey mixture of coarse sand and silt. Presence of a shell at the base of the unit.

Unit II (15-28.5 cm): Olive green sandy fraction.

Unit III (28.5-46 cm): Laterally disturbed sediments. Presence of sand, grey silt and brown clay.

Unit IV (46-56.5 cm): Homogeneous, dark brown sandy fraction.

Unit V (56.5-61 cm): Alternations of dark grey fine sand and brownish yellow silt.

Figure F.3: Photos (left), interpretative scheme (center) and granulometry (right) of sediment cores BA16-5, modified from Py-Circan (2017).